

Alma Mater Studiorum – Università di Bologna

DOTTORATO DI RICERCA IN
BIOINGEGNERIA

Ciclo XXIX

Settore Concorsuale di afferenza: 09/G2

Settore Scientifico disciplinare: ING-IND/34

***IN VITRO* FULL-FIELD METHODS FOR THE
BIOMECHANICAL CHARACTERIZATION
OF SPINE SEGMENTS**

Presentata da: **Marco Palanca**

Coordinatore
Prof. Elisa Magosso

Relatore
Prof. Luca Cristofolini

Correlatore
Dott. Enrico Dall'Ara
Dott. Gianluca Tozzi

Controrelatore
Prof. Angelo Cappello

Esaminatore Esterno
Prof. Harry van Lenthe

Bologna, Marzo 2017

A Me
A Te
A Noi

Abstract

The spine is a complex and a still partially unexplored structure. Due to the constantly increasing longevity and the sedentary life-style typical of the industrialized countries, spinal diseases are becoming a serious problem inside the modern society and a deeper knowledge of spine biomechanics is required.

In the literature a series of works investigated the biomechanics of the spine in order to characterize the overall spine, its organs, its tissues separately, in physiological, pathological and after treatment conditions. *In vivo* tests are performed evaluating the range or motion and the spinal loads in living subjects. *In vitro* tests allow measuring the strain on vertebrae and intervertebral discs and testing new spinal devices. Moreover, *in silico* tests are useful to simulate different loading scenarios, pathologies, and devices, especially when used in synergies with *in vivo* and *in vitro* tests. A methodology to merge the evaluation of the range of motion with the full-field strain measurement was not been implemented. A clear description of the strain associated to physiological tasks can help the clinicians, can improve the design of new devices and can guide the development of new surgical procedures. In order to achieve this goal, the mapping of the strain distribution must be achieved simultaneously on the vertebrae and the intervertebral discs.

The aim of my PhD thesis was the implementation and improvement of the methodologies to quantify the displacements and strains in spine segments in a full-field view and a contactless way, in order to characterize the biomechanics of the spine as a whole and in the details of its organs.

The first part of this thesis focuses on the evaluation of the displacements and strains distribution on the entire spine surface. In order to achieve this goal a contactless, full-field measurement technique was employed and optimized: the Digital Image Correlation (DIC). Before starting to use the Digital Image Correlation, the tool was deeply validated, starting from mechanical specimen (aluminum beam) up to biological specimen (vertebrae). A factorial-design allowed optimizing the procedure to prepare a repeatable and reproducible speckle pattern and identifying the best acquisition/elaboration parameters. The optimization reduced the systematic error to 10 microstrain and the random error to 110 microstrain. Porcine spine segments, with intervertebral discs, were used to explore the feasibility of measuring strain on the entire specimen surface using the Digital Image Correlation. To measure the strain distribution on the hard and soft tissues, the spine segments were prepared with a random white-on-black speckle pattern and tested in simplified loading conditions to reproduce the anterior bending and the lateral bending. The displacements and the strains were thus evaluated, simultaneously on the vertebrae and on the intervertebral discs, using the optimized Digital Image Correlation showing the potentiality of exploring the spine as a whole and in detail.

The second area of research consists in going beyond the evaluation of measurements on the specimen surface, and providing the three-dimensional displacements and strains maps inside the specimen through Digital Volume Correlation (DVC). Of course the measurement uncertainties cannot be taken for granted. Even more than in the Digital Image Correlation, the reliability of Digital Volume Correlation must be assessed; because of no other measurement techniques are able to provide comparable measurements. Different studies were developed from the tissue-level (bovine cortical and trabecular bone cores) up to organ-level (porcine vertebrae and murine tibiae). Both laboratory micro-CT (voxel size 10-40 micrometers), and synchrotron radiation micro-CT (voxel size 1.6 micrometers – Diamond Light Source) were used to assess the impact of the quality and resolution of the input images. As no alternative measurement technique can be used to quantify the errors of DVC, multi-factorial (tissue types, imaging techniques, spatial resolutions, DVC approaches, DVC parameters) studies were designed based on datasets shared between different research centres (like Round-Robin test). This allowed to assess the effect of the single parameters on the final displacement and strain measurements. All the specimens were scanned twice without any repositioning and without any loads, because this procedure is the only way to know certainly the strains (zero-strain) within the specimen. Furthermore the algorithms were verified using artificially translated images. All these tests did not complete the validation of the Digital Volume Correlation that is still challenging, but defined the minimum and unavoidable intrinsic measurement errors related to the compromise between measurement uncertainties and measurement spatial resolution. The original goal was to obtain a measurement uncertainty lower than 200 micrometers in order to use the DVC also for the measurement of strain related to physiological loads. The threshold was reached with a measurement spatial resolution of $\approx 2\text{mm}$ for laboratory source microCT based DVC and 40/80 micrometers for Synchrotron radiation microCT based DVC. The acquired background about the optimization of the DVC parameters was exploited to start measuring the strain distribution within a vertebral body under load. This final work showed the strain gradients inside the vertebra in a destructive stepwise loading, highlighting, already in the elastic regime, the highest strain region where failure will start.

In conclusion, the project highlighted the importance of a careful validation before using these novel measurement techniques and confirmed that after optimizing the experimental details it is possible to apply these new procedures on spine segments. The methodologies can be considered as completed, but in the next years the application of the methods should be performed on human specimens: applying more complex loading scenarios and exploring the biomechanics in physiological, pathological and instrumented specimens.

Contents

1. Introduction.....	pag. 13
1.1 Background.....	pag. 14
1.2 Pathologies.....	pag. 16
1.3 The implications of the spinal diseases on our society	pag. 17
1.4 How can we explore the spine biomechanics?.....	pag. 18
1.5 What is it still unsolved?	pag. 20
1.6 Aim of my PhD project.....	pag. 20
1.7 Outline of the thesis	pag. 21

PART I

DISPLACEMENT AND STRAIN MEASUREMENT ON THE SPECIMEN SURFACE

2. Overview of applications of Digital Image Correlation in biomechanics.. .	pag. 23
2.1 Introduction	pag. 24
2.1.1 Why is it important to measure full-field displacement and strain.....	pag. 24
2.1.2 Overview of full-field, contactless optical measurement technique.....	pag. 24
2.1.3 Aim.....	pag.25
2.2 Introducing Digital Image Correlation (DIC)	pag. 25
2.2.1 History of DIC	pag. 25
2.2.2 Operating principle	pag. 38
2.3 Surface pattern preparation on biological specimens	pag. 39
2.4 Correlation algorithm parameters	pag. 41
2.4.1 Facet size	pag. 41

In vitro full-field methods for the biomechanical characterization of spine segments (M. Palanca)

2.4.2 Grid spacing	pag. 41
2.4.3 Strain computed window.....	pag. 42
2.4.4 Validity quote	pag. 42
2.4.5 Filtering	pag. 42
2.5 Error affecting DIC measurement in biomechanics	pag. 43
2.5.1 Accuracy and precision.....	pag. 43
2.5.2 Errors due to the pattern	pag. 44
2.5.3 Errors due to the acquired images.....	pag. 45
2.5.4 Errors due to the correlation process	pag. 45
2.5.5 Recommendations to minimize measurement errors in biomechanical applications.....	pag. 45
2.6 Example of biomechanical applications.....	pag. 46
2.6.1 Applications to soft tissue	pag. 47
2.6.2 Applications to hard tissue.....	pag. 49
2.7 Synergies with Finite Element in Biomechanics	pag. 50
2.8 Other image correlation tools.....	pag. 51
2.9 Conclusions.....	pag. 52
Appendix	pag. 53
3. Optimization and Validation of Digital Image Correlation	pag. 55
3.1 Introduction	pag. 56
3.2 Material and Methods	pag. 56
3.2.1 Optimization of the preparation of the speckle pattern	pag. 56
3.2.2 Benchmark test	pag. 57
3.2.3 Preliminary test on a vertebra specimen	pag. 58
3.3 Results.....	pag. 58
3.3.1 Optimal speckle pattern	pag. 58
3.3.2 Accuracy and precision in the benchmark test.....	pag. 59
3.3.3 Results of the test on a vertebra specimen.....	pag. 62
3.4 Discussion	pag. 63
4. Application of Digital Image Correlation on spine	pag. 64
4.1 Introduction	pag. 65

In vitro full-field methods for the biomechanical characterization
of spine segments (M. Palanca)

4.2 Material and methods	pag. 66
4.2.1 Specimen and patten preparation.....	pag.66
4.2.2 Mechanical testing.....	pag.67
4.2.3 Digital Image Correlation	pag. 68
4.3 Results.....	pag. 69
4.3.1 Strain error	pag. 69
4.3.2 Anterior bending – frontal view	pag. 70
4.3.3 Anterior bending – lateral view.....	pag. 71
4.3.4 Lateral bending – frontal view.....	pag. 71
4.3.5 Lateral bending – lateral view	pag. 72
4.4 Discussion	pag. 72
4.5 Conclusion.....	pag. 74

PART II

DISPLACEMENT AND STRAIN MEASUREMENT INSIDE THE SPECIMENS

5. Errors in Digital Volume Correlation in the biomechanical field	pag. 76
.....
5.1 Introduction	pag. 77
5.2 Digital Volume Correlation operating principles	pag. 77
5.3 Causes of errors	pag. 78
5.4 How can we account accuracy and precision?	pag. 80
5.4.1 Zero-strain scenarios	pag. 80
5.4.2 Known strain scenarios	pag. 81
5.5 Metrics	pag. 82
5.6 Summary of the validation works.....	pag. 82
5.6.1 Tissue level	pag. 82
5.6.2 Organ level	pag. 88
5.7 Conclusion.....	pag. 88

6. Validation of Digital Volume Correlation at tissue level-microCT	pag. 89
6.1 Introduction	pag. 90
6.2 Material and Methods	pag. 91
6.2.1 Specimens and images	pag. 91
6.2.2 DVC approaches under investigation	pag. 93
6.2.3 Influence of sub-volume size	pag. 95
6.2.4 Metrics to quantify the accuracy and precision	pag. 95
6.3 Results	pag. 97
6.3.1 Displacement	pag. 97
6.3.2 Strain	pag. 100
6.3.3 Computational Costs	pag. 108
6.4 Discussion	pag. 109
6.5 Conclusion	pag. 110
7. Validation of Digital Volume Correlation at tissue level with biomaterials-microCT	pag. 113
7.1 Introduction	pag. 114
7.2 Methods	pag. 115
7.2.1 Specimens	pag. 115
7.2.2 Experimental procedures and volumes of interest (VOIs)	pag. 116
7.2.3 Digital Volume Correlation (DVC) approaches	pag. 117
7.2.4 Evaluation of errors as a consequence of the computation sub-volume	pag. 118
7.3 Results	pag. 119
7.4 Discussion	pag. 123
7.5 Conclusions	pag. 128
8. Validation of Digital Volume Correlation at organ level-microCT	pag. 129
8.1 Introduction	pag. 130
8.2 Material and Methods	pag. 131
8.2.1 Specimens and images	pag. 131
8.2.2 Local vs. global approach	pag. 132
8.2.3 Quantification of the errors (error metrics)	pag. 134

8.3 Results.....	pag. 135
8.3.1 Errors over VOI-0	pag. 135
8.3.2 Errors over VOI-1	pag. 136
8.4 Discussion	pag. 139
Supplementary material.....	pag. 145
9. Validation of Digital Volume Correlation at tissue level and organ level - synchrotronCT	pag. 146
9.1 Introduction	pag. 148
9.2 Material and Methods	pag. 149
9.2.1 Specimen preparation, tomography and image processing	pag. 149
9.2.2 DVC protocol.....	pag. 151
9.2.3 Quantification of errors.....	pag. 153
9.3 Results.....	pag. 153
9.3.1 Random error for the displacements.....	pag. 153
9.3.2 Accuracy and precision: average of components.....	pag. 155
9.3.3 Systematic errors for each component of strain	pag. 156
9.3.4 Random errors for each component of strain	pag. 158
9.3.5 Strain distribution of the errors	pag. 159
9.4 Discussion	pag. 160
9.5 Conclusion.....	pag. 162
10. Conclusions	pag. 163
Appendix (Application of Digital Volume Correlation on vertebrae).....	pag. 167
1. Introduction	pag. 168
2. Methods	pag. 170
2.1 Material and experimental procedures.....	pag. 170
2.2 Digital Volume Correlation (DVC).....	pag. 171
3. Results	pag. 172
4. Discussion	pag. 176
5. Conclusions	pag. 177

***Bibliography* pag 179**

***Acknowledgements* pag 203**

***Scientific Publications of the candidate*..... pag. 204**

Papers in International Journals pag. 204

Proceedings of International Conferences pag. 205

Proceedings of national Conferences pag. 207

Chapter I

Introduction

1.1 Background

The spine is one of the most complex portions of the skeleton to study (White III and Panjabi, 1990): it consists in an alternation of vertebrae (seven cervical, twelve thoracic, five lumbar and four/five fused sacral, three-five fused coccyx vertebrae) and intervertebral discs, stabilized by a series of ligaments (Fig. 1). In the next lines I will not deal with the spine anatomy in detail, instead I will briefly describe the organs, which constitute the spine, and their biomechanical function.

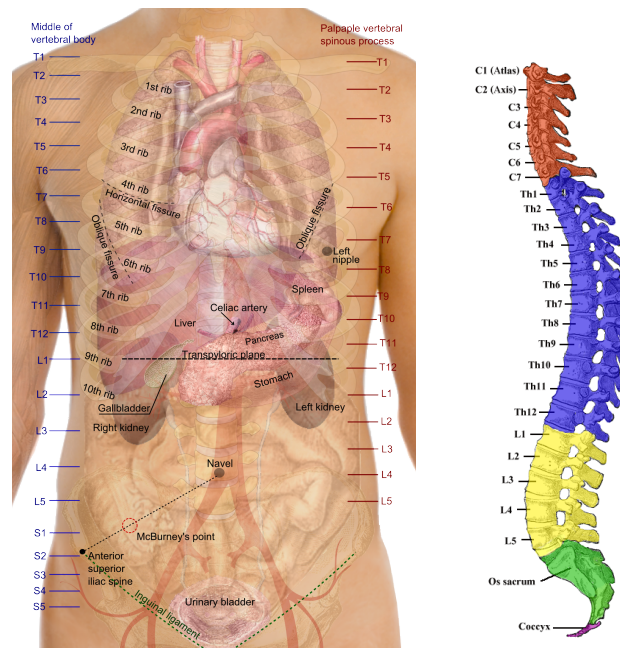


Fig. 1: On the left (Image from: By Mikael Häggström [Public domain], via Wikimedia Commons): The spine occupies a central position in the human body and plays a fundamental role to sustain organs. On the right (Image from: Henry Vandyke Carter [Public domain or Public domain], via Wikimedia Commons): In the spine, five different segments can be distinguished in relation to vertebrae shape, from top to down: cervical (red), thoracic (blue), lumbar (yellow), sacrum (green), coccyx (purple).

The vertebrae (Fig. 2) are irregular bones, their dimension varies according to their position in the spine, posture, load, pathology (Gray, 1858). Each vertebra has a vertebral body, a thick layer of cortical bone that surrounds the trabecular bone, a posterior arch and the processes, with a thicker cortical bone. Finally between the body and the arch there is the spinal cavity, where the spinal cord is placed. The vertebrae are the hard tissues of the spine. The principal functions of the vertebrae are:

- Supporting the body, forming the vertebral column;
- Allowing the movement, in fact the upper and lower surfaces of the vertebrae are attached to the ligamenta flava, which allow the movements of the upper body;
- Protecting the spinal cord, due to vertebra shape and geometry.

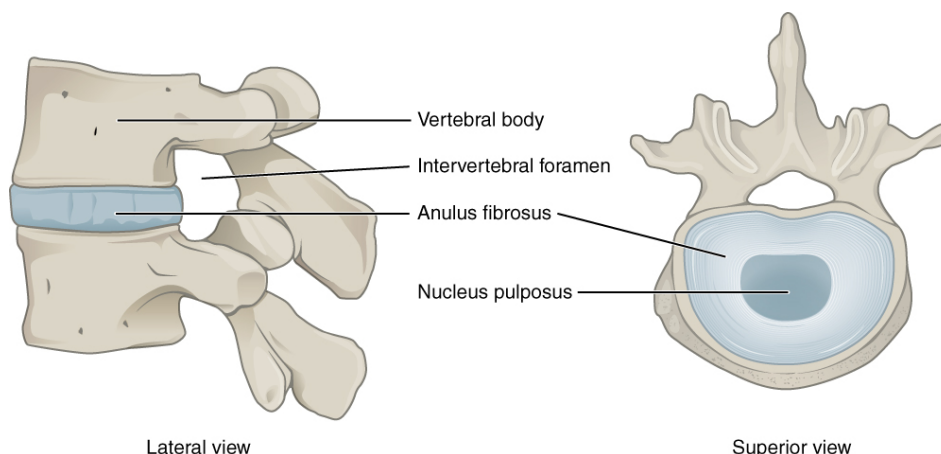


Fig. 2: Vertebrae and intervertebral disc. In the vertebra can be distinguished the vertebral body, the processes, and the posterior arch. The intervertebral discs instead is represented on the left between the vertebrae and, on the right, sectioned. On the sectioned view is possible appreciate the nucleus pulposus surrounded by the annulus fibrosus (Image from: OpenStax College - Anatomy & Physiology, Connexions Web site. <http://cnx.org/content/col11496/1.6/>, Jun 19, 2013., CC BY 3.0)

The intervertebral discs (Fig. 2) are composed of two soft tissues (Cassidy et al., 1989): the *anulus fibrosus*, layers of fibrocartilages, and inside the *nucleus pulposus*, fibers scattered in a mucoprotein gel. The structure of the intervertebral discs allows them to carry out the function of shock absorber, distributing the pressure in all directions and dumping the force peaks from the lower limbs. Furthermore connecting the vertebrae each other, the intervertebral discs restrain some movements of the spine: constrain the translations and allow the rotations, preserving the neighboring nervous tissues. The vertebrae and intervertebral discs are connected by the endplates, made of hyaline cartilage. The endplates contain the discs and provide anchorage of the collagen fibers.

Finally, the spinal ligaments (anterior longitudinal, posterior longitudinal, ligamentum flavum, facet capsular ligament, intertransverse ligament, interspinous ligament, supraspinous ligament) are fibrous bands or sheets of connective tissue, made of collagenous fibers (Fig. 3). Each of the ligaments has its specific function (Aspden, 1992) but, generally, they play the role of interconnecting the vertebrae each other and preserving the upright posture, avoiding excessive movements or movement in certain directions.

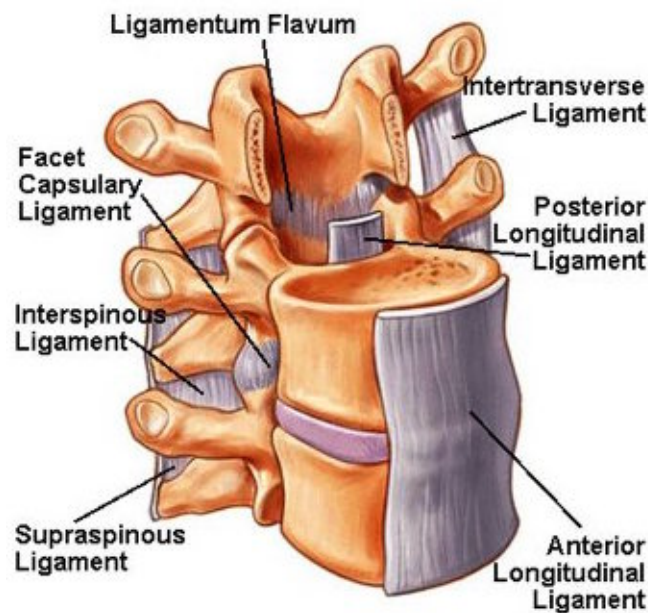


Fig. 3: Description of the common and principal ligaments on spine (Image from: <http://ranzcrpart1.wikia.com/wiki/File:PicA2.jpg>)

Each of these organs has specific characteristics, behaviors and specific roles in the musculoskeletal apparatus and they are actually different from each other. But looking at the spine as a whole, it plays the fundamental roles of supporting the body in a standing position allowing a wide range of movements and protecting the spinal cord.

1.2 Pathologies

The effects of spine diseases and failures affect a large portion of populations. They could be done to different causes and could affect different organs: vertebrae, intervertebral discs and ligaments.

The scoliosis (Aebi, 2005; Donzelli et al., 2015), hyper-kyphosis (Barrett et al., 2014) and hyper-lordosis (Been and Kalichman, 2014) are the most frequent syndromes of the spine. They could affect young and old people, with a large variety of emphases, symptoms and effects. These syndromes consist in a degeneration of a spine segment, more or less extended, (not concentrated on the single organ) that change the physiological spine curvature. The different levels of the syndrome can evolve in different issues: from the back pain, passing to cardio-respiratory diseases up to immobility.

The vertebrae, as other bones, can be affected by pathologies such as osteoporosis and osteopenia (WHO, 1994, 2007). These pathologies entail, respectively, the gradual loss of bone density (Morita et al., 1994; Ritzel et al., 1997) and of bone mineral density (Karaguzel and Holick, 2010), reducing the strength of the bone. These conditions increase the risk of vertebral fractures, and concurrently of forearm and hip fractures, in the elderly under daily loading conditions (Myers and Wilson, 1997; Silva, 2007); with the consequent high risk

of correlated diseases on the neighbor nervous tissue. Moreover, the function of the vertebrae could be compromised by metastasis, usually from prostate or lung cancers. In this case, the vertebrae show a significantly reduction of the bone mass, and consequently the reduction of their strength section (Botelho et al., 2013; Choi et al., 2010). A well-defined surgical procedure is missing, due to the poor number of cases and the advances in technologies. It entails to increase the risk associated to this pathology and the deep influence on the life quality.

The intervertebral discs, as the vertebrae, are subjected to a series of pathologies that compromise their function and could lead to immobility. As described above, the intervertebral discs have the function of shock absorber, so they are continuously stressed during the normal daily activity. The most known pathology affecting the intervertebral discs is the slipped disc (Jordan et al., 2011): it consists in a bulge over the edge of the intervertebral disc, due to the loss of their elasticity becoming brittle and cracked. There are different level of slipped disc and related different symptom, from the totally asymptomatic to the immobility for the spinal cord compression. The spondylolisthesis, another disc pathology, represent the translation of a vertebra on another (Matz et al., 2016). It could involve in back pain and immobility. Clinicians through screws and bars systems, as for other spinal pathologies, restore the regular anatomy of the spine, but after a first asymptomatic period, in the 40% of the cases (Jutte and Castelein, 2002), the system fails in proximal junctional kyphosis (Lee and Park, 2016), bars/screws failure (Luca et al., 2016).

These pathologies, or syndromes, involve entire spine segments, and not the single organs, such as the singles vertebra or the single discs. This multifactoriality increases the difficult to work on a so complicated system.

1.3 The implications of spinal diseases on our society

The consequences of these diseases can affect with different endings the subject's life. In the best case, the subject lives with spine diseases without any pain or symptoms and without changing his/her life style. The worst-case scenario, instead, corresponds to the immobilized patient, with consequents morbidities, that deeply affects the life quality, up to mortality (Christodoulou and Cooper, 2003; Cooper et al., 2006; Holroyd et al., 2008; WHO, 2004).

The spinal pathologies, of course, had a high impact also on the healthcare systems in terms of costs, because of complex and expensive patient specific treatments/devices, high rate failure and long convalescence (Boos, 2009).

For example, the average cost for lumbar spinal surgery is of 28 000 \$ (Boos, 2009) (quasi-twice the cost for a knee or hip replacement (Polly et al., 2007)) and it is rising despite the lack of a clinical evidence of their effectiveness compared to other treatments (Fairbank et al., 2005). In fact some treatments, such as the pedicle screw fixation or the augmentation (vertebroplasty or kyphoplasty), are technically demanding and associated with high complications rates. For the pedicle screw fixation, one or more complications were been found in 40% of the cases (Esses et al., 1993; Jutte and Castelein, 2002;

Pihlajamaki et al., 1997), while for the augmentation the complications were around the 20% of the cases (Yang et al., 2008).

Moreover, this spinal diseases scenario is continually worsening due to the increasing longevity, not ever associated to a high-quality life, and the widespread sedentary lifestyle (Affairs, 2007). Just to mention, in the United States of America, 31 million people (10% of the population) suffer of back pain (Agency for Healthcare Research and Quality).

1.4 How can we explore the spine biomechanics?

In literature a series of work investigated the biomechanics of the spine *in vivo*, *in vitro* and *in silico* in order to characterize the overall spine, its organs, its tissues independently, in physiological, pathological and after treatment conditions.

The *in vivo* works mainly described the kinematic of the spine in different motor tasks. Initially, the goal was reached videotaping the subjects using normal cameras (Cholewicki and McGill, 1996). The researchers then had to manually define the markers and compute the range of motions, with unavoidable issues of repeatability and reproducibility. During the years, improved measurement systems, such as the stereophotogrammetry (Lee et al., 1993) or the inertial and magnetic sensors (Tafazzol et al., 2014), allowed reducing the measurement uncertainties (Stagni et al., 2009) of the procedure and defining the spine kinematics in various field, as swimming (de Magalhaes et al., 2015) or running (Preece et al., 2016). The last improvement in terms of defining the spine kinematics is using MRI or CT scans (Anderst et al., 2014; Fujimori et al., 2014). This procedure has the advantages of solving the problem of the markers application and providing a tridimensional kinematic of the single vertebra of the spine. In fact with the other techniques, the markers are applied on the skin, or are wearable with consequent problems of defining the spine movements instead of the spine and surrounding soft tissues. On the other hand, the CT scans is connected to a minimal radiation dose. Other *in vivo* tests were carried out to define the spinal loads. The group of Prof. Bergmann provided a wide knowledge about the spinal loads (as well as other anatomical districts) *in vivo* using telemeterised prosthesis. A telemeterised vertebral body replacement was implanted in patients who had a compression fracture on a vertebra (Dreischarf et al., 2015; Rohlmann et al., 2007) to define the loads for each vertebra in daily tasks. Expanding the knowledge to spine segment, custom-made internal spinal fixators were used in patients with spine instability (Rohlmann et al., 1994; Rohlmann et al., 1997; Rohlmann et al., 1999). It allows defining the ranges of loads in different loading scenario, in different spine zones. A hybrid *in vivo/in silico* work instead provided the loads on healthy intervertebral discs (Wang et al., 2014), helping to understand the intrinsic biomechanics of the spine and the related organs.

The *in vitro* works mainly described the biomechanical characteristics of the spine, considering the spine as a whole, or a vertebra and its next, or a more or less extended spine segment (Brandolini et al., 2014). The Panjabi and White's

group (Panjabi et al., 1976) evaluated the three-dimensional load-displacement curves of the thoracic spine, defining the mechanical characteristics of each motion segment. A series of works defined the range of motion of human spine (Oda et al., 2002; Panjabi et al., 1981; Panjabi et al., 1994). Other works, in addition to the range of motion, computed the stiffness of the spine in different motor tasks (Anderson et al., 2009; Busscher et al., 2010a; Busscher et al., 2010b; Busscher et al., 2009; Hansson et al., 1987; Wilke et al., 1997). The range of motion and the stiffness were frequently used to compare the physiological spines, with pathological and instrumented ones (Alkalay et al., 1999; Oxland and Lund, 2000; Schultheiss et al., 2006; Wilke et al., 2006). These two parameters offer a useful but rather delimited description of the biomechanics of the spine. In fact, some processes, such as the bone remodeling (Wolff's law) or the bone fracture (Bayraktar et al., 2004; Cristofolini, 2015), are well known as strain-based ones. Moreover, the biological specimens are often inhomogeneous and anisotropic and full-field measurements are mandatory to deeply characterize the tissues. Finally, experimental full-field measurements can validate complex finite element model. *In vitro* works allow also measuring experimentally the strain on the specimens. Some works investigated qualitatively the strain distribution on a spine segment using the brittle paint or photoelasticity (Shah et al., 1976). Of course, these measurement techniques provided useful information, especially for a complex geometry such as the one of the spine, to describe the biomechanics of the spine. At the same time, the boundary conditions of these techniques were actually far from the reality and considerably affected the measurements. A quantification of the strain was possible using the strain gauges. They granted stability and precision but strain gauges provided only point-wise measurement. Nevertheless, the reinforcement effect, typical of the strain gauges, limited their employment only on hard tissues (Cristofolini et al., 2013; Danesi et al., 2016a; Shah et al., 1978). More complex was the quantification of the strain on the intervertebral discs, due to their intrinsic characteristic, such as a relatively low Young's modulus (Cassidy et al., 1990; Karakolis and Callaghan, 2015; Spera et al., 2011). And this difficulty, can be seen, to date, as a gap between the know-how on vertebrae and intervertebral discs. Bragg's fibers were used to evaluate the strain but only for a limited portion of the surface (Stokes, 1987).

Moreover, the exploration of the spine goes over the knowledge about vertebrae and intervertebral discs: an increasing number of works studies the behavior, the function and the characterization of the ligaments (Gillespie and Dickey, 2004; Hindle et al., 1990; Panjabi et al., 2009; Shim et al., 2006). Other experimental works compared the different surgical techniques, to highlight the pros and cons connected to each ones (Cardoso et al., 2008; Lee et al., 2010).

Finally, it is not negligible that a wide portion of literature is based on *in silico* tests through finite element analysis. As in other fields, the finite element analysis shows high potentiality but, before starting to use it, a validation is needed (Dall'ara, 2012; Dall'Ara et al., 2013; Dall'Ara et al., 2010). In this case, the synergies with *in vivo* (Zander et al., 2015) and *in vitro* (Cristofolini et al., 2010b; Noailly et al., 2007; Reitmaier et al., 2012) tests allow going beyond this problem and increasing the knowledge in the field. In fact, using finite elements models is possible simulating pathologies, bone remodeling, devices, overloads, and a long list of situations hard to reproduce in laboratory for *in vitro* tests or

on human on *in vivo* tests. The spine is deeply investigated with finite element analysis by the “MySpine group”, coordinated by Prof. Lacroix (Galbusera et al., 2011; Malandrino et al., 2014; Malandrino et al., 2009). Their research covered both the vertebrae and the intervertebral discs and their aim was the creation of a computing platform to be used in clinical images.

On this topic, the Avicenna roadmap (Viceconti et al., 2016) written by Prof. Viceconti of the Insigneo (Institute for In Silico Medicine) and approved by the European Commission define the route by which *in silico* techniques of computer simulation will be introduced into clinical trials, the studies that are routinely conducted to establish the safety and efficacy of new medical interventions.

1.5 What is still unsolved?

The spine is described through a detailed evaluation of

- The kinematics in different conditions and using different *in vitro*, *in vivo* and *in silico* tests;
- The overall stiffness;
- The mechanical characteristics of the tissues component the bone, the intervertebral discs and the ligaments;
- A series of models usable to simulate different scenarios.

To date, a methodology to merge the evaluation of the range of motion with the full-field strain measurement is not implemented.

But, what happens in the interface between vertebrae and discs, where is the failure point on spines, how the vertebrae and the discs works when an implantable devices is used, is not actually well known. More generally, a quantification of the strain taking into account the spine segments as a whole is missing and can be very useful in the biomechanical field. A clear description of the strain associated to physiological tasks can help the clinician to better understand the pathologies related to spine, can improve the design of new implantable devices with a lower failure rate and can develop new surgical procedures, beneficially, less invasive.

1.6 Aim of my PhD project

The aim of my project consisted in improving the methodologies and procedures to test, and consequently widely characterize, the biomechanics of the spine *in vitro* in different conditions.

The entire work mainly focused on the application of quantitative full-field displacement/strain measurement techniques able to provide new essential data helpful to open the way to new studies on the spine, to better understand its pathologies and to develop improved devices. In order to offer a wide and complete methodology, surface and internal strains and displacements measurements were explored. Initially, the uncertainties were evaluated to

know the level of reliability for each measurement techniques; then the know-how was applied to answer to biomechanical questions: such as the strain distribution on a multi-vertebrae spine segments, or what happens in the trabecular bone of a vertebra.

1.7 Outline of the thesis

The work was conceptually split in two areas of research: the strain measurement on the surface of the specimen and the measurement inside the specimen.

In order to achieve my goal, a series of steps were needed.

For the strain measurement on the surface of the specimens:

- Review of the literature of the application of Digital Image Correlation in the biomechanical field (Chapter 2);
- Quantification of the measurement uncertainty of the surface measurements, obtained through Digital Image Correlation, on biological specimens and its relative optimization (Chapter 3);
- Application of the acquired know-how in terms of surface measurement on multi-vertebrae spine segments providing a full-field strain maps (Chapter 4);

For the strain measurement inside the specimens:

- Review of the literature focusing the reliability of the Digital Volume Correlation and comparing the different tools, approaches (Chapter 5);
- Quantification of the measurement uncertainty of the measurements inside the specimen, obtained through Digital Volume Correlation, on different biological specimens with different image sources (Chapter 6, 7, 8, 9);
- Preliminary applications of the optimized procedures to obtain internal full-field strain maps on animal specimens (Appendix);
- General conclusion of the work with the next step planned (Chapter 10).

Part I

Displacement and strain measurement on the surface of the specimens

“You, who live in a world with shades of light, who have two eyes, who have an innate knowledge of perspective and depth, you, who can actually see an angle and an entire figure from the happy perspective of three dimensions - how can I possibly make clear to you the extreme difficulty that we in Flatland experience in recognizing one another's configuration?”

E. Abbott - Flatlandia

Chapter II

Overview of the applications of Digital Image Correlation in Biomechanics

from the manuscript:

The use of Digital Image Correlation in the Biomechanical Area: a Review

M. Palanca¹, G. Tozzi², L. Cristofolini¹

¹ School of Engineering and Architecture, Alma Mater Studiorum – Università
di Bologna, Bologna (IT)

² School of Engineering, University of Portsmouth, Portsmouth (UK)

Published in: *International Biomechanics*, 2016, 3(1): 1 - 21

2.1 Introduction

2.1.1 Why is it important to measure full-field displacement and strain

The measurement of displacement and strain is an important task in experimental biomechanics because it allows the characterisation of biological tissues, organs, and their interactions with biomedical devices. For instance, the stiffness is computed as the ratio between the load and the displacement; bone remodelling is a well-known stress/strain-driven process (Wolff's law); bone fracture is governed by a strain-based failure criterion (Bayraktar et al., 2004). Due to the features of biological specimens, which are mainly inhomogeneous and anisotropic, it is extremely important to obtain full-field measurements, ideally with a contactless technique (Haddadi and Belhabib, 2008). On the computational side, finite element (FE) analysis results require experimental data as an input, and must be validated against experimental tests. Point-wise (averaged over a small surface) measurements, such as the ones provided by strain gauges, sometimes are not sufficient to fully monitor an experiment. Full-field measurements are very important when local damages, such as a crack initiation or propagation, must be identified.

2.1.2 Overview of full-field, contactless optical measurement technique

Among the different optical techniques, the ones most frequently used nowadays are the digital ones that allow automation of the acquisition and analysis process. After an initial stage of general diffidence during the 80s' followed by the first successful applications on mechanical tests in the 90s', optical measurement techniques are become very appealing and are increasingly applied in the industrial and research environments. These measurement techniques allow:

- Full-field measurement through visualization of strain gradients and concentrations. This produces a more complete description of the behavior of biological specimens during *in vitro* tests;
- Contactless measurements that enable the measurement of strain without disturbing the local mechanical response of the material. This requirement is particularly important for deformable materials such as soft tissues (liver, intervertebral discs, etc.);
- Relatively simple preparation of the surface compared to other measurement techniques, such as the application of strain gauges or fibre Bragg grating sensors.

Such features are mandatory for typical biomechanical tests on non-homogeneous and anisotropic materials, and specimens with a complex geometry. At the same time, an optical measurement technique must be accurate and precise.

Some optical measurement techniques, such as holographic interferometry, speckle interferometry (including its digital version, electronic speckle pattern interferometry (ESPI) are highly accurate, but they are too sensitive to small displacements, and therefore unsuitable for deformable materials such as biological tissues (Freddi et al., 2015). Other optical techniques such as Moiré

interferometry, require the preparation of a regular pattern on the specimen surface (Post and Han, 2008) (Freddi et al., 2015), which can be very difficult for biological specimens having an irregular geometry. In general all such techniques have recently found very limited application because of their complexity in practical use. A promising optical technique for the biomechanical field is the Digital Image Correlation (DIC) (Sutton et al., 2009), which is able to overcome most of such limitations (Freddi et al., 2015).

2.1.3 Aim

The purpose of this paper is to provide an overview on the operating principles of Digital Image Correlation (DIC), and of its applications in biomechanical area. This review is conceived for biomechanicians who want to improve their knowledge about DIC, and need to critically understand the underlying benefits and limitations related to biomechanical applications.

2.2 Introducing Digital Image Correlation (DIC)

2.2.1 History of DIC

The increasing diffusion of DIC can be explained by its flexibility, scalability to a wide range of dimensions, the robustness of its operating principle, and its (apparent) ease of use (Amiot et al., 2013) (Freddi et al., 2015; Pan et al., 2009; Soons et al., 2012; Sutton et al., 2009; Tyson et al., 2002). DIC was introduced in the early of 80s, with the first system developed at the University of South Carolina (Bruck et al., 1989; Chu et al., 1985; Peters and Ranson, 1982; Sutton et al., 1983), and has been subsequently improved (Helm et al., 1996; Luo et al., 1994; Luo et al., 1992). The first applications of DIC in biomechanics date back to the 90s (Bay, 1995; Bay et al., 1999b). During the first decade of the new century, DIC was applied regularly in the biomechanical field, with home-written algorithms (Nicoletta et al., 2001; Zhang et al., 2002a; Zhang et al., 2002b). Later on, several companies developed proprietary DIC systems (Table 1-2). Additionally, DIC libraries are also available as part of software suites, such as Matlab (MathWorks, Natick, Massachusetts, USA) and Mathematica (Wolfram, Champaign, IL, USA). Reviews on the use of DIC for traditional engineering materials can be found (Pan et al., 2009) (Hild and Roux, 2006).

Table 1 – Papers presenting applications of DIC to biomechanical investigations of the soft tissues. References are listed in chronological order within each subsection.

Specimen	Field view	of Pixel size (μ m)	Type of random pattern	Type of mechanical Test	of Reported quantities	Number of specimens	of DIC system	DIC parameters	Note	References
Cardiovascular - human										
Human tissue	aortic	N.A.	N.A.	Inflation test	Displacement and strain distribution	4	Aramis 3D	N.A.		(Kim et al., 2011)
Human heart	100x100 mm ²	147	Natural pattern	Myocardial movements	Displacement and strain distribution	1	DaVis	F_S: 121x121 G_S: 1	<i>In vivo</i>	(Hokka et al., 2015)
Cardiovascular - animal										
Bovine Aorta	25x18 mm ²	20	Airbrush	Tensile test	Full-field displacement; strain distribution	N.A.	Home written	N.A.		(Zhang et al., 2002a)
Mice arterial	carotid 290x770 μ m ²	2.2	Powder	Pressure test	Lagrangian strain	1	Vic-3D modified	F_S: 43x43; G_S: 5		(Sutton et al., 2008a)
Mice arterial	carotid	N.A.	Ethidium nuclear bromide	Pressure and tensile test	Displacement and strain distribution	1	Vic-3D	F_S: 15x15	Singular speckle pattern	(Ning et al., 2010)
Mice arteries	carotid	N.A.	Airbrush	Pressure test	Strain distribution	1	Home written	G_S: 8x4		(Genovese et al., 2011)

Mice aorta with abdominal aneurysm	suprarenal with	N.A.	N.A.	Airbrush	Pressure test on lesions	Strain distribution	1	Home written	N.A.	pDIC	(Genovese et al., 2012)
Mice aorta	suprarenal	N.A.	N.A.	Airbrush	Pressure test	Strain distribution	1	Home-written	N.A.		(Genovese et al., 2013b)
Porcine aortic arch		N.A.	N.A.	Airbrush	Pressure test	Strain distribution	1	Home written	N.A.	pDIC	(Genovese and Humphrey, 2015)
Porcine ventricular wall	left	N.A.	N.A.	Airbrush	Indentation test	Displacement and strain distribution	1	Home written	N.A.	Combined with a Projection method	(Genovese et al., 2015)
Cartilage - human											
Human cartilage from patellae		N.A.	4	N.A.	Tensile test	Normal strain	10	Home written	N.A.		(Narmoneva, 2002)
Cartilage - animal											
Bovine carpometacarpal joint cartilage		888x703 μ m ²	0.683	Natural pattern	Unconfined compression	Young's modulus; Poisson ratio	21	N.A.	F_S: 20/40/60 G_S: from 8 to 120		(Wang et al., 2002)
Bovine articular cartilage		N.A.	N.A.	N.A.	Unconfined compression	Young's modulus; Poisson ratio	15	Home-written	N.A.		(Wang et al., 2003)
Porcine articular cartilage		N.A.	59.56	Airbrush	Tensile test	Displacement distribution	1	Home written	N.A.	Comparison with ESPI	(Zhang et al., 2005)

Porcine Intervertebral disc (FSU L4-L5)	51.2x10.2 mm ²	23	Powder	Compression test	Strain distribution	1	Home written	F_S: 9x9	(Spera et al., 2011)
Eye - human									
Human sclera	posterior 20x20 mm ²		Powder	Inflation test	Displacement distribution; circumferential and meridian strain	57	Vic-3D	N.A.	(Coudrillier et al., 2012)
Human sclera; optic nerve	posterior 100x75 mm ²	30	Airbrush	Inflation test	Displacement and strain distribution	1	Home written	F_S: 9x9; C_W: 21x21	(Pyne et al., 2014)
Eye - animal									
Bovine cornea	21x21 mm ²	30	Powder	Inflation test	Displacement distribution	9	Vic-3D	F_S: 35x35	(Boyce et al., 2008)
Bovine sclera	posterior 40x40 mm ²	3.4	Airbrush	Inflation test	Displacement distribution	10	Vic-3D	N.A.	(Myers et al., 2010)
Tendon and ligament - human									
Human ligaments	vocal 8.5x6.8 mm ²	6.7	Airbrush	Tensile test	Axial strain	1	Vic-2D	N.A.	(Kelleher et al., 2010)
Human tendon	N.A.	N.A.	Airbrush	Tensile test	Normal and shear in-plane strain	6	Vic-3D	N.A.	(Luyckx et al., 2014)

Tendon and ligament – animal

Mice tendon	Achilles	N.A.	N.A.	Powder	Tensile test	Axial displacement and strain	8	Home written	N.A.	Use of ultrasound images	(Okotie et al., 2012)
Porcine uterosacral and cardinal ligaments		N.A.	N.A.	Poppy seeds as marker	Tensile test	Axial displacement and strain	18	ProAnalyst	N.A.		(Tan et al., 2015)
Porcine uterosacral and cardinal ligaments		N.A.	N.A.	Poppy seeds as marker	Bi-axial test	Displacement and strain distribution	22	ProAnalyst	N.A.		(Becker and De Vita, 2015)

Keratinized tissue – human

Human skin	100 x 70 mm ²	N.A.	N.A.	N.A.	In-plane loading	point Displacement distribution	1	Vic-3D	N.A.	<i>In vivo</i>	(Evans and Holt, 2009)
Human skin	12 x 38 mm ²	50		Airbrush	Tensile test	Displacement distribution	32	Vic-3D	N.A.	High-speed camera	(Ottenio et al., 2015)

Keratinized tissue – animal

Bovine hoof horn	8.5x6.4 mm ²	13.3		Airbrush	Tensile test	Full-field displacement; strain distribution	1	Home-written	N.A.		(Zhang and Arola, 2004)
Chondrocyte seeded agarose hydrogels		N.A.	N.A.	Natural pattern	Compression test	Axial and lateral strain	N.A.	Home written	N.A.		(Kelly et al., 2006)

Beaks of granivorous birds	14x17 mm ²	6.8	Airbrush	Bending test	Displacement distribution; in-plane normal strain, in-plane shear strain	2	Home-written	F_S: 21x21 G_S: 10 C_W: 50x50	(Soons et al., 2012)
Scales of Cyprinus carpio	5.6 x 4.2 mm ²		Airbrush	Tensile test	Strain distribution	10	Home-written	N.A.	Microscopy DIC (Marino Cugno Garrano et al., 2012)
Mice skin	N.A.	N.A.	N.A.	Tensile test	Strain distribution	6	N.A.	N.A.	(Karimi et al., 2015)
Internal organs - human									
Human cervical tissue	N.A.	N.A.	Airbrush	Tensile test	Axial and lateral strain	10	Vic-2D	N.A.	(Myers et al., 2008)
Human liver	25x25 mm ²		Airbrush	Inflation test	Displacement and strain distribution	15	Vic-3D	F_S: 21x21 G_S: 5	(Brunon et al., 2011)
Internal organs - animal									
Porcine liver	100x80 mm ²	3.3	Airbrush	Indentation test	Deformation distribution	1	Aramis 3D	N.A.	(Ahn and Kim, 2010)
Porcine livers	N.A.	N.A.	Natural pattern	Tensile test	Strain longitudinal direction	in 10	Home written	N.A.	(Gao and Desai, 2010)
Porcine brain	N.A.	N.A.	Airbrush	Unconfined compression test	Displacement distribution	N.A.	Vic-3D	N.A.	(Libertiaux et al., 2011)
Lamb gallbladder	N.A.	N.A.	Airbrush	Pressure test	Full strain distribution	1	Home written	F_S: 21x21 C_W: 41x41px	pDIC (Genovese et al., 2014)

Human lower limb muscles	N.A.	N.A.	Natural pattern	Compression test	Displacement distribution	4	Home written	N.A.	Use of ultrasound images	(Affagard et al., 2014)
Artificial soft tissue										
Heart valve tissue	N.A.	N.A.	N.A.	Indentation test	Displacement and strain distribution	N.A.	Aramis 3D	N.A.		(Cox et al., 2008)
Synthetic vocal fold	N.A.	11	Airbrush	Airflow test;	Displacement and strain distribution	N.A.	Vic-3D	F_S: 23x23	Use of high speed camera; 3D with a single camera	(Spencer et al., 2008)
Silicon gel	N.A.	N.A.	Painted	Indentation test	Deformation distribution	1	Vic-3D	N.A.		(Moerman et al., 2009)

Legend:

N.A. = information not available

F_S = facet size

G_S = grid spacing

C_W = computation window

Istra-4D by Dantec Dynamics (Skovlunde, Denmark),

Aramis 3D by GOM (Braunschweig, Germany),

Vic-2D and Vic-3D by Vision Solution (Irvine, California, USA),

StrainMaster and DaVis by LaVision (Goettingen, Germany)

ProAnalyst by Xcited (Woburn, Maine, USA)

Rapid Correlation by XStream Software (Ottawa, Ontario, Canada)

Table 2 – Papers presenting applications of DIC to biomechanical investigations of hard tissue. With each subsection, references are listed in chronological order.

Specimen	Field of view	Pixel size (μm)	Type of random pattern	Type of mechanical Test	Reported quantities	Number of specimens	DIC system	DIC parameters	Note	References
<i>Tissue level - human</i>										
Trabecular bone from human femoral head	N.A.	N.A.	Natural pattern	Compression test	Displacement distribution	6	Home written			(Bay, 1995)
Slices of human thoracic spinal motion segments	N.A.	N.A.	Natural pattern	Compression test	Strain distribution	6	Home written		With radiographs unit	(Bay et al., 1999b)
Trabecular bone of human cadaveric knee	N.A.	N.A.	Natural pattern	Compression test	Strain distribution; principal strain	8	Home written		with radiographs unit	(McKinley and Bay, 2003)
Interface human bone cement	N.A.	8.9	N.A.	Shear fatigue test	Interface displacement	25	Rapid Correlation	F_S:40x40		(Mann et al., 2008)
Human trabecular bone from femur	N.A.	N.A.	Airbrush	Compression test	Displacement and strain distribution	12	Istra-4D	N.A.		(Cyganik et al., 2014)
Human cortical bone from femur	3.6 x 2.7 mm ²	2.6	Natural pattern	Shear test	Displacement and strain distribution	29	DaVis		Use of optical microscope	(Tang et al., 2015)

Tissue level - animal

Cortical bone of bovine tibias	180x141 μm^2 ; 445x350 μm^2	0.137; 0.339	Natural pattern	Micro-crack in stressed cortical bone	Principal strain	N.A.	Home-written	F_S: 9x9x; 19x19; 31x31; 63x63	(Nicolella et al., 2001)
Cortical bone of bovine tibias	180x141 μm^2 ; 445x350 μm^2	0.137; 0.339	Natural pattern	Tensile test	Strain distribution; maximum principal strain	N.A.	Home written	F_S: 51x51	(Nicolella et al., 2005)
Cortical bone of bovine tibias	180x141 μm^2 ; 445x350 μm^2	0.137; 0.339	Natural pattern	Tensile test	Principal strain	7	Home written	F_S: 24x18 G_S: 50; F_S: 14x10 G_S: 10	(Nicolella et al., 2006)
Bovine cortical bone	2.6x2 mm^2 ; 1.3x1 mm^2	1.30; 0.65	Natural pattern	Compression test; Nano-indentation test	Axial strain	4; 3	Home written	F_S: 60x60	(Hoc et al., 2006)
Ovine early bone callus	23.2x15.4 mm^2	7.7	Powder	Compression test	Strain distribution, minimal principal distribution	N.A.	Vic-2D	F_S: 29x29	(Thompson et al., 2007)
Cortical bone from bovine femoral shaft	8x8.7 mm^2	17	Airbrush	Three-point bending	Normal strains and shear strain	20	Home written	F_S: 36x36	(Yamaguchi et al., 2011)
Bovine fibro lamellar bone	N.A.	N.A.	Airbrush	Tensile test	Axial and transversal		Home written	F_S: 30x70	Use of high-speed camera (Benecke et al., 2011)

Single trabecular of bovine femora	N.A.	N.A.	Ink printing	jet Three point bending	Displacement and strain distribution	10	Vic-2D	N.A.	High speed photography	(Jungmann et al., 2011)
Whole organ - human										
Human teeth	3x4 mm ²	3	Powder	Crack propagation	Displacement distribution	N.A.	Home written	F_S: 15x15	fatigue and fracture	(Zhang et al., 2007)
Human femurs	N.A.	N.A.	Natural pattern	Sideways fall	Horizontal and vertical displacement; strain distribution	22	Home-written	N.A.	Use of high-speed camera	(Op Den Buijs and Dragomir-Daescu, 2011)
Dried mandible	N.A.	N.A.	Airbrush	Compression test	Major principal strain	N.A.	Aramis 3D	N.A.		(Tanasic et al., 2012)
Human femur	87x87 mm ²	250	N.A.	Sideways fall	Principal minimum strain	1	Strain Master	F_S: 32x32; G_S: 50%	Use of high-speed camera	(Helgason et al., 2014)
Human vertebra	100x67 mm ²	N.A.	Airbrush	Accuracy and precision test	Principal strain	1	Istra-4D	F_S: 15x15, 19x19, 21x21, 25x25 G_S: 4,7,11,15 C_W: 3, 5, 7, 9, 11, 13, 15		(Palanca et al., 2015a)
Human femur	N.A.	100	Manually applied with	Compression	Principal	3	Vic-3D	F_S: 25x25	Use of high-speed DIC	(Grassi et al., 2011)

				marker	test	strain			G_S: 1, 5 px	al., 2014)
Whole organ - animal										
Cemented total hip replacement	19x14 mm ²	9.3	N.A.		Fatigue test	Full-field displacement, strain distribution	1	Home-written	N.A.	(Zhang and Arola, 2004)
Chelipeds of lobster	2x4 mm ²	9.5	Airbrush		Tensile test	Displacement and strain distribution	8	Aramis 3D	F_S: 23x23; G_S: 10 px	(Sachs et al., 2006)
Mouse tibia	16x12 mm ²	12	Airbrush		Compression test	Strain (average)	4	Aramis 3D	F_S: 19x19 G_S: 9	(Sztefek et al., 2010)
Fresh ovine femur	N.A.	N.A.	Airbrush		Compression test	Strain distribution	N.A.	Vic-3D	N.A.	(Ghosh et al., 2012)
Rat femora	N.A.	N.A.	Airbrush		Compression test till failure	Principal strain	9	Vic-3D	N.A.	(Amin Yavari et al., 2013)
Mouse tibia	15x12 mm ²	6	Airbrush		Compression test	Max and average strain	3	Aramis 3D	F_S: 19x19 Overlap: 20%	(Carriero et al., 2014)
Synthetic										
Dental composite	N.A.	N.A.	Airbrush		Curing process	Axial and transversal strain	10	Strain Master	N.A.	(Li et al., 2009)
Composite femur	25 area of 5 mm ²	50	Airbrush		Press/flection test	Strain (sensitivity/ experimental error)	N. S.	Vic-3D	N.A.	(Dickinson et al., 2011)

Osseointegrated Transfemoral Implant System	N.A.	47	N.A.	Bending test	Displacement and strain distribution	12	Vic-3D	F_S: 27x27 G_S: 10px C_W: 150px ²	(Thompson et al., 2011)
Dental composited	N.A.	N.A.	Powder	Curing process	Axial and transversal displacement	32	Vic-2D	F_S: 21x21	(Chuang et al., 2011)
Acrylic resin mandibular with and without implant	50x37.5 mm ²	35	Airbrush	3-point bending	Strains in horizontal direction and in-plane shear strain	N.A.	Strain Master	N.A.	(Tiossi et al., 2011)
Composite hemi-pelvis	36 area of 5x5 mm ²	N.A.	Airbrush	Compression test	Displacement distribution; principal strain	N.A.	Vic-3D	N.A.	(Dickinson et al., 2012)
Acrylic resin mandibular with and without implant	50x37.5 mm ²	35	Airbrush	3-point bending	Strains in horizontal direction and in-plane shear strain	N.A.	Strain Master	N.A.	(Tiossi et al., 2012)
Composite femur	115x57 mm ²	200	Airbrush	Sideways fall	Displacement distribution; minimum principal strain	20	Strain Master	N.A.	(Gilchrist et al., 2013)
Composite femur	N.A.	N.A.	Airbrush	Press/flection test	Principal strain	6	Vic-3D	N.A.	(Grassi et al., 2013)
Composite femur	N.A.	N.A.	Airbrush	Compression test	Principal strain	6	Vic-3D	N.A.	(Vaananen et al., 2013)

Legend:

N.A. = information not available

F_S = facet size

G_S = grid spacing

C_W = computation window

Istra-4D by Dantec Dynamics (Skovlunde, Denmark),

Aramis 3D by GOM (Braunschweig, Germany),

Vic-2D and Vic-3D by Vision Solution (Irvine, California, USA),

StrainMaster and DaVis by LaVision (Goettingen, Germany)

ProAnalyst by Xcited (Woburn, Maine, USA)

Rapid Correlation by XStream Software (Ottawa, Ontario, Canada)

2.2.2 Operating principle

DIC is based on sets of images of the surface of the specimen in the undeformed (reference) and deformed states (Fig. 1). DIC can be implemented both in a bi-dimensional (2D-DIC, with a single camera), and a tri-dimensional (3D-DIC, using two or more cameras) version. A calibration is necessary to initialize the spatial correlation processes of DIC. The images are divided in smaller sub-images (facets), and a matching algorithm is used to match the facets between the reference and deformed states. The displacement field is then computed. Subsequently, the strain field is obtained by derivation. More details about the operating principle are reported in Appendix 1. The main advantages and disadvantages of DIC (Schmidt et al., 2003; Sutton et al., 2009) are summarized in Table 3.

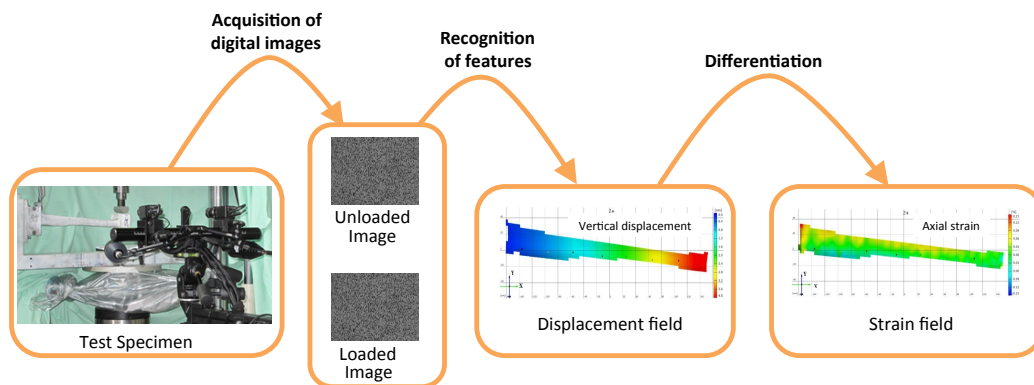


Fig. 1 – Workflow of DIC displacement and strain measurement: as an example, a 3D-DIC arrangement was used to investigate a human tibia.

Table 3 - Summary of the main potentialities and limitations of DIC.

Advantages	Disadvantages
<ul style="list-style-type: none"> - Full-field measurement of displacement/strain - For any size and material of specimens - Determination of strain gradient and stress concentrators - Both for small and large deformation - Usable <i>in vivo</i> - Synergies with FE - Not invasive* 	<ul style="list-style-type: none"> - Less accurate and precise than others measurements techniques - Need of a carefully optimization for the specific application - Not real-time - Need of optical access to the specimen - Requires surface preparation*

*In most cases, a surface preparation is required. It is a layer of paint or powder fixed on the surface. Sometimes, the natural pattern is usable to

2.3 Surface pattern preparation on biological specimens

For an optimal use of DIC, the surface of interest must have a random pattern, which deforms together with the specimen surface. If the specimen presents a natural random pattern, due to an intrinsic texture or inhomogeneity, this can be directly exploited by the DIC system. In all other cases, a random pattern must be generated. To ensure accuracy and precision of the computed displacements and strains, the speckle pattern should meet some requirements (Barranger et al., 2010; Crammond et al., 2013; Lecompte et al., 2006; Pan et al., 2008; Sutton et al., 2009; Yaofeng and Pang, 2007):

- Random distribution, in order to make each area of the surface of the specimen univocally identifiable;
- High contrast, to allow the image correlation algorithm works effectively;
- Black/white ratio of 50:50, to avoid regions that cannot be properly recognized;
- Roughness should be kept at minimum, in order to avoid alteration of the surface geometry.
- Probably the most important issue in biomechanical applications is the size of the speckle dots (in relation to the specimen size), in order to optimally exploit the resolution of the camera (Lionello and Cristofolini, 2014). In fact, the larger the measurement window, the larger the corresponding area covered by each pixel (for a given sensor resolution) and therefore the dots of the speckle pattern. In order to obtain the best speckle pattern for the specific application, the dimension of the speckle should be different for each application. The ideal size of the speckle dots corresponds to 3-5 pixels (Sutton et al., 2009). The magnification factor, M , is defined as the ratio between the number of pixels on the long side of the camera sensor and the long side of the measurement window (M indicates how many pixels correspond to the unit length of the physical specimen). Thus, the ideal size of the speckle dots corresponds to 3-5 pixels divided by M . For example, using a camera-sensor of 5 Megapixels (2448x2050 pixels) on a field of view of 2mm x 2mm (e.g. few trabeculae), yields an optimal dimension of the speckle pattern of about 0.003mm. The same camera-sensor applied to a larger area of interest of 2m x 2m (e.g. a whole human body) would require larger speckle dots, about 3.25mm. Usually, round dots were prepared, because of its "easy" preparation with different techniques, but also linear marks could be potentially used taking in account the above reported requires.

Recently, a tool (a script in Matlab) was developed to evaluate the quality and suitability of a given speckle pattern for a given DIC application (Estrada and Franck, 2015).

The techniques to prepare a speckle pattern most commonly used are (Table 1-2):

- High-contrast paint sprayed with an airbrush airgun (Fig. 2a): this technique is suitable for both small and large deformations (Barranger et al., 2010; Lionello and Cristofolini, 2014), as the speckle dot itself is strained during the deformation.

- A dispersion of toner/graphite powder (Fig. 2b) randomly placed on the specimen: this is a remarkable technique in case of small deformations, particularly for soft tissues, due to an optimal adhesion on moist surfaces. Conversely, in case of large deformations it can produce an underestimation of the strain, as the powder particles displace but do not strain when the underlying specimen is deformed (Barranger et al., 2010).

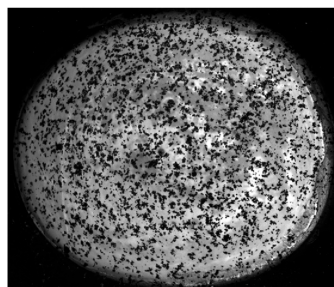
The black-on-white speckle pattern is most frequently used: first a uniform white background is created, on which black speckles are added. This preparation provides the optimal contrast. If the surface of the specimen itself is already of a light colour (i.e. bone), preparation of the white background could be avoided. The use of water-based paints minimises the alteration on biological specimens (Freddi et al., 2015).

In sporadic cases (Genovese et al., 2013b; Lionello et al., 2014; Luyckx et al., 2014), especially for soft tissues, the white-on-black speckle pattern can be used (Fig. 2c). The difference lies in the colour of the background (black or dark blue), and of the speckles (white). The dark background is obtained through immersion of the specimen in some colouring agent (typically methylene blue staining). This prevents delamination and crumbling of the background layer even at large deformations, which may occur with a paint layer. The white speckle pattern is then produced with an airgun. It has been shown that application of methylene blue on ligaments increases their stiffness by 0.8%. Deposition of the white pattern further increased the stiffness to 1.7% (Lionello et al., 2014).

A different preparation of the specimen was used, where ethidium bromide nuclear staining was used to incorporate a high-contrast pattern (Ning et al., 2010). This allows a permanent incorporation of the pattern into the microstructure of the specimen.



a) black-on-white; airbrush



b) black-on-white; powder



c) white-on-black; airbrush

Fig. 2 – Example of specimens with different speckle patterns: (a) Black-on-white speckle pattern created with the airbrush airgun technique on a porcine vertebral body; (b) Black-on-white speckle pattern created with the powder technique on a bovine cornea (picture courtesy of dr. Brad L. Boyce, (Boyce et al., 2008)); (c) Speckle pattern created with airbrush airgun technique, white-on-black, on a human Achilles tendon (picture adapted from (Luyckx et al., 2014)).

2.4 Correlation algorithm parameters

In order to obtain the best results from this versatile measurement technique, a number of parameters must be adapted to the specific application (Fig. 3):

- Facet size (dimension of the sub-image used in the computation);
- Grid spacing (step between consecutive facets);
- Strain computation window (typically larger than the single facet) used to derive the strain field over a larger area, in order to attenuate the noise
- Validity quote (Minimum percentage of computation points that must be available for strain to be calculated over a given computation window);
- Filtering (sometimes applied at the different stages of the correlation to reduce noise).

The values assigned to such parameters determine the accuracy, precision and spatial resolution (Palanca et al., 2015a) (see below). There is no universally optimal set of parameters, due to the numerous possible uses of DIC, particularly in biomechanics. A choice must be made in relation to the specific application (i.e. tissue, anatomy and dimensions of the specimens). Only in few papers the DIC parameters are detailed (Table 1-2).

2.4.1 Facet size

The digital images are divided into sub-images, called facets, of $M \times N$ pixels (typically squared). Each facet is represented by a grey-level distribution, which is, in most cases, interpolated by a bi-cubic spline to obtain an approximation of grey-scale between adjacent pixels. Each facet is summarized by the information about the pattern, and its location in space. The correlation algorithm identifies the best-matching region at different load steps. The influence of the facet size is remarkable (Lava et al., 2009). The facet size must be defined according to: the specimen size (or the field of view), the size of the speckles, and the strain gradients expected based on the loading conditions and the anatomy (Carriero et al., 2014; Freddi et al., 2015).

The facet should be larger than speckle dots, to allow detection of small displacements, in relationship to the granularity of the speckle pattern (Sutton et al., 2009). However, the facet should not be unnecessarily large, to avoid loss of resolution (Lionello and Cristofolini, 2014).

2.4.2 Grid spacing

This parameter indicates the distance between two consecutive facets. It describes the density of facets in the measurement window: the smaller the grid spacing, the larger the number of facets (at a higher computational cost). The influence of the grid spacing on the precision and accuracy of the computed displacement field is minimal (Lava et al., 2009). Conversely, the overlap provides advantages in terms of precision and accuracy of the computed strain field. The density of measurement points should be selected based on the test

details (type of specimen, field of view, pattern and strain gradient). For an expected uniform strain (e.g. long bone in bending) larger grid spacing can be preferable. Conversely, if high strain gradients are expected (e.g. specimens with complex geometry), a smaller grid spacing is necessary (Palanca et al., 2015a; Sutton et al., 2009).

2.4.3 Strain computed window

Once the displacements have been computed for each facet, the strain field is computed by derivation. While in principle 2 x 2 facets are sufficient to compute the local strain, larger windows are often used to attenuate the noise in the derived strain field. While larger strain computation windows reduce the noise in the DIC-computed strain distribution, this also may result in an attenuation of existing strain gradients, which can be detrimental when analysing specimens with an irregular geometry (which often occurs with anatomical specimens). This effect is thus similar to the effect of grid spacing (Palanca et al., 2015a; Sutton et al., 2009).

2.4.4 Validity quote

The validity quote represents the tolerance for computing/ignoring the strain a certain region: if the number of valid neighbouring points is below the threshold, the software does not evaluate the strain. A high-level of the validity quote means that strains are computed only where redundant information is available, thus providing a more reliable strain value. If the specimen has a complex geometry (i.e. a vertebra, or a pelvis), a lower threshold might be necessary, resulting in less reliable strain estimates.

2.4.5 Filtering

In general, DIC allows obtaining very precise displacement fields (i.e. affected by very low noise, typically sub-pixel). However, as the operation of derivation acts as the opposite of a filter, the strain field is generally affected by large random error (being obtained through the derivation of the displacement field). Filtering can be applied to the digital images, to the DIC-computed displacement field, and/or to the DIC-computed strain field (Baltoni et al., 2016). There are several filters that mainly differ in the intensity of attenuation, and filtering strategy (whether local or global). However, this also smoothens any gradient or stress/strain concentration, resulting in a loss of information.

For a homogeneous deformation (i.e. in the diaphysis of a long bone, or a tendon under tension) a smoothing spline can be successfully used to attenuate the noise by averaging the results over the field of view. Larger averaging areas are associated with more severe loss of information (Lava et al., 2010). Conversely, when the specimen is subject to high strain gradients (i.e. an irregular bone such as a vertebra, or a complex structure such as the sclera) a local filtering, should be preferred (at the cost of noisier results, (Wang et al., 2012)). Alternatively, strain can be computed by means of an FE solver, where DIC-measured displacements are imposed to the FE nodes (Evans and Holt, 2009). The continuum assumption (which is intrinsic to FE modelling), acts as a low-pass filter.

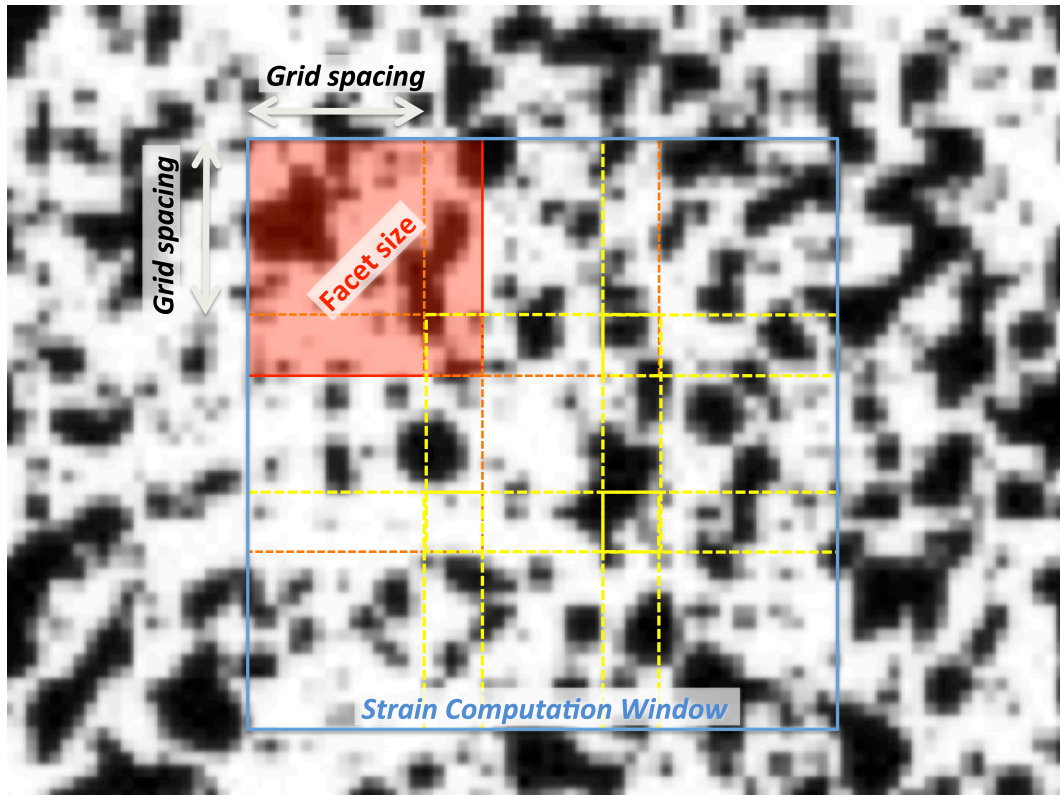


Fig. 3 – Detail of the specimen surface prepared with a random speckle pattern, as seen after acquisition as a digital image (i.e. discretized in pixels). The DIC software parameters are illustrated: to compute the displacement field, the digitized image is divided in sub-images (facets, 20 x 20 pixels in this case); a grid spacing of 15 pixels is used in this case (resulting in a partial overlap of 5 pixels); a larger area (computation window, 3 x 3 facets in this case) is used to compute the strain field.

2.5 Error affecting DIC measurements in biomechanics

2.5.1 Accuracy and precision

It is important to distinguish between systematic error (bias of the average, resulting in lack of accuracy), and random error (large standard deviation, resulting in lack of precision). In fact, accuracy and precision of the DIC measurements cannot be taken for granted if the measurement system and the numerical processing have not been optimized and validated (Fig. 4). The errors affecting displacement and strain are originally induced by the overall quality of the native images. The DIC-computed displacement field is less sensitive to modifications of software parameters; their effect is larger on strains (Nicolella et al., 2001; Palanca et al., 2015a). Accuracy and precision of the DIC in computing the displacements are in the order of 0.01 pixel (Amiot et al., 2013; Nicolella et al., 2001; Zhang and Arola, 2004); with some optimizations errors can be further reduced (Barranger et al., 2010). DIC-computed strains are generally quite accurate (systematic errors of the order of few microstrain are negligible in most biomechanical applications). Conversely, large noise usually

affects DIC-computed strains: a precision of some hundreds of microstrain can be achieved only under optimal conditions.

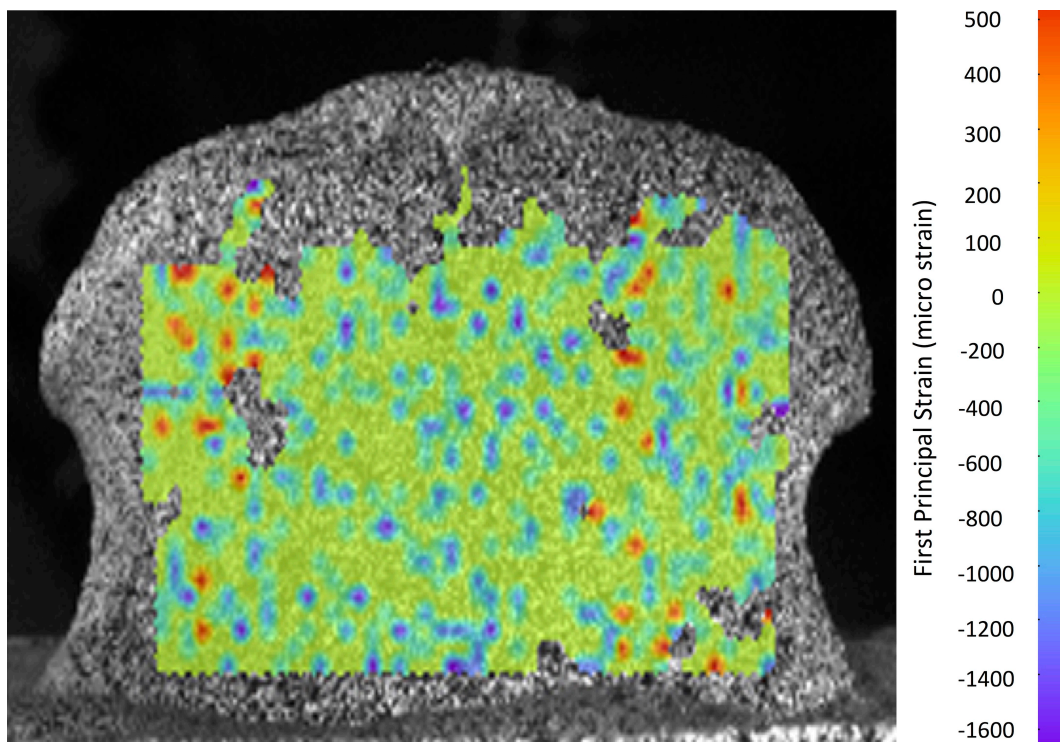


Fig. 4 – Example of errors affecting the DIC-computed strain distribution. A porcine vertebra was examined in a zero-strain condition. Strains were computed with DIC software with default (i.e. not optimized) settings. Any strain readout different from zero is due to errors (a combination of systematic error and random error).

2.5.2 Errors due to the pattern

The DIC analysis relies on the presence of a suitable pattern on the specimen surface. In order to evaluate the errors related to the morphology of the pattern, digital images of the speckle patterns were virtually translated (Haddadi and Belhabib, 2008), numerically deformed (Lecompte et al., 2006), correlated in a zero-strain condition (Carriero et al., 2014). An unsuitable speckle pattern is likely to make the correlation impossible at some facets, reducing the number of measurements points (Haddadi and Belhabib, 2008). An optimal ratio exists between the facet size and the mean speckle size to reduce errors affecting DIC-computed displacements (Lecompte et al., 2007; Lecompte et al., 2006). They also showed that a limited scatter of speckle sizes yields more accurate displacement measurements, and that larger dots result in larger random errors in the displacement field. The differences between black-on-white and white-on-black speckle patterns are negligible in terms of measurement quality (Barranger et al., 2010). A clear relationship exists between the measurement error and the uniqueness of the pattern, which depends on the speckle size and shape, and on the facet size (Crammond et al., 2013). The airbrush airgun method provides a better control of the dots dimension compared to the use of powder (Myers et al., 2010). Even if an airbrush airgun and only to a limited

extent be adjusted to produce the desired speckle dots (Crammond et al., 2013), the performance of DIC is quite robust and tolerant (Wang et al., 2012). A small unavoidable compromise should be taken in account when DIC is used on biological specimens. In fact, the thin paint layer can potentially affect the specimen mechanical characteristics and complicate the hydration of the biological specimen. Specific solution, as water-based paint, should be selected to solve these issues (Palanca et al., 2015a).

2.5.3 Errors due to the acquired images

Random errors affect the images acquired by the digital camera, such as thermal noise (or dark noise), excess noise due to the CCD sensor, and electromagnetic noise of the relative measurement chain (Freddi et al., 2015). Moreover, a source of systematic error in 2D-DIC derives from out-of-plane displacements of the specimen during loading. 2D-DIC is often chosen in investigations at the tissue-level (Pan et al., 2013; Sutton et al., 2008b). They explained the combined effect of the out-of-plane motion of the tested object surface and of the cameras.

2.5.4 Errors due to the correlation process

Suboptimal choice of the software parameters can result in large noise, or, conversely, could hide existing strain gradients (Baldoni et al., 2016). The optimal parameters can be identified through virtually-imposed displacement tests (Haddadi and Belhabib, 2008). Numerically deformed images were prepared to evaluate the accuracy and precision in the displacement field, and identify the optimal parameters (Lava et al., 2009; Lava et al., 2010; Lava et al., 2011) (Wang et al., 2012). A zero-strain test was applied on a vertebra (Fig. 4) to investigate the software parameters to estimate the accuracy and precision (Palanca et al., 2015a).

2.5.5 Recommendations to minimize measurement errors in biomechanical applications

It is possible and to some extent mandatory to validate DIC measurements by comparison against independent measurements: (Gilchrist et al., 2013; Sutton et al., 2008a; Zhang and Arola, 2004) compared the DIC-computed strains against single strain gauges. A more extensive validation may include the use of specimens with known material properties, subjected to well-defined loading conditions (Gilchrist et al., 2013; Sutton et al., 2008a; Zhang and Arola, 2004). Moreover, preliminary tests to identify the spatial displacements could help in avoiding out-of-plane artefacts in a 2D-DIC.

To optimize the speckle pattern for biological specimens (Lionello and Cristofolini, 2014; Lionello et al., 2014; Palanca et al., 2015a) proposed a factorial-design to adjust the airbrush settings so as to a pattern having the desired average speckle size with minimal scatter.

The lens distortion generates a systematic error, which can be partially compensated through dedicated algorithms (Yoneyama, 2006), or an appropriate calibration (Patterson et al., 2007; Sebastian and Patterson, 2012). Such artefacts can be completely eliminated with telecentric lenses (Pan et al., 2013), or by exploiting the central portion of the lens angle (Palanca et al.,

2015a). An in-house smart solution consists in performing 3D deformation measurements with a single camera using a biprism to avoid distortion of the images (Genovese et al., 2013a; Genovese et al., 2013b). The illumination must be stable and uniform to reduce the noise and obtain better native images. Moreover, due to the nature of biological specimens, cold light illumination is preferable (i.e. using LED technology). Noise and its influence can be somehow reduced, but not completely eliminated, with high-performance hardware (i.e. lenses, cameras, frame grabber, etc).

To reduce correlation errors due to unsuitable settings, it is important to have a provisional estimate of the expected strain gradients. In case of homogeneous deformation a large facet size, large grid spacing and large computation window are able to produce accurate and precise measurement with limited computation cost (Sutton et al., 2009). Conversely, stress/strain concentrations should be investigated with a high spatial resolution (i.e. small facets and computation windows), to avoid loss of detail.

Filtering can help reduce the noise in the DIC-computed strains. However, filtering should be used with extreme caution to avoid loss of information in high-gradient regions, such as anatomical specimens with an irregular geometry, or in highly inhomogeneous tissues (Baldoni et al., 2016). A careful optimization of the entire measurement chain can reduce the errors (Fig. 5) and provide more accurate and precise outputs (Palanca et al., 2015a).

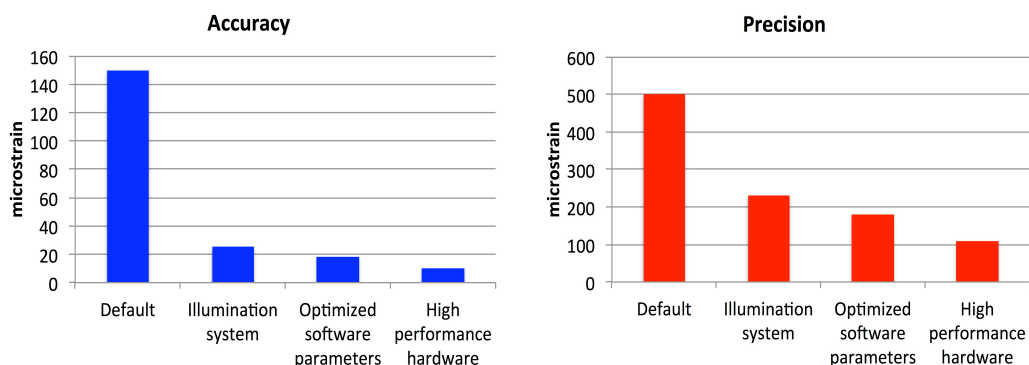


Fig. 5 – Plots showing how the systematic error and the random noise were dramatically high if no special care was taken to reduce them, and how effective an optimization following the principles of DOE can be, to improve precision and accuracy (Palanca et al., 2015a).

2.6 Example of biomechanical applications

Big potentiality of DIC lies in its suitability to investigate different kinds of materials, such as soft and hard biological tissues, independently their mechanical behaviour (brittle/ductile, isotropic/anisotropic, homogeneous/inhomogeneous), for small or large deformation (Sutton et al., 2009).

2.6.1 Applications to soft tissue

Before the introduction of DIC, strain in soft tissue structures have been initially measured by means of extensometers (Larrabee, 1986; Nagarkatti et al., 2001). This method significantly perturbs the specimen under observation, both in terms of local stiffening, and notching. A better alternative is based on optical extensometers (i.e. (Holzapfel, 2006; Weisbecker et al., 2012)). The main limitation of optical extensometers is that they track the displacement of only two points in the specimen. Therefore, the strain field between such points is averaged, with no information about the local strain distribution. Furthermore, most optical techniques tend to loose correlation when large displacements are involved, which often occurs with soft tissues. DIC overcomes such problems, opening possibilities to new measurements and new data in the experimental tests (Table 1). For example, DIC opened the way to measurements on micrometric scales (tissue-level).

DIC enabled improvements in the field of microindentation. Originally, indentation focused only on the force-indentation relationship. DIC allows measuring the surface deformation around the point of load application. This methodology was assessed on a silicon gel (Moerman et al., 2009) and on a porcine liver (Ahn and Kim, 2010). Single-camera-DIC combined with a radial-fringe-projection was used to measure the displacement field in the indentation tests on porcine ventricle (Genovese et al., 2015). As the reliability of DIC with microindentation has been proven *in vitro*, this technique has the potential to be deployed *in vivo* for future diagnostic purposes.

In vitro application of DIC to measure the strain distribution in various components of the cardiovascular system is extremely important, for potential its impact to improve the understanding of pathologies, and delivery better treatment. However, the state of stress/strain is difficult to measure, because of the inherent pseudoelastic nature, the small dimensions of the specimens, and the difficulty in reproducing the physiological working condition. Initially, bovine aorta specimens were investigated by means of DIC by (Zhang et al., 2002a): the Poisson's ratio was determined from the displacements, and the corresponding strains up to 40%, in the axial and circumferential directions. This work was based on simplified boundary conditions: the specimens were loaded in a uniaxial tensile test, far from the physiological conditions. Additional experiments were conducted with silicone rubber sheets, providing a validation of DIC under large strains. Later, other works included an improved resemblance to the physiological condition. Mice carotid arteries were subjected to a pressure test to identify significant variations in constitutive material response (Sutton et al., 2008a). This test was performed using a microscopic 3D-DIC, with a field of about 0.2 mm^2 . Due to the 3D anatomy, only a restricted region of the surface was investigated. The entire surface of a mice carotid was investigated out using a conic mirror, while a single camera was moved (Genovese and Humphrey, 2015; Genovese et al., 2011). The distribution of mechanical properties was obtained from the strain field, exploiting an inverse material characterization. As this method allows measuring displacements and strains on the entire surface, complex pathological conditions such abdominal aortic aneurysms could be investigated (Genovese et al., 2012). The anisotropy of tissue-engineered heart valves was investigated with indentation tests at a microscopic scale (Cox et al., 2008).

A pioneering rudimentary DIC system allowed evaluating the strain distribution in the human cornea by measuring the *in vitro* displacement of only few (6) discrete particles (Shin et al., 1997). In order to understand the non-linear viscoelastic and anisotropic behaviour of the cornea, a 3D-DIC was used (Boyce et al., 2008). Bovine corneas were constrained in a custom pressurization chamber and loaded with physiological and pathological pressure. The potentialities of 3D-DIC were exploited to measure the out-of-plane displacements and to obtain the pressure-displacement response. The response at various pressure rates and the creep at different pressures of the bovine posterior sclera were investigated (Myers et al., 2010). A consolidated protocol to measure the spatial displacement field during an inflation test was used for an in-depth investigation of the behaviour of physiological and pathological human posterior sclera (Coudrillier et al., 2013; Coudrillier et al., 2012). A system where the camera can be rotated by 90-degrees around two orthogonal axes (sequential-DIC) allows improving the out-of-plane resolution of a single camera, without losing sensitivity (Pyne et al., 2014). They used sequential-DIC for mapping the optic nerve head deformation. As sequential-DIC requires some time to acquire the images from different angles, it cannot be used for time-critical experiments such as measuring viscoelastic properties. The advent of DIC enabled the incorporation of loading conditions that better replicate the complex *in vivo* mechanical environment in the eye structure, compared to the crude simplifications of the past (uniaxial tests (Boyce et al., 2007)).

Cartilage tissue specimens (1-mm cubes) were subjected to unconfined compression tests; 2D-DIC was used to measure the equilibrium modulus and the Poisson ratio (Wang et al., 2003; Wang et al., 2002). Similarly, the Poisson ratio was measured at the tissue-level in tension for the human patellar cartilage (Narmoneva, 2002; Zhang et al., 2005).

Intervertebral disks are difficult to study, both for their mechanical behaviour and for their anatomical position. Traditionally (Causa et al., 2002; Panjabi, 2007) the force-displacement curve of functional spinal units was extracted from displacement transducers under uni- or multi-axial simulators. The strain distribution in the disks was measured with 3D-DIC at the organ-level under simulated physiological loading (Spera et al., 2011).

The distribution of strain in the entire human Achilles tendon was examined through DIC (Luyckx et al., 2014), while in the past only the average strain could be assessed by means of extensometers. An image correlation process was applied to dynamic ultrasound images to measure the *in vivo* strain distribution in mice tendon (Okotie et al., 2012). This technique exploited the “natural” speckle pattern of ultrasound images.

The biomechanics of bovine hoof has been investigated in uniaxial tension using DIC, so as to obtain a full-field description of the axial strain distribution (Zhang and Arola, 2004). The strain gradients observed indicated an inhomogeneous distribution of the mechanical properties, which would otherwise be difficult to assess.

The interplay between the uterine cervix tissue and its macroscopic mechanical properties was investigated with DIC (Myers et al., 2008). Strain distributions in the range from 5% to 30% were measured with DIC, and plotted against stress.

Recent works were done on porcine uterosacral and cardinal ligaments in uniaxial (Tan et al., 2015) and bi-axial (Becker and De Vita, 2015) loading

conditions, deploying a simplified DIC (a limited number of poppy seeds used as markers). They determined the mechanical properties (elastic moduli, ultimate tensile strength and strain) of the two major ligaments that support uterus, cervix and vagina. The bi-axial test, moreover, investigated deeply the orthotropic behaviour of these ligaments, formulating a new three-dimensional constitutive model.

The spatial deformation of the vocal folds was measured by means of DIC (Kelleher et al., 2010; Spencer et al., 2008). This study focused on the superior surface of a synthetic model of the vocal folds sprayed with a speckle pattern. To extend this promising technique to clinical laryngoscopic evaluations, a non-toxic speckle pattern would be required. DIC was used *in vitro* to evaluate the spatial deformation field for an entire vocal ligament. FE models, based on the DIC-derived material properties, were created to evaluate how variations of cross-section, inhomogeneity, and anisotropy affect the fundamental frequency of vibration (Kelleher et al. 2010).

An area where DIC outperforms most other strain measurement techniques is that of *in vivo* measurements, thanks to its limited invasiveness. *In vivo* applications of DIC are hindered by a number of factors: difficulty/impossibility to create a dedicated speckle pattern, and limited control on the boundary conditions. The displacement of a non-linear elastic, viscoelastic, anisotropic material, highly variable and sensitive to the environment condition, such as the human skin was measured *in vivo* using DIC under large deformation, enabling the creation of a library of material properties (Evans and Holt, 2009). Fast and accurate measurement of the displacements and strain of the heart during cardiac surgery can help assessing the best strategy: DIC (exploiting the natural pattern on the myocardium) was adopted in the surgical theatre during a cardiopulmonary bypass surgery (Hokka et al., 2015). DIC was applied to ultrasound breast images to identify cancerous tissue, based on its deformation and stiffness (Han et al., 2012). DIC with ultrasound images has also been used to measure *in vivo* deformation in tendons (Okotie et al., 2012) and lower limb muscles (Affagard et al., 2014).

2.6.2 Applications to hard tissue

Historically, the main way to measure strain in hard tissues was by means of strain gauges (Cristofolini et al., 2013; Cristofolini et al., 2010a; Cristofolini and Viceconti, 1997; Yang et al., 2011). However, the reinforcement effect of strain gauges may not be negligible (Ajovalasit and Zuccarello, 2005; Little et al., 1990). Strain gauges are sometimes too large when compared to the scale at which strains gradients are evaluated in biological tissues (Amin Yavari et al., 2013; Cristofolini et al., 1997; Nicoletta et al., 2001). Furthermore, strain gauges only measure at the discrete points where they are attached. Extensometers have sometimes been used to measure deformation in bone specimens, e.g. (Keaveny et al., 1997). Similarly to soft tissue, extensometers may induce micro-damage in bone, and measure the average strain over the gauge length. Relevance of transmission photoelasticity to bone testing is limited by the fact that model materials such as araldite are homogeneous and isotropic. With reflection photoelasticity real bone can be tested, but large errors arise due to the reinforcement effect (Cristofolini et al., 1994; Cristofolini et al., 2003). An overview of applications of strain gauges, in-fibre Bragg grating sensors, DIC and

Digital Volume correlation (DVC) was recently published (Grassi and Isaksson, 2015).

DIC shows its benefits also with hard tissue, allowing operating at different dimensional scales (Table 2): from small specimens (tissue-level), such as cortical bone (Hoc et al., 2006), teeth (Gao et al., 2006), up to large specimens (organ-level), such as whole bones (Tayton et al., 2010). In this case small strains are involved, never exceeding 10 000 microstrain (Bayraktar et al., 2004). The problem of characterizing cortical bone at the tissue-level (Haversian system) to assess local phenomena, such as micro-damage or bone remodelling, was solved with DIC (Hoc et al., 2006; Nicoletta et al., 2001). Single trabeculae of cancellous bone have been investigated with DIC and a high-speed camera in a three-point-bending test (Jungmann et al., 2011).

A whole-organ investigation was carried out on teeth (few millimetres) to optimize the stiffness and load transfer in dental implants (Tiozzi et al., 2011). DIC and strain gauges were used on mouse tibias under axial compression (Sztefek et al., 2010). It was concluded that the spatial resolution of the strain gauges was inadequate to measure the localized peak strains identified by DIC. Similarly, (Vaananen et al., 2013) showed the effectiveness of DIC in identifying the location and modality of fracture in bones (in this preliminary study composite femurs were used). Strains measured with DIC at selected regions were used to validate an FE model of the same composite femur built from computed tomography (Dickinson et al., 2011). This research was further extended by (Grassi et al., 2013), who performed a much larger number of DIC measurements on similar composite femurs. A similar work was carried out on cadaver femurs: a high-speed cameras was used to measure strain and fracture with 2D-DIC, and validate the corresponding FE models (Op Den Buijs and Dragomir-Daescu, 2011). This approach was further extended to 3D-DIC using two high-speed cameras (Grassi et al., 2014; Helgason et al., 2014). Due to their limited resolution (1 Megapixel or lower, depending on the frame rate), high-speed cameras were originally introduced to biomechanical investigations only to qualitatively investigate fracture (Cristofolini et al., 2007; de Bakker et al., 2009; Juszczak et al., 2011) (Schileo et al., 2008b; Zani et al., 2015). High-speed cameras with sufficient resolution to be integrated in a DIC system became available only recently.

A preliminary application to the human vertebra was recently published, where the methods were fine-tuned to minimize errors (Palanca et al., 2015a).

2.7 Synergies with finite element in biomechanics

Another important feature of DIC is its ability to integrate with FE models, in different ways (Babuska and Oden, 2004; Cristofolini et al., 2010b; Jones and Wilcox, 2008):

1. Experimental identification of model parameters: the high complexity involved in FE models (often including patient-specific detail, inhomogeneous material properties, non-linear interfaces, etc) requires experimental measurements to identify the input parameters.

2. Experimental validation of model predictions: as reliability of numerical predictions cannot be taken for granted, quantitative comparison with experimental data is necessary. DIC (if properly optimized) has a similar systematic error, but larger random error than strain gauges. However, DIC can provide full-field information. For instance, DIC was used to validate FE models of the proximal femur for the prediction of strains and fracture, both qualitatively (Helgason et al., 2014), and quantitatively (regression between DIC-measured and FE-computed stiffness and strain (Dickinson et al., 2011; Grassi et al., 2013; Op Den Buijs and Dragomir-Daescu, 2011)).
3. Use of numerical models to improve the experiment: the synergy between a local approach (implemented in most DIC software) and a global approach (FE) can be exploited to reduce the errors in DIC-computed strain field. In fact, usually low-pass filters are used to reduce the noise in the strain maps obtained by derivation of the displacements (Baltoni et al., 2016). This can result in loss of information due to the smoothing of existing gradients. Alternatively, strain can be computed by means of an FE solver, where DIC-measured displacements are imposed to the FE nodes (Evans and Holt, 2009). The continuum assumption (which is intrinsic to FE modelling), acts as a low-pass filter.
4. Use of numerical models for inverse material characterization, based on experimental measurements: integration of numerical and experimental methods allows non-destructive assessment of mechanical properties that are otherwise difficult to measure experimentally. For instance, to investigate the mechanical response of the skin, *in vivo* strain under point loading was measured by DIC; such measurements were fed into an FE model to estimate the hyperelastic parameters (Evans and Holt, 2009). Similarly, specimen-specific FE models of the sclera were fed with DIC-measured quantities (Coudrillier et al., 2013).

2.8 Other image correlation tools

DIC allows calculating the displacement and/or strain only on the surface of the specimens. An important step forward in the characterisation of biological structures consists in measuring displacement and strain fields on entire volumes (Freddi et al., 2015; Roberts et al., 2014). The concept of DVC was introduced by (Bay et al., 1999a; Smith et al., 2002) as a natural extension of DIC to a three-dimensional domain. With the rapid improvement of micro-focus computed tomography (micro-CT), DVC has gained increasing attention as a powerful tool to examine full-field deformations in trabecular bone (Dall'Ara et al., 2014; Gillard et al., 2014; Liu and Morgan, 2007; Nazarian and Müller, 2004; Palanca et al., 2015b), cortical bone (Dall'Ara et al., 2014; Palanca et al., 2015b), whole bones (Hussein et al., 2012; Hussein et al., 2013), cellular scaffolds (Madi et al., 2013) and bone-cement interface (Tozzi et al., 2012, 2014).

2.9 Conclusions

This review has shown the potential usefulness of DIC as a full-field, contactless and versatile technique. In fact successful biomechanical applications of DIC can be found at different dimensional scales (from the microscopic tissue-level, to macroscopic organ-level specimens), on a wide range of biological specimens (both soft and hard tissue) and for a variety of tests, including fracture.

DIC can measure displacements with very high accuracy and precision. However, to obtain accurate and precise measurement of strain, great care is needed to optimize the surface preparation, and the hardware and software settings. Thanks to the versatility of DIC, it can be foreseen that more and more application will be developed in biomechanics in the forthcoming years, both *in vitro* and *in vivo*.

Acknowledgments

The Authors wish to thank dr. Thomas Luyckx and dr. Brad L. Boyce for providing the pictures reproduced in Fig. 2.

Appendix

DIC uses digital images to track the displacement of portions of the speckled surface (Fig. 1). In the case of 2D-DIC, images of specimen surface in the undeformed (or reference) and deformed states are acquired by one high-spatial-resolution digital image acquisition device (such as a regular digital camera, a high-speed camera, an optical microscope). The digital images (typically in grey-scale) are divided into sub-images (facets). In order to obtain an approximation of grey-scale between pixels instead of discrete and independent values, the grey-scale distributions are interpolated, usually with a bicubic spline. Images of the deformed states are compared to the reference one in order to match facets and track the displacement. The degree of matching between facets is evaluated by a normalized cross-correlation function such as (Eq. 1):

$$\rho_{CC} = \frac{\sum_{i=1}^N \sum_{j=1}^M F(x_i; y_j) G(x'_i; y'_j)}{\sqrt{\sum_{i=1}^N \sum_{j=1}^M F^2(x_i; y_j) \sum_{i=1}^N \sum_{j=1}^M G^2(x'_i; y'_j)}} \quad (\text{Eq. 1})$$

Or a normalized sum-of-squared-differences such as (Eq. 2):

$$\rho_{SSD} = \sum_{i=1}^N \sum_{j=1}^M \left[\frac{F(x_i; y_j)}{\sqrt{\sum_{i=1}^N \sum_{j=1}^M F^2(x_i; y_j)}} - \frac{G(x'_i; y'_j)}{\sqrt{\sum_{i=1}^N \sum_{j=1}^M G^2(x'_i; y'_j)}} \right]^2 \quad (\text{Eq. 2})$$

Where $F(x,y)$ and $G(x',y')$ represent the grey-scale value for the pixel at the coordinate (x,y) of the reference image and the coordinate (x',y') of the deformed image, respectively. N and M are the dimensions of the facet, usually square. After matching the facets, the full-field displacement is automatically computed by tracking the change in position of points on digitized images. In fact, the coordinates in the reference image (x,y) and in the deformed one (x',y') describe the deformation between the two states (Eq. 3):

$$\begin{aligned} x' &= x + u + \frac{\partial u}{\partial x} \Delta x + \frac{\partial u}{\partial y} \Delta y \\ y' &= y + v + \frac{\partial v}{\partial x} \Delta x + \frac{\partial v}{\partial y} \Delta y \end{aligned} \quad (\text{Eq. 3})$$

where u and v represent the displacements for the facet centres in the x and y directions, respectively. Δx and Δy are the distances in the x and y directions, from the centres of the facet to the point in coordinates (x, y) . The gradient terms in Eq. 3 indicate that the initial facet of $(M \times N)$ pixels will be strained to

optimally match the correspondent facet in the deformed status (Bruck et al., 1989; Peters and Ranson, 1982; Wang et al., 2002).

The strain tensor (Eq. 4) is obtained by derivation on displacement gradients (Sutton et al., 2009):

$$\begin{aligned}
 e_{xx} &= \frac{\partial u}{\partial x} + \frac{1}{2} \left[\left(\frac{\partial u}{\partial x} \right)^2 + \left(\frac{\partial v}{\partial x} \right)^2 \right] \\
 e_{yy} &= \frac{\partial v}{\partial y} + \frac{1}{2} \left[\left(\frac{\partial u}{\partial y} \right)^2 + \left(\frac{\partial v}{\partial y} \right)^2 \right] \\
 e_{xy} &= \frac{1}{2} \left(\frac{\partial u}{\partial y} + \frac{\partial v}{\partial x} \right) + \frac{1}{2} \left[\left(\frac{\partial u}{\partial x} \right) \left(\frac{\partial u}{\partial y} \right) + \left(\frac{\partial v}{\partial x} \right) \left(\frac{\partial v}{\partial y} \right) \right]
 \end{aligned}
 \tag{Eq. 4}$$

In order to find the six deformation parameters $(u, v, \left(\frac{\partial u}{\partial x}\right), \left(\frac{\partial u}{\partial y}\right), \left(\frac{\partial v}{\partial x}\right), \left(\frac{\partial v}{\partial y}\right))$ and match the facet, an approximate-solution method is adopted. Usually, the Newton-Raphson algorithm is used because of its computational economy (Kelley, 1999). Other algorithms are also adopted, such as the Levenberg-Marquardt. When the method converges, the displacement field is obtained but discontinuities might appear due to the local grey-scale value. A smoothing algorithm is needed to provide a continuous displacement field and perform a strain analysis. Among the available smoothing algorithms (Wahba, 1975; Woltring, 1985), some are better suited than others, depending on the features of the noise to be attenuated (Baltoni et al., 2016).

3D-DIC can be considered as an extension of 2D-DIC, as the operating principles are similar, but extended on a third dimension (Luo et al., 1992) by using two or more cameras in stereoscopic vision.

Chapter III

Optimization and Validation of Digital Image Correlation

from the manuscript:

Use of Digital Image Correlation to investigate the biomechanics of the vertebra

M. Palanca, T. M. Brugo, L. Cristofolini

School of Engineering and Architecture, Alma Mater Studiorum – Università di Bologna, Bologna (IT)

Published in: *Journal of Mechanics in Medicine in Biology*, 2015, 15(2):
1540004 1-10

3.1 Introduction

Digital image correlation (DIC) is a tool that allows the contact-less and full field measurement of displacement and strain in specimens with different sizes. In the last ten years the diffusion of the DIC in the biomechanical field was constantly increasing (Palanca et al., 2016a). This was due to its high flexibility and potentiality. In fact, it allows measuring displacements and strains at a tissue-level, e.g. on cortical bone (Hoc et al., 2006), as well as at the organ-level, on soft tissue (Boyce et al., 2008; Luyckx et al., 2014) and hard tissue (Grassi et al., 2013; Tayton et al., 2010).

DIC algorithms generally allow the measurement of displacement with an excellent accuracy and precision (Freddi et al., 2015; Sutton et al., 2009). However, the excellent accuracy and precision are lost when computing the strain distribution. In fact, the differentiation process involved enhances the noise present in the computed field of displacements.

Before starting to use the DIC in a biomechanical study, a validation was required both for the specimen preparation and the acquisition and processing parameters (Lionello and Cristofolini, 2014; Sutton et al., 2008a; Wang et al., 2009; Zhang and Arola, 2004). Because the accuracy and precision cannot be taken for granted, a benchmark test was performed.

The aims of this work were:

- To define a repeatable and reproducible procedure to create an optimal speckle pattern;
- Optimize as much as possible the performance of a DIC system;
- Perform a preliminary test on biological tissue: a vertebra specimen.

3.2 Material and Methods

3.2.1 Optimization of the preparation of the speckle pattern

In order to have correct recognition of the specimen's surface, and an accurate and precise strain measurement, a speckle pattern must have the following features (Palanca et al., 2016a; Palanca et al., 2015b; Sutton et al., 2009):

- A random distribution;
- A high contrast;
- A black-to-white ratio close to 50%.

The specimen surface of an aluminum beam was coated with a water-based paint (white matt, Chrèon, Lechler, Como, Italy). For the speckle dots, a black paint was used (black matt, Chrèon, Lechler). The paints were deposited on the specimens by means of an airbrush spray gun (AZ3 HTE 2, Antes Iwata, Torino, Italy) with a nozzle of 1.8 mm, a round jet and a spray distance of 300 mm.

It has been found that to achieve satisfactory correlation results the black speckles should be 2-3 times the pixel dimension of the acquired image (Bruck et al., 1989) and their size should have a low dispersion.

In order to produce the speckles with the features just mentioned, 9 patterns were produced on the same aluminum specimen, after achieving a good intra- and extra-operator reproducibility, exploring different settings of the airbrush. A factorial design was planned, where two factors were investigated, each at three levels:

- The air pressure: 500 kPa, 1000 kPa and 1500 kPa;
- The airflow: 1 turn, 2 turns, 3 turns of the knob from the close all position.

The images of the patterns so made were acquired with a dimensional reference scale. The quality of the speckle pattern was analyzed with a home-written algorithm in MATLAB (Math Works Inc, Natick, Massachusetts, USA) to compute the average and standard deviation of the speckles dimension (Lionello and Cristofolini, 2014).

3.2.2 Benchmark test

3.2.2.1 Selection of the software parameters

A flat aluminum specimen was prepared with the best speckle pattern identified with the previous tests (Palanca et al., 2016a; Sutton et al., 2009). The specimen was acquired in a zero-displacement and zero-strain condition by the two cameras of a 3D DIC system (Q-400, Dantec Dynamics, Skovlunde, Denmark), equipped with 17-mm lenses (Xenoplan, Schneider-Kreuznach, Bad Kreuznach, Germany). The Istra-4D software (Dantec Dynamics) was employed to elaborate the images and compute the displacement and strain distribution. Both the axial and the transversal strain were computed to investigate the presence of preferential directions for strain measurement in the algorithm.

In order to understand the effects of the variation of the parameters of the DIC software, a factorial design was performed. The parameters investigated in this work were:

- The facet size, the dimension of the computation area: 15, 19, 21, 25 pixels;
- The grid spacing, the step between consecutive facets: 4, 7, 11, 15 pixels;
- The local regression (Palanca et al., 2016a) used to reduce noise of the computed strain by extending the computation on a larger domain: 3, 5, 7, 9, 11, 13, 15 facets.

For each of the 112 combinations of parameters, the strain in the axial and transversal direction was computed on the same computation area of 100 mm x 67 mm. Because the specimen was in a zero-strain condition, the expected strain was zero. Consequently, any strain different from zero was accounted as an error:

- The systematic error: bias of the average, i.e. lack of accuracy;
- The random error: standard deviation of the readout, i.e. lack of precision.

3.2.2.2 Selection of the hardware parameters

After defining the best setting of the software parameters, the following hardware parameters were studied, when the same aperture was used, and the same lighting was delivered on the specimen:

- The gain (i.e. the gain applied to the signal acquired by the camera sensor): 0 db, 3 db and 9 db;

- The image exposure (i.e. the lightness/darkness of the image, which was controlled by adjusting the shutter time): couples of images from highly underexposed (55/255 average value) to highly overexposed (248/255 average value) were acquired.
- The effect of the distortion of the lenses: a couple of images were acquired and elaborated. A virtual circular strain gauge of 10 mm of diameter was placed in the center of the image and moved to the corner passing along the diagonal.

3.2.3 Preliminary test on a vertebra specimen

Finally, the acquired know-how was moved from the benchmark test to investigate a biological specimen. A human vertebra specimen (L5) was obtained through an ethically approved international donation program (IIAM, Jessup, PA, USA). The donor was a male, 49 years old, without any muscular-skeletal pathology, died because of pneumonia. All soft tissues, including the intervertebral disks, tendons and ligaments were removed. The vertebral body was degreased with acetone and was fixed in a pot with acrylic bone cement. An optimized speckle pattern was painted following the guidelines above. The DIC system was set on the best parameters, based on the previous tests. A zero-strain condition was implemented also for the vertebra. In order to know the quality of the measurement on a biological tissue, the strain was computed on the prepared vertebral body.

3.3 Results

3.3.1 Optimal speckle pattern

The dimension of the speckle dots increased for higher airflow rates, and it decreased for higher air pressure (Fig. 1). The results also showed that increasing the airflow rate, the dispersion tended to increase, while increasing the pressure the dispersion decreased. For a given resolution of the cameras of the DIC system (2592 x 1936 pixels), the dimension of the computation area (100 mm x 67 mm), and the recommended average dimension of the speckles (2-3 pixels), the desirable dimension of the speckle should be between 0.077 mm and 0.116 mm. The best combination (optimal average size with minimal dispersion) of the factorial design corresponded to specimen number 5 (Table 1).

Table 1 - Summary of the investigated parameters of the airbrush spray gun, and the relative dimension obtained of the speckle pattern

<i>Specimen number</i>	<i>Flow rate (knob turns)</i>	<i>Pressure (kPa)</i>	<i>Average speckle area (mm²)</i>	<i>St. dev. speckle area (mm²)</i>
1	1	500	0.094	0.068
2	2	1000	0.065	0.045
3	3	1500	0.063	0.044
4	1	500	0.120	0.110

Specimen number	Flow rate (knob turns)	Pressure (kPa)	Average speckle area (mm ²)	St. dev. speckle area (mm ²)
5	2	1000	0.099	0.108
6	3	1500	0.099	0.113
7	1	500	0.127	0.129
8	2	1000	0.091	0.088
9	3	1500	0.075	0.057

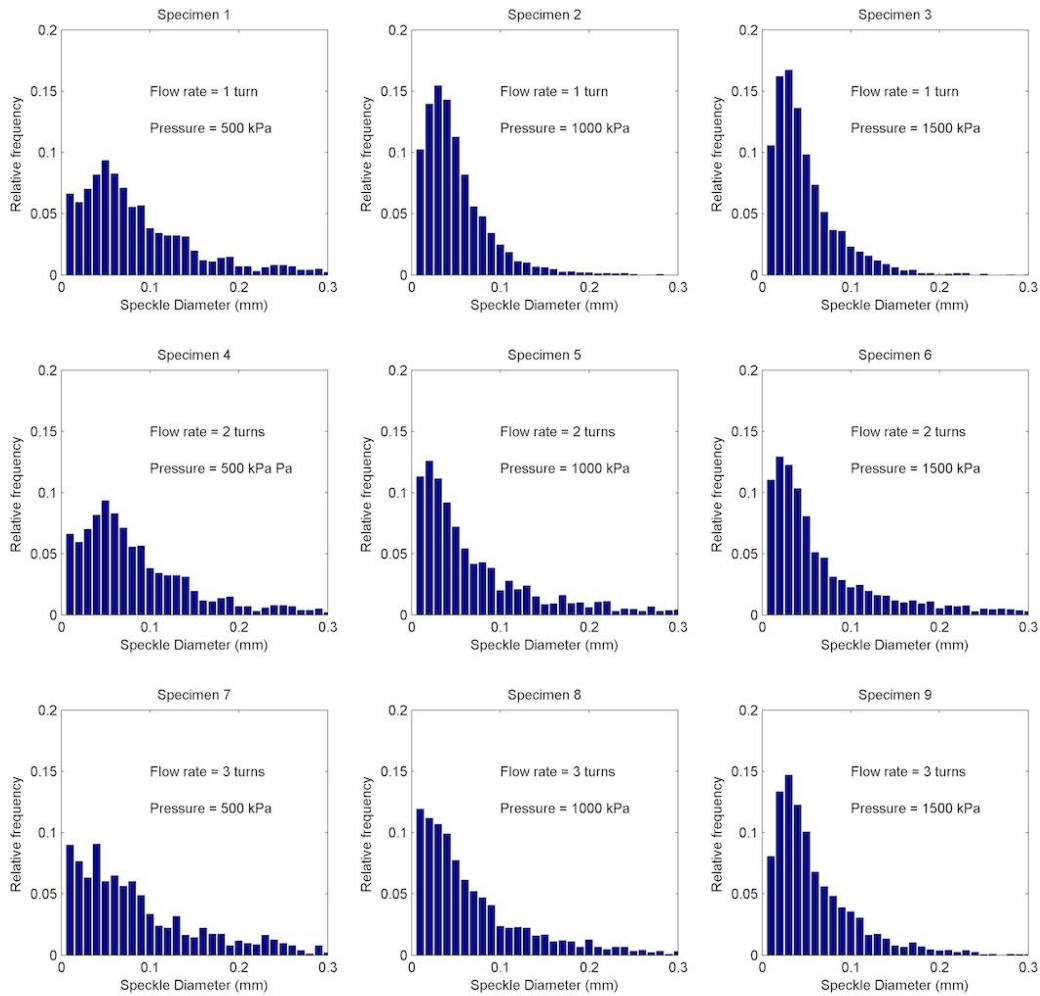


Fig. 1 – Histograms of the distribution of the speckle patterns for the different airbrush gun settings.

3.3.2 Accuracy and precision in the benchmark test

3.3.2.1 Influence of the software parameters

The outputs of the test allowed knowing the effect of the changing of single parameters. The total error (sum of systematic and random error) was similar in the axial and transversal directions, and it showed the influence of facet size, grid spacing and filtering. For sake of brevity, only the errors for the axial strains are presented (Fig. 2):

- The facet size slightly reduced the total error: when the other parameter were optimized, the total error was 254 microstrain with a facet of 15 pixels, 244 microstrain with a facet of 19 pixels, 232 microstrain with a facet of 21 pixels, 211 microstrain with a facet of 25 pixels.
- The grid spacing markedly reduced the total error. The grid spacing decreased the total error on the computed strain by a factor 2, when the larger local regression window was applied. Such a benefit rose to a factor 5 when a smaller regression window (i.e. milder filtering) was implemented.
- As expected, the local regression acted as a filter: the larger the regression window, the lower the error on the computed strain. Filtering allowed reducing the errors by a factor 3.

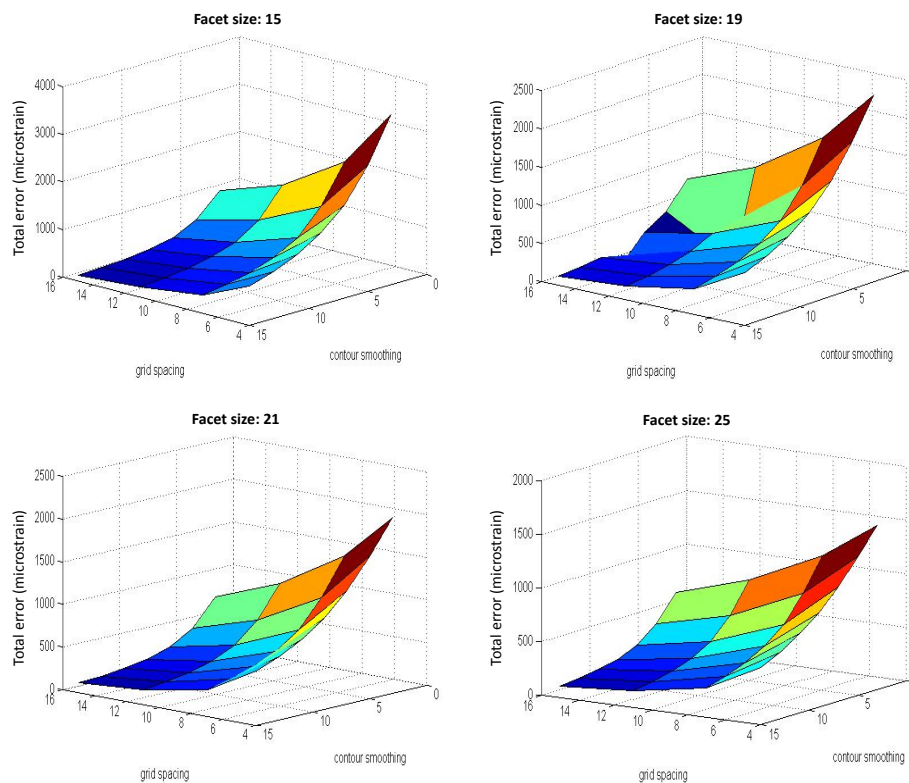


Fig. 2 – Effects of the software parameters on the total error (sum of systematic and random error) in computing the strains.

It must be noticed that increasing the grid spacing and the filtering (local regression) reduces the random error, but at the same time it is associated with a worse resolution (possibly causing loss of details in high gradient regions).

In the following, we will focus on a limited range of facet size, step and local regression, which correspond to a computation area between 1.5 and 3.5 mm (this is the typical size of strain gauges used in biomechanical investigations addressing whole bones (Cristofolini et al., 2013; Cristofolini et al., 2010a)). When the two components of error were examined separately (Fig. 3):

- The systematic error was not significantly influenced by the software parameters;

- The random error strongly depended on the software parameters. In fact, increasing the grid spacing and the dimension of the local regression decreased the noise.

Limiting the resolution on a limited range needed in biomechanical field it was possible select the best software parameters, for the specific test and the specific condition (lighting, hardware, software):

- Facet size: 25 pixels
- Grid spacing: 11 pixels
- Local regression: 9 x 9 facets

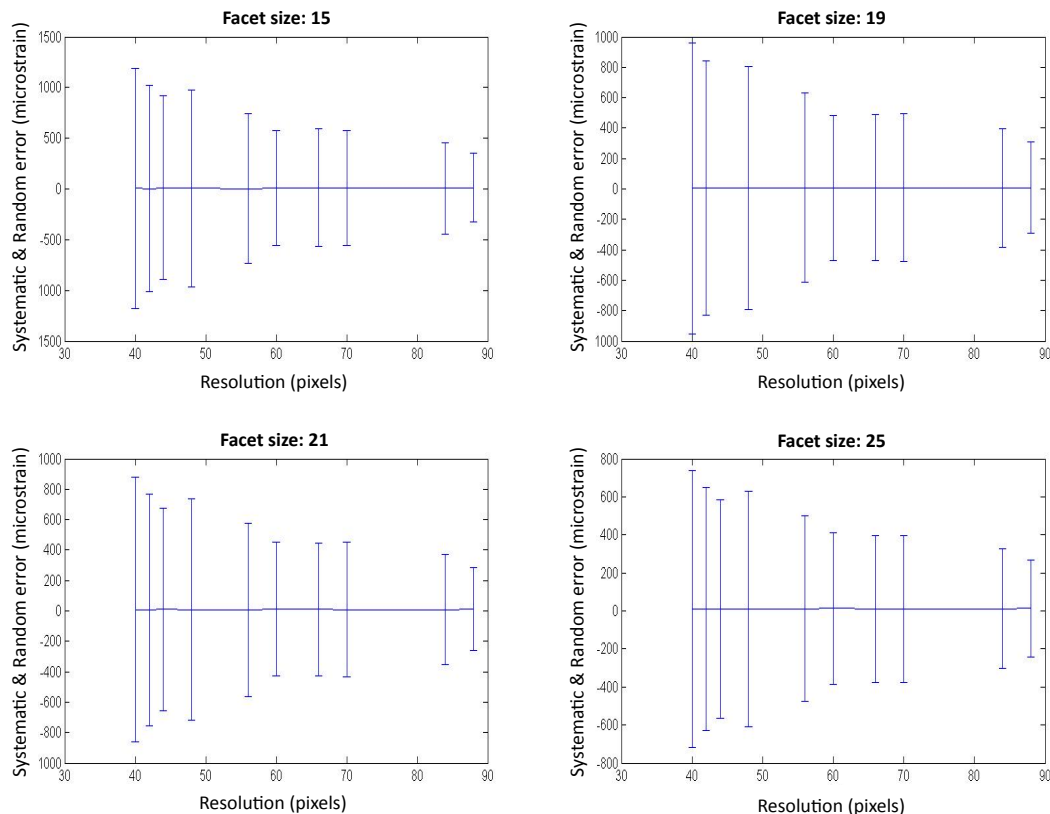


Fig. 3 – Analysis of the error affecting the DIC-computed strain as a function of the spatial resolution. The range explored was equivalent to a strain gauge length between 1.5 mm and 3.5 mm. The horizontal line indicates the average error (systematic bias); the vertical bars indicate the random error (noise).

3.3.2.2 Influence of the software parameters

Similar to the tests on the software parameters, the systematic error was not influenced by the gain. Conversely, it was found that increasing the gain resulted in higher noise (larger random error): with 0 dB gain the random error was 130 microstrain, with 3 dB it raised to 160 microstrain, and with 9 dB it went up to 210 microstrain.

The exposure test allowed finding a value of exposure better than the one recommended by the Istra-4D software. In fact, moving from underexposure to overexposure the random error decreased. The minimum noise (120 microstrain) was found with a level of exposure of 210/255. Over this point, the random error increased quickly (the image was mostly saturated to white).

Finally, the variations of the systematic and random error due to image distortion were analyzed from the center of the image to the corner. Near the center of the image the errors had their minimum value (systematic error: 10 microstrain, random error: 390 microstrain). Near the corners the error increased (systematic error: 100 microstrain; random error: 950 microstrain).

3.3.2.3 Summary of the reduction of the systematic error and noise

The optimization of the software and hardware parameters allowed reducing the systematic and random errors. It was shown that the facet step and the regression window are more powerful tools in reducing the error than the facet size by itself. It was also confirmed that suitable illumination is needed to allow optimal image sharpness without the need of increasing the gain. This optimization process reduced the systematic error from 150 microstrain (before) to 10 microstrain (after); the random error was from 600 microstrain down to 110 microstrain.

3.3.3 Results of the test on a vertebra specimen

The preliminary test conducted on a vertebra specimen showed that it is possible using the DIC on a biological specimen with a complex geometry, like a vertebra. The portion of observed surface where correct correlation was achieved was about 80%. In the zero-displacement, zero-strain tests, systematic and random errors were visible (Fig. 4). The magnitude of the apparent strain computed in the vertebra in the zero-strain condition was higher than that in the benchmark test.

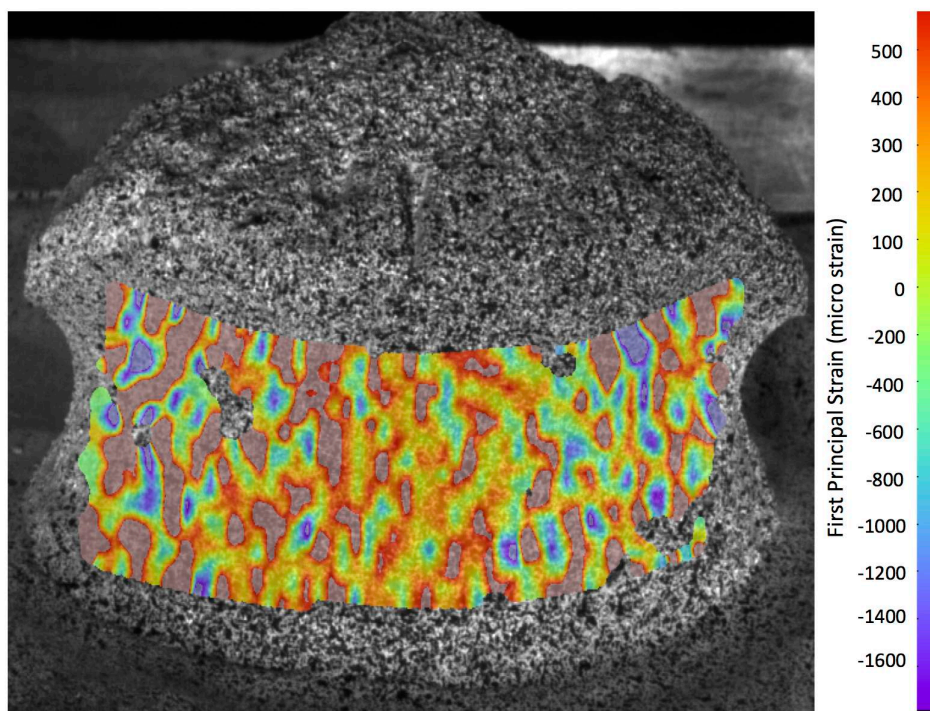


Fig. 4 – Test of correlation on a vertebra specimen (L5, anterior view): the apparent strain in a zero-strain, zero-displacement condition is shown, without application of any filtering.

3.4 Discussion

The work showed the importance of a careful optimization of the DIC software and hardware settings to minimize random and systematic errors. As in the work of (Amiot et al., 2013; Barranger et al., 2010; Lava et al., 2009; Lava et al., 2010; Lava et al., 2011), a benchmark test allowed to understand the behavior of the algorithms, and defining the best setting for the parameters. The study about the software parameters was consistent with the work of (Carriero et al., 2014). In general, the settings that allowed minimizing the random errors were associated also with averaging over a larger area, and were therefore associated with poorer spatial resolution.

To the Authors' knowledge this is the first work that analyzed the effect of the exposure on the errors affecting the DIC-computed strains. The optimization of the gain of the hardware parameters was in line with the conclusions of (Pallottino, 2011): when the exposure was low, a higher gain was needed which worsened the signal-to-noise ratio (the dark noise due to thermal excitation of the electrons is approximately constant, whereas the image signal was lower). When the pictures were brighter, this allowed using a lower gain, providing better accuracy and precision in the computed strains.

The distortion due to the lenses deserves special attention. In fact, while the other tests allowed the identification of specific parameters, this test allowed only the identification of the less critical area within the frame. This did not offer quantitative information about any adjustable parameter, but only a qualitative consideration about the most critical regions. The solution to reduce the error due to the distortion of the lenses is to replace the lenses with one with less distortion (longer focal length).

Finally, the work moved from a simplified specimen to a biological one, with a more complex geometry. The influence of the complex geometry and, the consequent reduction of accuracy and precision, were highlighted.

Future tests will allow measuring the displacements and strains of biomechanical specimens, exploiting the acquired know-how.

Chapter IV

Application of Digital Image Correlation on spine

from the manuscript:

Exploring the strain distribution of thoracolumbar spine segments: An application of Digital image correlation

M. Palanca¹, M. Marco², M.L. Ruspi¹, C. Faldini^{3,4}, L. Cristofolini¹

¹School of Engineering and Architecture, Alma Mater Studiorum – Università di Bologna, Bologna (IT)

²Department of Mechanical Engineering – Universidad Carlos III de Madrid

³2nd Orthopaedic and Traumatologic Clinic, Rizzoli Orthopaedic Institute

⁴Department of Biomedical and Neuromotor Sciences, Alma Mater Studiorum – Università di Bologna

Paper under preparation

4.1 Introduction

The spine is one of the most complex structures of the musculoskeletal apparatus. It consists of a sequence of hard tissues (vertebrae) and soft tissue (intervertebral discs), stabilized by the ligaments. The spine has the function of supporting the body in a standing position and protecting the spinal cord. The morbidity and mortality associated to spine diseases are an increasingly concerning issue (Johnell and Kanis, 2006). Spine characterization is a fundamental task in biomechanics because it could help engineers and clinicians, to design implants with a higher success ratio (Luca et al., 2016; Smith et al., 2011).

To reach this know-how, the spine segments were frequently investigated in experimental tests applying known motions (Corse et al., 2003; Gillespie and Dickey, 2004; Hindle et al., 1990) or known loads (Busscher et al., 2009; Hansson et al., 1987; Panjabi et al., 1994). From these tests, the range of motion and the stiffness can be evaluated, describing the kinematics of the spine segment as a whole, in physiological (Ahn and DiAngelo, 2007; Cook et al., 2015; White III and Panjabi, 1990), pathological (Oda et al., 2002) and after treatments conditions (Metzger et al., 2016).

Just in few cases the local strain distribution was experimentally evaluated, separately either on the vertebra or on the intervertebral disc. Strain in the vertebra was measured by means of strain gauges (Cristofolini et al., 2013; Danesi et al., 2016a; Pintar et al., 1995; Shah et al., 1978): this provides accurate measurements, but measurement is limited to the point of application of the strain gauge. Moreover, the reinforcement effect of strain gauges is not negligible (up to 9%), especially on the thin shell of osteoporotic bones (Ajovalasit et al., 2007; Cristofolini et al., 2013; Little et al., 1990). Measuring the local strain in the intervertebral disc is even more difficult, due to the intrinsic nature of the disc itself (low stiffness, inhomogeneous, anisotropic). One of the first measurements of the strain on the outer part of the disc (*annulus fibrosus*) was based on stereo-photogrammetry, and covered a limited field of view (Stokes, 1987). More recently, the entire disc surface was investigated (excluding the adjacent vertebrae), using digital image correlation (DIC) (Spera et al., 2011). On the other hand, Digital Volume Correlation (DVC) (Roberts et al., 2014) was deeply investigated to be used with enough confidence on vertebrae (Palanca et al., 2016b), and has already been applied on spine segments (Hussein et al., 2012). Nevertheless, DVC remains connected with the time-consuming procedure of the images acquisition, which could be a problem with viscoelastic specimens, such as the bone or the intervertebral discs. In fact, the loading speed of physiological motor task is far from the time necessary for a CT scan. And, consequently, being the behaviour of a time-dependent material strictly connected with the loading speed, the provided strain describes only a circumscribed and limited condition.

However, what is the local deformation of spine segments under loading, what is the strain pattern, how it is affected by spinal fixation devices, where is the failure region located, are just few of the unsolved questions about the spine. In fact, to date, an experimental description of the strain distribution on the surface of a spine segment that includes both the vertebrae and the discs is missing.

The aim of this work was to explore the feasibility of using DIC to measure the strain distribution simultaneously on the vertebral bodies and the intervertebral discs of thoracic and lumbar spine segments in different loading configurations.

4.2 Materials and Methods

4.2.1 Specimen and pattern preparation

Three porcine spine segments were obtained from animals sacrificed for alimentary purposes, and stored at -28°C before the preparation and the testing. The animals were all female, of the same breed, approximately 9 months old and 100 kg at sacrifice. The segments consisted of four thoracolumbar vertebrae (T7-T10/T11-T14/L2-L5).

The muscles, the anterior longitudinal ligament, the periosteum and the ribs (where presents) were carefully removed using surgical tools, without damaging the vertebral bodies and the intervertebral discs.

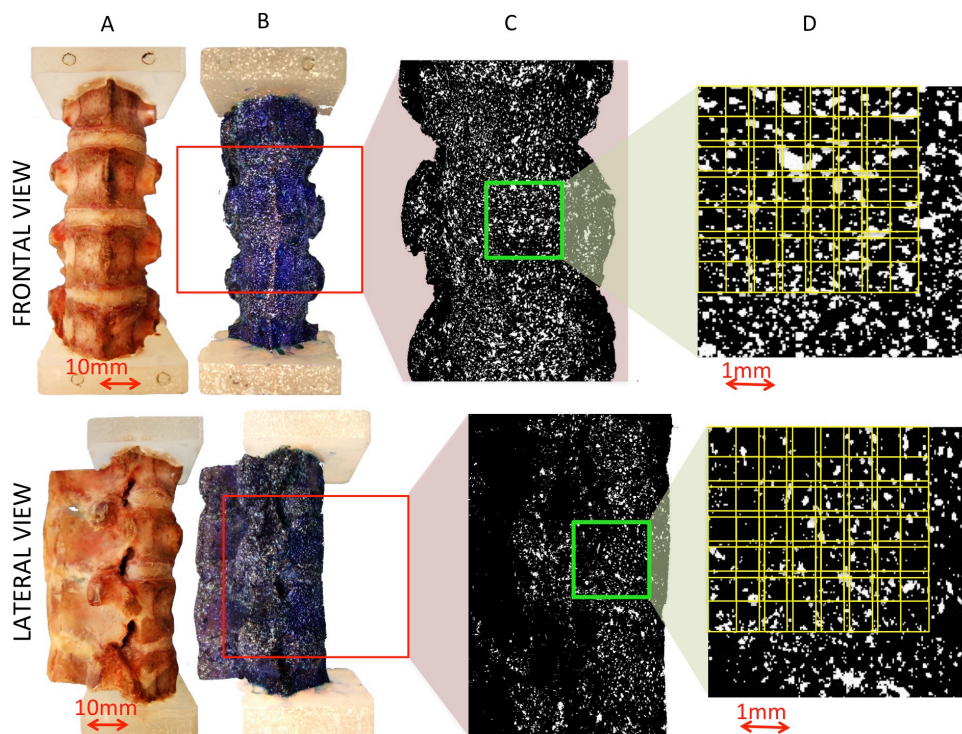


Fig. 1 - Overview at different dimensional scales of specimen preparation and analysis. The porcine spines were cleaned removing the surrounding tissues (A), and preparing the white-on-black speckle pattern (B): the red windows represent the field of view recorded by the DIC cameras. Binarized images of the entire region of interest (which covered the central disc and the two adjacent vertebrae) were generated to evaluate the dimensions of the white speckle dots (C). The facet size and grid spacing (yellow lines) can be compared to the speckle dot size in the binarized images (D).

The interspinous, supraspinous and posterior longitudinal ligaments, and the capsules were left intact in order to preserve the natural kinematics during the tests. The specimens were aligned using a six-degree-of-freedom clamp so that

the central disc of each segment (respectively, the disc between vertebrae T8 and T9, between T12 and T13, and between L3 and L4) was aligned horizontally in the frontal and lateral views (Rohmann et al., 2001). In this configuration, two pots of poly-methyl-methacrylate (PMMA) were created parallel to one another, where the upper half of the most cranial vertebra and the lower half of the most caudal vertebra, were embedded (Fig. 1).

In order to enable DIC to address the entire spine segments (both the vertebrae and the intervertebral discs), a high-contrast white-on-black speckle pattern (Palanca et al., 2016a) was prepared (Fig. 1). The spine segments were first stained with a dark background, with a solution of methylene-blue and water (4g of methylene-blue per 100 ml of water) (Lionello et al., 2014; Luyckx et al., 2014). Two applications were required for the intervertebral discs and three for the vertebrae in order to obtain a uniformly dark background. Dying was preferred to surface painting to avoid crumbling and cracking problems due to the large deformations, typical of the soft tissues such as the intervertebral discs. The white speckle pattern was prepared achieving the qualitative and quantitative requirements widely described in (Sutton et al., 2009). A white water-based paint (Q250201 Bianco Opaco, Chrèon, Italy) was diluted at 40% with water and sprayed using an airbrush-airgun (AZ3 HTE 2, nozzle 1.8mm, Antes Iwata, Torino, Italy). The spraying distance (around 300mm), and the pressure (1000kPa) were optimized (Lionello and Cristofolini, 2014) so as to obtain the desired average dot (0.18mm – equal to 6 pixels on the cameras sensors) with a small standard deviation (0.18mm) (Fig. 1). The actual size of the speckle dots was measured in the digital images of the relevant areas through a homemade script developed for this work.

4.2.2 Mechanical testing

In order to assess the feasibility of measuring strains on such complex specimens, different loading conditions were applied to explore the different loading configurations normally imposed to spine segments.

The specimens were tested using a servo-hydraulic testing machine (8032, Instron, High Wycombe, UK) in displacement control. In order to avoid the transmission of any undesired component of load, free rotation of the loading plate was allowed by means of a ball joint, while free horizontal translations were granted by means of two low-friction linear bearings.

Two different loading configurations were simulated, which are frequently investigated in the literature (Brandolini et al., 2014) (Fig. 2):

- Anterior bending: the vertical force had an anterior offset equal to the 20% of the antero-posterior depth of the central intervertebral disc;
- Lateral bending: the vertical force had a lateral offset equal to the 20% of the lateral-lateral width of the central intervertebral disc.

Ten preconditioning cycles were applied between 0 and 1.0 mm of compression, at 0.5Hz. A compression of 3.0 mm was applied for each loading configuration in 0.1mm steps, where DIC images were acquired at each step (see below). This value of the compression was chosen to prevent damage of the specimens based on preliminary tests. In fact, this allowed reaching a strain below 2000 microstrain on the bone, (this is comparable to the strain associated to physiological load (Cristofolini, 2015)), and below 100 000 in the intervertebral

discs (this is comparable to the physiological strain in the discs (O'Connell et al., 2011)). These loading configurations did not aim at mimicking any specific motor task.

4.2.3 Digital Image Correlation

A commercial 3D-DIC system (Q400, Dantec Dynamics, Skovlunde, Denmark) with directional custom designed arrays of LEDs (10000 lumen in total) was used. Images were acquired by two cameras (5 MegaPixels, 2440 x 2050 pixels, 8-bit) equipped with 35mm lens (Apo-Xenoplan 1.8/35, Schneider-Kreuznach, Bad-Kreuznach, Germany) for a stereoscopic view, positioned vertically on a tripod.

The field of view was set to 70 mm by 60 mm, which involved a spatial resolution of 28 micrometers, with depth of field of 20mm (this related to the selected aperture of f/16). This allowed evaluating displacement and strain on the region of interest: the central intervertebral disc and the two adjacent cranial and caudal vertebrae. The field of view was wide enough to avoid losing portion of the region of interest due to the movements under large deformations (Fig. 1). Calibration was performed before the tests using a dedicated calibration target (A14-BMB-9x9). To explore the possibility of assessing the different sides of the spine, two different acquisitions were performed for each loading configuration and each specimen (Fig. 2) without moving the cameras system and rotating the specimens:

- Frontal view: the cameras pointed the anterior wall of the spine segment;
- Lateral view: the cameras pointed the lateral side (either right or left) of the spine segment.

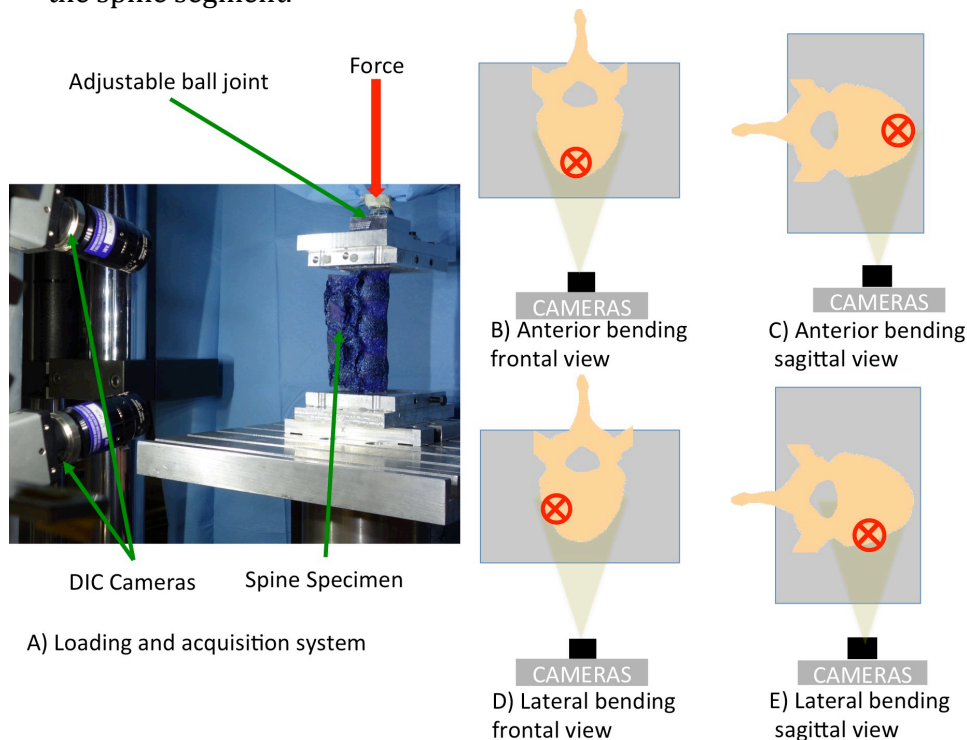


Fig. 2 - The different loading configurations were reproduced using a uniaxial testing machine and a dedicated system of low-friction linear and ball bearings to avoid transmission of undesired force components (A). The different loading configurations (anterior bending (B, C),

lateral bending (D, E)) and the different views (frontal (B, D), lateral (C, E)) are sketched, viewed from top: the red cross represents the compressive force applied to the specimen; the two cameras are aligned in this top view.

A deep optimization and validation of the system was preliminarily performed (Palanca et al., 2015a). Couples of images of the unloaded spine segments were captured and analysed with the optimal hardware and software settings in order to assess the measurement uncertainties in a known configuration (zero-strain). Being in a zero-strain configuration, any strain different from zero was accounted as measurement error. The Kolmogorov-Smirnov test was used to check that the errors followed a Gaussian distribution. The systematic and random errors (Palanca et al., 2015a) were computed, for each specimen, as the average and the standard deviation of the maximum and minimum principal strains evaluated on the frontal and sagittal view of the specimens.

During the actual mechanical tests, series of images were acquired, starting from the unloaded condition (reference step), and every 0.1mm step of compression. The test lasted few seconds, and between a test and another, the specimen was hydrated spraying saline solution.

The maximum and minimum principal strains were evaluated with Instra 4D (v.4.3.1, Dantec Dynamics, Skovlunde, Denmark) using the following parameters (Fig. 1):

- a) Facet size: 33pixels;
- b) Grid spacing: 19pixels;
- c) Contour smoothing: local regression with a kernel size of 5x5;

This resulted in a measurement spatial resolution of around 3mm.

4.3 Results

Measurements could be successfully performed on all specimens, over the entire region of interest in both the frontal and sagittal view, for both loading configurations, during the entire tests. Similar strain distributions were found in the three specimens.

4.3.1 Strain error

In the zero-strain test, the apparent strains (i.e. the errors) followed a Gaussian distribution (Kolmogorov-Smirnov), with no significant variations between different portions of the region of interest. In the anterior view the maximum principal strain had a systematic error of 30 microstrain and a random error of 80 microstrain; the minimum principal strain had a systematic error of -10 microstrain and a random error of 90 microstrain (the values reported are the median over three specimens). In the lateral view, the maximum principal strain had a systematic error of 5 microstrain and a random error of 140 microstrain; the minimum principal strain had a systematic error of -10 microstrain and a random error of 140 microstrain (median over three specimens).

4.3.2 Anterior bending – frontal view

During the anterior bending, in the frontal view, 4.4% of the region of interest lost correlation between the first and the last step. The discs underwent larger deformations compared to the vertebral bone (Fig. 3). In this frontal view, the strain in the discs followed a strain gradient, with peaks in the central portion.

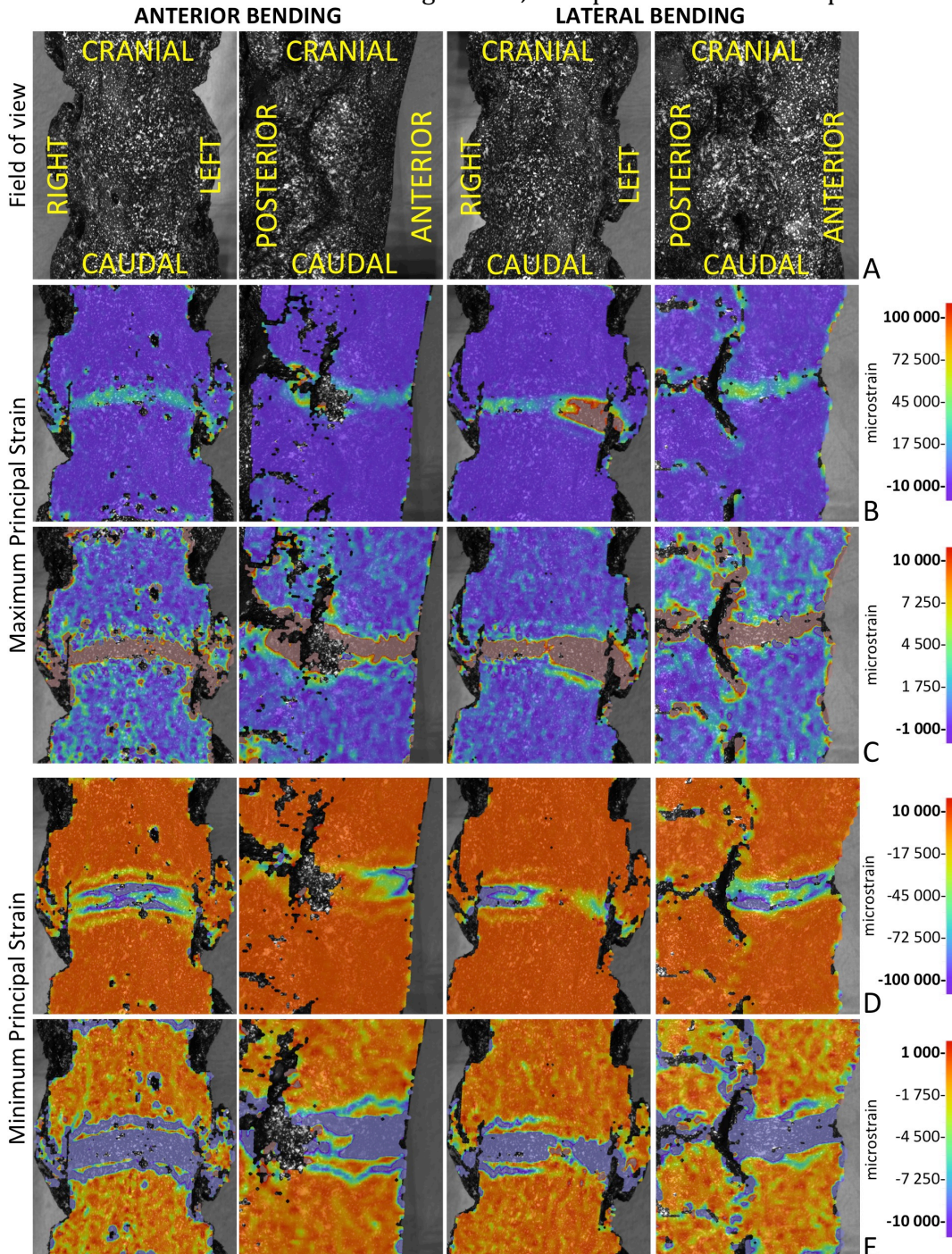


Fig. 3 - Results for a spine segment for anterior bending (images on the left) and for lateral bending (images on the right), both in the frontal and lateral view. The results for lateral bending with compression on the right side of the spine are shown; results for bending in the opposite direction were quite similar. The images as recorded by the DIC system are shown (A). The maps of the maximum (B, C) and minimum (D, E) principal strain are reported for the last step of

the test (compression of 3 mm). As the strain in the intervertebral disc and in the vertebral bone exhibited different orders of magnitude, the strain distributions are shown twice: with a full-scale suitable for the disc (B, D) and for the vertebra (C, E). For brevity, results are shown only for one of the three specimens. The magnitude and distribution of strain were similar in all three specimens.

In the discs, a maximum principal strain of the order of +20000 microstrain (aligned circumferentially) and a minimum principal strain of the order of -40000 microstrain (aligned axially) were observed.

The vertebrae had lower strains: peak of the order of +500 microstrain for the maximum principal strain and around -1500 microstrain for the minimum principal strain (Fig. 3). As the vertebrae came from relatively young pigs, larger strains were visible on the growth cartilages.

4.3.3 Anterior bending – lateral view

During the anterior bending, in the lateral view, 5.7% of the region of interest lost correlation between the first and the last step. In this scenario, the discs presented a strain gradient: they were more deformed in absolute value in the posterior than in the anterior side (Fig. 3). The maximum principal strains on the intervertebral discs varied between +12000 microstrain (anterior side) and +87000 microstrain (posterior side). The minimum principal strain followed a similar gradient, from -87000 microstrain (anterior) to -18000 microstrain (posterior). The direction of the maximum principal strain changed from circumferential (anterior side), to axial (posterior). Therefore, in anterior bending the discs tended to swell in the anterior part, and to stretch in the posterior side.

The vertebrae experienced lower strains: below +600 microstrain for the maximum principal strain, and -1500 microstrain for the minimum principal strain (Fig. 3).

4.3.4 Lateral bending – frontal view

During the lateral bending, in the frontal view, 1.5% of the region of interest lost correlation between the first and the last step. Lateral bending was applied both towards the right and the left sides, to all specimens: the outputs, in terms of strain distribution on intervertebral discs and vertebrae were symmetrical. In the frontal view, the discs showed tension and compression respectively on the left and right sides, depending on the direction of the imposed bending (Fig. 3). The maximum principal strains varied between +6000 microstrain (compressed side) and +143000 microstrain (stretched side). The minimum principal strains were varied from -85000 microstrain (compressed side) to +12000 microstrain (stretched side). The orientation of the maximum principal strain changed from circumferential on the compressed side, to axial on the stretched side.

The vertebrae had lower strains than the discs: the maximum principal strains were lower than 500 microstrain and the minimum principal strains did not exceed -1700 microstrain (Fig. 3). In this configuration it was possible to observe also tension and compression in the growth cartilages.

4.3.5 Lateral bending – lateral view

During the lateral bending, in the lateral view, 5.2% of the region of interest lost correlation between the first and the last step. When the specimen loaded in lateral bending was observed from the lateral side, the strains on the discs were rather uniformly distributed (Fig. 3). When the side in compression was observed, the maximum principal strains in the disc were of the order of +40000 microstrain, and the minimum principal strain of the order of -60000 microstrain.

The vertebrae had lower strains than the discs: the maximum principal strains were lower than 700 microstrain and the minimum principal strains did not exceed -1400 microstrain (Fig. 3).

4.4 Discussion

The main aim of this work was to develop a procedure to measure the strain distribution on thoracic and lumbar spine segments (Borchers et al., 2004), simultaneously on hard tissues (the vertebral bone) and soft tissues (the intervertebral discs) by means 3D-DIC (Sutton et al., 2009). Two different loading configurations were explored in this study, frequently simulated in the biomechanics literature (Busscher et al., 2009; Hansson et al., 1987; Oda et al., 2002; Panjabi et al., 1994) by two different viewpoints.

The results of this work showed the technical feasibility of investigating spine segments quantifying the strain distribution during the entire tests. Moreover, the measured strain distributions were highly inhomogeneous, confirming the importance of investigating the spine using a full-field tool, to complement the evaluation of the range of motion and stiffness performed in the past.

A compromise was sought between reduction of measurement uncertainty and spatial resolution. The hardware (camera resolution, lenses, field of view) and software parameters (facet size, grid spacing, contour smoothing) provided a measurement spatial resolution of about 3mm. This is comparable with the grid length of the strain gauges typically used in these applications (1-5 mm) (Cristofolini et al., 2009; Field and Rushton, 1989; Sobczak et al., 2011; Weinans and Blankevoort, 1995). The strain measurement uncertainties (below 150 microstrain) were acceptable for biomechanical purposes. Such uncertainties would not prevent detecting failure of the bone (around 10 000 microstrain (Cristofolini, 2015)), as well as strain associated to physiological loads (1 000 - 2 000 microstrain (Lanyon et al., 1975)). The same considerations are confirmed for the intervertebral discs: as the failure strain is around 250 000 microstrain (Stokes, 1987), and the physiological strain is below 150 000 microstrain (O'Connell et al., 2011), DIC can be used to investigate both physiological deformations and failure.

Even if large deformations and displacements were involved, correlation was satisfactory throughout the tests. The correlated surface covered the desired field of view, with a loss of correlation lower than 5.7% of the initial correlated surface. This loss of correlation was due mainly to the leakage of marrow or blood from the vertebral body during the compression, especially in the frontal

view. Additionally, the out-of-plane movements of the posterior elements (capsule) caused some out-of-focus in the lateral view. The white-on-black pattern prepared confirmed its suitability both for hard and soft tissues (Lionello et al., 2014). In fact, the background, prepared with methylene-blue, did not crumble during the tests, while the white dots remained sharp and adherent to the specimen's surface.

The evaluated strains confirmed the expected trends in all the performed tests: larger strains were measured in the intervertebral discs (in the order tens thousands microstrain), lower strains in the vertebrae (below 2 000 microstrain). Such strain gradients are consistent with the expected biomechanics of the spine (White III and Panjabi, 1990). DIC discriminated the portion of the discs subjected to tension/compression, with the expected orientation of the principal strains. In fact, DIC was able to capture the compression and its relative bulging of the discs: in the compressed side of the discs the minimum principal strains were axial, as expected; the maximum principal strains were large, and with a horizontal orientation.

Moreover, the combination of the selected pattern, software parameters, and hardware allowed easily recognizing the deformation on the growth cartilages of the vertebrae. This would otherwise be impossible to evaluate, e.g., with traditional strain gauges. Being the spine obtained by young pigs (Taylor, 1975) the growth cartilages were not closed, and so they were subjected to larger deformation compared with vertebrae (Fig. 3).

To the authors' best knowledge, this is the first time that strain patterns were measured simultaneously on the vertebrae and intervertebral discs of the same spine specimens. Measurements were carried out in a frontal and a sagittal full-field view, in different loading configurations, frequently explored in literature (Brandolini et al., 2014). Usually, *in vitro* spine segments were investigated in terms of range of inter-segment motion (Busscher et al., 2009; Oda et al., 2002; Panjabi et al., 1994; Wilke et al., 1997) and overall stiffness (Anderson et al., 2009; Busscher et al., 2009; Hansson et al., 1987; Shim et al., 2006). In other works the spine was investigated, accounting local deformation either in the vertebrae or in the intervertebral discs. In the vertebrae, strains were evaluated in a point-wise way using strain gauges, which offer an accurate and precise value of the strain, but only on those points where strain gauges are applied. At the same time, strain gauges cause a reinforcement effect, especially on thin osteoporotic tissues (Cristofolini et al., 2013; Danesi et al., 2016a). Otherwise, the vertebrae were studied using DIC (Gustafson et al., 2016; Palanca et al., 2015a), but without evaluating the contiguous discs. Conventional strain gauges cannot be used on the discs, due to their low elastic modulus: strain measurement is possible with optical methods (Spera et al., 2011; Stokes, 1987). A work that focused on the strain distribution on spine segments was developed by Holsgrove et al. (Holsgrove et al., 2015). They used high-speed 3D-DIC to evaluate the strains on the anterior side of porcine cervical spine segments in axial impacts. They identified the peak surface strain at failure, but they did not report a quantitative full-field strain map.

A limitation of this work could be the use of porcine spine instead of human spine. This choice was mandatory because of ethical motivations: this was an exploratory methodological work to assess, for the first time, the applicability of this procedure to the thoracolumbar spine. The porcine spines are different

from the human ones in some details, but are a valid biomechanical model (Busscher et al., 2010a; Wilke et al., 2011) to demonstrate the feasibility of this novel approach. In fact, this work aimed to define a new procedure to investigate spine segments, not to quantify the biomechanics of the porcine spine itself. The applied loading configurations were not intended to replicate any specific physiological motor task, but included separate components of load which are present in physiological motor tasks (anterior bending and lateral bending), and which are typically found in spine biomechanics (Brandolini et al., 2014). These loading configurations were implemented to identify possible limitations of this technique.

Finally, this work showed the importance of exploring the full-field strain pattern on spine segments, due to the high strain gradients and differences between the bone and the discs. Our findings entail new possible applications for basic biomechanics research and clinical innovations, such as fixator devices.

4.5 Conclusion

This work showed that starting from the preparation of an adequate speckle pattern, through a validation of the DIC system and the selection of optimal DIC parameters, the full-field strain distribution can be evaluated on a complex structure composed of soft and hard tissues, such as a spine segments. Application of DIC to the spine can increase the understanding in the spine field, and open the way to a new approach both to basic, and translational research.

Part II

Displacement and strain measurements inside the specimens

*“Est modus in rebus sunt certi denique fines,
Quos ultra citraque nequit consistere rectum”*

Orazio – Satire I

Chapter V

Errors in Digital Volume Correlation in the biomechanical field

5.1 Introduction

The last years have seen the success and increasing application of Digital Volume Correlation (DVC) (Bay et al., 1999a; Roberts et al., 2014) in measuring displacements and strains inside bones (Grassi and Isaksson, 2015). Using the keywords “Digital Volume Correlation bone” on PubMed only few works were published more than 5 years ago, while the first application is dated 1999 (Bay et al., 1999a). The principal reason of this exponential diffusion releases in the ability of measuring, for the first time, displacement and strain inside the specimens, by means three-dimensional images. Of course, this diffusion was incited by the decreasing cost of computational power, storage and high-resolution computed tomography (CT) or magnetic resonance imaging (MRI) scans and the equivalent increasing potentiality of them. At the same time, the DVC ability of measuring inside specimens coincides with its weak point, because no other measurement techniques were able, today, to provide the same kind of measurements. It implicates the issue of validating this tool. In fact, the exportable data were potentially interesting but the reliability of them, in term of measurement uncertainties, cannot be taken for granted. A large number of questions, about the effect of quality/noise of images, of spatial resolution, of the specimens, of the surrounding, of algorithms, of setting parameters were without answers.

Due to the necessity of validating this tool, and the opportunity of expanding the biomechanics knowledge, the Digital Volume Correlation became, before a measurement tool, a tool to validate. Different studies assessed the effect of single inputs, with different techniques, contributing to the creation of a shared benchmark test to evaluate the performance of a new DVC algorithm, a methodology to estimate the errors and the sources of error, the diffusion of a new reliable technique.

This review born to the necessity of a critical judgment of forthcoming data, which will be available by means of DVC, and the frequent lack of *a priori* evaluation of the tool.

The aim of this review was to summarize the know-how about the validation of DVC, splitting two *scenarios* of zero-strain condition and non-zero-strain condition, covering the problem from tissue-level to organ level, in order to assess the effect of different parameters. This review is conceived for DVC users, developer, and all the related companies (i.e. micro-CT developers) and it would improve their application to open the way to a clinical use.

5.2 Digital Volume Correlation operating principles

The description of the DVC-based functions and algorithms (Freddi et al., 2015; Roberts et al., 2014) falls outside the aims of this review, but rudiments of the operating principles are necessary to understand the related problems.

The first step is the image acquisition of the specimens before and during the application of the load. A high-resolution 3D imaging system, such as a

laboratory desk micro computed tomography, with a loading stage (Madi et al., 2013; Tozzi et al., 2012) is required for the stepwise loading. The acquired images of the specimen are used to compute the displacement and strain field. Two different DVC approaches are available:

- The global approach (Barber and Hose, 2005; Barber et al., 2007; Dall'Ara et al., 2014; Madi et al., 2013), which analyses the whole volume of interest for the recognition of identical features, superimposing a selectable grid and minimizing the sum of square differences with respect to the unknown kinematics degrees of freedom;
- The local approach (Madi et al., 2013; Palanca et al., 2015b), which divides the volumes of interest in smaller and selectable subvolumes that are then individually cross-correlated (using fast-Fourier transformer, or direct-correlation).

When the correlation procedures have converged, and the quality of these correlations is expressed with the residuum, the displacement field is computed. As for the Digital Image Correlation (Palanca et al., 2016a), the displacement field should have a subvoxels accuracy to evaluate the displacement in elastic regime. In order to achieve this goal, different orders of interpolations are used (Bay et al., 1999a). The last step is the evaluation of the strain field starting from the displacement field. For the two approaches the operations are different, but the related problem is in common. In fact, the strain can be obtained by differentiation of the displacements, but the displacement fields have discontinuities that do not allowed the differentiating operations. To solve this problem, the local approach computed the strain field from the displacements evaluated on the center of each subvolume using center finite differences (Palanca et al., 2015b). The global approach, instead, converted the grid in a finite element mesh. So the displacement at the nodes of grid becomes the boundary conditions for the computation of strain through a finite element solver (Dall'Ara et al., 2014).

5.3 Causes of errors

A series of parameters, from the acquisition of the images to the elaboration of the strain, can affect the measurement uncertainties. The selection of some parameters sometimes is imposed, such as the available technology to acquire the images; other times the selection of the parameters can be optimized in order to reduce the uncertainties, such as the dimension of the measurement spatial resolution. The principal parameters (Fig. 1) were:

- The imaging technology: it is the machine (technology) used to acquire the 3D-images of the specimen (Mobilio et al., 2015; Stock, 2009; Stoller, 2006). It could be: MRI, microMRI, CT, microCT, SynchrotronCT, OCT. Pros and cons are connected for each technology. The discriminating factor for the selection of the technology is the kind of specimen: hard or soft tissue, in vivo or in vitro. The technology with an higher signal-to-noise ratio could reduce the measurement uncertainties, for example the SynchrotronCT, but cannot be ever used, i.e. for in vivo tests;

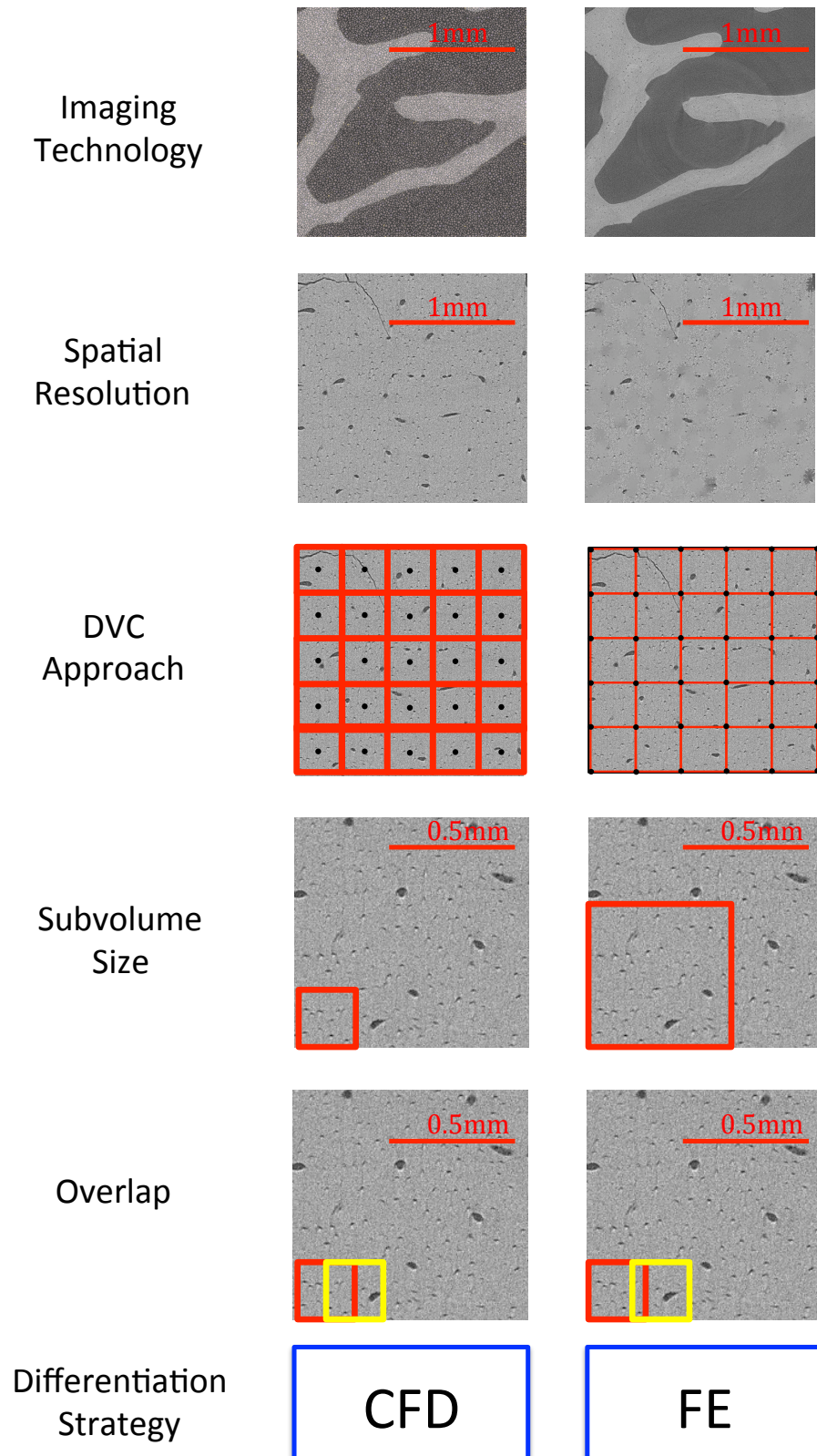


Fig. 1: Exemplification of the principal parameters affecting the measurement uncertainties. Imaging technology: traditional microCT vs synchrotron microCT; spatial resolution: 1.6 μ m vs 10 μ m; DVC approach: local vs global; subvolumes: small vs large; overlap: 50% vs 25%; differentiation strategy: centred finite differences vs finite element solver.

- The spatial resolution: this is deeply connected to the imaging technology (Leclerc et al., 2012). The smaller the spatial resolution, the higher the feature resolvable. But a small voxel size cannot be ever obtained; sometimes it is due thanks to a high radiation dose, other times through a long time scanning session. A compromise between spatial resolution and the kind of specimen and test is mandatory;
- The DVC approach: two macro-family are available: the local approach, and the global approach (Hild and Roux, 2012). The differences rely in the volumes (subvolumes or the entire volume) taken into account for the evaluation of the displacement;
- The sub-volume size: it is the three-dimensional equivalent of the facet for the DIC. It is the dimension of the sub-3D-image used to recognize the features;
- The overlap: is the step between consecutive sub-volumes;
- The strain evaluation: the strains were obtained differentiating the displacement field. But, in some points the displacement field has discontinuity, so it is necessary a method to pass through this problem and that limited the error.

5.4 How can we quantify accuracy and precision?

A brief explanation of the issue related to the validation of the DVC is mandatory. The DVC, as its surface counter part: the Digital Image Correlation (Palanca et al., 2016a; Sutton et al., 2009), showed an impressive accuracy and precision for the displacement measurement. This is due to the correlation process, previously described, that allows containing the measurement uncertainties of the displacement under one tenth the voxel size (Palanca et al., 2015b; Roberts et al., 2014). Another level of uncertainties, instead, is connected to the strain. In fact, the strain is obtained through differentiation that acts in the opposite way of a filter, enhancing the noise. A series of works showed procedures and optimizations in order to reduce the strain measurement uncertainties starting from the preparation of the 3D-images. To these reasons, the following sections of the work focused mainly on the strain analysis.

5.4.1 Zero-strain scenarios

The zero-strain tests represent the simplest way to access the minimum strain error of DVC. It consists in a pair of 3D images, of the same specimen without any load, obtained:

- Scanning twice without any repositioning (later referred to as “Repeated-Scan-Test”)(Bay et al., 1999a; Dall’Ara et al., 2014; Gillard et al., 2014; Liu and Morgan, 2007; Palanca et al., 2015b; Palanca et al., 2016b; Tozzi et al., 2017; Verhulp et al., 2004; Zael et al., 2006);
- Scanning once and virtually moving it for the second image (later referred to as “Virtually-Moved-Test”)(Benoit et al., 2009; Dall’Ara et al., 2014; Madi et al., 2013; Palanca et al., 2015b; Roux et al., 2008);

- Scanning once and repositioning the specimen for the second scan, manually or virtually (later referred to as “Repositioned-Scan-Test”)(Dall'Ara et al., 2014; Gillard et al., 2014; Hussein et al., 2012; Verhulp et al., 2004).

These tests are far from the loading condition, but they can account the minimum and unavoidable strain measurement error.

Respectively:

- The Repeated-Scan-Test assesses the errors due to the noise of images. The same specimens, in the same position, but scanned with different machines and/or relatively parameters, could have large differences in terms of strain errors;
- The Virtually-Moved-Test assesses the capability of the approach to recognise rigid-body-motion of the specimen, without accounting the noise level of the image. Using this test is possible, moreover, having an estimation of the displacement errors. In fact, being in zero-strain conditions does not mean being in zero-displacement. In this case, it is possible to evaluate the bias between the imposed displacement and the measured displacement; while in other condition of zero-strain, it is not possible because of unavoidable movements of specimen inside CT, the detector of CT, and so on;
- The Repositioned-Scan-Test instead merges the previous errors above described. The approach has to recognise images with different level of noise, because they are scanned twice, with the specimen moved into the space, manually or virtually, moving bold a second scan image.

On the other hand, these tests are not enough reliable for evaluation of the displacement measurement errors, especially for the differences between the evaluated and the expected value. In fact, there is an intrinsic problem related to the evaluation of displacement systematic errors for these tests. While the computation of a strain, is strictly related to the applied load; the displacements measurement is inevitably connected to the micro-movements of the imaging tool during the scans that is impossible to quantify (Liu and Morgan, 2007).

5.4.2 Known strain scenarios

As mentioned above, the accuracy and precision of a reliable measurement technique cannot be taken for granted. Usually, an estimation of accuracy and precision can be carried out comparing the outputs of the tool to validate with the ones of a validated. But no other measurement techniques are able to provide comparable measurements with the ones of DVC. Due to these reasons, only verification is possible instead of a validation (Babuska and Oden, 2004) for scenarios different from zero.

A test developed to estimate the strain measurement uncertainties in scenario different from zero could be obtained scanning the specimen and then virtually stretching the obtained images of a known quantity (later referred to as “Virtually-Stretched-Test”) (Christen et al., 2012). The capability of the approach to identify and estimate the deformation of the specimen was tested but all the issues related to the acquisition of the second scan were not contemplated (i.e. the noise of the images and the micro-movements of the machine). Moreover,

the deformation modalities of a biological specimen are so far from an imposed virtual deformation, and this problem could reduce its usefulness.

A partial validation could be performed in non zero-strain condition on the surface of the specimen (Wentzell et al., 2015). In fact, more than a measurement technique could be used. But this procedure does not represent the best condition, because the evaluation of strain with optics full-field measurement tools on the boundary of the specimen could be affected by large errors.

5.5 Metrics

DVC provided full-field measurements of the specimens, but in order to compare the output of different approaches, or simulations developed with different parameters, simplified indexes were computed:

- The accuracy (bias, systematic error): that is defined as the difference between the average of all the measurements point of the specimens and the expected values. It represents the distance between the expected strain and the evaluated strain;
- The precision (scatter, random error): that is defined as the standard deviation of all the measurements point of the specimens. It represents the dispersion of the measurements around their average value.

Some works evaluated the accuracy and precision for each component of strains, others instead average the components providing a single index of comparison but losing information.

5.6 Summary of the validation works

5.6.1 Tissue level

The works here described cover the field of DVC validation for tissue specimens. The first to perform a DVC analysis and an estimation of the errors is (Bay et al., 1999a). They worked on different samples of trabecular bone (human vertebra, tibia and femur), with a level of precision in zero strain condition useful to explore the elastic regime of bone, opening the way to a new kind of knowledge. The same group (Smith et al., 2002), working on the rotation of a trabecular bone specimen, developed the first optimization. (Verhulp et al., 2004) performed a new wide factorial design for the spatial resolution and the computational parameters, connected to the exploration of the displacement and strain on a single trabecula instead of the continuum. A new improvement of the approach was tested by (Zauelet al., 2006). They evaluated also the strains in the trabecular bone of a human vertebra during an axial compression and compared them to the results obtained by a validated FE model. Another wide factorial design was planned using 6 different bone types, 3 DVC approaches, 4 sub-volume sizes by (Liu and Morgan, 2007). At the end of their work, the

authors defined the DVC a reliable tool to estimate the pre and post yielding on bone. (Christen et al., 2012) proposed a big improvement of the imaging using the synchrotron radiation micro computed tomography, instead of laboratory source micro computed tomography for scanning the cortical bone of a murine tibia. This combination was tested with virtually moved test and virtually deformed test. The results showed an impressive improvement in the evaluation of displacement (precision of 130nanometers), almost an order of magnitude better than the other works (1.66-6 micrometers). But, at the same time, a large systematic and random error was obtained due to the small spatial resolution. (Gillard et al., 2014; Madi et al., 2013), as in other works, evaluated the performance of two different DVC approaches, before starting to use it on stepwise loading tests. (Dall'Ara et al., 2014; Palanca et al., 2015b) evaluated the displacement and strain measurement uncertainties on bovine cortical and trabecular bone, using a microCT, with virtually moved and repeated scans, elaborating the images with global and local approach: this work showed how the uncertainties could be reduced optimizing the DVC parameters. The results obtained compressing trabecular bone by DVC and a microCT based finite element models were compared showing an excellent correlation in all the planes. (Wentzell et al., 2015) introduced the using of the confocal microscope to perform DVC analysis on the lacunae of cortical bone. Moreover, a validation under actual loading condition was performed comparing the strain evaluated on the surface by means DVC and DIC, showing strains for the Digital Volume Correlation larger than 2-5 fold compared with Digital Image Correlation. Finally, a wide study of the effect of the structure was performed analyzing the uncertainties correlated to cortical bone, trabecular bone, cement and the interdigitation between cement and trabecular bone, using global and local approach (Tozzi et al., 2017). It showed the robust algorithm of the global approach that is less sensitive to the boundary condition compared to the local approach.

All the reported works focused the importance of a validation, and showed different strategies to reduce the measurement uncertainties. Nevertheless, a real and appropriate validation is still challenging and could define the reliability of this tool.

Table 1: Summary of the validation works performed at tissue type. They are reported in chronological order because the evaluation of the computational performance, can allow using more efficient parameters, and potentially better results. For more details on the results, please check the reference.

Ref	Tissues	Imaging technique	Voxel size (micrometers)	Validation tests	Parameters	Accuracy achieved (microstrain)	Precision achieved (microstrain)	Note
(Bay et al., 1999a)	Trabecular bones (human vertebra, tibia, femur)	microCT	35	Repeated scan	SV: 61 OL:0		211-457	
(Smith et al., 2002)	Trabecular bones (human vertebra)	microCT	35	Virtually moved test	SV: 51			Evaluated only the displacement errors
(Verhulp et al., 2004)	Al foam, like trabecular bone	microCT	12, 20, 36	Repeated scan; Repositioned scan	SV: 7, 13, 21	< 5000	40 000 20 000 10 000	Results reported only on plots, hard to define the exact values

Ref	Tissues	Imaging technique	Voxel size (micrometers)	Validation tests	Parameters	Accuracy achieved (microstrain)	Precision achieved (microstrain)	Note
(Zauel et al., 2006)	Trabecular bones (human vertebra)	microCT	35	Repeated scan	SV: 35		39-100	Comparison between FE and DVC
(Liu and Morgan, 2007)	Trabecular bones (bovine femur, tibia, rabbit femur, tibia, vertebra, human vertebra)	microCT	36	Virtually moved; Repeated scan	SV: 20,30,40,50	400-1300	150-600	Results for the subvolume size of 40 voxels

Ref	Tissues	Imaging technique	Voxel size (micrometers)	Validation tests	Parameters	Accuracy achieved (microstrain)	Precision achieved (microstrain)	Note
(Christen et al., 2012)	Cortical bone (murine tibia)	Synchrotron microCT	0.74	Virtually moved; Virtually deformed		0-50 000	11 000 – 13 000	
(Madi et al., 2013)	Scaffold implant, like cartilage and bone	microCT	20	Virtually moved	SV: 32, 64 OL: 0, 50%		30-200;	
(Gillard et al., 2014)	Trabecular bone (porcine femur)	microCT	24.6	Repeated scans; Repositioned scan	SV: 24, 48, 64, 96 OL: 50%	-25 - 40	20-75	
(Dall'Ara et al., 2014)	Cortical and trabecular bone (bovine femur)	microCT	9.96	Repeated scans; Repositioned scan; virtually moved	SV: 5, 10, 15, 20, 25, 30, 35, 40, 50	0.1 – 65 477	0.1 – 23 308	

Ref	Tissues	Imaging technique	Voxel size (micrometers)	Validation tests	Parameters	Accuracy achieved (microstrain)	Precision achieved (microstrain)	Note
(Palanca et al., 2015b)	Cortical and trabecular bone (bovine femur)	microCT	9.96	Repeated scans; virtually moved	SV: 5, 10, 15, 20, 25, 30, 35, 40, 50	425 – 211 119 –	202 - 103 332	
(Wentzell et al., 2015)	Cortical bone (human femur)	Multifoton Confocal microscope	0.82	Comparison with DIC	SV: 51			Validation of the surface strain under loading condition
(Chen et al., 2016)	Trabecular bone (human and bovine femur)	microCT	17,22 9.92	Comparison with microFE	SV: 12, 25			Excellent correlation $R^2=0.99$
(Tozzi et al., 2017)	Cortical, Trabecular, biocement (porcine vertebra)	microCT	39	Repeated Scan	SV: 16, 48	-50 - 5600	50-80 000	

5.6.2 Organ level

A series of works in literature instead used the DVC to explore the biomechanics at organ level. The authors of these works initially validate the methods and then moved the know-how to their applications. The group of Hardisty and Whyne validated and applied the DVC analyses at organ level (vertebrae). The correlation procedures (Hardisty and Whyne, 2009) were similar to the tissue level: they used repeated scans and virtually deformed tests. The novelty was the simultaneous study of different microstructures: such as the vertebral body and the growth plate (Hardisty et al., 2010), or in metastatically involved vertebrae (Hardisty et al., 2012). In this way, the interaction between different structures in a complex geometry can be highlighted.

The DVC was also used to study the interaction between screws and bone (Basler et al., 2011). They used a HR-pQCT for in vivo scanning and studied the mechanical interaction between bone (femoral head) and implant (hip screws). They performed two series of validation: one based on repeated scans virtually moved and deformed, and another based on real displacement: showing an excellent precision in the displacement evaluation (1/1000 of the image resolution) and a valid precision (around 300 microstrain) in the strain evaluation for the measurements in the elastic regime.

The spine was explored studying the rat vertebrae (Hussein et al., 2012) and then the intervertebral discs (Hussein et al., 2013). The errors were evaluated with repositioned scans, showing an error magnitude potentially useful to explore the elastic regime (740 +/- 630 microstrain, with a measurement spatial resolution of 4.8 mm).

Finally, preliminary validation study, and following DVC applications were performed on porcine natural vertebrae and augmented vertebrae. (Palanca et al., 2016b) explored the parameters to minimize the errors in both the kinds of vertebrae (errors lower than 200 micrometers at a measurement spatial resolution of 1.8mm). (Tozzi et al., 2016) explored the biomechanics of natural vertebrae under loading condition, showing the capability of DVC in computing the strain in elastic regime. (Danesi et al., 2016b) enlarged the study, studying the interdigitation between cement and trabecular bone inside porcine vertebrae in axial loading conditions.

5.7 Conclusions

This review wants to show and reminds the necessity of the optimization and the validation of the Digital Volume Correlation. As new measurement tool, the DVC allowed a series of measurements that will improve the knowledge on the biomechanical field. At the same time, it is mandatory to know, and cannot be ignored, the reliability level of this new measurement tool and of its provided measurements. The series of works reported here, showed that when sufficient care is dedicated to the knowledge and adjustment of all the parameters, the DVC can become an actual powerful tool.

Chapter VI

Validation of Digital Volume Correlation at tissue level - microCT

from the manuscript:

Three-Dimensional Local Measurements of Bone Strain and Displacement: Comparison of Three Digital Volume Correlation Approaches

M. Palanca¹, G. Tozzi², L. Cristofolini¹, M. Viceconti³, E. Dall'Ara³

¹ School of Engineering and Architecture, Alma Mater Studiorum – Università di Bologna, Bologna (IT)

² School of Engineering, University of Portsmouth, Portsmouth (UK)

³ Department of Mechanical Engineering and INSIGNEO Institute for in Silico Medicine, University of Sheffield, Sheffield

Published in: *Journal of Biomechanical Engineering (ASME)*, 2015, 137(7):
071006 1 - 14

6.1 Introduction

Digital Volume Correlation (DVC) is a novel and useful tool for quantifying the internal 3D deformation across the entire volume of various biological tissues, such as bone (Roberts et al., 2014). In fact, DVC was originally developed by Bay and co-workers (Bay et al., 1999a) to investigate the volumetric strain distribution throughout the bone trabecular structure. This was done to overcome the limitation of its 2D counterpart, known as digital image correlation (DIC), which has the ability to compute strain and displacement fields only on the external surface of the specimen (Gates et al., 2010). The benefit of DVC relies in the use of volumetric images, that can be obtained by methods such as magnetic resonance imaging (MRI) (Barber et al., 2007), microscopy (Khodabakhshi et al., 2013), computed tomography (CT), or high-resolution micro-CT (Dall'Ara et al., 2014; Gillard et al., 2014; Liu and Morgan, 2007; Madi et al., 2013; Tozzi et al., 2014), to track the deformation of internal features, by registering elastically the images of undeformed and deformed specimens. The procedure outputs a full-field 3D displacement vector. Afterwards, the displacement fields are differentiated using various numerical differentiation approaches to obtain full-field strain maps (Pan et al., 2014).

Since it was introduced, DVC in combination with micro-CT allowed the determination of displacement and strain field inside trabecular bone (Bay et al., 1999a; Dall'Ara et al., 2014; Gillard et al., 2014; Liu and Morgan, 2007), cortical bone (Christen et al., 2012; Dall'Ara et al., 2014), trabecular bone substitutes (Madi et al., 2013), Aluminum foams (Smith et al., 2002) and also trabecular/cortical-cement composites (Tozzi et al., 2014). However, DVC employs a number of computational strategies to recognize the features of the undeformed (fixed) and deformed (moved) volumes and, therefore, to provide estimates of displacement and strain distribution. Comparison studies among different DVC approaches are mandatory as accuracy and precision may vary significantly, depending on factors such as quality of the images, typology of the specimen under investigation and intrinsic nature of the computational approach (Dall'Ara et al., 2014; Roberts et al., 2014; Tozzi et al., 2014). In fact, while numerical and experimental methods can validate each other if similar testing arrangements are defined, there is no golden standard to date for the assessment of the accuracy and precision of a DVC strategy, due to the unavailability of other accurate techniques able to measure internal strains. A first attempt to compare different DVC approaches used to investigate the performance of a trabecular bone substitute (porous polymeric scaffold) was carried out by Madi et al. (Madi et al., 2013), who compared the output of a local correlation algorithm based on Fast Fourier Transform (FFT) and another one based on a continuous and global home-written code (Benoit et al., 2009; Roux et al., 2008). However, in Madi et al. (Madi et al., 2013) displacement and strain uncertainties of the two DVC methodologies were assessed only in relation to a virtual imposed rigid displacement test. Hence, the strain fluctuation associated with repeated scans (Dall'Ara et al., 2014; Gillard et al., 2014) was not considered.

The accuracy and precision of DVC in quantifying displacements and strains have been investigated for trabecular bone (Dall'Ara et al., 2014; Gillard et al., 2014;

Liu and Morgan, 2007), cortical bone (Christen et al., 2012; Dall'Ara et al., 2014) and whole bones (Hussein et al., 2012; Hussein et al., 2013), where a single DVC software, either commercial or home-written, was employed. Moreover, in most cases errors are quantified in terms of average of the strain components (Dall'Ara et al., 2014; Liu and Morgan, 2007). Only in one case the error affecting the DVC-computed single components of displacement and strain has been quantified for trabecular bone (Gillard et al., 2014). For all these reasons, further comparative accuracy investigations of DVC methodologies are needed to interpret the results obtained in bone applications. Only in this way the suitability of a specific DVC approach can be evaluated against both bone structure (i.e. cortical, trabecular, cortical and trabecular together) and 'scale' of examination (i.e. dimension of the specimen, particular set of loading conditions).

The aim of this study was to perform a more extensive validation of the DVC, to better elucidate the sources of error affecting both displacement and strain calculations at the tissue level. Specifically, we compared the output of three different DVC approaches applied on the same micro-CT scanned specimen (trabecular and cortical bone) by investigating:

- The accuracy and precision in computing the displacement and strain fields for two zero-strain conditions: a virtually simulated 3D rigid displacement, and a specimen re-scan condition;
- The influence of different computation settings on the final outputs;
- The presence of preferential directions for strain measurement in the different algorithms.

6.2 Material and Methods

6.2.1 Specimens and Images

Two specimens (Fig. 1) were obtained from a fresh bovine femur: a cylinder of cortical bone was extracted from the diaphysis (3 mm diameter, 20 mm height), and a cylinder of trabecular bone was extracted from the greater trochanter (8 mm diameter, 12 mm height). The specimens were already used in a previous study (Dall'Ara et al., 2014) and were collected from an animal sacrificed for alimentary purposes.

In order to compare the displacement and strain uncertainties using different DVC techniques, virtual image translation and zero-strain repeated scans (Liu and Morgan, 2007) were employed. Micro-CT scans were performed in saline solution (SkyScan 1172, Bruker, Belgium; scanned height: 9.323 mm; 10 Megapixels 12-bit digital cooled ORCA-HR CCD; 2000 x 1048 pixel; 1 mm Aluminum beam hardening filter; power: 10 W; voltage: 59 kV for the trabecular bone and 70 kV for the cortical bone; voxel size: 9.96 micrometer; exposure: 1180 ms; rotation step: 0.7°; total rotation 180°; images averages: x2). Each specimen was scanned twice (Dall'Ara et al., 2014), without any repositioning between the scans (Scan1 and Scan2). In order to avoid possible artifacts due to small movements of free trabeculae at the outer surface, a volume of interest (VOI) consisting of a parallelepiped with a section of 180 voxels x 180 voxels and

a height of 932 voxels, was cropped in the central portion of the scanned cylinders. Two tests were performed on the VOI extracted from both cortical and trabecular specimens (Fig. 1):

“Repeated-Scan-Test”: Scan1 and Scan2 were correlated in order to obtain a condition of zero-strain and real displacements, due to the machine micro-movements.

“Virtually-Moved-Test”: Scan1 was virtually translated of two voxels (19.92 micrometer) in each direction (Scan1_Moved) in order to obtain a known, controlled displacement with a zero-strain field. Correlation of Scan1_Moved was computed with reference to the original Scan1. A bounding box of ten voxels was added all around the specimen in order to avoid losing part of the image.

The cropping and translation were performed by means of a free imaging processing toolkit MeVisLab (MeVis Medical Solution AG, <http://www.mevislab.de/>).

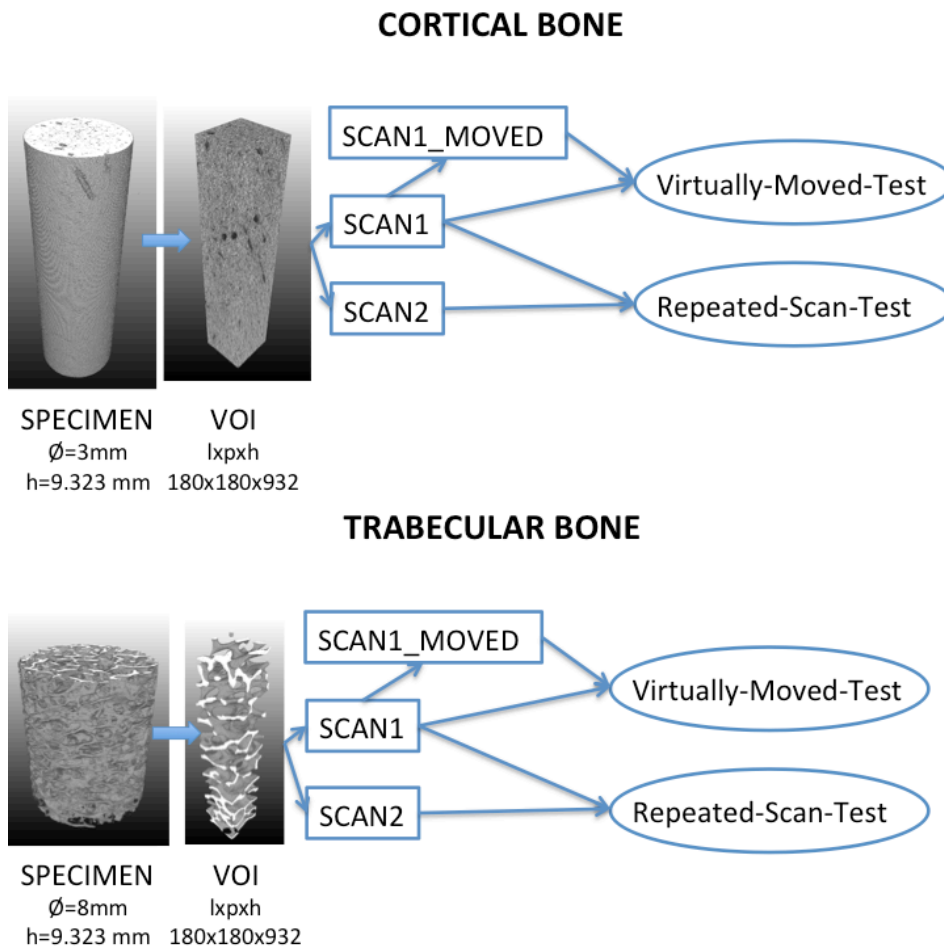


Fig. 1 – Schematic of the two specimens obtained from a fresh bovine femur: a cylinder of cortical bone was extracted from the diaphysis (3 mm diameter, 20 mm height), and a cylinder of trabecular bone was extracted from the greater trochanter (8 mm diameter, 12 mm height). Each specimen was scanned twice (height of 9.323 mm). Identical Volumes of Interest (VOI) were extracted from each specimen. The displacements and strains were computed for such a zero-strain condition, both between Scan 1 and Scan 2, and by virtually displacing Scan 1.

6.2.2 DVC approaches under investigation

The outputs of three DVC approaches were compared (Fig. 2), for both specimens and for both Repeated-Scan-Test and Virtually-Moved-Test.

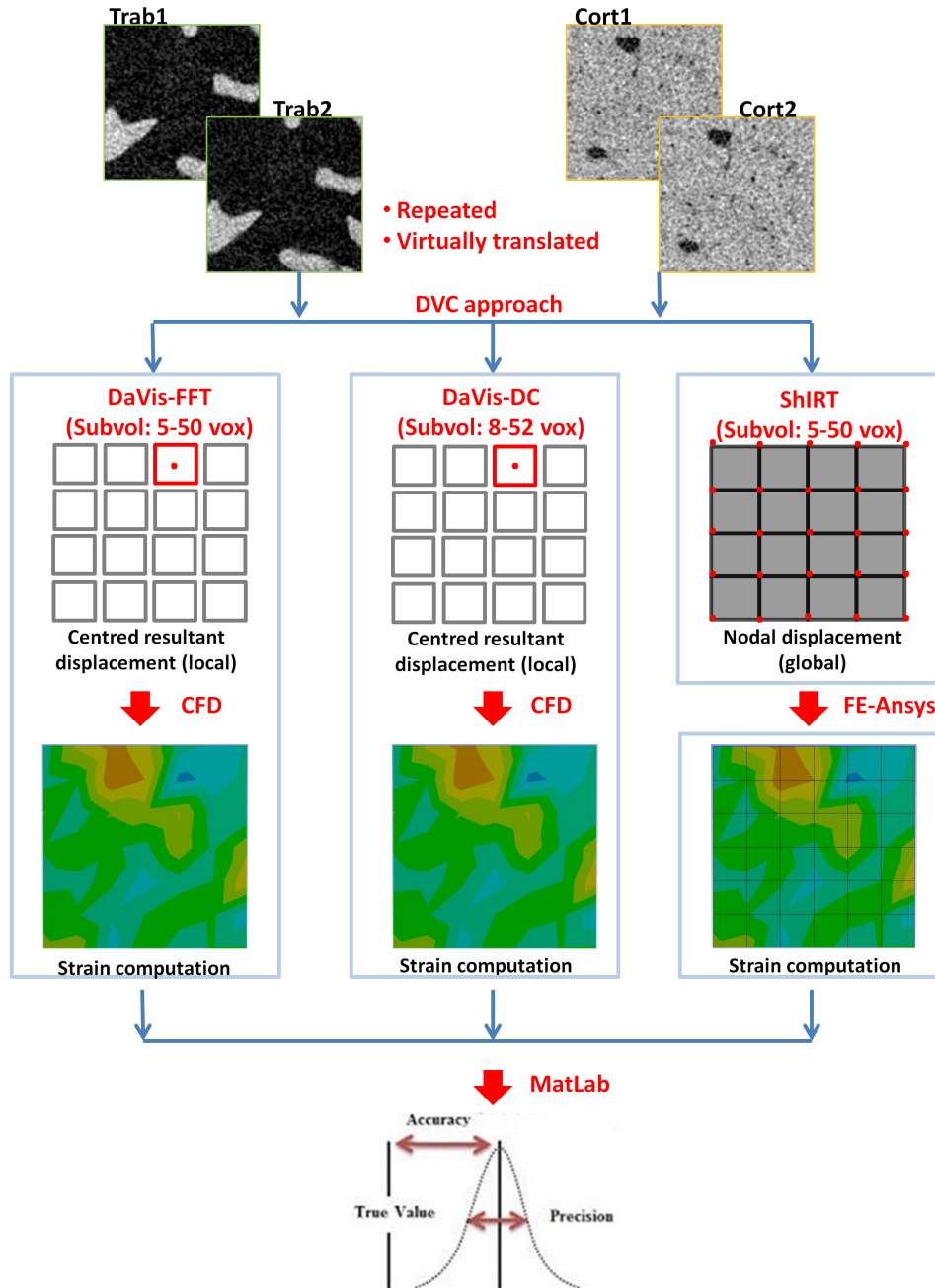


Fig. 2 – Description of the three DVC approaches for the determination of strain accuracy and precision. DaVis software enabled both Fast Fourier Transform (DaVis-FFT) and Direct Correlation (Davis-DC) displacement calculation and strain was computed using a Centred Finite Difference (CFD) scheme. A custom-written software (ShIRT) in combination with a finite element (FE) solver was also tested.

The first two approaches are implemented in commercial DVC software: DaVis 8.2.1 (LaVision Ltd, Goettingen, Germany). The volume correlation begins with the division of the 3D images into smaller and selectable sub-volumes,

represented as a discrete function of grey levels. Recognition of identical features is possible via Fast-Fourier-transform (FFT, later referred to as “Davis-FFT”) (Gillard et al., 2014; Madi et al., 2013) or via Direct-Correlation (DC, later referred to as “Davis-DC”) (Cheminet et al., 2014). Either way, a piece-wise linear shape function for the reference-deformed mapping and a cross-correlation function are employed to quantify the similarity between the images (Gillard et al., 2014; Madi et al., 2013). For both DaVis-FFT and DaVis-DC, a normalized cross-correlation coefficient, r_{DaVis} , based on grey level gaps is used:

$$r_{DaVis} = \frac{\sum_{\underline{X}(x,y,z) \in VOI} f(x,y,z)g(x',y',z')}{\sqrt{\sum_{\underline{X}(x,y,z) \in VOI} f(x,y,z)^2 \sum_{\underline{X}^*(x,y,z) \in VOI} g(x',y',z')^2}} \quad (\text{Eq. 1})$$

where: $X(x, y, z)$ and $X^*(x, y, z)$ refer to coordinates (in voxels) of a same point in the initial state and in the deformed state; f and g are the grey levels respectively in the initial and deformed images. The main difference between DaVis-FFT and DaVis-DC lies on the use of a Fourier space for the calculation in DaVis-FFT (Scarano, 2013), rather than a direct coupling for DaVis-DC. A tri-linear interpolation is used in the case of DaVis-FFT, and a 3rd order spline interpolation in DaVis-DC. The estimated full 3D displacement field is then computed, with sub-voxel precision, through a predictor-corrector approach with decreasing subset sizes, and an intensity interpolation Gaussian algorithm fitted to the correlation peak. This process, also known as multi-pass, allows the calculated displacements from the predictor step to be used to inform the next corrector step. The process is iterated as the sub-volume size decreases to its final defined size. This process provides a full 3D field of displacement vectors, which describes the mapping from reference to deformed state. From the field of resultant displacement vectors at the center of each sub-volume, the field of strain components is computed using a centered finite difference scheme.

The third approach (later referred to as “SHIRT-FE”) consists in combining a home-written elastic registration software SHIRT (Barber and Hose, 2005; Barber et al., 2007; Khodabakhshi et al., 2013) with a Finite Element (FE) simulation in ANSYS Mechanical APDL v.14.0 (Ansys Inc., USA). The procedure, reported in (Dall'Ara et al., 2014), focuses on the recognition of identical features in the two 3D images by superimposing a homogeneous cubic grid with certain nodal spacing (sub-volume) to the images to be registered. The software computes the nodal displacements that map each point in the first image (Scan1), into the ones in the second image (Scan2), solving the equations in the nodes of the grid (Barber and Hose, 2005; Dall'Ara et al., 2014). Briefly, the procedure consists in finding the displacement functions $u(x,y,z)$, $v(x,y,z)$ and $w(x,y,z)$ that map the fixed image $f(x,y,z)$ into the moving image $m(x',y',z')$. As described in Barber et al. (Barber et al., 2007) an additional intensity displacement function $c(x, y, z)$ is included in order to account for changes in the grey levels. For small displacement values we need to solve:

$$f - m \approx \frac{1}{2} \left(u \left(\frac{\partial f}{\partial x} + \frac{\partial m}{\partial x} \right) + v \left(\frac{\partial f}{\partial y} + \frac{\partial m}{\partial y} \right) + w \left(\frac{\partial f}{\partial z} + \frac{\partial m}{\partial z} \right) - c(f + m) \right) \quad (\text{Eq. 2})$$

However, as this problem would be underdetermined if solved for each voxel, ShIRT solves the equations only in the nodes of a cubic grid superimposed to the images and with elements as large as the imposed sub-volume. The displacements are interpolated with a tri-linear function between the nodes. The problem is then solved when the coefficients \mathbf{a} of the displacement functions are found:

$$\begin{cases} u = \sum_i a_{xi} \varphi_i \\ v = \sum_i a_{yi} \varphi_i \\ w = \sum_i a_{zi} \varphi_i \end{cases} \quad (\text{Eq. 3})$$

ShIRT adds an additional smoothness constraint on the mapping by including in the solution a term based on the Laplacian operator \mathbf{L} , and the coefficient λ that weights the relative importance of smoothing. Therefore, it can be demonstrated that for suitable values of λ , a robust solution is obtained by solving the following equation in matrix form:

$$(\mathbf{f} - \mathbf{m}) = (\mathbf{T}^T \mathbf{T} + \lambda \mathbf{L}^T \mathbf{L}) \mathbf{a} \quad (\text{Eq. 4})$$

where \mathbf{T} is a $K \times N$ matrix (K number of voxels in the image, and N number of nodes in the grid). \mathbf{T} is derived from integrals of the image gradients multiplied by the basis functions of the displacements. For large displacements the method can iterate to a correct solution as shown in (Barber et al., 2007). The grid is then converted into an 8-noded hexahedrons mesh. The displacements computed by ShIRT at each node of the grid are imposed as boundary conditions for the computation of the strain field with a commercial FE solver (ANSYS).

6.2.3 Influence of sub-volume size

In order to compare the results of the different DVC approaches an analysis on the dependency of the accuracy and precision in function of the selected sub-volume size (5-50 voxels) was performed (Table 1). In particular, for the DaVis approaches, no overlap or multi-pass approach was used for a fair comparison. However, a correlation using a multi-pass approach incorporated in DaVis for that specific VOI (extending the computation sub-volume up to 52 voxels, Table 2) was also implemented in order to investigate the effect of other features typical of the DaVis commercial software, for this specific type of images. As the DaVis software did not allow selecting any arbitrary sub-volume size when the DC was used for feature recognition, the nearest sub-volume size available was used (8-52 voxels).

6.2.4 Metrics to quantify the accuracy and precision

The components of displacement and strain were extracted from the different approaches and processed with a home-written script MatLab 2014a, (The MathWorks, Natick, USA). For the three approaches, accuracy (average) and precision (standard deviation-SD) were quantified for each component of the displacement. Quantitative comparisons were performed on the strains in two ways:

- Scalar comparison: in order to compare the outputs of the different approaches for strain estimation, following the indications available in literature (Dall'Ara et al., 2014; Liu and Morgan, 2007), mean absolute error (MAER) and standard deviation of the error (SDER) were quantified as the average and the SD of the average of the absolute values of the six strain components.
- Comparison by component: in order to investigate the presence of preferential components of strain in the algorithms, accuracy (average) and precision (SD) were reported and compared for each component of the strain.

Table 1: Comparison of the correlated volumes for the different computation approaches, for both specimens (cortical and trabecular) and both tests, and according to the size of the sub-volume. *Note: In the ShIRT-FE approach the computation occurs only in the nodes of the elements of the selected grid. Although the number of measurement points was less than the number of measurement points of the other two approaches (DaVis-FFT and DaVis-DC), this allows a correlation on the whole volume.

	Nominal sub-volume size (voxels)	DaVis-FFT		DaVis-DC		ShIRT-FE	
		Actual sub-volume size (voxels)	Correlated volume (%)	Actual sub-volume size (voxels)	Correlated volume (%)	Actual sub-volume size (voxels)	Correlated volume (%)
Cortical Virtually-Moved-Test	5	5	25.9%	8	100.0%	5	100%*
	10	10	79.5%	10	100.0%	10	
	15	15	100.0%	16	100.0%	15	
	20	20	100.0%	20	99.2%	20	
	25	25	100.0%	24	99.3%	25	
	30	30	97.2%	28	99.6%	30	
	35	35	100.0%	34	96.6%	35	
	40	40	100.0%	40	96.7%	40	
	45	45	100.0%	44	84.4%	45	
50	50	100.0%	52	96.6%	50		
Trabecular Virtually-Moved-Test	5	5	30.3%	8	100.0%	5	100%*
	10	10	79.8%	10	100.0%	10	
	15	15	100.0%	16	100.0%	15	
	20	20	100.0%	20	99.2%	20	
	25	25	100.0%	24	99.3%	25	
	30	30	97.2%	28	99.6%	30	
	35	35	99.9%	34	96.6%	35	
	40	40	100.0%	40	96.7%	40	
	45	45	100.0%	44	84.4%	45	
50	50	100.0%	52	96.6%	50		
Cortical Repeated-Scan-Test	5	5	37.1%	8	100.0%	5	100%*
	10	10	94.4%	10	100.0%	10	
	15	15	100.0%	16	99.9%	15	
	20	20	100.0%	20	99.1%	20	
	25	25	100.0%	24	99.3%	25	
	30	30	100.0%	28	99.9%	30	
	35	35	100.0%	34	99.9%	35	
	40	40	100.0%	40	99.7%	40	
	45	45	100.0%	44	98.5%	45	
50	50	91.8%	52	79.6%	50		
Trabecular Repeated-Scan-Test	5	5	45.4%	8	100.0%	5	100%*
	10	10	95.8%	10	100.0%	10	
	15	15	100.0%	16	99.9%	15	
	20	20	99.9%	20	99.1%	20	
	25	25	100.0%	24	99.3%	25	
	30	30	100.0%	28	99.9%	30	
	35	35	100.0%	34	99.9%	35	
	40	40	100.0%	40	99.7%	40	
	45	45	100.0%	44	98.5%	45	
50	50	91.8%	52	79.6%	50		

The trends were analyzed plotting the errors as a function of the sub-volume sizes. Different interpolating laws were tested (linear, polynomial, power-law) in terms of adjusted determination coefficient.

Some sub-volumes could not be correlated by the DaVis algorithms (i.e. because they contained only voxels of constant intensity). Due to the algorithm locally normalizing the intensity, no correlation at all is possible for such sub-volumes, and as such, no corresponding displacement vector can be calculated. To avoid misinterpretation of the results, the correlated volume was evaluated for each computation sub-volume size (Table 1) as the ratio between the numbers of correlated voxels and the total number of voxels of the VOI. This applied to the DaVis approaches only; as of the ShIRT-FE the correlated volume is 100% by definition.

Finally, the computational cost of each approach was estimated as the sum of the computation time needed for the different analyses. For the DaVis-FFT and DaVis-DC the computation time was calculated as the total time for the feature recognition, the time necessary for the computation of the displacement field and the time needed for the computation of the strain field. For the ShIRT-FE approach, the computational cost was estimated as the time needed for the registration with ShIRT plus the time for computing the strain with the FE solver.

Table 2: Parameters used in the multi-pass approach for both the DaVis-FFT and the DaVis-DC.

Step	Sub-volume size (voxels)	Overlap between sub-volumes	Number of iterations
1	96	50%	1
2	64	50%	2
3	52	75%	3

6.3 Results

The correlated volume (both trabecular and cortical bone) seemed to increase for the DaVis-FFT and to decrease for the DaVis-DC, as the computation sub-volume increased, although no clear trend was observed (Table 1). Because of the different computational approach, such analysis does not apply to the ShIRT-FE, which is based on a global analysis on the total volume.

6.3.1 Displacement

The comparison of the displacement among the different approaches is reported only for the “Virtually-Moved-Test”, as the actual displacement in the “Repeated-Scan-Test” is unknown.

The accuracy errors for the displacements were comparable for the cortical and trabecular specimens (Table 3). For the different sub-volume sizes (from 5-8 to 50-52 voxels) and specimen types (trabecular and cortical), the largest accuracy error was found for the Davis-FFT approach (up to 13 micrometer), which was larger than those found with the Davis-DC (never exceeding 0.1 micrometer),

Table 3 Accuracy of the computed components of displacement (micrometer) in the Virtually-Translated-Test for the three DVC approaches and different sub-volumes in both cortical and trabecular specimen. The z-direction is the axis of rotation of the specimen during imaging in the micro-CT.

		DaVis-FFT			DaVis-DC			ShIRT-FE		
	Nominal Sub-volume size (voxels)	Accuracy along x-axis (micrometers)	Accuracy along y-axis (micrometers)	Accuracy along z-axis (micrometers)	Accuracy along x-axis (micrometers)	Accuracy along y-axis (micrometers)	Accuracy along z-axis (micrometers)	Accuracy along x-axis (micrometers)	Accuracy along y-axis (micrometers)	Accuracy along z-axis (micrometers)
CORTICAL BONE	5	13.54	13.18	14.11	0.0019	0.0019	0.00045	0.0015	0.0013	0.00073
	10	5.02	4.43	5.98	0.0079	0.0079	0.0017	0.00044	0.00023	0.00041
	15	5.10	4.78	4.47	0.080	0.079	0.013	0.00047	0.00101	0.0029
	20	5.02	4.74	3.94	0.026	0.033	0.054	0.0000059	0.000081	0.0000080
	25	5.00	4.76	3.59	0.04	0.04	0.0017	0.0000091	0.0000068	0.0000044
	30	4.18	3.95	3.13	0.047	0.047	0.0084	0.00018	0.00016	0.000501
	35	4.32	4.12	3.16	0.052	0.052	0.0099	0.00027	0.000014	0.000025
	40	5.25	5.07	2.90	0.063	0.064	0.008	0.0027	0.000053	0.00015
	45	3.66	3.39	2.88	0.052	0.051	0.00033	0.000022	0.0000050	0.000018
50	5.47	5.26	2.96	0.074	0.074	0.0095	0.0000032	0.0000047	0.000012	
TRABECULAR BONE	5	14.48	14.33	14.86	0.0011	0.0013	0.00074	0.0012	0.0012	0.0013
	10	7.79	7.50	9.27	0.0034	0.0056	0.00062	0.00034	0.00025	0.00089
	15	8.75	8.55	9.23	0.0092	0.011	0.0012	0.00068	0.00071	0.0029
	20	9.21	8.97	9.58	0.014	0.00065	0.018	0.000080	0.000042	0.000034
	25	9.43	9.33	9.51	0.0083	0.011	0.0031	0.000011	0.000016	0.000022
	30	9.42	9.28	9.12	0.0097	0.011	0.0014	0.0000088	0.000096	0.000047
	35	9.35	9.10	8.84	0.012	0.011	0.0029	0.000048	0.0000023	0.000011
	40	8.67	8.31	8.37	0.012	0.011	0.00099	0.000403	0.000028	0.00016
	45	8.54	8.22	7.61	0.012	0.012	0.0012	0.000045	0.000004	0.000012
	50	7.14	6.96	6.85	0.012	0.011	0.0011	0.0000026	0.0000004	0.0000098

Table 4 Precision of the computed components of displacement (micrometer) in the Virtually-Translated-Test for the three DVC approaches and different sub-volumes in both cortical and trabecular specimen. The z-direction is the axis of rotation of the specimen during imaging in the micro-CT.

		DaVis-FFT			DaVis-DC			ShIRT-FE		
	Nominal Sub-volume size (voxels)	Precision along x-axis (micrometers)	Precision along y-axis (micrometers)	Precision along z-axis (micrometers)	Precision along x-axis (micrometers)	Precision along y-axis (micrometers)	Precision along z-axis (micrometers)	Precision along x-axis (micrometers)	Precision along y-axis (micrometers)	Precision along z-axis (micrometers)
CORTICAL BONE	5	6.62	6.73	6.53	0.32	0.33	0.17	0.086	0.086	0.37
	10	8.12	8.04	7.40	0.15	0.16	0.093	0.017	0.017	0.067
	15	5.29	5.20	5.36	0.22	0.22	0.093	0.019	0.019	0.077
	20	4.87	4.84	3.92	1.06	1.03	0.42	0.0024	0.0023	0.0092
	25	4.83	4.81	3.44	0.078	0.079	0.054	0.00093	0.00095	0.00044
	30	3.93	3.89	2.75	0.082	0.081	0.04	0.0037	0.0037	0.014
	35	3.85	3.81	2.95	0.085	0.085	0.041	0.00093	0.00066	0.00074
	40	4.37	4.32	2.48	0.087	0.086	0.038	0.0057	0.0011	0.0036
	45	3.67	3.52	2.76	0.082	0.081	0.054	0.00063	0.00054	0.00076
50	3.94	3.88	2.88	0.084	0.084	0.039	0.00013	0.00013	0.00016	
TRABECULAR BONE	5	6.19	6.22	5.79	0.35	0.33	0.28	0.087	0.087	0.37
	10	8.37	8.24	7.30	0.19	0.18	0.21	0.017	0.017	0.068
	15	7.38	7.05	7.05	0.11	0.11	0.15	0.019	0.019	0.078
	20	7.29	6.98	6.79	0.66	0.57	0.22	0.0025	0.0025	0.0097
	25	7.22	6.78	6.95	0.07	0.059	0.089	0.00093	0.00095	0.00045
	30	6.90	6.49	6.82	0.054	0.045	0.064	0.0033	0.0033	0.012
	35	6.63	6.14	6.57	0.036	0.032	0.039	0.00058	0.00065	0.00075
	40	6.36	5.87	6.32	0.026	0.023	0.028	0.0014	0.00105	0.0034
	45	5.55	5.12	5.73	0.024	0.021	0.018	0.00059	0.00052	0.00073
50	5.10	4.72	5.17	0.016	0.016	0.015	0.00011	0.00011	0.00014	

and larger than those obtained with the ShIRT-FE (never exceeding 0.01 micrometer). The smallest accuracy errors for the DaVis-FFT and DaVis-DC were found along the z-direction (i.e. the rotation axis of the micro-CT during imaging). Conversely, errors were slightly larger in the z-direction for ShIRT-FE. The tendency of the DaVis-FFT and ShIRT-FE was for an improved accuracy for larger sub-volume sizes.

Similarly, the largest precision errors (Table 4) were found for the DaVis-FFT (several micrometers), followed by DaVis-DC (between 0.1 and 1 micrometer), and then by the ShIRT-FE (never exceeding 0.1 micrometer). The smallest precision errors for the DaVis-FFT and DaVis-DC were found once more along the z-direction, whereas errors were slightly larger along the z-direction for ShIRT-FE. The precision of all three DVC approaches tended to improve as a function of the computation sub-volume size.

6.3.2 Strain

6.3.2.1 Scalar Comparison

The first comparison is based on the scalar magnitudes, calculated similarly to (Liu and Morgan, 2007).

For the “Virtually-Moved-Test”, the errors for the strains were comparable for the cortical and trabecular specimens. Both MAER (Fig. 3) and SDER (Fig. 4) error were largest for the Davis-FFT (at best: 4670 and 1718 microstrain, respectively), which was larger than with Davis-DC (at best: 18 and 6 microstrain, respectively), and ShIRT-FE approach (below one microstrain). Both MAER and SDER showed a steady improvement for larger sub-volumes for all three DVC approaches, following a power-law relation (Fig. 3, 4). For the DaVis-FFT, the multi-pass approach provided a lower MAER (Fig. 3) and SDER (Fig. 4) than the same algorithm at 50 voxels. Conversely, the multi-pass approach did not improve the outcomes of the DaVis-DC at similar sub-volume size (52 voxels).

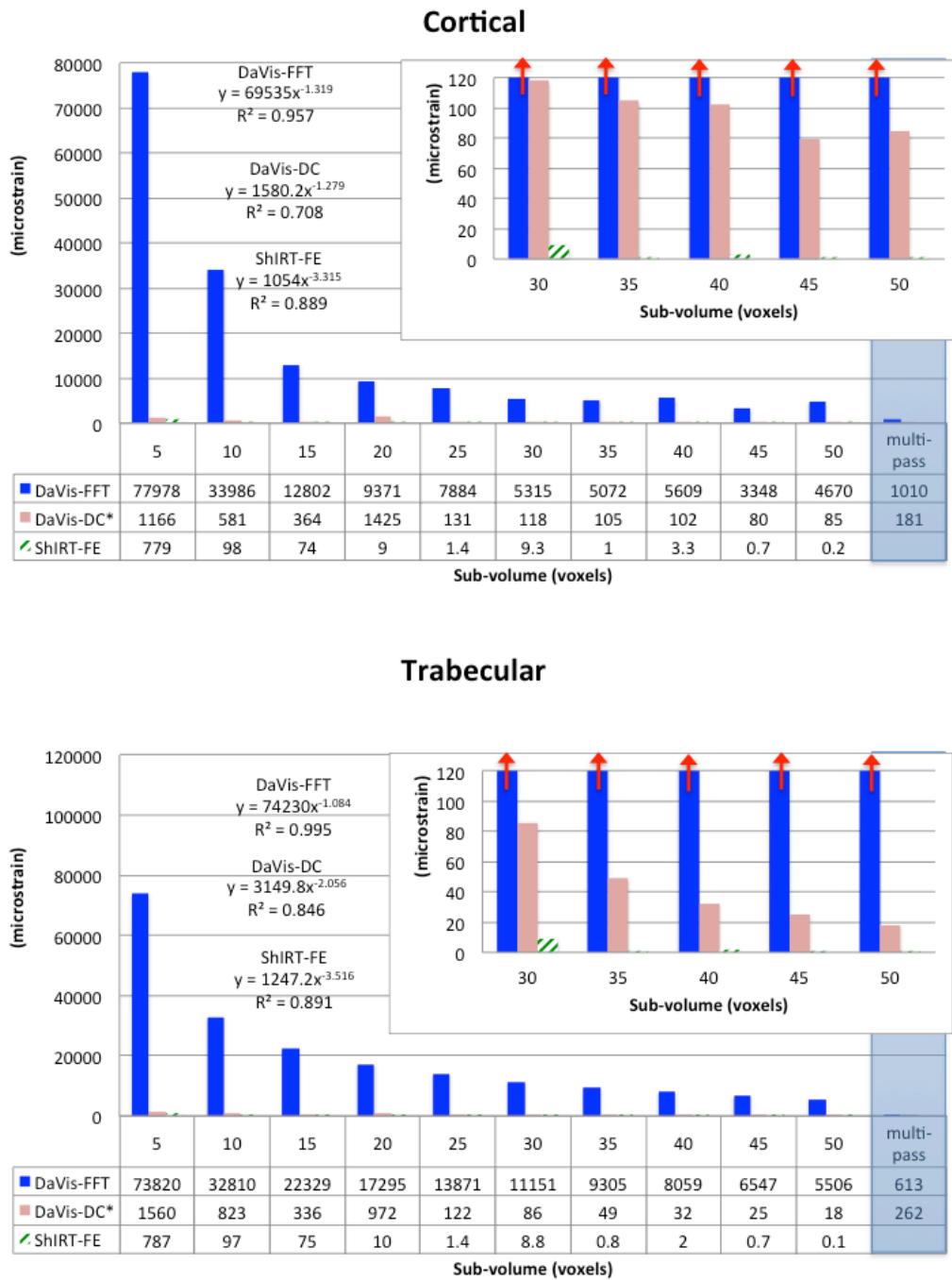


Fig. 3: Virtually-Moved-Test: trend of MAER (microstrain) for both cortical and trabecular specimen, as a function of the sub-volume size (voxels). MAER of the three DVC approaches was first computed as a scalar, consistently with Liu & Morgan, 2007). The trendline equation (power-law relation and R²) is also reported.

*The sub-volume was different for DaVis-DC. Refer to Table 1 for more details.

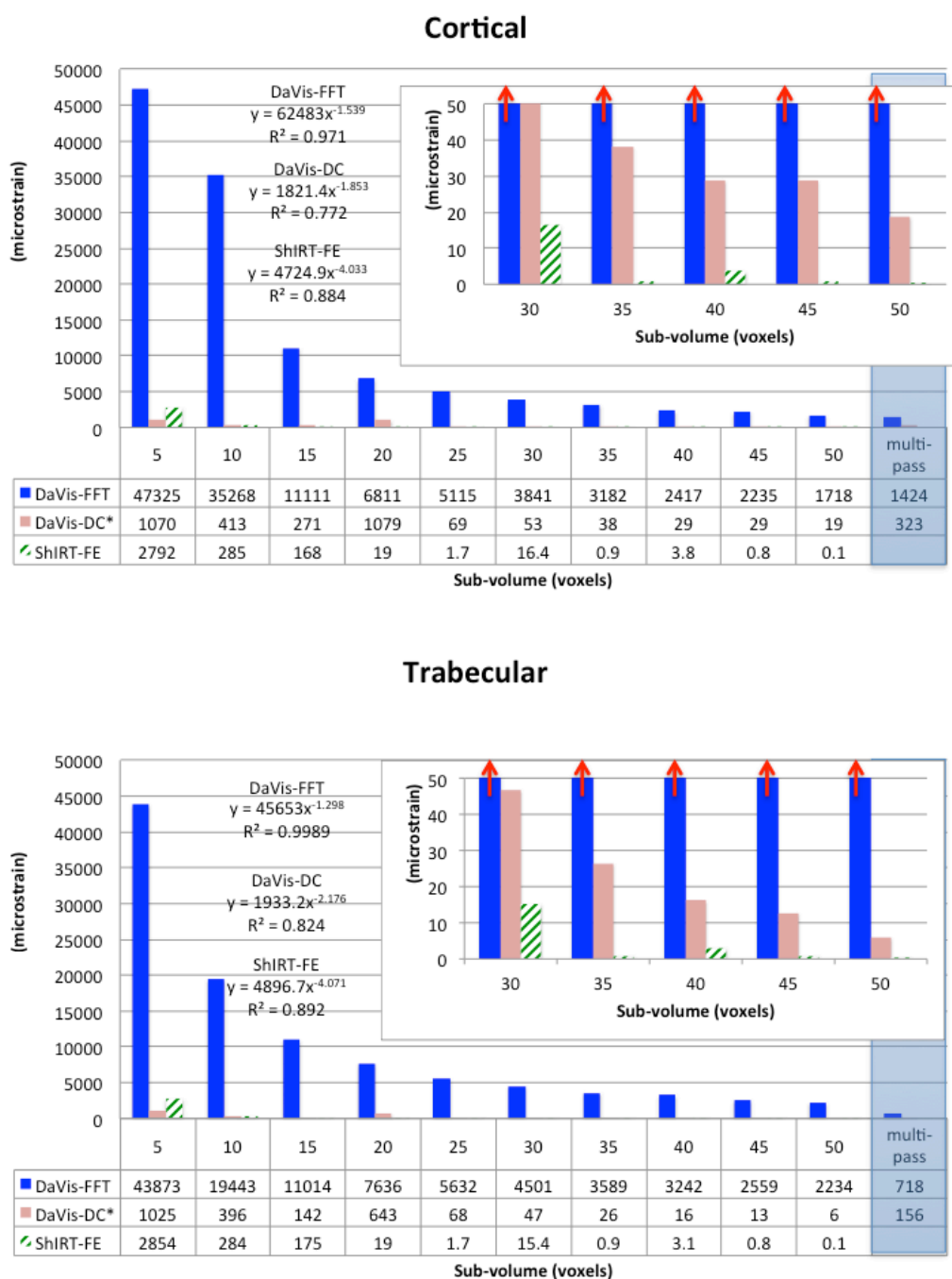


Fig. 4: Virtually-Moved-Test: trend of SDER (microstrain) for both cortical and trabecular specimen, as a function of the sub-volume size (voxels). SDER of the three DVC approaches was first computed as a scalar, consistently with Liu & Morgan, 2007). The trendline equation (power-law relation and R^2) is also reported.

For the “Repeated-Scan-Test”, the errors were larger for the cortical bone than for the trabecular bone. For all three DVC approaches, both accuracy (Fig. 5) and precision (Fig. 6) improved for larger sub-volumes, following a power-law relation. Similar trends to the “Virtually-Moved-Test” were observed, but with lower differences. The accuracy error for all approaches was between hundreds and thousands of microstrain for the best settings: errors were largest for the

Davis-FFT, followed by the Davis-DC, and by the ShIRT-FE (Fig. 5). The lowest precision error was of the same order of magnitude for DaVis-DC and ShIRT-FE (a few hundreds of microstrain at best) and was larger for DaVis-FFT, particularly for the cortical bone (Fig. 6). In this test, the multi-pass approach provided worse accuracy and precision than the largest sub-volume alone, for both the DaVis-FFT and the DaVis-DC.

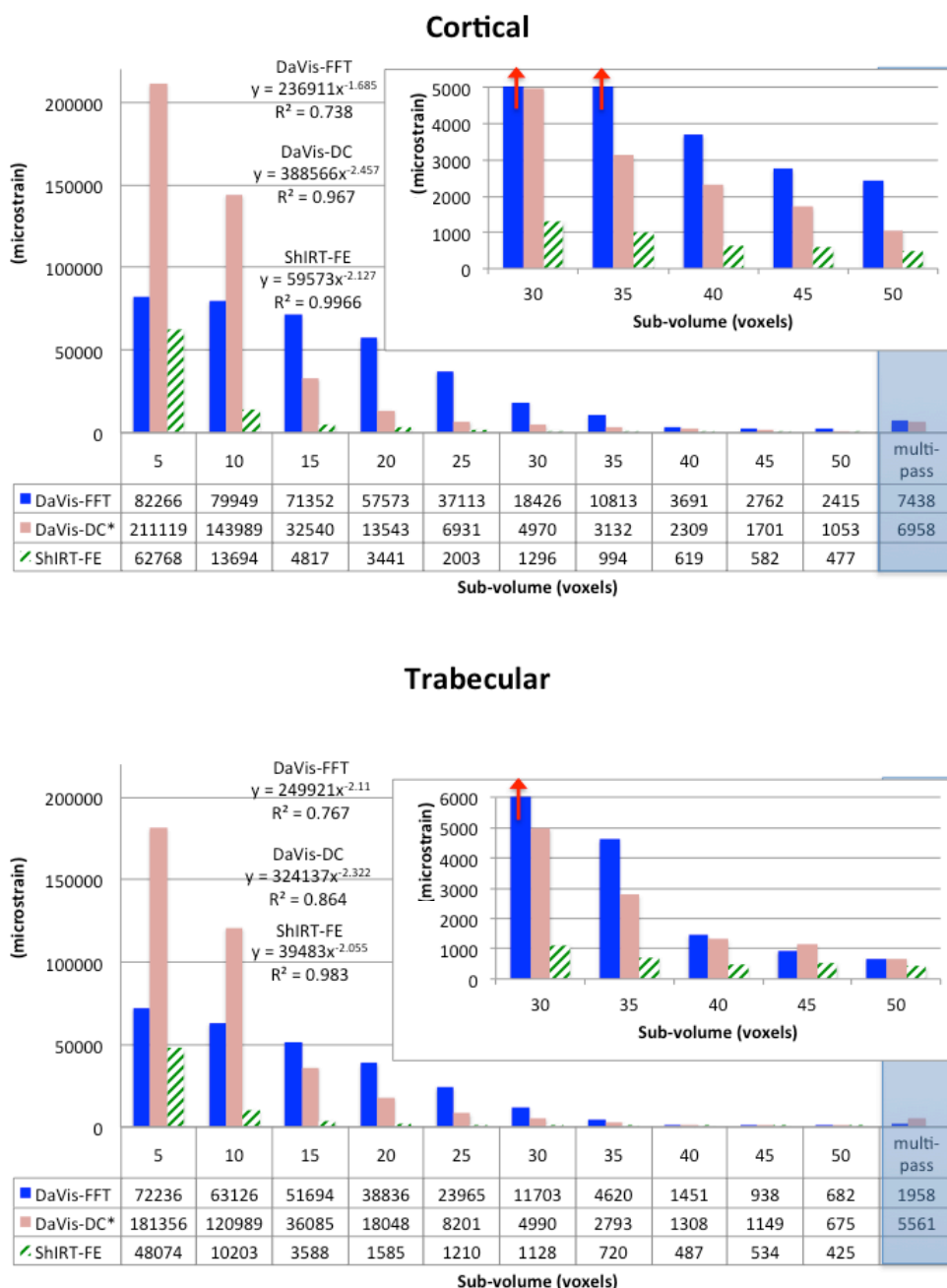


Fig. 5: Repeated-Scan-Test: trend of MAER (microstrain) for both cortical and trabecular specimen, as a function of the sub-volume size (voxels). MAER of the three DVC approaches was first computed as a scalar, consistently with Liu & Morgan, (2007). The trendline equation (power-law relation and R^2) is also reported.

* The sub-volume was different for DaVis-DC. Refer to Table 1 for more details.

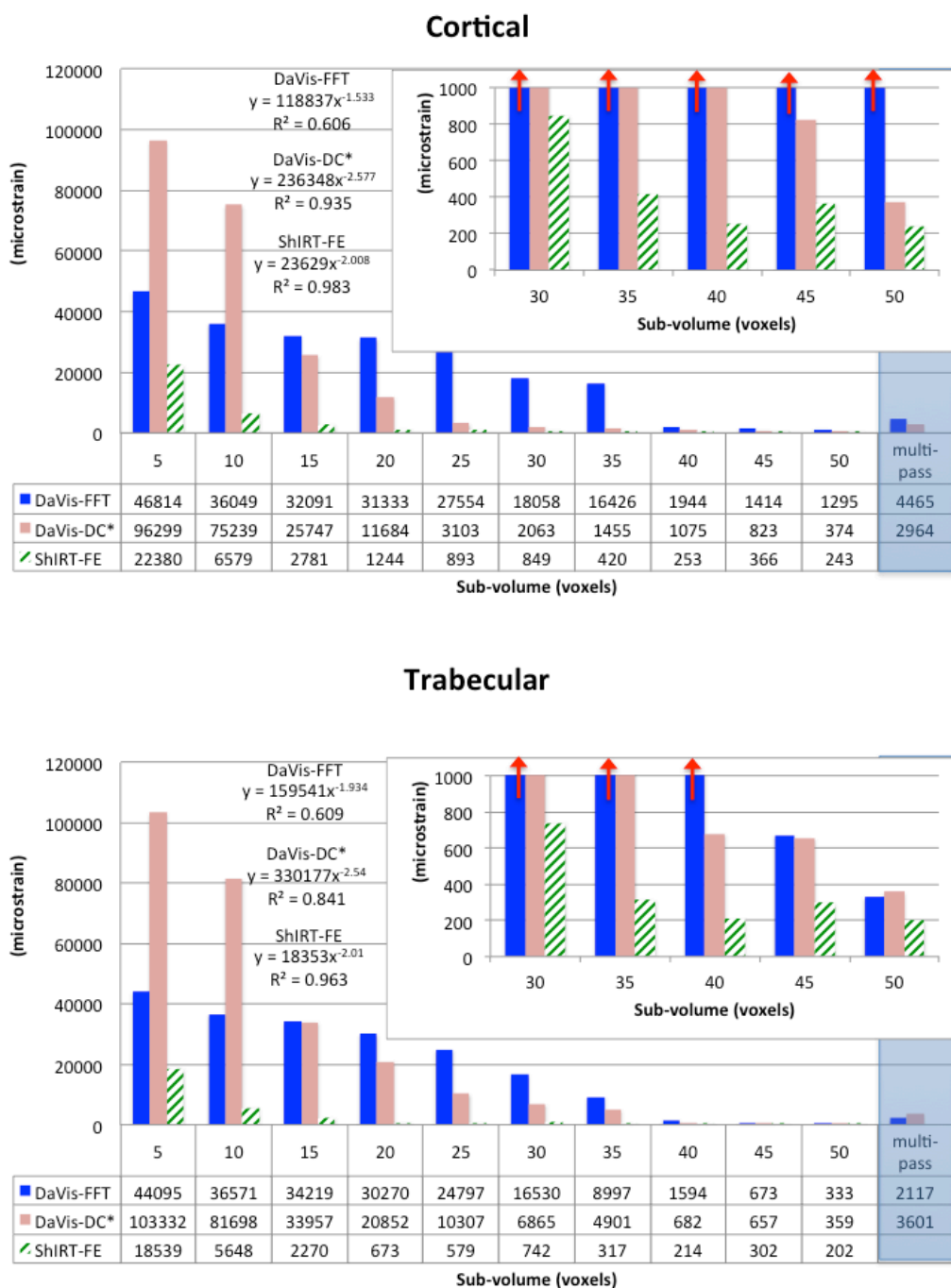


Fig. 6: Repeated-Scan-Test: trend of SDER (microstrain) for both cortical and trabecular specimen, as a function of the sub-volume size (voxels). SDER of the three DVC approaches was first computed as a scalar, consistently with Liu & Morgan, 2007). The trendline equation (power-law relation and R^2) is also reported.

* The sub-volume was different for DaVis-DC. Refer to Table 1 for more details.

6.3.2.2 Comparison by component

When the individual components of strain were analyzed separately, the same trend was observed between the three computation approaches (worst: DaVis-FFT; best: ShIRT-FE), for both the accuracy and precision (Figs. 7-10).

In the “Virtually-Moved-Test” the accuracy (Fig. 7) and precision (Fig. 8) errors with the Davis-FFT and in particular Davis-DC were larger for the normal strain components, than for the shear strains. Among the normal strain components, errors were smaller in the z-direction. Conversely, the accuracy was similar for each component for the ShIRT-FE (and closer to zero than the DaVis-FFT and DaVis-DC).

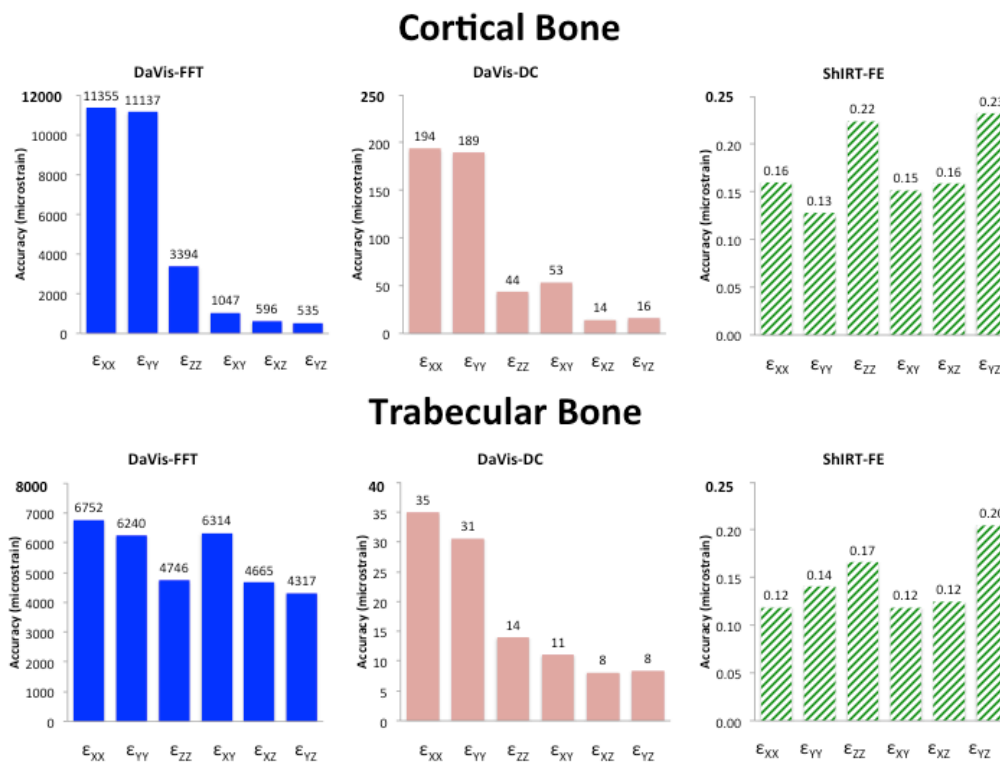


Fig. 7: Virtually-Moved-Test: Analysis of the accuracy of the six components of strain (microstrain), in both cortical and trabecular specimen, for the largest sub-volume size considered (50 voxels ShIRT & DaVis-FFT, 52 voxels DaVis-DC). The Z-axis represents the axis of rotation of the specimen during imaging in the micro-CT. The accuracy of the three DVC approaches was computed as the average of the absolute values of each component of strain. Different scales are used for the three computation approaches due to large differences in absolute values.

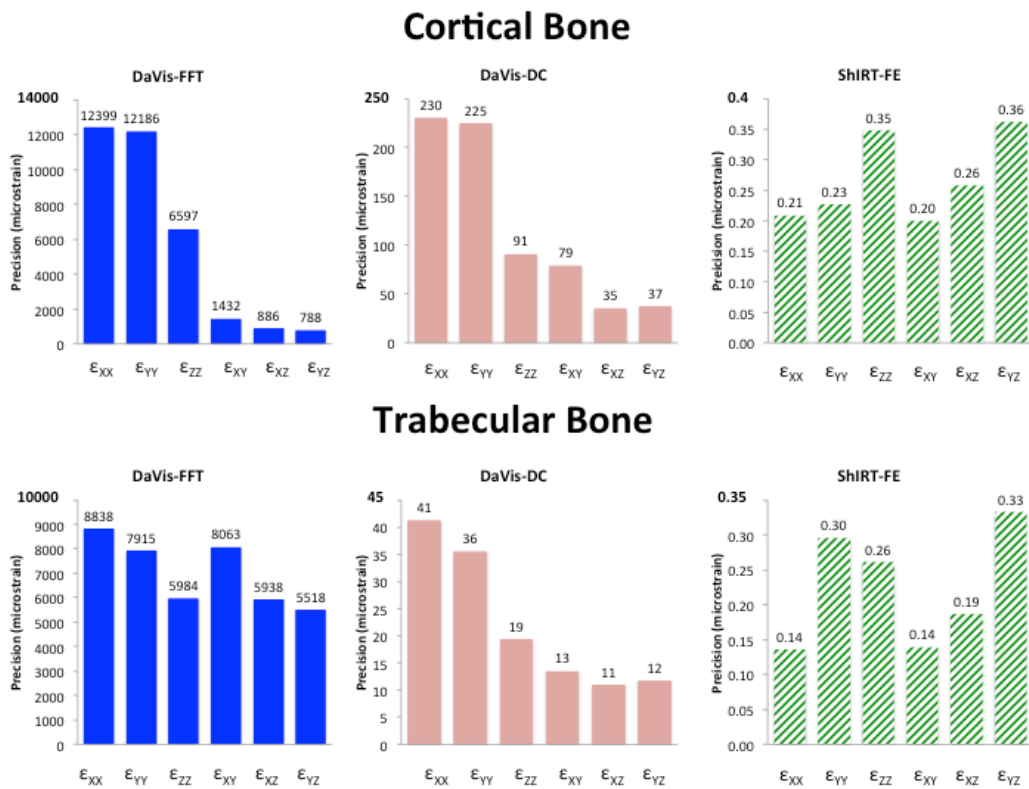


Fig. 8: Virtually-Moved-Test: Analysis of the precision of the six components of strain (microstrain), in both cortical and trabecular specimen, for the largest sub-volume size considered (50 voxels ShIRT & DaVis-FFT, 52 voxels DaVis-DC). The Z-axis represents the axis of rotation of the specimen during imaging in the micro-CT. The precision of the three DVC approaches was computed as the standard deviation of the absolute values of each component of strain. Different scales are used for the three computation approaches due to large differences in absolute values.

No systematic difference was observed between strain components for the “Repeated-Scan-Test”, although the accuracy (Fig. 9) and precision (Fig. 10) errors were generally larger for the normal strains.

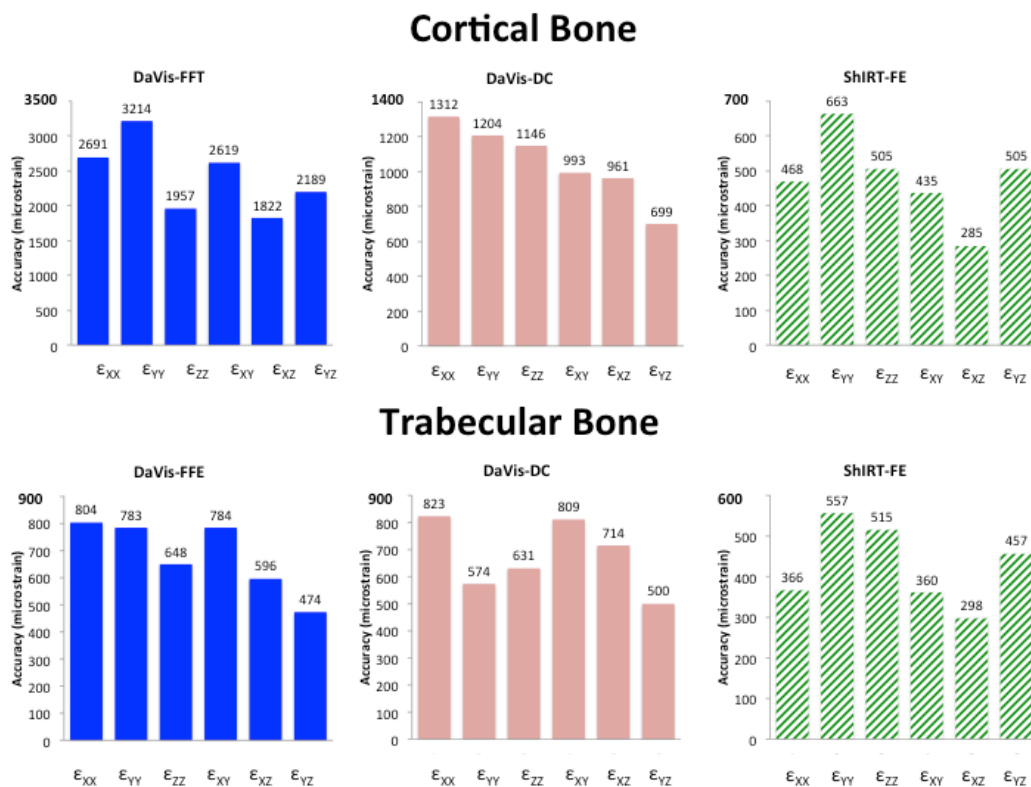


Fig. 9: Repeated-Scan-Test: Analysis of the accuracy of the six components of strain (microstrain), in both cortical and trabecular specimen, for the largest sub-volume size considered (50 voxels ShIRT & DaVis-FFT, 52 voxels DaVis-DC). The Z-axis represents the axis of rotation of the specimen during imaging in the micro-CT. The accuracy of the three DVC approaches was computed as the average of the absolute values of each component of strain. Different scales are used for the three computation approaches due to large differences in absolute values.

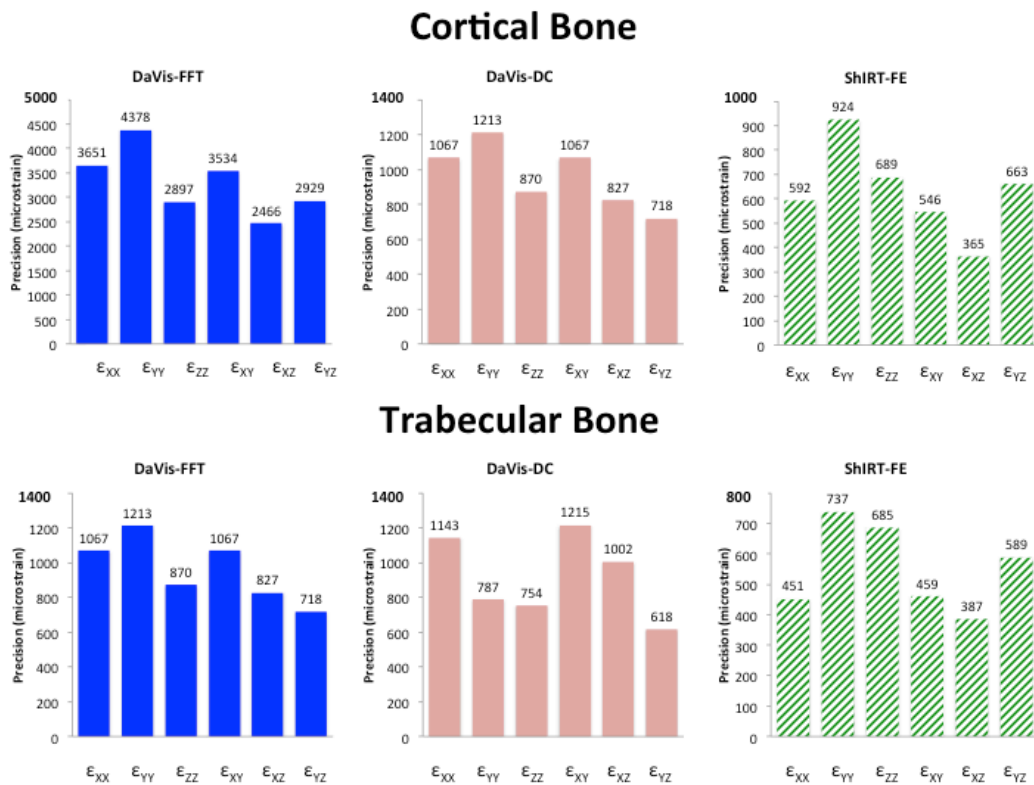


Fig. 10: Repeated-Scan-Test: Analysis of the precision of the six components of strain (microstrain), in both cortical and trabecular specimen, for the largest sub-volume size considered (50 voxels ShIRT & DaVis-FFT, 52 voxels DaVis-DC). The Z-axis represents the axis of rotation of the specimen during imaging in the micro-CT. The precision of the three DVC approaches was computed as the standard deviation of the absolute values of each component of strain. Different scales are used for the three computation approaches due to large differences in absolute values.

6.3.3 Computational Costs

The total computation times were:

- For the DaVis-FFT: 8 seconds for a computation sub-volume of 5 voxels, and 5 seconds for 50 voxels (3.4 GHz quad-core i7, 32 GB Ram, solid state disk);
- For the DaVis-DC: 146 seconds for a computation sub-volume of 8 voxels, and 80 seconds for 52 voxels (3.4 GHz quad-core i7, 32 GB Ram, solid state disk);
- For the ShIRT-FE: 404 seconds for a computation sub-volume of 5 voxels, and 120 seconds for 50 voxels (2.9 GHz dual-core i7, 8 GB Ram, solid state disk). This does not include the time for migrating from the correlation software to the FE package.

6.4 Discussion

The aim of this study was to compare the accuracy and precision of different DVC approaches used in computing the displacements and strains from micro-CT images of cortical and trabecular bone. Three DVC approaches were tested in a zero-strain condition (Repeated-Scan-Test) and with a virtual rigid displacement (Virtually-Moved-Test).

We investigated the strengths and limitations of two commercial approaches (DaVis-FFT and DaVis-DC) that implement different local correlation algorithms to estimate the displacement and strain fields, and a third approach (ShIRT-FE), which exploits a global correlation strategy, by combining an elastic registration algorithm to estimate the displacements, and an FE solver for computing the strain (Dall'Ara et al., 2014).

In this study, all the DVC approaches showed non-linear trends for the measurement uncertainties of the strain, as a function of the considered sub-volume: the larger the sub-volume, the lower the error. However, it is important to remember that increasing the sub-volume size reduces the spatial resolution of the method. An inverse relationship between the size of the computation sub-volume and the displacement/strain uncertainties is typical for both local and global approaches (Hild and Roux, 2012). Such trends were reported when DVC was applied to synthetic and natural trabecular bone (Gillard et al., 2014; Madi et al., 2013), and in a validation study on the DIC (Lionello and Cristofolini, 2014; Nicoletta et al., 2001). MAER and SDER of the three DVC approaches showed an asymptotic trend, when the sub-volume exceeded a size of 25-30 voxels for the displacements, and around 50 voxels for the strains. Given the voxel size (9.96 micrometers) this corresponds to the typical dimension of trabeculae (50-500 micrometers (Currey, 1982; Fung, 1980)) and osteons (150-250 micrometers (Currey, 1982; Fung, 1980)). This consideration could be the explanation for the slightly better behavior of the DVC applied to the trabecular bone (coarser pattern; closer to the ideal condition of 1:1 solid-porosity ratio) as opposed to the cortical one. It is possible to deduce that a relatively large sub-volume investigated in this study (larger than 30 voxels) provides an optimal trade-off between spatial resolution, and error when applied to bone tissue. The three DVC approaches differed among each other in terms of accuracy and precision, both as a scalar (average of the error components, similarly to (Liu and Morgan, 2007)), and for the individual components (similarly to (Gillard et al., 2014)) of displacement and strain. The ShIRT-FE approach showed the best accuracy and precision for the displacements in the Virtually-Moved-Test. The errors on the displacements estimated by DaVis-DC were comparable with ShIRT-FE, while the errors affecting the DaVis-FFT were some order of magnitude higher. The accuracy and precision achieved on the displacements by ShIRT-FE and DaVis-DC with optimal settings (sub-volume larger than 25 voxels) were generally better than 0.1 micrometers. Such an accuracy and precision is sufficient for most applications with hard tissue. Consequently, as the strain field is obtained by differentiation of the displacement field in DaVis, similar trends were found for the errors affecting the computed strain. The best accuracy and precision achieved on the strains for the Repeated-Scan-Test by ShIRT-FE and DaVis-DC with optimal settings (sub-volume of 50-52 voxels) were of the order of a few

hundred microstrain (in case of cortical bone up to 1053 and 477 microstrain for DaVis-DC and ShIRT-FE, respectively). Such an error is one order of magnitude lower than the failure strain of bone tissue (7000 microstrain in tension, 10000 microstrain in compression, (Bayraktar et al., 2004)). Therefore, one can at least discriminate between yielded and not-yielded regions. However, the present results suggest that, in order to further improve the accuracy and precision, larger computation sub-volumes should be used, with the concurrent limitations in terms of resolution. While for the cortical bone the differences among the approaches were higher, in case of trabecular bone the DaVis-DC approach provided MAER and in particular SDER closer to the ShIRT-FE approach, when moving towards larger sub-volumes. When making such comparisons one should remember that the global approach (ShIRT-FE) is based on a method where each element is affected by up to eight neighboring elements (Madi et al., 2013). In fact, the improvement of MAER and SDER we found may be, among the other parameters, driven by the continuity assumption. The results of this study for the repeated scans confirm that similar uncertainty levels are obtained for a global approach (ShIRT-FE) with a mesh two times finer than the one used for a local one (DaVis-FFT) [21]. Moreover, it should be also noted that the SDER and MAER for the DaVis-DC were underestimated as the solution covered a lower correlated volume (80% for sub-volume equal to 52 voxels): if the entire VOI was forcedly included (including regions affected by poor correlation), the overall error would have been larger. Further studies in this direction will be done in the future in order to quantify these effects.

To the Authors' knowledge, this is the first paper that compares three different DVC approaches, and different bone microstructures. In reference (Madi et al., 2013) two DVC approaches were compared, on a single porous polymeric specimen and only for a virtual rigid displacement. Similarly to our study, they concluded that a global correlation approach gives lower errors than a local DVC algorithm. However, it was also reported how, for that particular specimen and set of images, the local FFT-based approach (DaVis-FFT) might be appropriate and provided a good compromise between computational cost and accuracy (strain uncertainties of the order of 200 microstrain from virtually moved test). Conversely, in our study the DaVis-FFT approach showed high MAER and SDER for the cortical bone and, therefore, should be used carefully with similar images. In order to understand the true reliability of the strain and displacement results one should also consider the correlated volume, or the quantity of numerical outputs (i.e. displacements) relative to either the software calculation scheme, or a specific threshold chosen for the correlation function. Hence, using local algorithms (DaVis-FFT and DaVis-DC) there may be cases where a very small error can be achieved at the cost of excluding large regions that would increase the error indicators. In this study, no specific threshold value for the correlation function was adopted in DaVis. However, a certain amount of data is systematically lost in the correlation of sub-volumes containing voxels with constant intensities, due to the algorithm local normalization.

The selected sequence of sub-volumes (96-64-52), overlaps (50%-50%-75%) and iterations (1-2-3), used in this study for the multi-pass calculation in DaVis approaches (Table 2), did only improve the performance of DaVis-FFT for the Virtually-Moved-Test, in particular for the trabecular bone. This can be used as a valuable indication for future studies, where the same multi-pass cannot be used

as a universally valid matrix for all the cases and approaches, but parameters may be selected for that specific bone tissue, test, quality of images and sample size.

In terms of computational cost, the DaVis-FFT and DaVis-DC were lighter than ShIRT-FE. Between the two local algorithms, DaVis-DC was up to two orders of magnitude slower. It must be noted that while DaVis-FFT has been implemented earlier and was fully optimized in terms of computational efficiency, the current versions of DaVis-DC and of ShIRT-FE were not yet fully optimized. For further application on larger VOIs, and considering that the DVC is becoming increasingly common, a reduced computation time would be desirable.

In this study a step beyond the work of (Liu and Morgan, 2007) and (Dall'Ara et al., 2014) was done in order to investigate if strain components are better evaluated in some preferential direction. In fact, for both the Virtually-Moved-Test and the Repeated-Scan-Test, ShIRT-FE showed a more isotropic behavior, with similar errors for the six components of the strain. Conversely, in the Virtually-Moved-Test the DaVis-FFT and in particular DaVis-DC approaches showed better accuracy (Fig. 7) and precision (Fig. 8) for the shear strains than for the normal strain components, consistently with the findings reported by (Gillard et al., 2014). For these approaches it must be noted that when a scalar indicator of the error is computed averaging the different strain components (similarly to (Liu and Morgan, 2007) and (Dall'Ara et al., 2014), Fig. 3-6), this underestimates by about 50% the largest error, which is found for just one of the strain components (Fig. 7-10, DaVis-FFT and DaVis-Dc). However, these trends became less clear in the more interesting case of the Repeated-Scan-Test where, for all three approaches, similar errors were found for all strain components and highest errors were generally produced for one of the normal strains. In such a case, reporting the error in terms of averages is less critical.

A limitation of this work relates to the number of specimens: only one for the cortical bone and one for trabecular bone. Moreover, due to the limited diameter of the cortical bone specimen, only a limited range of sub-volume sizes was explored. The dimensions of the specimens were suitable for bone tissue, considering its osteomorphometric parameters (Öhman et al., 2008). Potential influences of specimen size (i.e. whole vertebra), image quality (i.e. variation of the level of noise) and scanning resolution (i.e. clinical CT) on the accuracy and precision obtainable with different DVC approaches (i.e. optimal multi-pass calculation for DaVis-FFT and DaVis-DC), are yet to be investigated. Moreover, in this study only trabecular and cortical specimens were considered. Further analysis shall be conducted on specimens composed of both cortical and trabecular tissue, and possibly incorporating biomaterials (i.e. implantable devices or injectable materials).

6.5 Conclusion

In conclusion, we have shown the importance of performing a quantitative optimization and validation of DVC approaches by using repeated scans and comparing the DVC outputs on the same set of specimens. While computed

displacements were generally highly accurate and precise, larger errors (decreasing with larger sub-volumes and with a similar behavior for each component) were found in the computed strain distributions. Our results show how the integration of DVC (for the computation of displacements) with an FE code (which imposes a continuum mechanics assumption on the structure) provides the most accurate and precise results, for this particular set of images. However, the local DaVis approaches, as a single software package, show reasonable results for large nodal spacing and particularly for trabecular bone. The results from the repeated scans showed that the multi-pass calculation scheme used in this study for the DaVis methods lead to larger errors compared to the largest sub-volume. Moreover, the errors from the Repeated-Scan-Test were similar for the different components for all three methods. Finally, this study indicates that every method should be used with sufficiently large sub-volumes in order to achieve reasonable accuracy and precision. Further work is needed to fully appreciate the performance of DVC for different bone structures, dimensions and imaging techniques/settings.

Chapter VII

Validation of Digital Volume Correlation at tissue level with biomaterials - microCT

from the manuscript:

Strain uncertainties from two digital volume correlation approaches in prophylactically augmented vertebrae: local analysis on bone and cement-bone microstructures

G. Tozzi¹, E. Dall'Ara², M. Palanca³, M. Curto¹, F. Innocente³, L. Cristofolini³

¹ School of Engineering, University of Portsmouth, Portsmouth (UK)

² Department of Oncology and Metabolism and INSIGNEO Institute for in Silico Medicine, University of Sheffield, Sheffield (UK)

³ School of Engineering and Architecture, Alma Mater Studiorum – Università di Bologna, Bologna (IT)

Published in: *Journal of the Mechanical Behavior of Biomedical Materials*,
2017, 67: 117-126

7.1 Introduction

The efficacy of prophylactic augmentation with injectable biomaterials (i.e. poly-methyl-methacrylate (PMMA)-based cements) in improving the mechanical stability of vertebrae is still a matter of debate (Kamano et al., 2011; Cristofolini et al., 2016). In particular, a deep understanding of internal microdamage in the bone tissue and at the cement-bone interface, which could potentially promote further damage to treated vertebrae, is currently missing.

This is probably due to the intrinsic limitations in most experimental techniques like digital image correlation (DIC) (Palanca et al., 2016) in not being able to capture and quantify internal microdamage evolution under load. In this perspective, digital volume correlation (DVC) is ideal to investigate the local internal damage in treated vertebrae. In fact, with the rapid progress of micro-focus computed tomography (micro-CT) in conjunction with *in situ* mechanical testing (Nazarian & Muller, 2004; Tozzi et al., 2012, 2013), DVC has become a powerful tool to examine full-field internal deformations in trabecular bone (Liu & Morgan, 2007; Gillard et al., 2014; Dall'Ara et al., 2014, Roberts et al., 2014), cortical bone (Christen et al., 2012; Dall'Ara et al., 2014), whole bones (Hussein et al., 2012, 2013; Danesi et al., 2016; Tozzi et al., 2016), cellular scaffolds (Madi et al., 2013) and cement-bone interface (Tozzi et al., 2014).

In order to expand the applications of DVC to biological tissues, including investigation of clinically relevant issues such as bone augmentation, it is important to understand what is the error associated to the DVC measurement for specific sets of images, scanning protocols and correlation strategies. To this extent, the uncertainties of DVC in calculating strain in bone tissue have been quantified (Roberts et al., 2014). Moreover, the strain uncertainties in relation to a virtual displacement applied to one single micro-CT image was also evaluated (Madi et al., 2013). However, it is recommended that strain uncertainties of any specific DVC approach are quantified on repeated scans (i.e. in a known deformation field such as zero-strain) to account for the intrinsic noise of the input images. This repeated scans methodology has been already adopted to quantify strain errors associated to trabecular bone (Liu & Morgan, 2007; Gillard et al., 2014; Dall'Ara et al., 2014), cortical bone (Dall'Ara et al., 2014), whole bones (Hussein et al., 2012) and cement-bone interface (Zhu et al., 2015). However, as DVC typically exploits different correlation and strain calculation strategies to compute strains (i.e. local vs global approaches, different registration metrics, etc.), it is important to quantify the level of uncertainty in the strain determination, by comparing two or more DVC methodologies using the same original image dataset. Palanca et al. (2015) compared the output of three different DVC approaches (a global and two local ones) applied on the same micro-CT biopsies of trabecular and cortical bone, where accuracy and precision in strain fields for both virtual displacements and repeated scans were investigated. Moreover, the presence of preferential components (normal or shear) for strain measurement in the different correlation approaches was also evaluated (Palanca et al., 2015).

Given a specific pattern/texture inside the bone specimen, DVC uncertainties are affected by the features that can be recognized in the sequence of images, which in turn depends on the spatial resolution of the image, and on the number of

voxels included in the computation window (sub-volume) (Roberts et al., 2014). This pattern distribution can be related to the intrinsic natural features of the material (i.e. trabeculae in trabecular bone) or to radiopacifier particles usually incorporated in bone cements (i.e. ZrO_2 and $BaSO_4$) (Lewis et al., 1997). Thus, the DVC-computed strain errors can be affected by the presence of biomaterials within the bone. Zhu et al. (2015) proposed a first attempt to investigate the strain uncertainties in specimens including cement and bone. They focused on images with voxel size of 22 micrometers, with smallest computation sub-volume of 32 voxels. The noise affecting computed strains was lowest within the cement (~ 500 microstrain), slightly higher in the bone regions partially interdigitated with cement (~ 700 microstrain), and more than doubled in the trabecular bone (~ 1400 microstrain). Zhu et al. (2015) used a single local DVC approach based on Fast Fourier Transform (described as DaVis-FFT in Palanca et al., 2015) with multipass and overlaps up to 75%, on one single cement-bone specimen in dry conditions, focusing on a single component of strain (the axial one, e_{zz}). However, recent literature in the DVC computation of bone tissue (Palanca et al., 2015) clearly indicated how DVC strain uncertainties obtained for the same local approach (DaVis-FFT) used in Zhu et al. (2015) are very much reduced if a direct correlation (described as DaVis-DC) is used instead of a FFT-based one (DaVis-FFT), and no overlap is used in multipass strategy. Furthermore, it is known (Gillard et al., 2014; Palanca et al., 2015) that looking at one single strain component (i.e. e_{zz}) is not sufficient for a complete understanding of the error pattern, as variability of strain error among the six components could be quite large. Very recently, uncertainty analyses of local and global DVC approaches applied to the whole natural and augmented porcine vertebrae were performed (Palanca et al., 2016b). In that study it was found that, despite the strain error produced similar trends in function of the computation sub-volumes for both groups, in the augmented vertebrae the random error of the strain components computed with the two DVC methods were different, especially for higher spatial resolution. In particular, the augmentation increased the error for the global approach, while reducing it for the local. It is not clear yet how the DVC errors are influenced by the tissue microstructure and by the biomaterial distribution.

The main aim of this study was to evaluate and quantify strain measurement uncertainties at tissue level in five specific locations within different augmented vertebrae. This was done in order to better understand how the bone microstructure (trabecular and cortical), the presence of biomaterial and its integration with bone (cement-bone interface) could explain differences in performance of the two DVC approaches.

7.2 Methods

7.2.1 Specimens

Five thoracic vertebrae (T1-T3) were harvested from fresh porcine thoracic spines. All the surrounding soft tissues were removed, as well as the growth plates. The endplate areas of the vertebrae were potted in poly-methyl-

methacrylate (PMMA) similar to Danesi et al. (2014). The spinous process was used to center the specimen in the transverse plane and align it about its vertical axis. The posterior arch was subsequently removed. Cement routinely used for vertebroplasty (Mendec Spine, Tecres, Italy) was then injected in the vertebral bodies by means of a proprietary device, following the instructions of the manufacturer. This is an acrylic-based cement, containing pellets of BaSO₄ (~300 micrometers) as a radiopacifier. The vertebrae were heated before and after augmentation in a circulating bath at 40°C, to allow optimal flow and consolidation of the cement.

7.2.2 Experimental procedures and volumes of interest (VOIs)

All the specimens (n=5) were placed in a loading device (CT5000, Deben Ltd, UK) equipped with a custom-designed environmental chamber, in order to closely simulate *in situ* loading conditions that are typically being applied to such vertebral bodies (Danesi et al., 2016; Tozzi et al., 2016). The specimens were immersed in saline solution and constrained against rotation inside the loading device with sandpaper disks glued to the bottom compressive platen. Each unloaded specimen was micro-CT imaged (XTH225, Nikon Metrology, UK) twice without repositioning, in order to reproduce a zero-strain condition. Prior to each imaging session a full conditioning of the micro-CT (up to 225 kV) was performed to stabilize x-rays and reduce at minimum fluctuations in the selected settings (i.e. kV, microA), throughout the duration of test. The micro-CT scanner was set to a voltage of 88 kV and a current of 110-115 microA. With an isotropic voxel size of 39 micrometers and exposure of 2 s, the image acquisition was performed with a rotational step of 0.23°, over 360° for a total scanning time of approximately 90 min.

In order to investigate the performance of the DVC approaches for the different bone tissues (cortical and trabecular), for the cement, and for the interdigitated regions, five volumes of interest (VOIs) were identified within each vertebral body. The five VOIs were cropped using MeVisLab (MeVis Medical Solution AG, Germany) and consisted in parallelepipeds of 300*300*432 voxels for the largest possible area that could be inscribed in all vertebrae (VOI-1, data presented in Palanca et al. (2016b) and reported here for completeness and for comparison) and of 152*152*432 voxels for smaller VOIs including areas of: fully cement-augmented trabecular bone (VOI-2), interface between augmented and non-augmented trabecular bone (VOI-3), trabecular bone (VOI-4), and regions containing both trabecular and cortical bone, with surrounding saline solution (VOI-5) (Fig.1). The VOI-5 region was selected to understand how inappropriate (or ineffective) image masking could influence the DVC performance in the two approaches, particularly for the local DVC. The dimensions for the smallest VOIs (2-5) were able to include the different regions of interest within the augmented vertebra. To allow for the most standardized and less operator-dependent workflow, and investigate the worst-case scenario, no beam hardening and noise artifacts were corrected in the images. In order to allow comparison between the results obtained from different DVC approaches, the image datasets used in the present study will be made available to the scientific community at

<http://dx.doi.org/10.6084/m9.figshare.4308926> or by contacting the corresponding author.

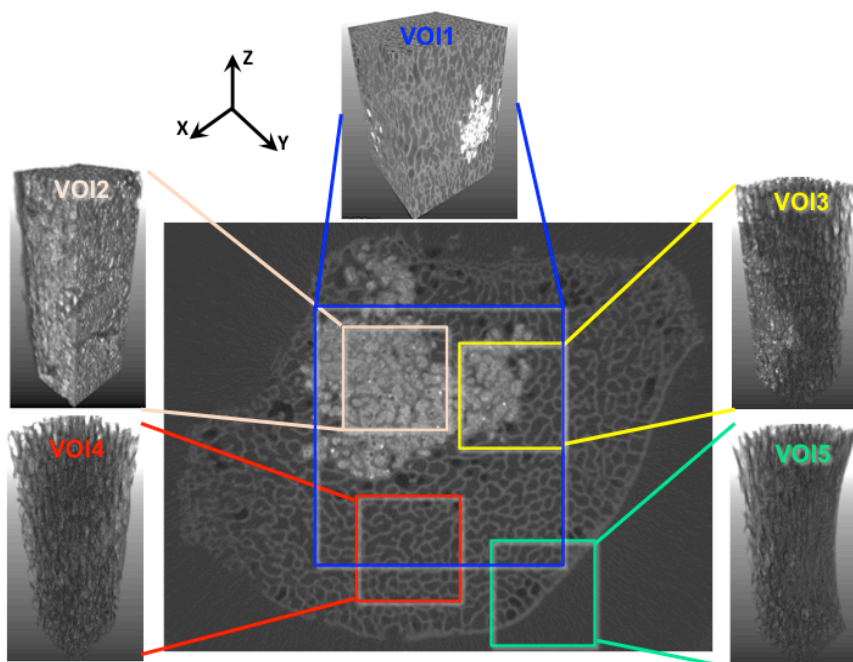


Fig 1: Transverse section of a vertebra, showing the five different volumes of interest (VOIs) selected for the DVC computation. Specifically, VOI-1 was the largest volume that could be inscribed in all vertebrae, VOI-2 a region of full cement-bone augmentation, VOI-3 a region of partial cement-bone augmentation, VOI-4 a region of trabecular bone, and VOI-5 a region of trabecular and cortical mixture surrounded by saline solution. Data related to VOI-1 has been reported for completeness and adapted from Palanca et al. (2016b).

For each VOI in each specimen, the solid volume fraction (SV/TV) was computed as the sum of the volume of cement and/or bone, divided by the total volume of the VOI (Table 2). In VOI-4 and VOI-5 the SV/TV is equivalent to the bone volume fraction (BV/TV). The values of SV/TV were obtained via a manual thresholding of the grey-scale histograms with ImageJ (NIH) software, using its BoneJ plugin (Doube et al., 2010). The images were segmented by using a single level threshold, chosen in the valley between the first and second peak of the frequency distribution of the greyscale (histograms). The threshold value was adapted by visual comparison of the segmented and greyscale image in order to separate bone and cement from the background values. The SV/TV value, computed as average \pm standard deviation between specimens for each VOI, was used to assess possible correlations with the DVC strain errors.

7.2.3 Digital Volume Correlation (DVC) approaches

Two different DVC approaches were compared in this work, namely a 'local correlation' and 'global correlation'. The operating principles of the two DVC methods have been detailed elsewhere (Palanca et al., 2015, 2016b). Briefly, the local approach (DaVis-DC) is implemented in the DaVis software (v8.2.1, LaVision, Germany). DaVis-DC sub-divides the 3D images into smaller sub-volumes that can be correlated independently as a discrete function of grey-levels. The matching between the sub-volumes is achieved via a direct cross-

correlation function (DC). Additionally, a piece-wise linear shape function and a third-order spline interpolation in the image reconstruction are employed to correlate the pattern information contained in the reference and deformed images. The displacement field vector is obtained at the center of each sub-volume and the strain field is subsequently computed using a centered finite differences (CFD) scheme. The employed global approach (ShIRT-FE) is a combination of an home-written elastic registration software known as Sheffield Image Registration Toolkit (ShIRT) (Barber et al., 2007) and a Finite Element (FE) software package (Ansys v.14.0, ANSYS, US) as reported in Dall'Ara et al. (2014). In ShIRT the recognition of corresponding features in the subsequent 3D images is obtained by superimposing a grid with selectable nodal spacing (or sub-volume) to the entire volume of interest. ShIRT solves elastic equations at the nodes of the selected grid to evaluate the nodal displacements. The grid is then converted into an eight-node hexahedral mesh and the displacements computed by ShIRT at each node are imposed as boundary conditions in the FE model, where the strain field is then computed.

In order to evaluate the random errors associated to the displacement and the systematic and random errors associated to the strain for both DVC methods, two sub-volume sizes of 16 and 48 voxels were investigated for the five VOIs in each specimen. The larger sub-volume (48 voxels – 1872 micrometers) was chosen in order to obtain sufficient measurement points in the VOIs, and while it showed acceptable uncertainties of the strain components averaged over the whole organ for augmented vertebrae, it also revealed different behavior for the two DVC methods (Palanca et al., 2016b). The lower sub-volume (16 voxels – 624 micrometers) was chosen in order to evaluate the error for smaller registration regions, which could be beneficial especially for the boundary between the cement and bone. Moreover, both sub-volume sizes produced a 100% of correlated volume (defined as in Palanca et al. (2015, 2016b)) for both local and global approaches. Finally, two different multipass schemes (available only on DaVis-DC) with decreasing sub-volume size of 128-112-96-80-64-48 voxels for VOI1 and 48-32-16 voxels for VOI2-VOI5 were tested with 0% overlap. In particular, the multipass was pushed to a final size of 16 voxels in the local VOIs (2-5), to explore the potential improvements for the local DVC approach, but still producing a larger number of measurement points (spatial resolution) when compared to 48 voxels.

7.2.4 Evaluation of errors as a consequence of the computation sub-volume

To quantify the errors, different indicators were computed:

- Ideally, the displacements were null; in the real experiment the actual displacements were affected by the inevitable unknown micro-movements of the moving parts of the scanner. To quantify the random error of the displacements, their variability was computed within each specimen. The systematic error for the displacements could not be quantified.
- As the test was based on a zero-strain condition, any non-zero values of strain were considered as error. Systematic and random errors for each specimen were computed as the average and standard deviation,

separately, for each component of strain. For each VOI and sub-volume size, the median of the values of the errors obtained for the five specimens was then reported for each strain component.

- The mean absolute error (MAER) and standard deviation of error (SDER) were computed as:

$$\text{MAER} = \frac{1}{N} \sum_{k=1}^N \left(\frac{1}{6} \sum_{c=1}^6 |\varepsilon_{c,k}| \right) \quad (\text{Eq. 1})$$

$$\text{SDER} = \sqrt{\frac{1}{N} \sum_{k=1}^N \left(\frac{1}{6} \sum_{c=1}^6 |\varepsilon_{c,k}| - \text{MAER} \right)^2} \quad (\text{Eq. 2})$$

where “ ε ” represents the strain; “c” represents the six independent strain components; “k” represents the measurement point; N is the number of measurement points. MAER and SDER correspond to the indicators formerly called as “accuracy” and “precision” (Liu & Morgan, 2007).

- Linear correlations between the SV/TV and the random error computed for each component of the strain, or the SDER, were computed for each VOI and for both DVC approaches (Mann-Whitney U test, $\alpha=0.05$, Minitab 17, UK).

7.3 Results

The random errors affecting the displacements ranged between 0.01 and 1.61 of the voxel size (from 0.66 to 63.08 micrometers) for DaVis-DC, and from 0.01 to 0.04 voxels (from 0.50 to 1.53 micrometers) for ShIRT-FE. Random errors were typically larger for smaller sub-volume sizes (Table 1) and this difference was more pronounced for DaVis-DC than ShIRT-FE. The multipass scheme available for DaVis-DC notably improved the performance in VOI-1 (sub-volume output of 48 voxels), VOI-4 (sub-volume output of 16 voxels) and partially in VOI-2 and VOI-3 (sub-volume output of 16 voxels) when compared to the results obtained with sub-volume of 16 voxels, obtaining values comparable to the case when a sub-volume of 48 voxels was used. Multipass in VOI-5 also (sub-volume output of 16 voxels) produced an improvement compared to the case in which a sub-volume of 16 voxels was used, but less relevant when compared to the results obtained with a sub-volume of 48 voxels.

Table 1: Random errors affecting the displacements (in micrometers) for DaVis-DC and ShIRT-FE, for a sub-volume size of 16 and 48 voxels for each VOI. The median over the five specimens is reported.

DISPLACEMENT RANDOM ERROR (MICROMETERS)							
VOI	Sub-Volume	DaVis-DC			ShIRT-FE		
		X	Y	Z	X	Y	Z
1	16	1.87	1.49	2.18	1.22	1.27	1.13
	48	1.56	1.10	1.16	1.25	1.35	1.24
	Multipass (48)	1.05	1.08	0.92	NOT AVAILABLE		
2	16	1.55	1.66	1.05	1.24	1.35	0.68
	48	1.11	0.89	0.47	1.24	1.23	0.63
	Multipass (16)	1.58	1.40	0.66	NOT AVAILABLE		

3	16	2.02	1.71	1.97	1.22	1.34	0.67
	48	1.47	1.19	0.76	1.15	1.30	0.54
	Multipass (16)	1.23	1.35	1.04	NOT AVAILABLE		
4	16	2.20	2.04	2.41	1.31	1.40	0.77
	48	1.73	1.57	1.36	1.25	1.35	0.54
	Multipass (16)	1.37	1.31	1.04	NOT AVAILABLE		
5	16	54.77	63.08	48.57	1.40	1.53	0.80
	48	2.59	2.04	2.18	1.18	1.55	0.50
	Multipass (16)	15.64	17.49	17.49	NOT AVAILABLE		

Both the local (DaVis-DC) DVC and the global (ShIRT-FE) approaches did not show a clear trend in the systematic (Fig. 2) and random (Fig. 3) errors affecting the specific components of strain. Moreover, the sub-volume size (16- or 48-voxel) did not seem to generally affect the order of magnitude of the systematic error. DaVis-DC experienced absolute systematic errors mostly lower than 100 microstrain, with a maximum peak of 350 microstrain (e_{xx} in VOI-3) for VOI-1, VOI-2, VOI-3 and VOI-4. The main exception was observed for DaVis-DC in relation to VOI-5 (Fig. 2), where considerably higher systematic errors (up to ~6000 microstrain) were found with the 16-voxel sub-volume size. However, the use of a 48-voxel sub-volume size produced errors ranging from -223 to 428 microstrain for e_{zz} and e_{xx} , respectively. The multipass strategy for DaVis-DC did not drastically reduce the strain uncertainties for all VOIs, but only in few cases such as e_{xx} in VOI-1 and e_{xx} , in VOI-3. In some other cases the multipass had a rather detrimental effect and considerably increased the strain error, particularly when compared with the 48-voxel sub-volume size (i.e. e_{xy} in VOI-1, e_{yy} in VOI-5 and e_{xy} in VOI-5). In ShIRT-FE, for the six components, absolute strain values were always lower than 100 microstrain (for all VOIs).

Once again the random error evaluation did not indicate any preferential direction in the six strain components for the different VOIs, but more regular patterns could be identified (Fig. 3, all values for sub-volume 48 in supplementary material). For the sub-volume size of 48 voxels in VOI-1, VOI-2, VOI-3 and VOI-4, DaVis-DC computed errors that were generally lower than 200 microstrain with a maximum value of 274 microstrain for e_{zz} in VOI-1. The sub-volume size of 16 voxels increased the random error to thousands of microstrain in DaVis-DC as well in VOI-1, VOI-2, VOI-3 and VOI-4, with a maximum of 1771 microstrain for e_{zz} in VOI-4. VOI-5 still presented the worst case with very large errors (several-thousands microstrain) for the 16-voxel sub-volume size, and up to 770 microstrain for the 48-voxel size. The multipass for DaVis-DC was only able to reduce the uncertainties for VOI-1, when a final sub-volume size of 48 voxels was used. For VOI-2, VOI-3, VOI-4 and VOI-5 the multipass, with a final sub-volume pushed at 16 voxels, could only mitigate the errors relative to the 16-voxel sub-volume alone, without any considerable improvements. In ShIRT-FE the strain uncertainties for all the components with a sub-volume size of 48 voxels were consistently lower or close to 200 microstrain. For a sub-volume size of 16 voxels ShIRT-FE produced a maximum strain error of ~1200 microstrain. Interestingly, this global approach seems to produce lower random errors for the normal strains, rather than the shear ones for all VOIs.

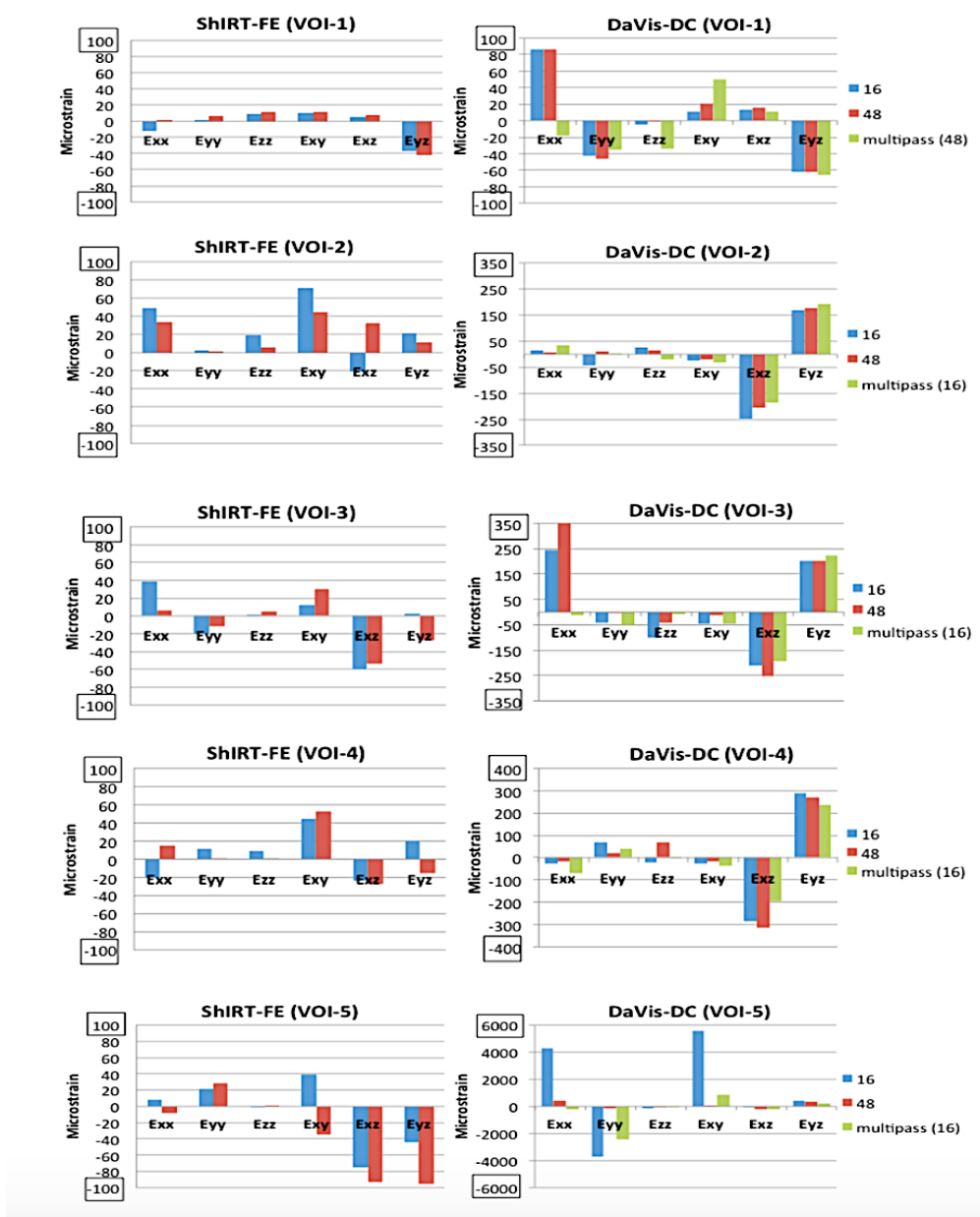


Fig 2: Systematic error with ShIRT-FE (left) and DaVis-DC (right) in the five VOIs (1-5): median between five specimens. Data related to VOI-1 has been reported for completeness and adapted from Palanca et al. (2016b).

The strain values obtained in DaVis-DC (local approach) for VOI-5 were clearly influenced by the presence of the saline solution in the micro-CT images as shown in Fig. 4 (a, b, d, e). Conversely, ShIRT-FE (global approach) seemed to be less sensitive to saline region, and the major strain uncertainty was related to boundary effect (Fig. 4a, c, d, f).

In order to facilitate the comparison with published literature the MAER and SDER were also computed as scalar values similar to (Liu & Morgan, 2007), so as to have a single value to be associated with each VOI (Fig. 5). Both MAER and SDER followed a decreasing trend with the increase of sub-volume size from 16 to 48 voxels.

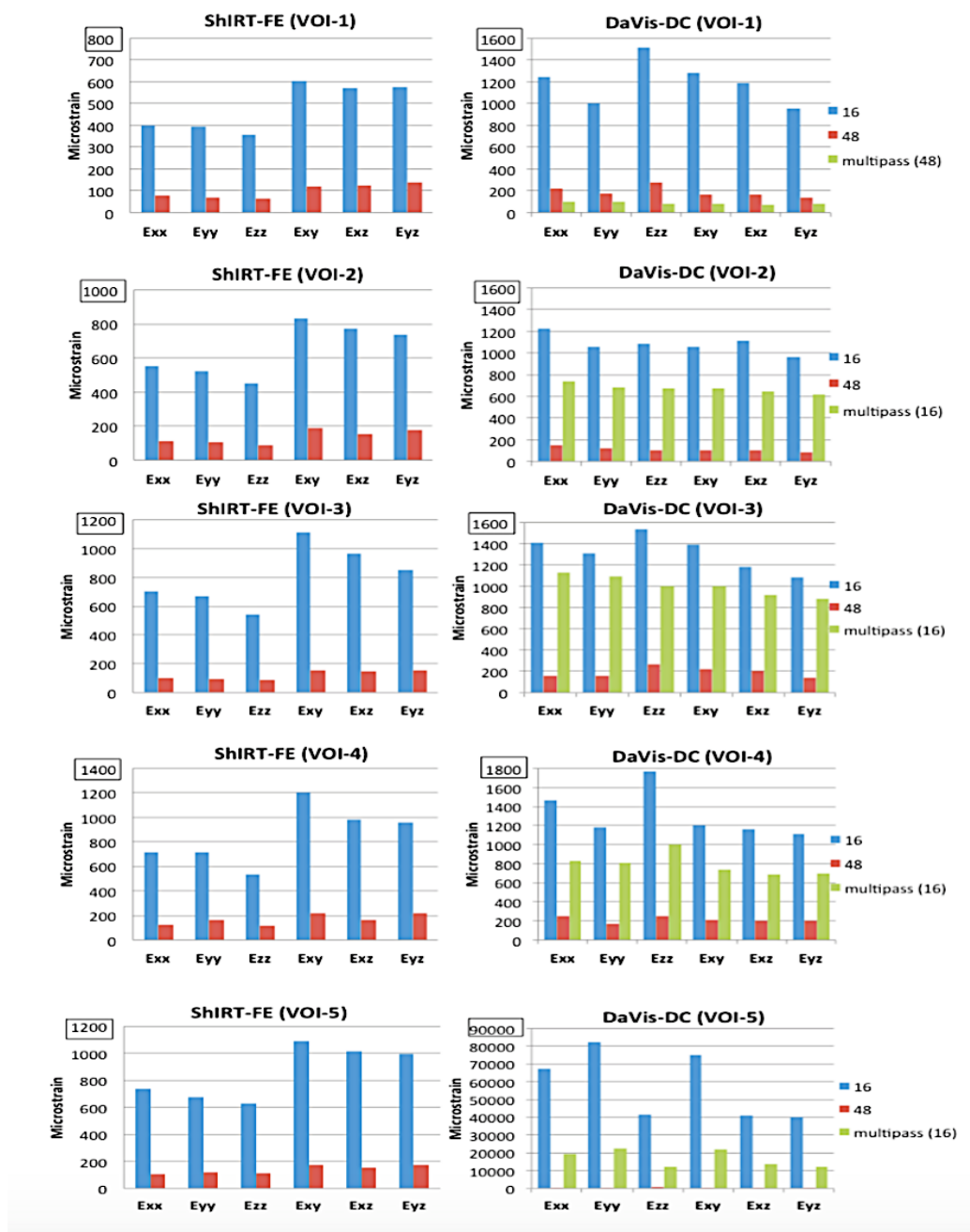


Fig 3: Random error with ShIRT-FE (left) and DaVis-DC (right) in the five VOIs (1-5): median between five specimens. Data related to VOI-1 has been reported for completeness and adapted from Palanca et al. (2016b).

In particular, for the 48-voxel sub-volume the MAER and SDER in VOI-1, VOI-2, VOI-3 and VOI-4 for both DaVis-DC and ShIRT-FE were consistently better or close to 200 microstrain and 100 microstrain, respectively. In VOI-5, DaVis-DC produced MAER and SDER (48 voxels) better than 400 microstrain and 200 microstrain, respectively. The multipass scheme was only able to reduce the error in VOI-1 (48-voxel final sub-volume), but not in the smaller VOIs (2-5) when the final sub-volume output was pushed to 16 voxels. ShIRT-FE confirmed the same trend as for the other VOIs with strain errors better than 150 microstrain.

The effect of SV/TV was not clearly associated with the strain uncertainties. In terms of SDER (48-voxel sub-volume, Table 2) the outputs of ShIRT-FE and DaVis-DC did not show any linear correlation with the SV/TV ($p > 0.21$). The random error for each strain component (not reported here for brevity) showed inverse linear correlation with SV/TV only for e_{xx} ($p = 0.012$, $R^2 = 0.61$) and e_{xz} ($p = 0.036$, $R^2 = 0.45$) computed in VOI-2 (48 voxels sub-volume) with DaVis-DC.

Table 2: SDER and solid volume fraction (SV/TV) for DaVis-DC and ShIRT-FE calculated for a sub-volume size of 48 voxels in the five specimens and for each VOI. SDER is reported as median and standard deviation, whereas SV/TV as average and standard deviation.

VOI	SDER DaVis-DC (microstrain)	SDER ShIRT-FE (microstrain)	SV/TV (%)
VOI-1 (300*300*432 voxels)	66 ± 52	35 ± 52	57.5 ± 10.9
VOI-2 (152*152*432 voxels)	45 ± 69	75 ± 48	84.1 ± 10.9
VOI-3 (152*152*432 voxels)	63 ± 47	52 ± 42	54.5 ± 6.4
VOI-4 (152*152*432 voxels)	61 ± 46	83 ± 48	32.9 ± 3.6
VOI-5 (152*152*432 voxels)	159 ± 406	51 ± 41	31.4 ± 5.2

7.4 Discussion

The main aim of this work was to evaluate the effect of bone microstructure, biomaterial and its integration with bone (cement-bone interface) on the systematic and random strain error distributions within prophylactically augmented vertebrae, when two different DVC approaches are used. For VOI-1, which was intended as an organ-level investigation, DaVis-DC and ShIRT-FE were similar in terms of magnitude of systematic and random errors. For more details please refer to Palanca et al. (2016b). For all VOIs the effect of sub-volume size on the systematic error seemed negligible as well as the multipass (16-voxel final sub-volume). Most of the strain components in VOI-2, VOI-3, and VOI-4 were included in the range ± 50 microstrain and absolute maximum strains of ~ 70 microstrain for ShIRT-FE (in VOI-2) and ~ 350 microstrain for DaVis-DC (in VOI-3). However, in VOI-5 there was a visible difference between the two DVC approaches. ShIRT-FE reported values comparable to the other VOIs, with absolute strains always lower than 100 microstrain, whereas DaVis-DC produced absolute errors up to ~ 5600 microstrain. Moreover, the effect of sub-volume size was remarkable in some strain components: some components of error (i.e. e_{xy}) for a 16-voxel sub-volume were ~ 200 times higher than for the 48-voxel sub-volume. This was expected for the local DVC approach due to the absence of trackable features outside the bone (Fig. 4), which becomes critical for the local DaVis-DC when computing smaller sub-volumes (higher spatial resolution).

Not surprisingly random errors for both approaches were largely influenced by the sub-volume size in all VOIs, where errors for the 16-voxel sub-volume were much higher than those for the 48-voxels, and a more repeatable trend in the strain components was observed (Fig. 3). In all VOIs except VOI-5, DaVis-DC produced strain errors up to in the order of thousand microstrain (maximum of ~ 1800 microstrain in VOI-4) for the 16-voxel sub-volume and errors in the order of hundred microstrain for the 48-voxel sub-volume (maximum of ~ 250 microstrain in VOI-4). The multipass was able to further reduce the error in VOI-1 (close or below 100 microstrain for all components) only when the final sub-volume was 48 voxels. In the smaller VOIs (2-4) where the final sub-volume was pushed at 16 voxels, the multipass was only able to reduce the error for the same sub-volume size without multipass to a minimum of ~ 600 microstrain in VOI-2.

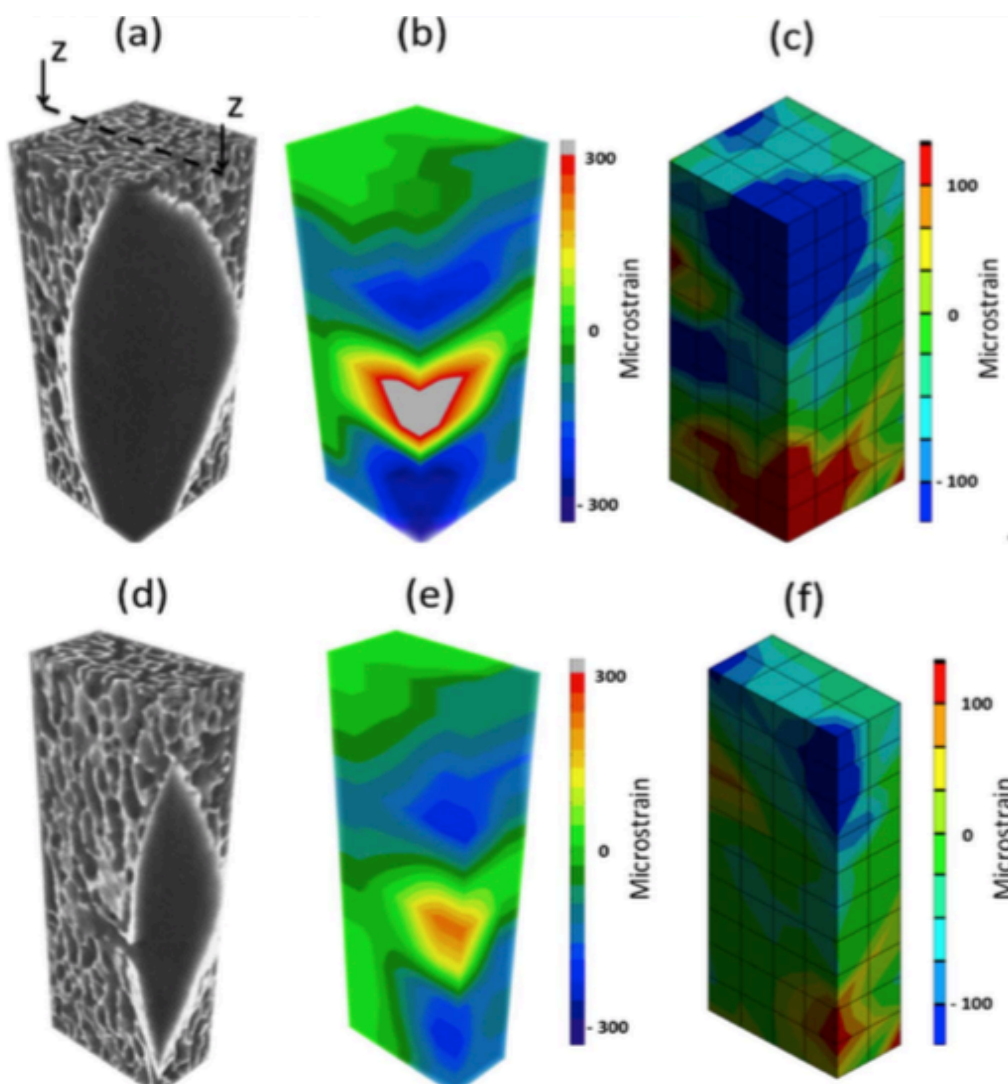


Fig 4: The first row reports the volumetric view of VOI-5 for micro-CT (a), DVC strain maps computed with DaVis-DC (b) and ShIRT-FE (c) with sub-volume size of 48 voxels. The second row reports the z-z planar section for micro-CT (d), DVC strain maps computed with DaVis-DC (e) and ShIRT-FE (f). For DaVis-DC the largest random errors mainly corresponded to the region of saline solution and negatively influenced the result in the trabecular/cortical region, whereas strain error in ShIRT-FE are localized mainly in the boundaries of the image.

This can be related to a lack of convergence of the different steps in the multipass due to the reduced number of features with the smallest final sub-volume (16 voxels). In VOI-5, ShIRT-FE reported the same trend shown in the other VOIs with errors constantly lower than 200 microstrain for the 48-voxel sub-volume and close or lower than 1000 microstrain for the 16-voxel sub-volume. Similarly to the systematic error, DaVis-DC showed high sensitivity to the saline solution surrounding the tissue also for random errors as documented in Fig. 4. While errors outside the bone are in most cases acceptable, care should be taken when interpreting the results on the border of the specimen, where local approaches are affected by the absence of reference features. A possible solution to the problem for local DVC could rely in the use of appropriate overlap strategies to ensure a higher degree of continuity during correlation. However, current overlap scheme implemented in DaVis did not produce any improvements in strain error (Palanca et al., 2015) and further work is needed on that side. Also, an appropriate and controlled masking is suggested when local DVC approaches are used. However, it must be noted that for sub-volume size of 48 voxels DaVis-DC generated errors in the range 209 – 770 microstrain, which suggests how even the minimal variation in the image gray-scale intensity for the individual sub-volume could result in an important improvement of the local correlation strategy. There was no evidence of a clear directionality associated to strain error in all VOIs for both DVC approaches. Only ShIRT-FE seemed to indicate lower errors for the normal strains when compared to the shear components (Fig. 3), but no clear trend could be observed. The random error reported for the displacements (Table 1) is in line with the strain results. This is important as different strain calculation strategies could affect the final outcome, starting from comparable displacements. However, particularly for VOI-4 the multipass produced better displacements even when compared to the 48 voxels. This opens up discussion on how strain is actually computed. In fact, in this study only the centered finite differences (CFD) scheme available in DaVis software was used, but the influence of different strain computation of primary DVC output (displacement) surely requires further investigation. Overall, for both sub-volume size and DVC approaches (excluding the VOI-5 for DaVis-DC), both systematic and random errors resulted not particularly related to the bone microarchitecture and or the presence of biomaterial. Therefore, it seems that local material heterogeneities should not affect the precision of the DVC calculation, provided that enough recognizable patterns are available in the images.

The MAER and SDER, reported as “accuracy” and “precision” in Liu & Morgan (2007) (Fig. 5), showed a clear reduction for both error indicators with a larger sub-volume, consistently with previous literature (Dall’Ara et al., 2014; Palanca et al., 2015). The multipass was still able to produce improvements for VOI-1, but not for the remaining VOIs (2-5), where the final sub-volume was 16 voxels. For VOI-4, containing only trabecular bone, both MAER and SDER were worse than those extrapolated via power law in Dall’Ara et al. (2014) for sub-volume size with physical dimension equal to 1872 micrometers and equivalent to the 48-voxel sub-volume in this study (MAER: ~200 microstrain in this study vs extrapolated 21 microstrain; SDER: ~50 microstrain in this study vs extrapolated 13 microstrain). This difference is probably due to the higher

spatial resolution of the images used in the study of Dall'Ara et al. (2014) with respect to the one of the images used in this study (voxel size ~ 10 micrometers vs 39 micrometers).

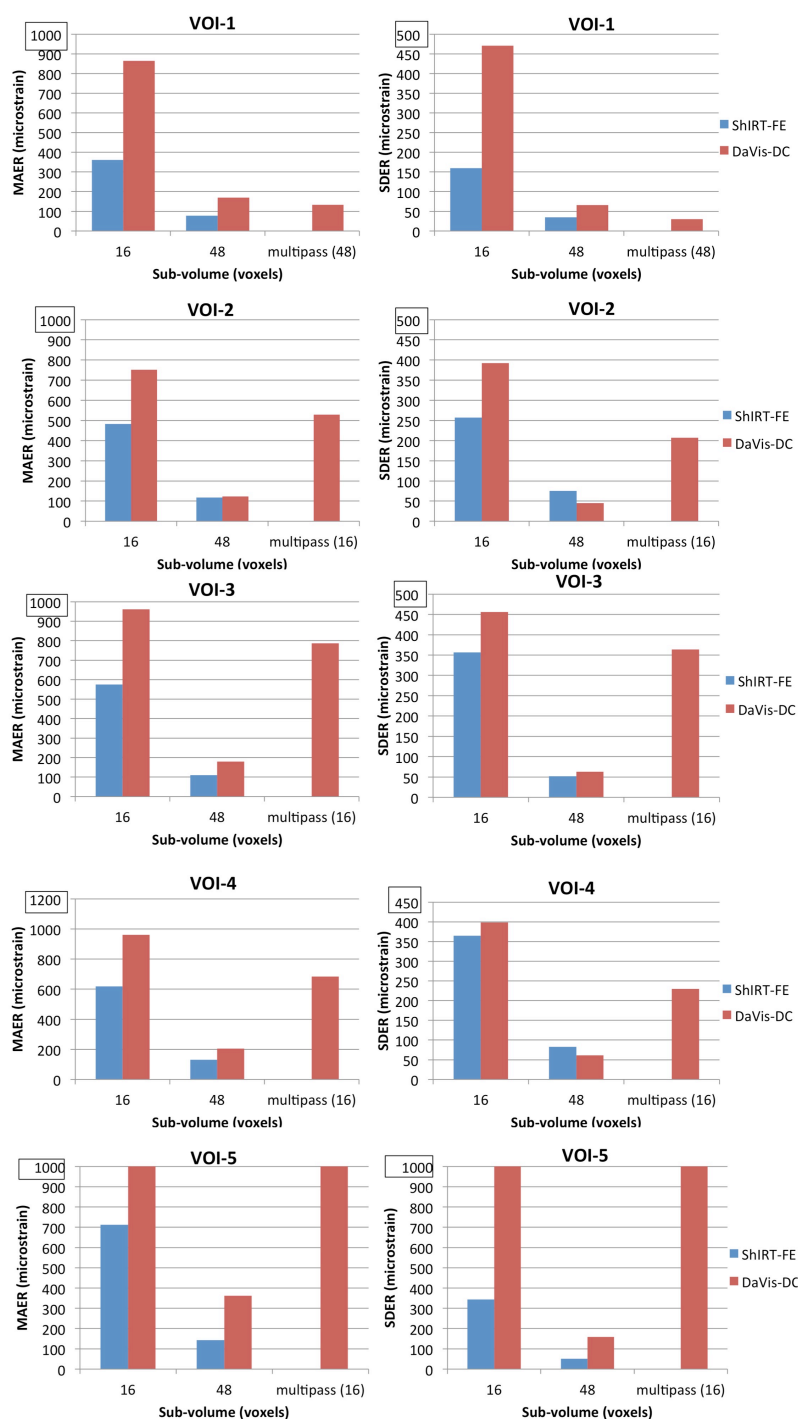


Fig 5: DVC strain uncertainties reported as 'MAER' (left) and 'SDER' (right) (formerly known as 'accuracy' and 'precision' respectively in Liu & Morgan, 2007) for both ShIRT-FE and DaVis-DC with sub-volume sizes of 16 and 48 voxels, and for the multipass scheme (only DaVis-DC, final sub-volume size equal to 48 for VOI-1 and 16 for the other VOIs). Data related to VOI-1 has been reported for completeness and adapted from Palanca et al. (2016b).

The SV/TV was calculated for each VOI in order to take into account the effect of both bone and cement on the SDER, for the two DVC approaches. This choice was preferred to the BV/TV involving only bone tissue (Roberts et al., 2014), as the influence of bone cement with pellets of BaSO₄ (~300 micrometers) or other radiopacifiers could strongly modify the material texture and, therefore, influence the DVC analysis. It was found that there is no linear correlation between the SDER calculated in DaVis-DC and ShIRT-FE with SV/TV for all VOIs ($p > 0.21$). With regards to the single components, the random strain error produced a weak inverse correlation with SV/TV in VOI-2 (48-voxel sub-volume) for DaVis-DC only for e_{xx} ($p = 0.012$, $R^2 = 0.61$) and e_{zz} ($p = 0.036$, $R^2 = 0.45$). This could be related to the intrinsic nature of local DVC approaches, where small interrogation volumes in two scans are registered independently to map local grey-scale intensities in the images (if enough features are available). Hence, the presence of radiopacifiers in the cement may have helped the local approach to produce lower errors, compared to areas with gradient of materials. However, this correlation is insufficient to justify the effect of microstructure or biomaterial in the strain error. The application of DVC to cement-bone composites was firstly introduced by Tozzi et al. (2014). In that study it was noted that the presence of radiopacifiers with suitable particle size in the cement helped the correlation process, producing better correlation in such areas. However, a detailed investigation of the effects of cement in the DVC strain uncertainties was not performed. Zhu et al. (2015) reported a first attempt to investigate this effect. They evaluated the DVC uncertainties with a local approach (DaVis-FFT) in zero-strain (repeated scans) on one cement-bone specimen in dry conditions (22 micrometers voxel size, smallest sub-volume of 32 voxels). They reported the MAER (referred to as “accuracy”) and SDER (referred to as “precision”) for only one strain component (e_{zz}). Thus, if results have to be compared with the current study, the SDER with DaVis-DC multipass for the 16-voxel subvolume (our 624 micrometers vs their 704 micrometers) on the e_{zz} would be more appropriate and represent the worst case in both studies. The current results did not show the same decreasing trend from trabecular to cement as in Zhu et al. (2015). In fact, the SDER from trabecular bone regions (current VOI-4), to partially interdigitated (current VOI-3), to cement (current VOI-2) in the current study remains pretty constant (<100 microstrain for both approaches). However, our SDER was consistently better than that reported in Zhu et al. (2015) for e_{zz} in the bone region (230 microstrain in this study vs ~1400 microstrain in that study), partially interdigitated (364 microstrain in this study vs ~700 microstrain in that study) and cement region (207 microstrain in this study vs ~500 microstrain in that study). This is surely due to the specific choice of FFT-based local DVC as well as extensive overlap (up to 75%) in Zhu et al. (2015), which were found to be less accurate when compared to a direct correlation approach for the same software (DaVis-DC) without any overlaps (Palanca et al., 2015). The present findings show that the local errors to be expected in the cement, bone, and in the interdigitated regions may not be so different, but that different sub-volume sizes may be required to minimize such errors in the different regions.

The current study has some limitations. Firstly, only two sub-volume sizes (16- and 48-voxel) were chosen in the present study. However, a more comprehensive trend for augmented vertebrae with sub-volume sizes up to 128

voxels has been recently reported in Palanca et al. (2016b). That study showed how random error could be reduced well below 100 microstrain in both DVC approaches for VOI-1. Thus, it is expected that also smaller VOIs could follow a similar trend. Secondly, the use of five specimens could not provide a statistical relevance, but only a trend that may be sufficient to have reliable information on strain uncertainties location and distribution. Thirdly, the strain error is only calculated in a zero-strain condition for repeated scans. This type of analysis should be expanded in order to take into account strain errors under load. Finally, the use of animal tissue is justified by easier handling and availability compared to human. This decision was taken for ethical reasons in this preliminary methodological work. Future work on DVC strain uncertainties from clinical CT images will expand our knowledge of the tool for a potential implementation in clinical practice.

7.5 Conclusions

The results obtained in this study aimed at better understanding the complexity of DVC strain uncertainties in prophylactically augmented vertebrae, and of how the bone microstructure and the presence of injectable biomaterial could influence the strain error. Two different DVC approaches were tested (global ShIRT-FE and local DaVis-DC) and strain errors were evaluated for two sub-volume sizes (16- and 48-voxel). It was found that systematic error was insensitive to sub-volume changes, whereas the random errors were lower for the 48-voxel sub-volume (all values around or lower than 200 microstrain) in volumes of interest with larger amount of solid volume fraction, for both DVC approaches. The bone microstructure as well as the presence of biomaterial did not seem to have an important affect on DVC computation for both approaches. When the liquid (uniform material) was included in the image, DaVis-DC experienced higher errors (770 microstrain in the best case) than ShIRT-FE. MAER and particularly SDER were substantially improved when compared to recent literature in cement-bone interface. The multipass approach for DaVis-DC further reduced the minimum random error for the largest volume of interest (48-voxel final sub-volume) and reduced the maximum random error (16-voxel final sub-volume) in the other volumes. Finally, no anisotropy was found for the errors affecting the different components of strain, where only ShiRT-FE seemed to produce lower random errors in the normal strain components.

Chapter VIII

Validation of Digital Volume Correlation at organ level - microCT

from the manuscript:

**Digital Volume Correlation can be used to estimate
local strains in natural and augmented vertebrae:
An organ-level study**

M. Palanca¹, L. Cristofolini¹, E. Dall'Ara², M. Curto³, F. Innocente¹, V. Danesi¹,
G. Tozzi³

¹ School of Engineering and Architecture, Alma Mater Studiorum – Università
di Bologna, Bologna (IT)

² Department of Oncology and Metabolism and INSIGNEO Institute for in
Silico Medicine, University of Sheffield, Sheffield

³ School of Engineering, University of Portsmouth, Portsmouth (UK)

Published in: *Journal of Biomechanics*, 2016, 49 (16): 3882-3890

8.1 Introduction

Digital Volume Correlation (DVC) has been used to explore the full-field displacement and strain distribution inside specimens from 3D images (Bay et al., 1999a; Grassi and Isaksson, 2015; Roberts et al., 2014). Since the introduction of DVC, several studies were performed to evaluate its reliability (measurement error). As no other experimental method allows measuring internal displacements and strains, validation experiments must be designed where the field of displacement and/or strain is known *a priori*.

DVC is extremely powerful in measuring displacements (overall error of 1/50 to 1/10 of the voxel size (Bay et al., 1999a; Dall'Ara et al., 2014; Freddi et al., 2015; Palanca et al., 2015b; Tozzi et al., 2017)). Conversely, DVC-computed strains are affected by significant errors. Tests in a zero-strain condition have been performed, from the tissue-level (trabecular or cortical bone (Bay et al., 1999a; Dall'Ara et al., 2014; Gillard et al., 2014; Liu and Morgan, 2007; Palanca et al., 2015b; Zhu et al., 2015)), to the organ-level (vertebral bodies (Hardisty and Whyne, 2009; Hussein et al., 2012)). Depending on the nature of the tissue type under investigation and on the voxel size of the input images, the accuracy of strain measurements can range between 300 and 794 microstrain, while the precision between 69 and 630 microstrain (Roberts et al., 2014). All these studies showed how the performance of DVC depends on the natural texture of the specimen (i.e. histomorphometric parameters in trabecular bone), and how DVC is suitable to examine the pre- and post-yield deformation in bone (Liu and Morgan, 2007; Tozzi et al., 2016).

The above-mentioned studies provided deep basic knowledge about the reliability and main benefits/limitations of the DVC applied to bone with no information about the variability of such errors between specimens. In fact, in those studies the DVC uncertainties were evaluated using only one (Bay et al., 1999a; Dall'Ara et al., 2014; Gillard et al., 2014; Palanca et al., 2015b; Zael et al., 2006) or two (Liu and Morgan, 2007) specimens.

It was probably (Bay et al., 1999) who first assessed the variability of errors between different trabecular bone cores. Later (Liu and Morgan, 2007) performed an evaluation on more bone types considering the intrinsic variability in different biological tissues (2 specimens for each type).

Another open issue relates to the reliability of DVC in bones interdigitated with biomaterials as opposed to natural bones. In fact, vertebroplasty has become increasingly popular to treat and/or prevent osteoporotic vertebral fractures (Wilcox, 2004). Vertebroplasty requires the injection of bone cement inside the vertebral body, through a cannula. Due to the potential clinical implications in investigating augmented bone, the reliability of DVC on such composite structures must be investigated.

To the authors' knowledge, a systematic comparison of the output of two different DVC approaches (i.e. local and global), at the organ-level, on specimens including different materials such as an augmented vertebra, and including inter-specimen variability, is currently missing.

The aims of this work were therefore to compare the output of a local and a global DVC approach on a stationary test, and specifically:

- To quantify the reliability (in terms of systematic and random error) of DVC when applied to natural and augmented bones;
- To investigate the spatial distribution of the errors, and the presence of any preferential direction;
- To assess the variability between different specimens;

In order to achieve these aims, zero-strain tests were performed on porcine natural and augmented vertebrae.

8.2 Material and methods

8.2.1 Specimens and images

Ten thoracic vertebrae were collected from six fresh porcine spines, obtained from the alimentary chain. Soft tissues, intervertebral disks and growth plates were removed. A sample of five vertebrae was used for augmentation (hereafter referred to as “augmented”). Acrylic vertebroplasty cement (Mendec Spine, Tecres, Italy) was injected in the vertebral body with its proprietary device, until the cement started leaking (typically ~1 ml of cement). The cement contained BaSO₄ pellets (average size: 300 micrometers) to increase radiopacity. To facilitate cement injection and curing, the vertebrae were heated, before and after augmentation, in a circulating bath at 40°C (Ye et al., 2007). Another sample of five vertebrae was left untreated (hereafter referred to as “natural”). Sampling was arranged so that the augmented and natural samples were well distributed within the thoracic spine segment (T1-T4), in order to avoid potential effects related to morphology. The posterior processes were removed for both samples. To allow consistent alignment inside the micro-CT, the extremities of each vertebra were potted in poly-methyl-methacrylate (PMMA) with a dedicated positioning device (Danesi et al., 2014).

In order to evaluate the reliability of DVC approaches, each specimen was scanned twice without any repositioning, in a zero-strain condition, similarly to Palanca et al. (2015). Micro-CT (XTH225, Nikon Metrology, UK) scans had an isotropic voxel size of 39 micrometers, and were performed with the following settings: voltage 88kV; current 110-115 micro-A; exposure 2s; rotation step 0.23°; total rotation 360°. The specimens were placed in the environmental chamber of a loading device (CT5000, Deben Ltd, UK) and immersed in saline solution, in order to closely simulate *in situ* loading conditions.

Two volumes of interest (VOIs, Fig. 1) were cropped from each reconstructed 3D-image (MeVisLab, Me Vis Medical Solution AG, <http://www.mevislab.de/>):

- VOI-0 contained the whole vertebral body, including the thin cortical shell and the interface between the bone and the surrounding saline solution. VOI-0 was a parallelepiped circumscribing the contour of the vertebral body in the transversal plane, including 432 slices. This region was analyzed to study how the strain error changes through the vertebra, the vertebral body edge and the surrounding interface;
- VOI-1 was inside the vertebral body. VOI-1 was a parallelepiped inscribed inside the vertebra of 300x300x432 voxels (consistent for all specimens). VOI-0 was analyzed to quantify the error only inside the vertebrae.

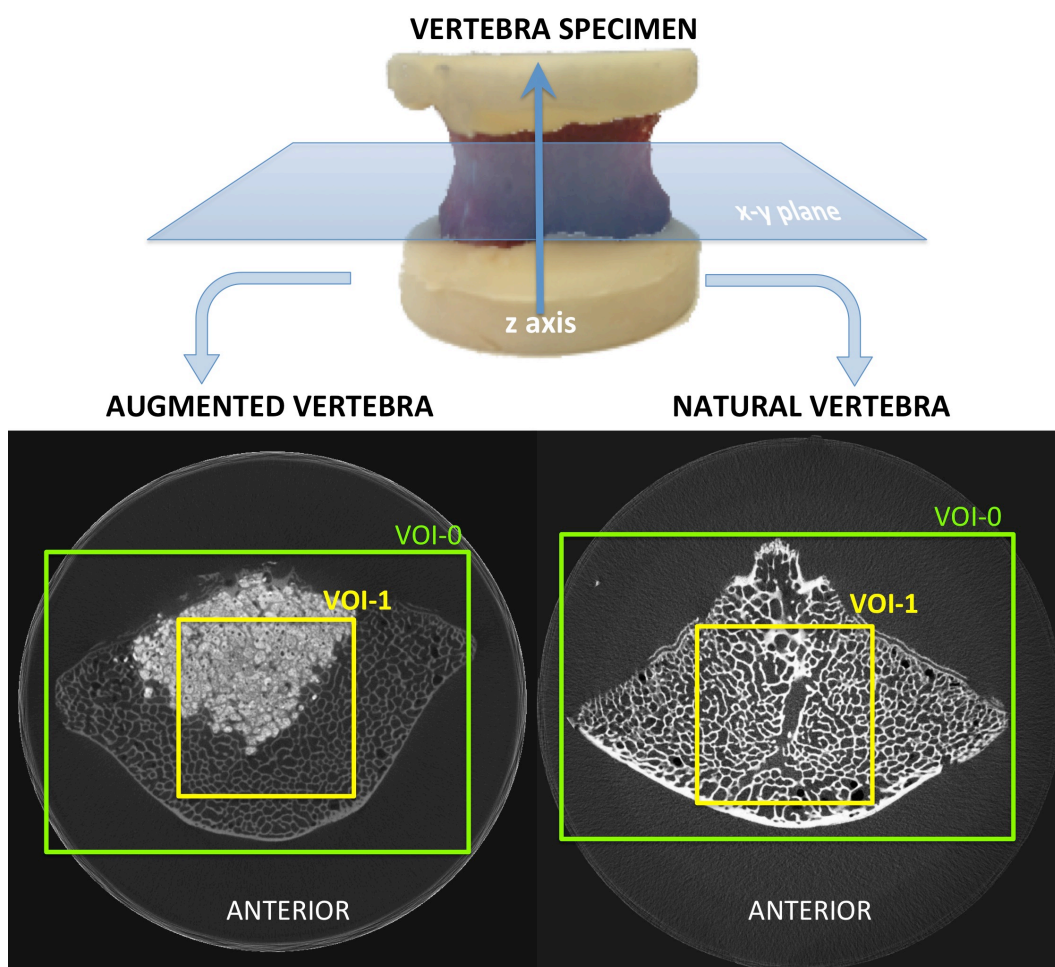


Fig. 1: The vertebra was aligned and potted in a PMMA support and then scanned with a micro-CT. In order to show the differences between VOIs, the slice at mid-height is reported for an augmented and a natural specimen. The larger box represents VOI-0: the entire vertebra with part of the surrounding saline solution. The smaller box represents VOI-1: a parallelepiped inscribed inside the vertebra.

In order to allow comparison between the results obtained from other DVC approaches, the image datasets used in the present study will be made available to the scientific community, at <https://dx.doi.org/10.6084/m9.figshare.4062351> or by contacting the Authors.

8.2.2 Local vs. global approach

Two DVC software packages, using either a local or a global approach, were compared in this work, similarly to (Palanca et al., 2015b). The local approach is implemented in a commercial package (DaVis 8.2.1, LaVision, Germany) later referred to as “DaVis-DC”. The global approach is a combination of a home-written elastic registration software ShIRT (Sheffield Image Registration Toolkit) (Barber and Hose, 2005; Barber et al., 2007; Khodabakhshi et al., 2013) and a Finite Element (FE) software package (Ansys v.14.0, ANSYS, Inc., Canonsburg, PA), later referred to as “ShIRT-FE” (Dall’Ara et al., 2014). The operating principles of the two DVC approaches were described in detail in (Palanca et al., 2015b). Briefly, DaVis-DC independently correlates sub-volumes from deformed

to undeformed state as a discrete function of grey-levels. The matching between the sub-volumes is done via direct correlation, which provided better results compared to FFT (Palanca et al., 2015b) for bone. A piece-wise linear shape function and a cross-correlation function are employed to quantify the similarity between the reference and deformed image. The displacement field is evaluated at the center of each sub-volume and the strain field is computed via centered finite differences. ShIRT-FE focuses on the recognition of identical features in the whole 3D images by superimposing a grid with selectable nodal spacing (sub-volume) to the images. ShIRT solves the elastic registration equations at the nodes of the grid to evaluate the displacement field. The grid is then converted into an eight-noded hexahedrons mesh and the displacements computed by ShIRT at each node are imposed as boundary conditions. The strain field is obtained using the FE solver to differentiate the displacement field obtained with ShIRT.

In order to compute the measurement errors, eight sub-volume sizes (from 16 to 128 voxels, in steps of 16 voxels) were investigated (Table 1). Moreover, a multipass scheme with final sub-volume size of 48 voxels (Table 2) was tested to explore the potentialities of the local approach. The multipass scheme is available only on DaVis-DC and is explained in (Palanca et al., 2015b). Based on the results reported in that study (Palanca et al., 2015b), 0% overlap was also used in the current study.

Table 1: Comparison of the correlated volume for the different approaches for both the augmented and the natural samples, and both VOIs, for each sub-volume size. The sub-volume was cubic in all cases, and its size is described by the side length, in voxels. The values reported for each sample are the median of the five augmented vertebrae and of the five natural vertebrae.

DaVis-DC is trying to maximize the coverage when sampling the VOI with the requested sub-volume size. In order to do that part of the boundary sub-volumes can be largely outside of the structure under investigation, which in turn causes lower correlation in those regions that can affect the overall correlated volume. For ShIRT-FE a grid is superimposed on the entire volume, and displacements and strains are computed on the nodes of the grid; so no regions are excluded.

VOI	SAMPLE	SUB-VOLUME SIZE (voxels)	DaVis-DC	ShIRT-FE
VOI-0	Augmented	16	100%	100%
		32	100%	
		48	100%	
		64	98%	
		80	99%	
		96	100%	
		112	97%	
		128	100%	
	Natural	16	100%	
		32	100%	
		48	100%	
		64	99%	
		80	98%	
		96	98%	
		112	94%	
		128	97%	

VOI	SAMPLE	SUB-VOLUME SIZE (voxels)	DaVis-DC	ShIRT-FE
VOI-1	Augmented	16	100%	100%
		32	100%	
		48	100%	
		64	94%	
		80	94%	
		96	97%	
		112	79%	
		128	100%	
	Natural	16	99%	
		32	100%	
		48	100%	
		64	94%	
		80	94%	
		96	97%	
112		80%		
128		100%		

Finally, to avoid misinterpretation of the results due to potential uncorrelated volumes, the percentage of correlated volume for each sub-volume size was computed as the ratio between the number of the correlated voxels and the total number of voxels (Table 1). The correlated volume is an essential indicator for the local approach, as the correlation of each sub-volume is independent from each other. For the global approach, instead, a grid is superimposed on the entire volume, and displacements and strains are computed on the nodes of the grid; so no regions are excluded.

8.2.3 Quantification of the errors (error metrics)

Given the zero-strain condition, any strain value different from zero was accounted as an error. The following analyses were carried out:

- *Errors by strain component:* for each specimen, the systematic and random errors were quantified as the average and standard deviation, for each component of strain. This analysis was repeated for VOI-0 and VOI-1 for the different sub-volume sizes.
- *Error distribution:* in order to identify the areas with larger errors, a qualitative analysis of the distribution of apparent strain (z-component) was performed on the cross-section of VOI-0, for both DVC approaches, both samples, for sub-volume size of 48 voxels (this sub-volume size was chosen as it corresponds to an acceptable lever of the error, see below).
- *Inter-specimen variability:* the systematic and random errors for each component of strain in VOI-1, for a sub-volume size of 48 voxels, were compared between specimens. In order to investigate potential relation between the magnitude of the error and the morphology of each specimen, the bone volume fraction (BV/TV: bone volume, divided by total volume) for the natural vertebrae, or the solid volume fraction (SV/TV: sum of volume of cement and of bone, divided by total volume) for the augmented vertebrae were computed. The images were segmented using a single threshold,

chosen in the valley between the first two peaks of the frequency distribution in the grey-scale (histograms). The threshold value was adapted by visual comparison of the segmented and grey-scale images, in order to separate bone (or bone and cement) from the background. Both BV/TV and SV/TV were calculated as ratio between the number of voxels in the solid volume divided by the total number of voxels (Rasband, W.S., ImageJ, U.S. National Institutes of Health, Bethesda, Maryland, USA, <http://imagej.nih.gov/ij/>, 1997-2015) (BoneJ plugin (Doubé et al., 2010)).

All the analyses were performed with a script in MatLab 2014a (MathWorks, US). Data were screened for outliers applying the criterion of Peirce (Ross, 2003).

8.3 Results

8.3.1 Errors over VOI-0

The systematic errors fluctuated around zero microstrain, apart from the peak for the smallest sub-volume size (Supplementary Materials). For small sub-volume sizes DaVis-DC had errors up to two orders of magnitude larger than ShIRT-FE; only with sub-volumes larger than 96 voxels the systematic errors were comparable (generally within 100 microstrain).

The random errors showed a clear decreasing trend towards larger sub-volume sizes (Supplementary Materials). The differences between DaVis-DC and ShIRT-FE were as high as two orders of magnitude, with maximum values of 126312 and 121281 microstrain, respectively, for augmented and natural sample with DaVis-DC and 2957 and 1124 microstrain, for augmented and natural sample, with ShIRT-FE. The multipass scheme on DaVis-DC (Table 2) was able to reduce both the systematic and random errors by up to a factor ten, with respect to those with the equivalent sub-volume (48 voxels). The errors on augmented vertebrae were consistently larger, up to 50%, than the ones on natural vertebrae.

Table 2: Series of steps implemented in the multipass approach, mp (48), without any overlap. This feature is available only on DaVis-DC.

STEP	SUB-VOLUME SIZE (voxels)	NUMBER OF ITERATIONS
1	128	1
2	112	2
3	96	2
4	80	2
5	64	2
6	48	2

The distribution of apparent strain within VOI-0 (Fig. 2) showed that the error increased passing from the trabecular tissue, rich of features, to the thin cortical bone, and finally to the surrounding saline solution. High gradients were localized at the interface between bone and saline solution, and in the regions

outside the vertebral body. A similar trend was observed with ShIRT-FE, but maximal errors were three orders of magnitude lower than for DaVis-DC.

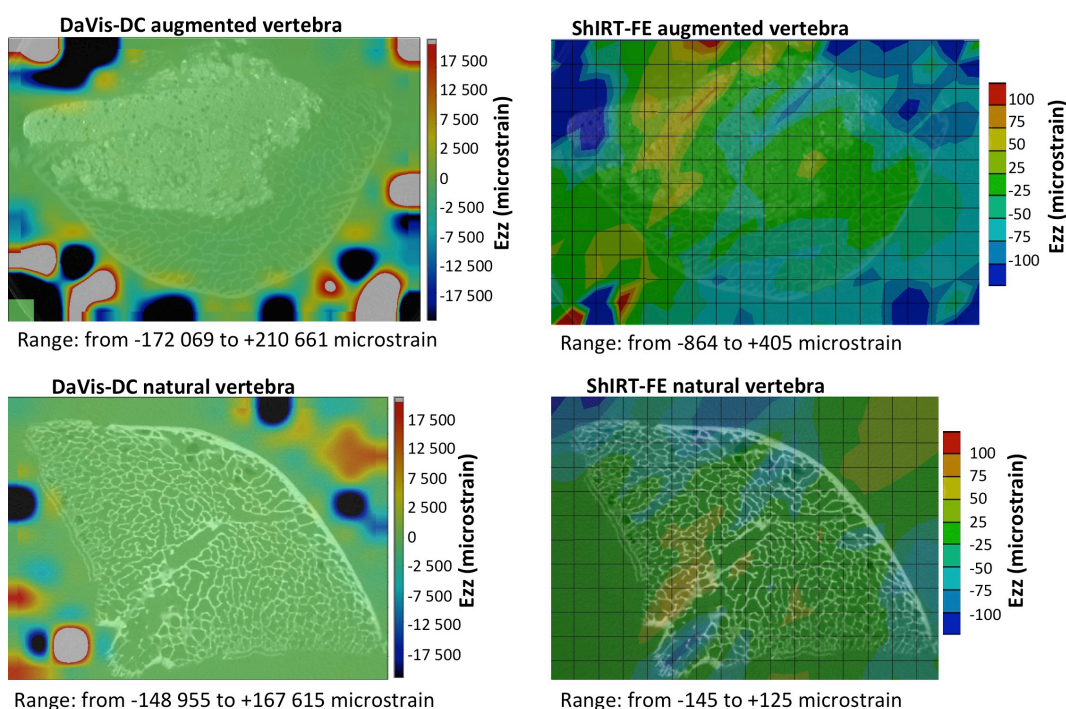


Fig. 2: Strain distribution in the z-direction with a sub-volume size of 48 voxels on a mid-height cross section of typical augmented and natural specimens, for, on the left the local approach (DaVis-DC) and, on the right, the global approach (ShIRT-FE). The scales on the right of each plot were selected to allow visualization of the strain distribution in the region of interest. The maximum ranges recorded are reported under each strain map.

8.3.2 Errors over VOI-1

The systematic and random errors were of the same order of magnitude for both DVC approaches and showed similar trends (Fig. 3 and 4).

DaVis-DC was affected by slightly larger (tens microstrains) systematic errors compared to ShIRT-FE. The effect of sub-volume size on the systematic error was negligible (Fig. 3).

As expected, the random error had a decreasing trend towards larger sub-volume sizes, for both DVC approaches (Fig. 4). The highest random errors for DaVis-DC (at 16 voxels) were in the range 960-1517 microstrain for the augmented vertebrae, and 807-1279 microstrain for the natural vertebrae. Random errors with DaVis-DC were generally lower than 200 microstrain with sub-volume size equal or larger than 48 voxels. The multipass scheme produced slightly reduced random errors in both samples augmented and natural vertebrae (from 69 to 103 microstrain for augmented vertebrae and from 43 to 69 microstrain for natural vertebrae) when compared to the same sub-volume size of 48 voxels without multipass (from 142 to 274 microstrain for augmented vertebrae and from 81 to 159 microstrain for natural vertebrae). For ShIRT-FE the highest random errors (at 16 voxels) were in the range 359-606 microstrain for the augmented vertebrae, and 445-1003 microstrain for the natural vertebrae. For larger sub-volumes random errors for ShIRT-FE were in most cases smaller than 200 microstrain. The two DVC approaches provided

comparable random errors for sub-volume size larger than 48 voxels, and were consistently lower than 200 microstrain above 64 voxels. While for DaVis-DC the random error steadily decreased for the range of sub-volumes explored, ShIRT-FE reached a plateau after 48 voxels. The random errors for the augmented vertebrae for DaVis-DC, were consistently higher, up to 50%, than the natural ones. For ShIRT-DC such differences between augmented and natural samples were smaller. No significant differences were found between the errors for the different components of strain, for any given sub-volume size, for both ShIRT-FE and DaVis-DC.

VOI-1

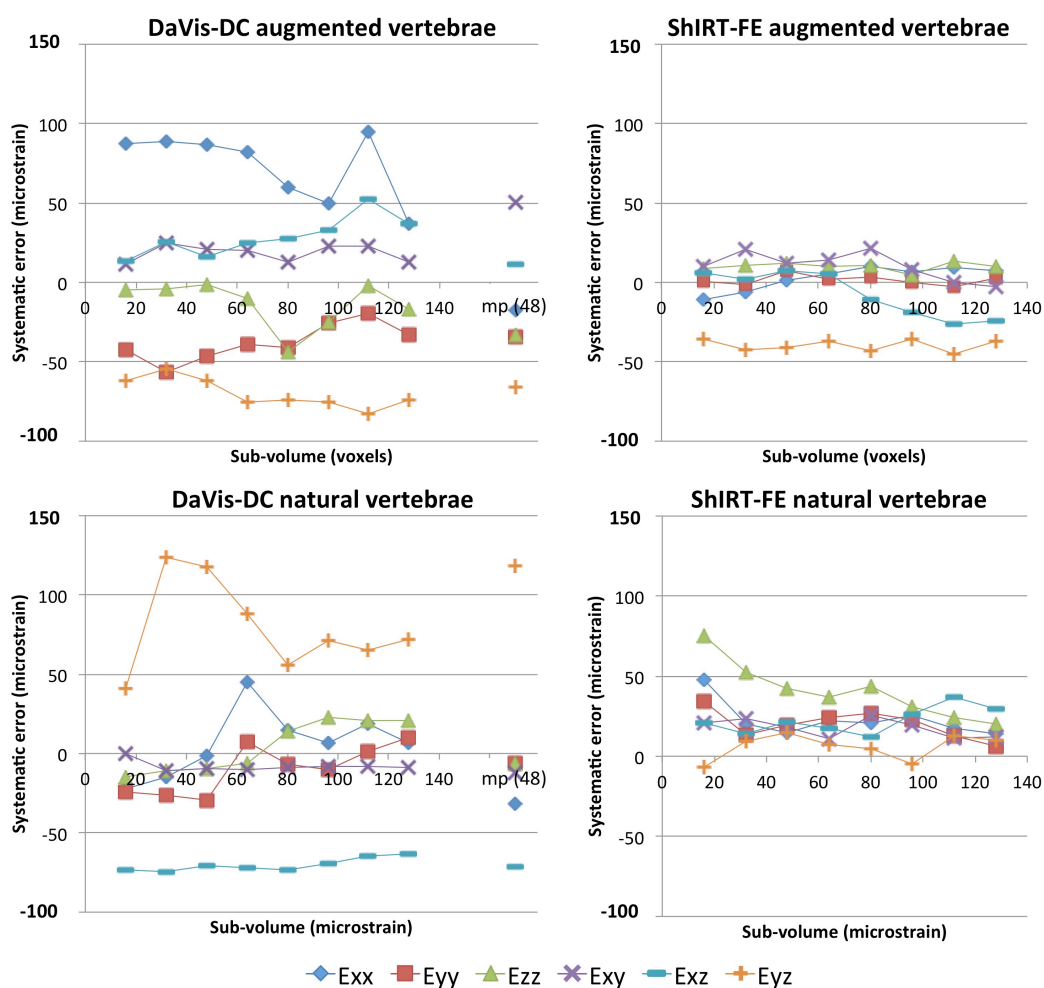


Fig. 3: Systematic errors for the local (DaVis-DC) and global (ShIRT-FE) DVC approaches, evaluated for VOI-1 in the augmented and natural vertebrae for sub-volume sizes ranging from 16 to 128 voxels. The multipass computation for DaVis-DC (mp (48); 6 passes from 128 to 48 voxels) is also reported. The median over the five augmented and five natural specimens is plotted.

Random errors showed large inter-specimen differences (Fig. 5), with maximum differences up to 2882 microstrain for DaVis-DC (augmented, Exz, specimen-1 vs. specimen-2) and up to 429 microstrain for ShIRT-FE (augmented, Exz, specimen-1 vs specimen-2). In particular, within the augmented sample,

considerably higher errors were found for specimen-1, with both DVC approaches. Similarly, specimen-3 (from a different donor) was associated with the largest error in the natural sample. The reason is not clear, as the error was not associated with the highest/lowest values of solid volume fraction, or bone volume fraction (Table 3). The Peirce's criterion identified these two specimens as outliers in terms of error values, but not in terms of volume fraction.

VOI-1

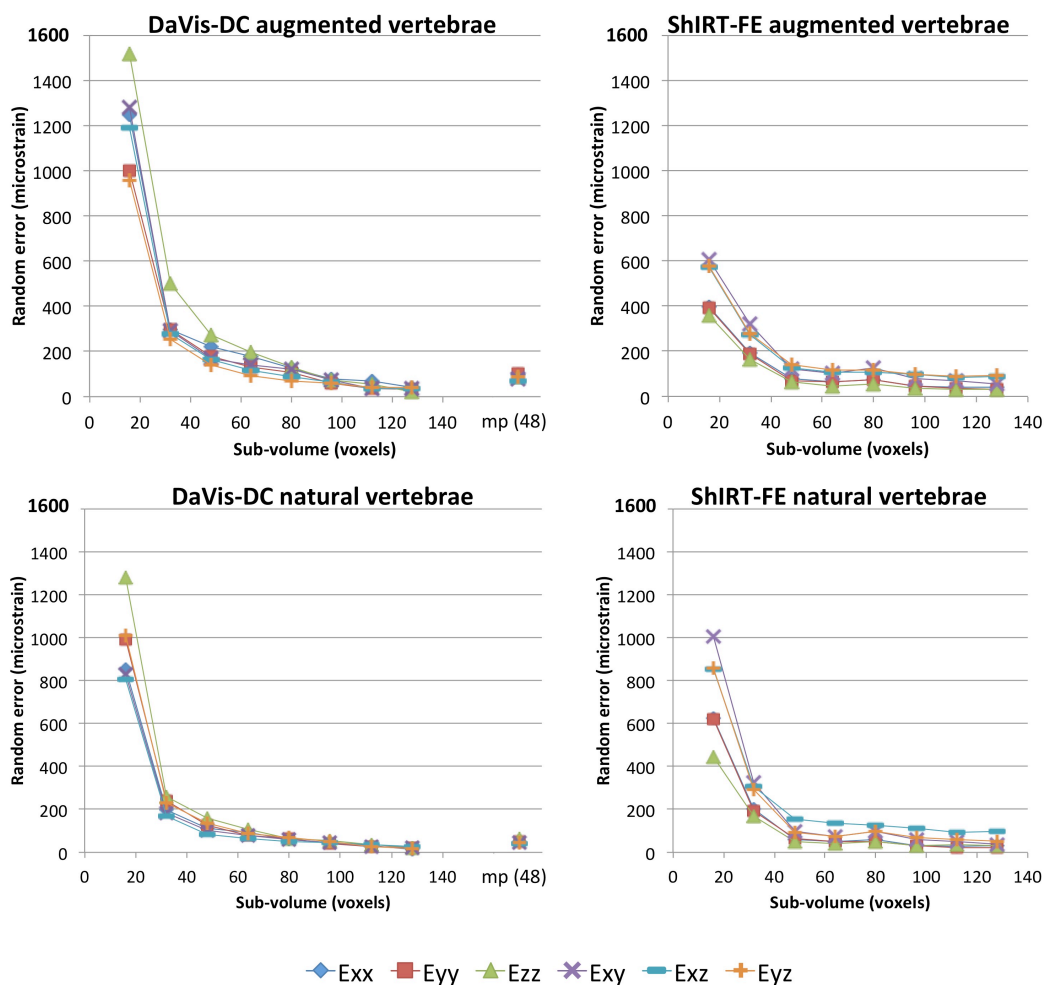


Fig. 4: Random errors for the local (DaVis-DC) and global (ShIRT-FE) DVC approaches, evaluated for VOI-1 in the augmented and natural vertebrae for sub-volume sizes ranging from 16 to 128 voxels. The multipass computation for DaVis-DC (mp (48); 6 passes from 128 to 48 voxels) is also reported. The median over the five augmented and five natural specimens is plotted.

Table 3: Solid Volume Fraction (SV/TV) evaluated as the ratio between the sum of the volume of the cement and the bone, and the total volume for the augmented vertebrae, and Bone Volume Fraction (BV/TV) evaluated as the ratio between the bone volume and the total volume for the natural vertebrae.

Augmented	SV/TV (%)
Specimen-1	44.4
Specimen-2	72.2
Specimen-3	50.1
Specimen-4	63.6
Specimen-5	57.1

Natural	BV/TV (%)
Specimen-1	29.5
Specimen-2	32.0
Specimen-3	29.0
Specimen-4	30.4
Specimen-5	27.7

8.4 Discussion

The aim of this work was to quantify the measurement uncertainties of different DVC approaches applied to augmented bones at the organ-level. More specifically, we intended to investigate how such uncertainties vary between specimens and if there is any anisotropy-related directionality in the measurement error.

Two DVC approaches were investigated: a local correlation algorithm (DaVis-DC) and a global strategy (ShiRT-FE). As no robust alternative reference method is available for measuring internal strains, repeated scans (zero-strain condition) of vertebrae were shared between our institutions in a sort of round-Robin test.

Our results showed that applying a local approach directly on images without masking (bone including the surrounding saline solution, VOI-0) yielded to large errors due to the lack of features provided by the saline solution. The analysis of the spatial distribution of the errors (Fig. 2) confirmed this hypothesis: the areas with large noise were mainly the outer boundaries of the bone and the saline solution; the areas where errors were substantially lower were all inside the specimen (which are typically the areas of interest). Therefore, average measurements over a volume including regions lacking features should be used with care if a local algorithm is applied. This effect could be an issue for specimens such as osteoporotic vertebrae, where fewer features are present compared to healthy denser vertebrae. Conversely, the global approach was almost insensitive to the surrounding saline solution. This suggests that a global approach may be more robust for strain measurements at the border of the specimen.

Inside the vertebra (VOI-1), the errors had the same order of magnitude for the local and global approaches. For both approaches, the systematic error (bias) fluctuated generally within 100 microstrain, meaning that the average of the strain components were close to zero, independently of the selected sub-volume size. Both approaches showed a decreasing trend of the random error towards larger sub-volumes. Results for sub-volumes of 48 voxels and larger were comparable for the two approaches.

The difference between augmented and natural samples was rather consistent, but small. This confirms the robustness of both DVC approaches on biomaterial interdigitation. This is confirmed in another tissue-level study (Tozzi et al., 2017). It must be noted that the present results were obtained with cement for vertebroplasty, which includes a radiopacifier (300 micrometers BaSO₄ pellets): this could have provided suitable features to the correlation algorithms. The multipass scheme available in DaVis-DC was able to reduce the random error (both natural and augmented) in both VOI-0 and VOI-1, when compared to the corresponding sub-volume of 48 voxels without multipass. Obviously, the effect of such scheme was less pronounced in VOI-1, where the errors were already much lower compared to the same sub-volume in VOI-0.

For both approaches and both natural and augmented vertebrae, the systematic and random errors did not show any correlation with the scan direction and/or specimen directionality: similar uncertainties values were found for all directions.

Some differences existed between specimens in absolute terms. To the authors' knowledge, inter-specimen variations and potential outliers have not been considered before at the organ level. In a sample of five specimens it is questionable to perform an outlier analysis (Ross, 2003). However, two specimens (Specimen-1 augmented, and Specimen-3 natural, Fig. 5) were clearly outliers for both DVC approaches.

Outliers were found both among the augmented (T4) and the natural (T2) vertebrae. The outliers did not come from the same animal. Other T4 and T2 vertebrae did not show large errors. All the scan sessions started in the morning, after a standard warm-up (as suggested by (Gillard et al., 2014)), and followed the same protocol. The outliers were not associated with any remarkable event from the log files and the lab diaries, nor with a specific day of the week.

The grey-scale distribution (over each slice of each vertebra and over the entire vertebra) of the outliers could be overlapped to those of the "regular" specimens. To understand if some scans contained higher noise, we analyzed the standard deviation of the grey-scale distribution in a parallelepiped (150x150x400 voxels) containing only saline solution: the standard deviation of all scans and all specimens were comparable (range: 221-946, 16-bit grey-scale count)

Despite all these checks, we could not identify a single event or parameter that could explain such outliers.

VOI-1

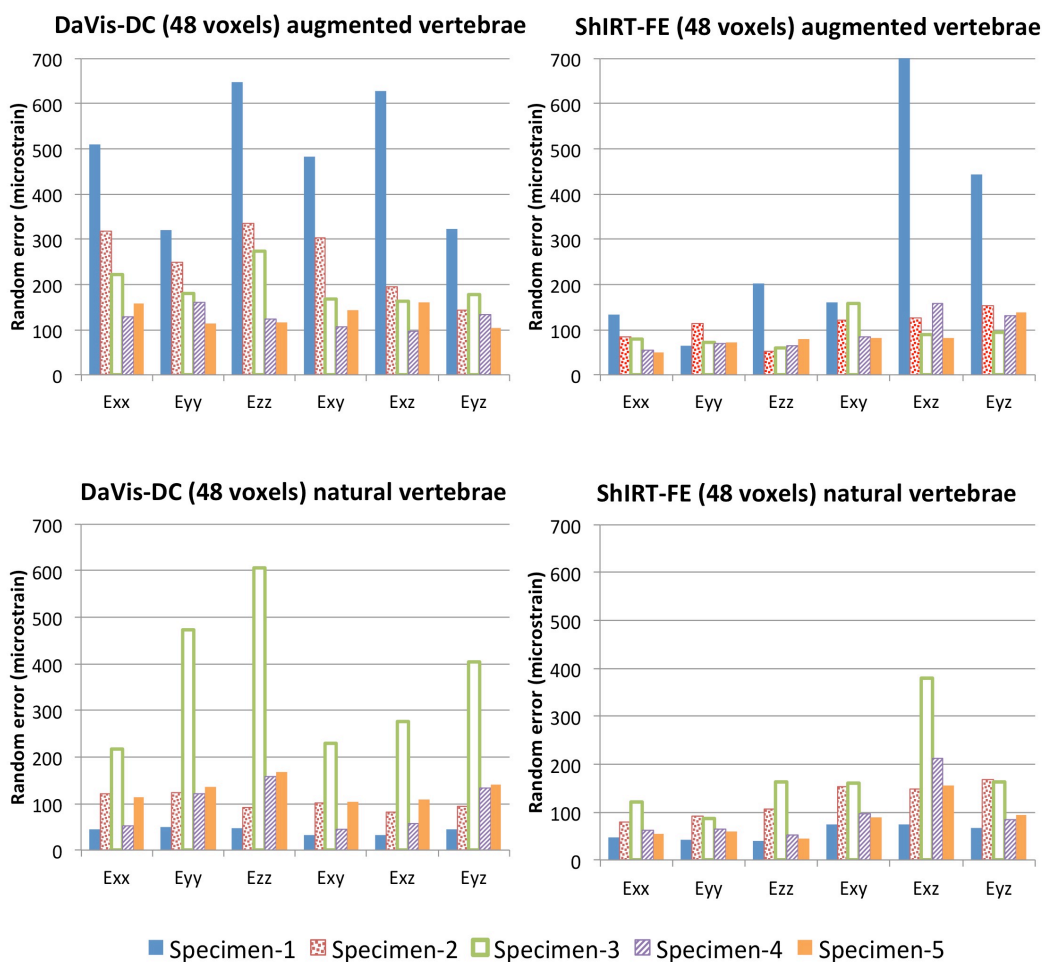


Fig. 5: Variability of the random error inside the augmented and natural vertebrae, for VOI-1, for a sub-volume size of 48 voxels. Similar trends were found for the systematic error.

This inter-specimen variability in the DVC uncertainties can be a warning for future studies, because a sequence of apparently high-quality images can unexpectedly result in large strain errors. Because of this variability, the authors recommend performing always a zero-strain test, before loading a specimen (repeated scan in the unloaded or preloaded condition). Unfortunately this kind of methodological analysis is frequently missing (Hardisty and Whyne, 2009). In case this approach would be inefficient for projects with large sample size, we suggest performing a zero-strain analysis on a reasonable number of specimens (e.g. five or more). A question left open with this work is whether some robust parameters exist and whether these are able to predict such errors.

A similar zero-strain study on human, bovine and rabbit trabecular bone was performed by (Liu and Morgan, 2007). They analyzed 4.3 mm cubes with a voxel size of 36 micrometers, and explored computation sub-volume of 20, 30, 40 and 50 voxels, with three DVC methods (based on home-written algorithm of digital particle image velocimetry and ultrasound elastography). In that paper a scalar indicator (which contains no information about the single strain components) was computed: the mean absolute error (MAER), referred to as accuracy, and the

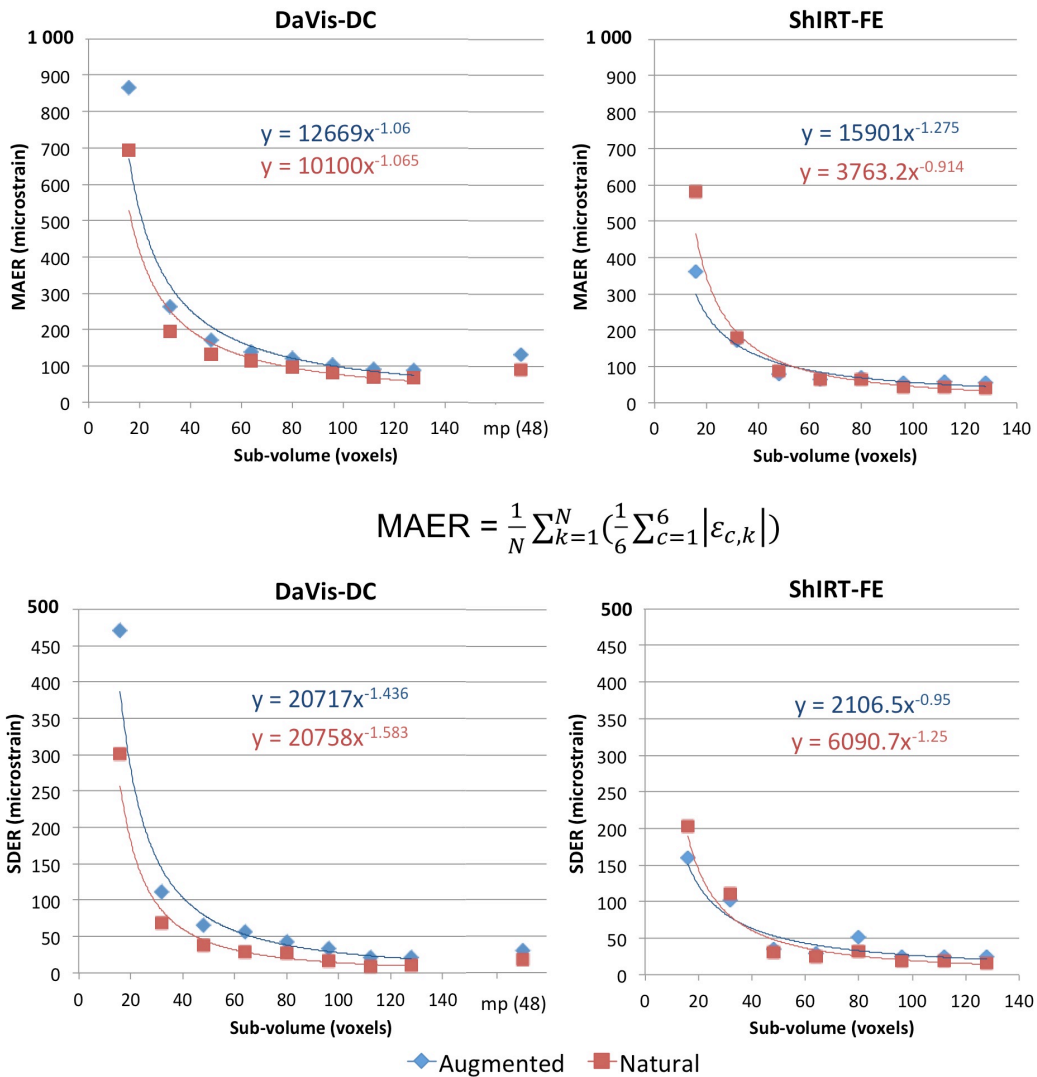
standard deviation of the error (SDER), referred to as precision, were quantified as average and standard deviation of the average of the absolute values of the six components of strain for each sub-volume. For the human vertebrae at 40 voxels sub-volume they found MAER in the order of 500 microstrain, and SDER of 150-200 microstrain. They found slightly lower errors for the bovine distal femur. The smallest total error they found was 345 microstrain. To allow comparisons, we computed the same scalar indicators for the augmented and natural sample for VOI-1 (Fig. 6).

In order to compare the results, interpolated power laws were used to estimate the MAER and SDER for the same sub-volume size of (Liu and Morgan, 2007). DaVis-DC showed a MAER of 275 and 215 microstrain for the augmented and natural vertebrae, respectively; ShIRT-FE had a MAER of 159 and 139 microstrain respectively. The SDER with DaVis-DC were 116 and 68 microstrain for the augmented and natural vertebrae; ShIRT had a SDER of 68 and 61 microstrain respectively. MAER and SDER of the present study confirmed the trend found in previous studies (Dall'Ara et al., 2014; Liu and Morgan, 2007; Palanca et al., 2015b).

An estimate of the measurement uncertainty was provided for human vertebrae in (Hussein et al., 2012). The voxel size (37 micrometers) was similar to the present work. They analyzed just a sub-volume of 4.8 mm (approximately 130 voxels). They found larger errors than in the present study: MAER=740 microstrain, SDER=630 microstrain. Their analysis was performed as a preliminary check before the actual compression test.

The current study has shown that, when sufficient care is dedicated to a preliminary methodological optimization, the strain measurement uncertainties of DVC may be not only adequate to investigate bone failure (7000-10000 microstrain (Bayraktar et al., 2004; de Bakker et al., 2009)), but also the strain distribution associated with physiological loads (strain of the order of 1000-2000 microstrain (Aamodt et al., 1997; Cristofolini, 2015)). The present findings suggest that for whole vertebrae DVC methods are sensitive enough for proper validation of the strain predictions from computational models only when sub-volumes equal or larger than 48 voxels (equivalent to approximately 2mm in side length) are used. However, in order to validate the strain at spatial resolutions of 10-30 micrometers, typical of micro-FE (Van Rietbergen et al., 1995), the measurement uncertainties of the current DVC approaches need to be reduced.

VOI-1



$$SDER = \sqrt{\frac{1}{N} \sum_{k=1}^N \left(\frac{1}{6} \sum_{c=1}^6 |\varepsilon_{c,k}| - MAER \right)^2}$$

Fig. 6: Accuracy and precision (with interpolated power laws) for the local (DaVis-DC) and global (ShIRT-FE) DVC approaches, evaluated for VOI-1 in the augmented and natural vertebrae for sub-volume sizes ranging from 16 to 128 voxels. The multipass computation for DaVis-DC (mp (48); 6 passes from 128 to 48 voxels) is also reported. The median over the five augmented and the five natural specimens is plotted. The plots report the MAER and SDER defined as in (Liu and Morgan, 2007), where “ ε ” is the strain; the subscript “c” identifies the strain components; the subscript “k” identifies the measurement points; N is the number of measurement points.

A limitation of this work is the use of porcine vertebrae instead of human ones. In this explorative study this decision was driven by an ethical choice. While the present results might not directly translate to human specimens in absolute terms, the trends and the general observations can certainly be applied. This study demonstrated the suitability of local and global DVC approaches to investigate natural and augmented bones. Systematic and random errors were rather isotropic, with no relation to bone anisotropy or micro-CT scanning

planes. While the errors were rather consistent between specimens, some specimens caused unpredictably and inexplicably larger errors: for this reason, it is highly recommended to perform a preliminary zero-strain check on each specimen.

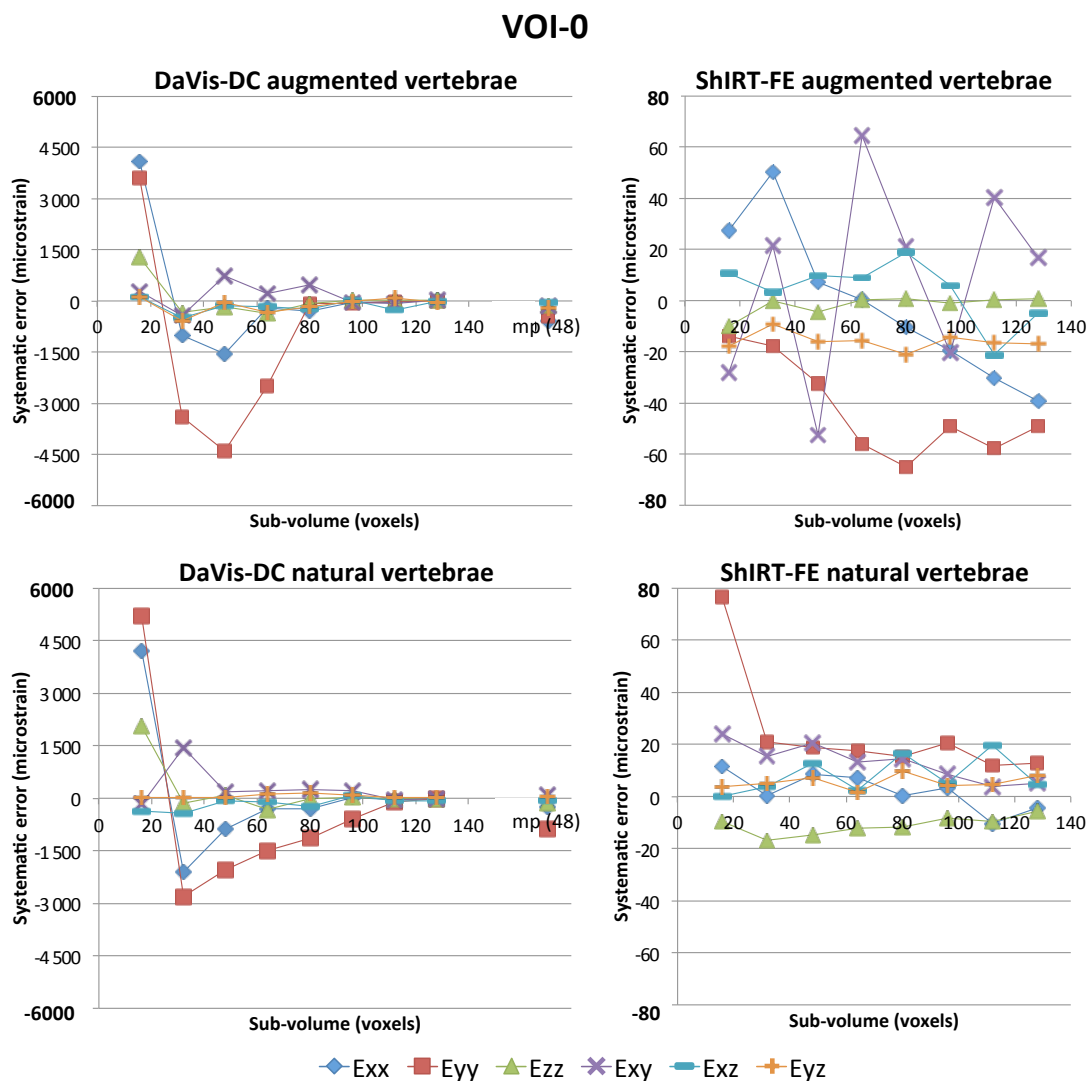
With the measurement uncertainties evaluated for a reasonable sub-volume size (i.e. 100-200 microstrain for sub-volume of 48 voxels), DVC becomes an attractive tool for the measurement of local properties (displacements and strains) in the elastic regime. This could be useful *per se*, to investigate bone micromechanics, but also to reliably validate computational models at the tissue level for spatial resolutions of approximately 2mm.

Acknowledgments

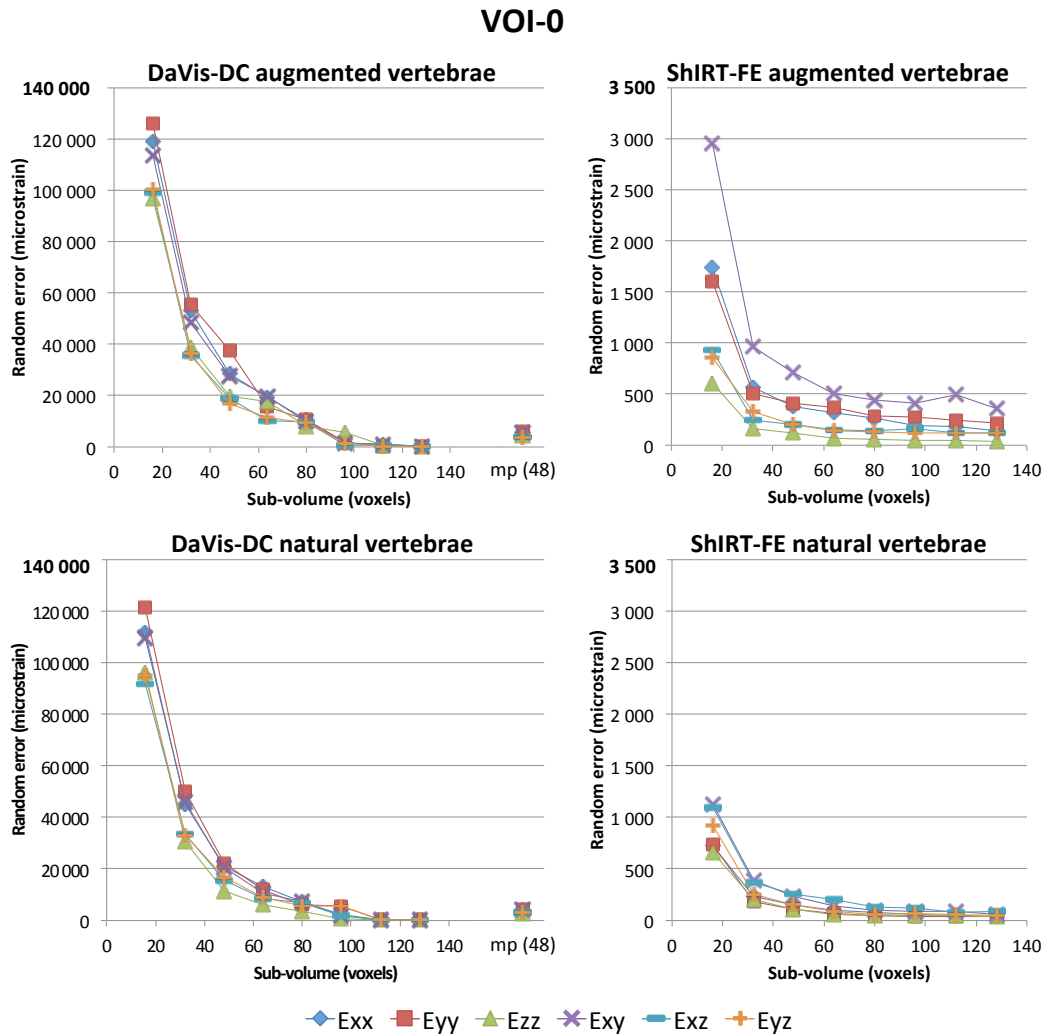
The authors wish to thank Remo Antelli for donating the porcine spines, Cinzia Viroli for the advice with the statistics, Renzo Soffiatti and Roberta Tosato (Tecres Spa, Sommacampagna, Italy) for the advice with the cement, Colin Lupton (University of Portsmouth) for technical support in micro-CT, Rod Hose and David Barber for sharing the ShIRT software. Funding was provided by Royal Society Research Grant (University of Portsmouth, Grant No. RG130831), EPSRC (University of Sheffield, project MultiSim, Grant No. EP/K03877X/1) and European Society of Biomechanics (Mobility Award 2014 to V. Danesi). The bone cement was donated by Tecres Spa (Italy).

SUPPLEMENTARY MATERIAL: STRAIN ERRORS IN VOI-0

Suppl. 1: Systematic errors for the local (DaVis-DC) and global (ShIRT-FE) DVC approaches evaluated for VOI-0 in the augmented and natural vertebrae, for sub-volume sizes ranging from 16 to 128 voxels. A multipass computation for DaVis-DC (mp(48); 6 passes, from 128 to 48 voxels) is also reported. The median over the five augmented and five natural specimens is plotted.



Suppl. 2: Random errors for the local (DaVis-DC) and global (ShIRT-FE) DVC approaches, evaluated for VOI-0 in the augmented and natural vertebrae, for sub-volume sizes ranging from 16 to 128 voxels. A multipass computation for DaVis-DC (mp(48); 6 passes, from 128 to 48 voxels) is also reported. The median over the five augmented and five natural specimens is plotted.



Chapter IX

Validation of Digital Volume Correlation at tissue level and organ level – synchrotronCT

from the manuscript:

Local displacement and strain uncertainties in different bone types by Digital Volume Correlation of synchrotron microtomograms

M. Palanca¹, A. J. Bodey², M. Glorgi³, M. Viceconti⁴, D. Lacroix⁴, L.
Cristofolini¹, E. Dall'Ara³

¹ School of Engineering and Architecture, Alma Mater Studiorum – Università
di Bologna, Bologna (IT)

² Diamond Light Source, Oxford (UK)

³ Department of Oncology and Metabolism and INSIGNEO Institute for in
Silico Medicine, University of Sheffield, Sheffield (UK)

⁴ Department of Mechanical Engineering and INSIGNEO Institute for in Silico
Medicine, University of Sheffield, Sheffield (UK)

Submitted to: *Journal of Biomechanics*

9.1 Introduction

Musculoskeletal pathologies, such as osteoporosis or bone metastasis, are associated with alterations of bone structures at different spatial scales. Assessment of bone quality (Bouxsein, 2003) and mineral density have become key to studying the effects of pathologies and related treatments at different bone hierarchical levels. Subject-specific computed tomography based finite element (FE) analyses have been used to estimate bone mechanical properties (Dall'Ara et al., 2013; Dall'Ara et al., 2012; Schileo et al., 2008a) and the effect of interventions (Keaveny et al., 2014; Zysset et al., 2015) *in vivo*. Combination of FE models and mathematical models of bone remodeling (Lerebours et al., 2015) can estimate bone changes over time. However, first we need to understand how well the structural FE models predict the local 3-dimensional strain field, which can be used to estimate the local cell activity on the bone structural units (Levchuk et al., 2014).

A possible way of validating the FE models at the tissue level is by using digital volume correlation (DVC) (Bay et al., 1999a). DVC is a full-field, contactless technique that provides both displacement and strain maps inside bone specimens via the comparison of 3D images acquired in, for example, the unloaded and loaded conditions (Grassi and Isaksson, 2015). DVC approaches based on 'laboratory source' micro-computed tomography (LS-microCT) can measure displacements in bones with sub-voxel accuracy and precision (ca. 1/10-1/20 of the effective voxel size) (Chen et al., 2016; Zauel et al., 2006). However, current LS-microCT-based DVC cannot measure strain in bone with enough precision to validate the model output within a bone structural unit (e.g. a trabecula or an osteon) (Dall'Ara et al., 2014; Roberts et al., 2014). To date, the typical measurement uncertainty enabled using DVC to discriminate the pre- or post-yielding conditions in vertebra bodies scanned with LS-microCT with a voxel size of approximately 35-40 micrometers (Danesi et al., 2016b; Hussein et al., 2012; Tozzi et al., 2016). In fact, as bone yields at a deformation of 7,000-10,000 microstrain (Bayraktar et al., 2004), a measurement uncertainty of approximately 700 microstrain could be acceptable for classifying regions starting to yield from those still in the elastic regime. After extensive optimization, DVC based on LS-microCT has reached acceptable accuracy and precision, on the order of 200 microstrain, but only if a strong compromise with measurement spatial resolution is accepted (measurements every 500-600 micrometers) (Dall'Ara et al., 2014; Palanca et al., 2015b). Unfortunately, due to the heterogeneity of bone tissue, DVC based on LS-microCT cannot be used to obtain accurate measurements of strain within the typical element size of microCT-based FE models (on the order of 10-20 micrometers).

In order to reduce the strain measurement errors of DVC we can try to improve the input images by, e.g., using synchrotron radiation microCT (SR-microCT). However, it is currently not clear if, and to what extent, better quality tomograms would improve the accuracy of DVC strain measurements. To the authors' knowledge, the only published study that characterized the accuracy of strains computed with DVC based on SR-microCT of bone focused on the crack propagation in murine femora (Christen et al., 2012). However, in that study the precision of the method was assessed only on virtually moved or stretched

images, which has been shown to underestimate the real error induced by image noise and artifacts (Dall'Ara et al., 2014). Therefore, the real potential of SR-microCT based DVC for bone applications is still partially unexplored as the potential benefits of using high-quality tomograms that allow resolving micro-features such as osteocyte lacunae are not yet known.

The aim of this study was to quantify the improvement that SR-microCT data could bring to global DVC for different bone tissues, by investigating the compromise between measurement spatial resolution and uncertainties.

9.2 Materials and Methods

9.2.1 Specimen preparation, tomography and image processing

In order to investigate the effect of microstructure on measurement errors, three different tissue types were used. The first sample consisted of four cortical bone cores obtained from the diaphysis of a fresh bovine femur (18 months old, killed for alimentary purposes). The second tissue type consisted of three trabecular bone cores obtained from the greater trochanter of the same femur. A diamond band saw (CP300, Exakt, Germany) was used to cut 12mm-high bone sections. Diamond core drills were used to extract cylindrical specimens (Fig.1a, b) (3mm in diameter for cortical bone; 8mm for trabecular bone). All machining was performed under constant water irrigation. The third sample consisted of four paired tibiae, which had been used in a previous study (Lu et al., 2015) (Fig.1c); these had been obtained from two 14-week old female C57BL/6J mice (Harlan Laboratories, Bicester, UK). The soft tissues around the tibiae were carefully removed with a scalpel. All specimens were dehydrated overnight at room temperature and then embedded in acrylic resin without bone infiltration.

Tomography was performed at the Diamond-Manchester Imaging Beamline I13-2 of Diamond Light Source, UK. A filtered (950 μ m C, 2mm Al, 20 μ m Ni) polychromatic 'pink' beam (5 to 35 keV) of parallel geometry was used with an undulator gap of 5mm. The propagation distance was approximately 10mm. Tomography data were acquired using a pco.edge 5.5 detector (PCO AG, Germany) coupled to a 750 μ m-thick CdWO₄ scintillator, with visual optics providing 4x total magnification. This led to an effective pixel size of 1.6 μ m and a field of view of 4.2x3.5mm. 4,001 projection images were collected at equally-spaced angles over 180° of continuous rotation, with an exposure time of 53ms. The total scanning time was approximately four minutes. The projection images were flat and dark corrected prior to reconstruction using the tomographic reconstruction module of Dawn v1.7 (Ashton et al., 2015; Basham et al., 2015), which incorporated ring artifact suppression (Titarenko et al., 2010). Samples were mounted such that their long axes corresponded to the rotation axis during data collection. Each specimen was scanned twice under zero-strain conditions and without any repositioning.

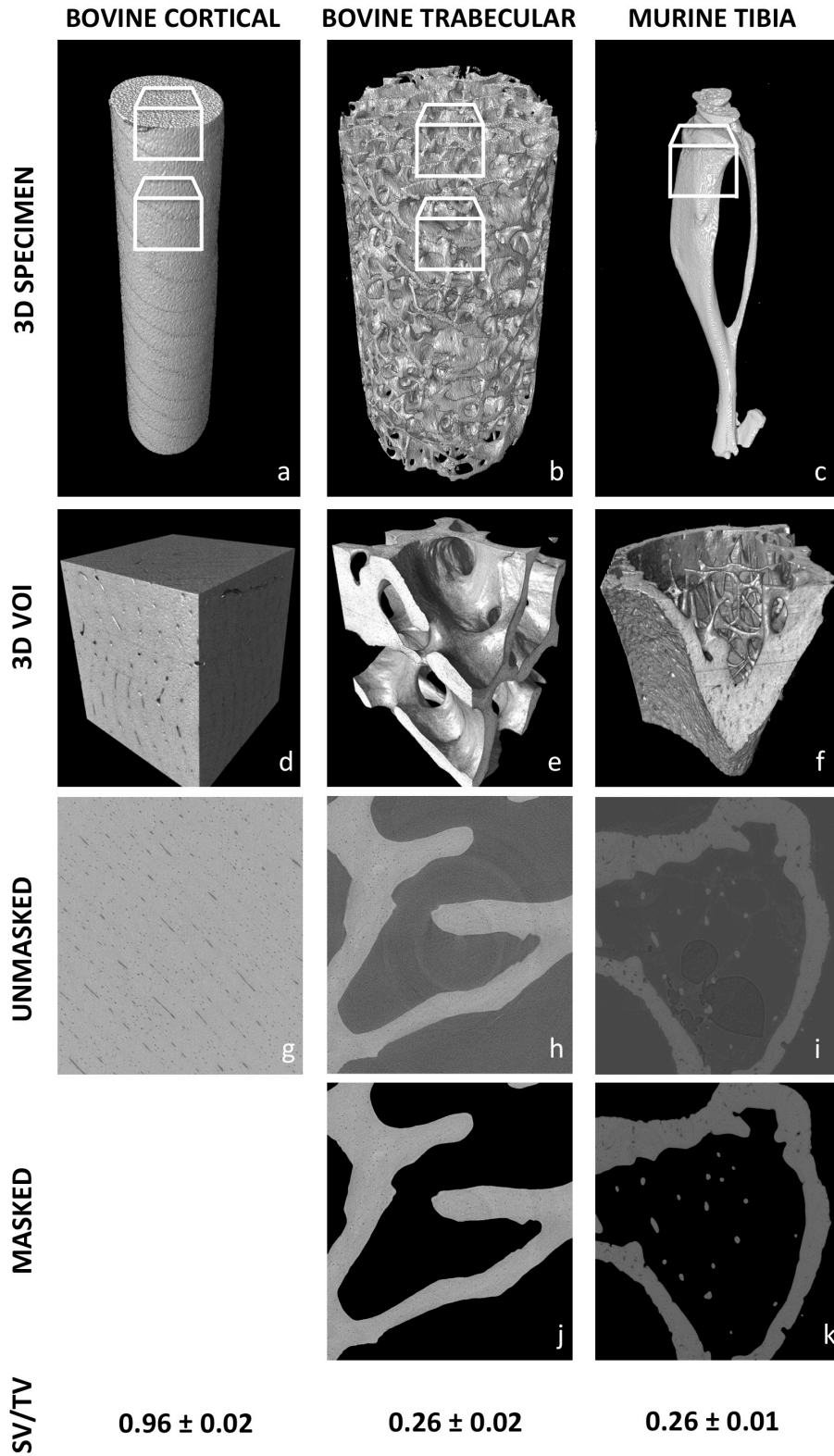


Fig.1: Typical specimen for each tissue type. From top to bottom: 3-dimensional (3D) representation of a typical specimen; 3D representation of typical VOI; 2-dimensional (2D) cross-section through the middle of each VOI; masked 2D cross-sections; solid volume fraction (SV/TV) values (median +/- standard deviation). The side length of each cross section is 1000 voxels, equivalent to 1600 micrometers.

Two cubic volumes of interest (VOIs), with side lengths of 1,000 voxels, were cropped from the middle of each cortical and trabecular specimen (Fig.1d, e, g, h) using ImageJ v1.49 (Rasband, W.S., ImageJ, NIH, Bethesda, Maryland, USA, <http://imagej.nih.gov/ij/>, 1997-2015). In order to include both trabecular and cortical bone, one cubic VOI (Fig.1f, i) was cropped from the proximal part of each murine tibia.

In order to evaluate the DVC errors only where bone tissue is present, masked images were created: after applying a Gaussian filter ($\sigma=4$) to reduce high-frequency noise, image segmentation was performed, followed by a single-level threshold in the valley between the first two peaks of the greyscale histogram. The threshold was adjusted visually by comparing the segmented and greyscale images. These binary images (0 for background, 1 for bone voxels) were then used also to mask the original bovine trabecular bone and murine tibia VOIs (Fig.1j, k).

For each VOI the solid volume fraction (solid volume / total volume, SV/TV), was determined as the ratio between the number of bone voxels and the total number of voxels in the VOI, using the ImageJ plug-in BoneJ (Doube et al., 2010). The potential benefit associated with SR-microCT could be due both to the signal-to-noise ratio and the voxel size. In order to evaluate the effect of the voxel size on the strain uncertainties, all original (not masked) VOIs were downsampled to a voxel size of 8 micrometers (by averaging the voxels grey-values) using ImageJ. With a similar approach, downsampled binary masks were created from the original masks for trabecular bone and murine tibiae and assigning 1 to any value greater than 0.

9.2.2 DVC protocol

The adopted DVC approach (ShIRT-FE) was a combination of a global deformable image registration algorithm (Sheffield Image Registration toolkit, ShIRT (Barber and Hose, 2005; Barber et al., 2007)) that computes the displacements maps, and a finite element (FE) software package for the calculation and visualization of the strains (Dall'Ara et al., 2014; Palanca et al., 2015b; Palanca et al., 2016b; Tozzi et al., 2017). Briefly, a grid with selectable nodal spacing (NS) was superimposed on the VOIs from pairs of repeated scans. ShIRT computes the displacements at the nodes of the grid by solving the registration equation (Barber and Hose, 2005; Barber et al., 2007). The grid is then converted into a linear hexahedral FE mesh, the computed displacements are assigned as boundary conditions (Fig.2), the models are solved linearly (ANSYS Mechanical APDL v. 15.0, Ansys, Inc., USA), and the six components of strain are computed at each node. As it has been demonstrated that nodal spacing (NS) affects uncertainties of the method (Dall'Ara et al., 2014), a series of NS values was used (from 10 to 300 voxels, equivalent to 16.0 to 480.0 micrometers) for every pair of repeated tomograms (Table1).

Table 1: List of investigated nodal spacing and nominal numbers of elements and nodes inside the VOI. Finer steps were used for lower NS (10, 15, 20, and 25) and coarser steps for higher NS values (50, 75, 100, 150, 200, 250, 300).

Nodal spacing (voxels)	Nodal spacing (micrometers)	Nominal number of elements inside VOI	Nominal number of nodes inside VOI
10	16.0	1 000 000	1 030 301
15	24.0	314 432	328 509
20	32.0	125 000	132 651
25	40.0	64 000	68 921
50	80.0	8 000	9 261
75	120.0	2 744	3 375
100	160.0	1 000	1 331
150	240.0	512	729
200	320.0	216	343
250	400.0	64	125
300	480.0	64	125

For the bovine trabecular bone and murine tibia samples, which showed lower SV/TV than the bovine cortical samples (approximately 96% for cortical bone versus approximately 26% for trabecular bone and murine tibia, Fig.1), two approaches were taken in order to investigate the effect of the inclusion of the marrow regions during the registration: either the whole VOI ('unmasked'), or only the parts of the VOI within the mask ('masked') were registered.

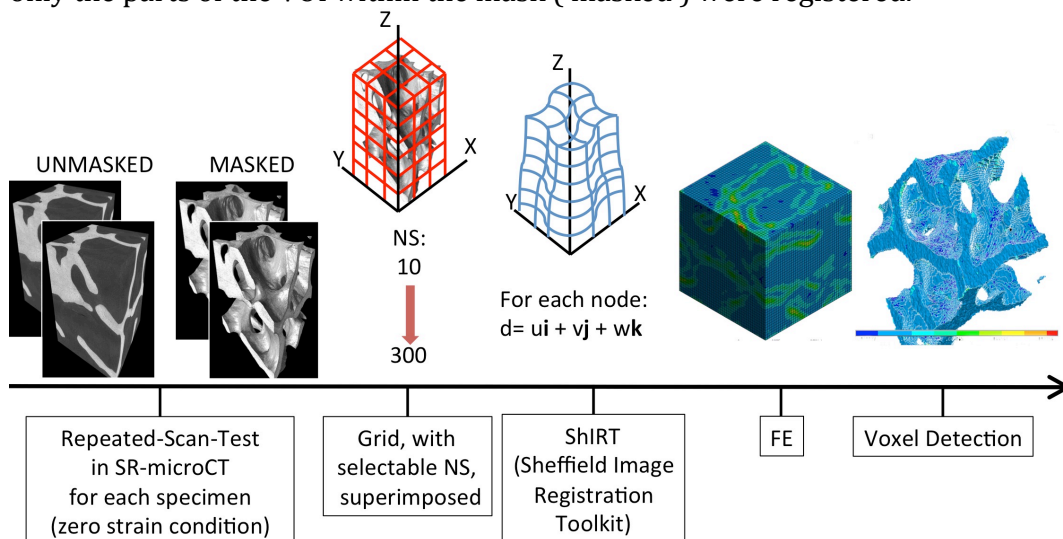


Fig. 2: Workflow of the registration procedure. Tomograms were obtained by scanning the specimens twice without any repositioning. From left to right: a grid of particular nodal spacing (NS, from 10 to 300 voxels) was superimposed on the cropped VOIs (unmasked or masked, in case of trabecular and murine tibiae); the displacements were evaluated at each node by ShIRT; the grid was converted to an FE mesh and computed displacements assigned as boundary conditions; the cells of the grid with all nodes outside the mask were ignored when evaluating measurement uncertainties.

In both cases (unmasked and masked) the cells of the mesh with all nodes outside the mask were ignored and the errors were averaged only in the remaining nodes (Fig.2), in order to account only for the errors within the bone tissue. The same protocol was applied also to the downsampled images using the downsampled masks.

9.2.3 Quantification of errors

The systematic error for the displacements could not be quantified, as the actual displacements were close to zero, but were affected by the inevitable unknown nano-movements of the moving parts of the scanner. To quantify the displacement random errors, their variability within each specimen was computed. Conversely, as the test was based on a zero-strain condition, any non-zero values of strain were considered as error, and both precision and accuracy could be estimated. Hence, the following parameters were computed for each registration:

- Random error for the displacement: standard deviation (SD) of each component of displacement, as in (Benoit et al., 2009; Madi et al., 2013; Palanca et al., 2015b; Roux et al., 2008);
- Mean absolute error (MAER): average of the average of the absolute values of the six components of strain in each node, referred as “accuracy” in (Liu and Morgan, 2007);
- Standard deviation of error (SDER): SD of the average of the absolute values of the six components of strain in each node, referred as “precision” in (Liu and Morgan, 2007);
- Systematic error for each component of strain: average of the respective component of strain on the evaluated nodes, as in (Gillard et al., 2014; Palanca et al., 2016b);
- Random error for each component of strain: SD of the respective component of strain on the evaluated nodes, as in (Gillard et al., 2014; Palanca et al., 2016b);

The median and standard deviation were computed within each sample for such errors.

Finally, a qualitative error distribution in the middle cross section of a generic VOI for each typical bone microstructure for the normal strain along the z-axis (axis of the scan revolution) was inspected.

9.3 Results

9.3.1 Random error for displacements

The random errors of each component of the displacement, obtained using the registration based on the unmasked images never exceeded 0.139 voxels (0.226 micrometers; for trabecular bone with a NS of 10, Table2). The maximal random errors, obtained at NS equal to 10, were smallest for the bovine cortical sample (below 0.054 voxels for z-direction, 0.088 micrometers), followed by the ones for the murine tibia sample (below 0.080 voxels for x-direction, 0.130 micrometers),

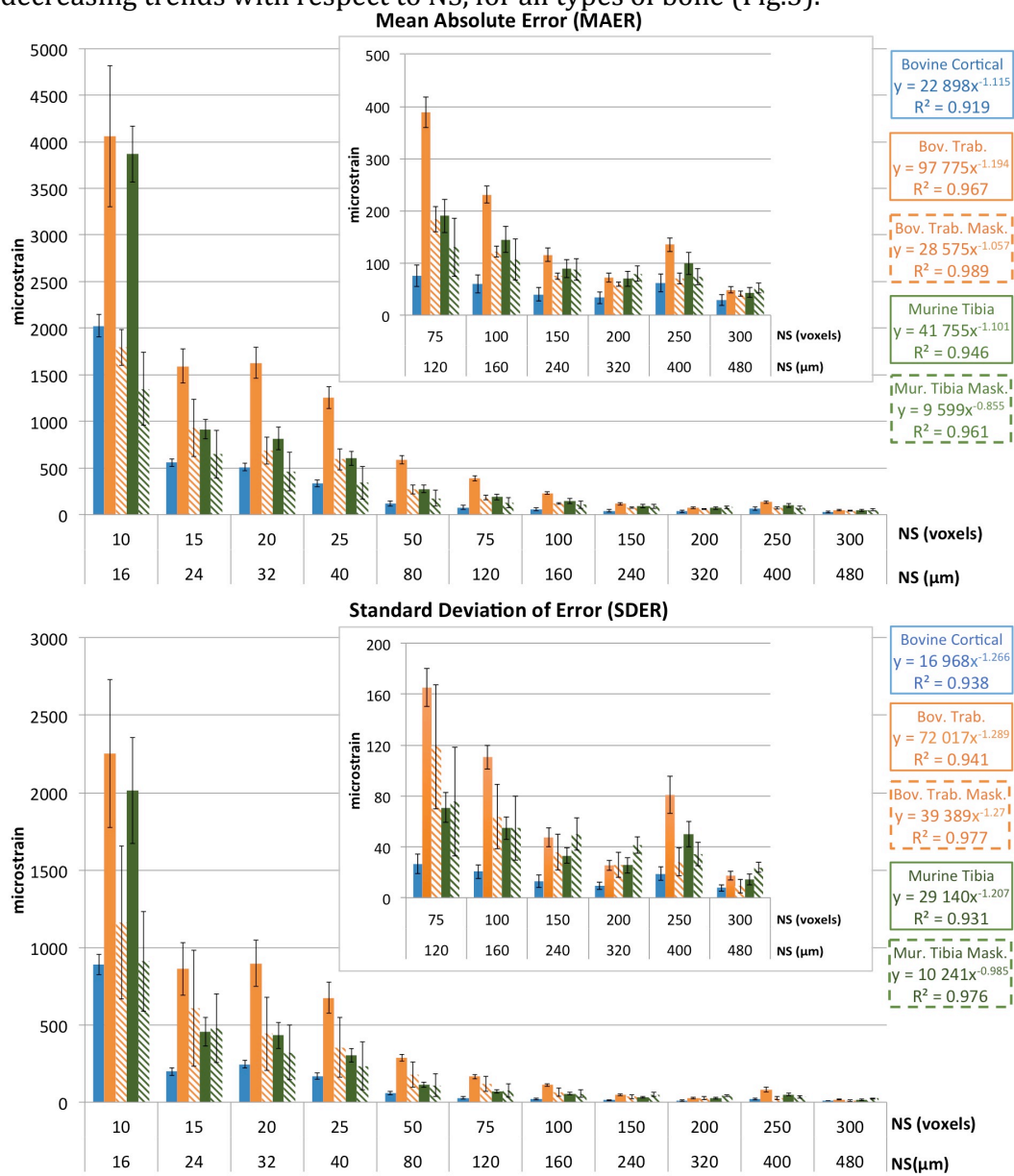
Table 2: Random errors for the components of displacement (micrometers) for each bone type.

NS	DISPLACEMENT RANDOM ERRORS (micrometers)														
	BOVINE CORTICAL			BOVINE TRABECULAR UNMASKED			BOVINE TRABECULAR MASKED			MURINE TIBIA UNMASKED			MURINE TIBIA MASKED		
	X	Y	Z	X	Y	Z	X	Y	Z	X	Y	Z	X	Y	Z
10	0.073	0.072	0.088	0.171	0.176	0.226	0.108	0.101	0.152	0.130	0.118	0.118	0.103	0.087	0.084
15	0.053	0.049	0.069	0.143	0.143	0.192	0.095	0.092	0.133	0.093	0.078	0.079	0.099	0.081	0.078
20	0.051	0.046	0.067	0.139	0.141	0.201	0.090	0.083	0.128	0.089	0.074	0.081	0.094	0.077	0.072
25	0.047	0.041	0.061	0.123	0.125	0.186	0.086	0.077	0.116	0.085	0.072	0.078	0.092	0.076	0.070
50	0.039	0.033	0.058	0.087	0.091	0.156	0.068	0.064	0.102	0.074	0.061	0.066	0.085	0.071	0.059
75	0.036	0.032	0.061	0.075	0.081	0.144	0.056	0.057	0.098	0.070	0.057	0.061	0.083	0.069	0.052
100	0.033	0.027	0.055	0.056	0.062	0.114	0.043	0.051	0.086	0.067	0.054	0.053	0.082	0.068	0.049
150	0.031	0.029	0.060	0.047	0.053	0.096	0.037	0.045	0.079	0.062	0.051	0.045	0.075	0.071	0.047
200	0.029	0.025	0.055	0.038	0.041	0.084	0.031	0.042	0.076	0.057	0.050	0.041	0.076	0.071	0.045
250	0.034	0.038	0.068	0.050	0.056	0.103	0.037	0.042	0.062	0.055	0.043	0.057	0.068	0.065	0.040
300	0.024	0.026	0.053	0.030	0.030	0.061	0.027	0.034	0.056	0.049	0.039	0.033	0.065	0.063	0.038

and largest for the ones computed for bovine trabecular sample (below 0.139 voxels for z-direction, 0.226 micrometers). The errors obtained for the displacements using the masked images were lower than those for the unmasked images for both bovine trabecular bone and murine tibia samples (Table2). A trend could be observed for all bone types: the higher the NS, the lower the random error. No preferential direction was observed.

9.3.2 Accuracy and precision: average of components

As expected from the results reported in previous studies on bone (Benoit et al., 2009; Dall'Ara et al., 2014; Palanca et al., 2016b) and on polypropylene-foam (Roux et al., 2008), the uncertainties of the DVC approach (MAER and SDER) had decreasing trends with respect to NS, for all types of bone (Fig.3).



■ Bovine Cortical ■ Bovine Trabecular ▨ Bovine Trabecular Masked ■ Murine Tibia ▨ Murine Tibia Masked
 Fig. 3: MAER (top) and SDER (bottom) for each bone type (bovine cortical bone in blue, bovine trabecular bone in orange and murine tibia in green), for unmasked and masked images (solid

and striped bars, respectively) as a function of the nodal spacing NS. Bars represent the median values, while error bars represent the standard deviation. On the right, the power laws and the coefficients of determination (R^2) are reported.

For a given NS, the values of MAER were larger than SDER.

The ranges (for NS of 16.0 to 480.0 micrometers) of the medians for MAER and SDER for bovine cortical bone sample were between 29-2,026 microstrain and between 8-890 microstrain, respectively. Errors for this bone type were lower than those obtained for the other types of bone (from registration based on masked or unmasked images). For bovine trabecular bone the MAER ranged between 49-4,058 microstrain and 41-1,795 microstrain for unmasked and masked images, respectively. For murine tibiae the MAER ranged between 43-3,868 microstrain and 51-1,394 microstrain for unmasked and masked images, respectively. Lower SDER was found for the bovine trabecular bone (between 17-2,253 microstrain and 9-1,162 microstrain for unmasked and masked images) and for the murine tibia sample (between 14-2,012 microstrain and 24-909 microstrain for unmasked and masked images).

Downsampling the images increased the median errors for all bone types for both MAER (113-11,971 microstrain for cortical bone, 265-14,650 microstrain for trabecular bone and 86-7,011 microstrain for murine tibiae) and SDER (36-4,790 microstrain for cortical bone, 124-8,985 microstrain for trabecular bone and 19-4,165 microstrain for murine tibiae). The power laws for MAER and SDER showed similar trends but different amplitude for native resolution, downsampled images and LS-microCT images of similar samples (Dall'Ara et al., 2014) (Fig.4).

9.3.3 Systematic errors for each component of strain

The systematic errors were independent from NS, for all bone types and for both registrations based on unmasked or masked images (see supplementary material). Only weak reductions of the systematic errors for the normal components have been observed for mouse tibiae for both unmasked and masked images. The medians of the systematic errors for the bovine cortical bone sample ranged between -43 and 80 microstrain, and were lower than those of the other two bone types (between -55 and 124 microstrain and between -133 and 88 microstrain for bovine trabecular bone with unmasked and masked images, respectively; between -17 and 197 microstrain and between -6 and 209 microstrain for murine tibiae using unmasked and masked images, respectively). In most cases no systematic preferential direction was observed. Larger errors were found for normal components in the mouse tibiae. The downsampled images confirmed the independence of the systematic errors from the NS, but showed higher values errors (between -74 and 264 microstrain for the bovine cortical bone, between -207 and 590 for the bovine trabecular bone, and between -12 and 219 for the murine tibiae).

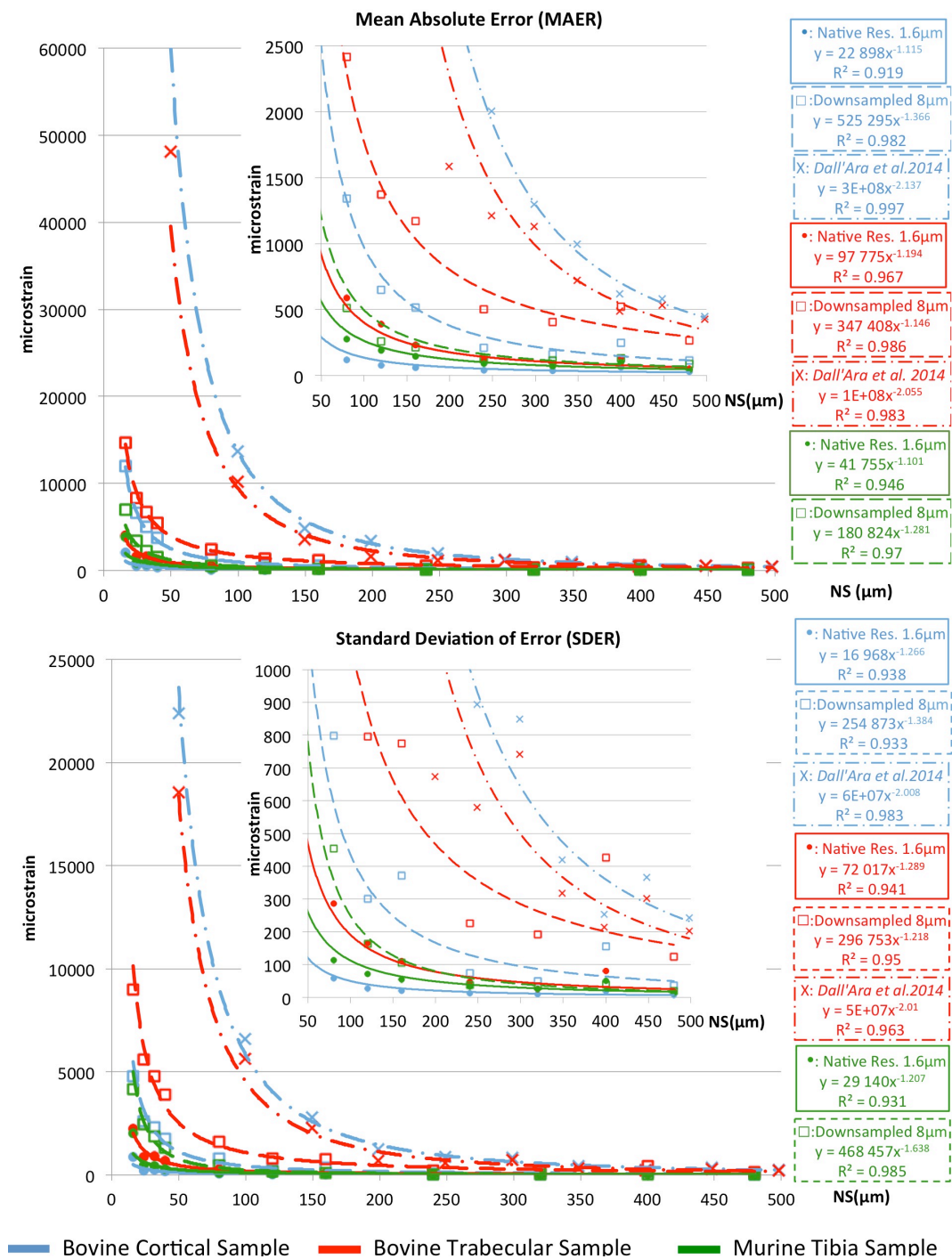


Fig. 4: Power laws computed for MAER (top) and SDER (bottom) for each bone type (bovine cortical bone in blue, bovine trabecular bone in orange and murine tibia in green), for native SR-microCT images (solid lines), downsampled SR-microCT images (dashed lines) and LS-microCT images from Dall'Ara et al. (2014) (dash-dot lines). On the right, the power laws and the coefficients of determination (R^2) are reported.

9.3.4 Random errors for each component of strain

For all registrations, increasing the NS reduced the random error for each component of strain (Fig.5).

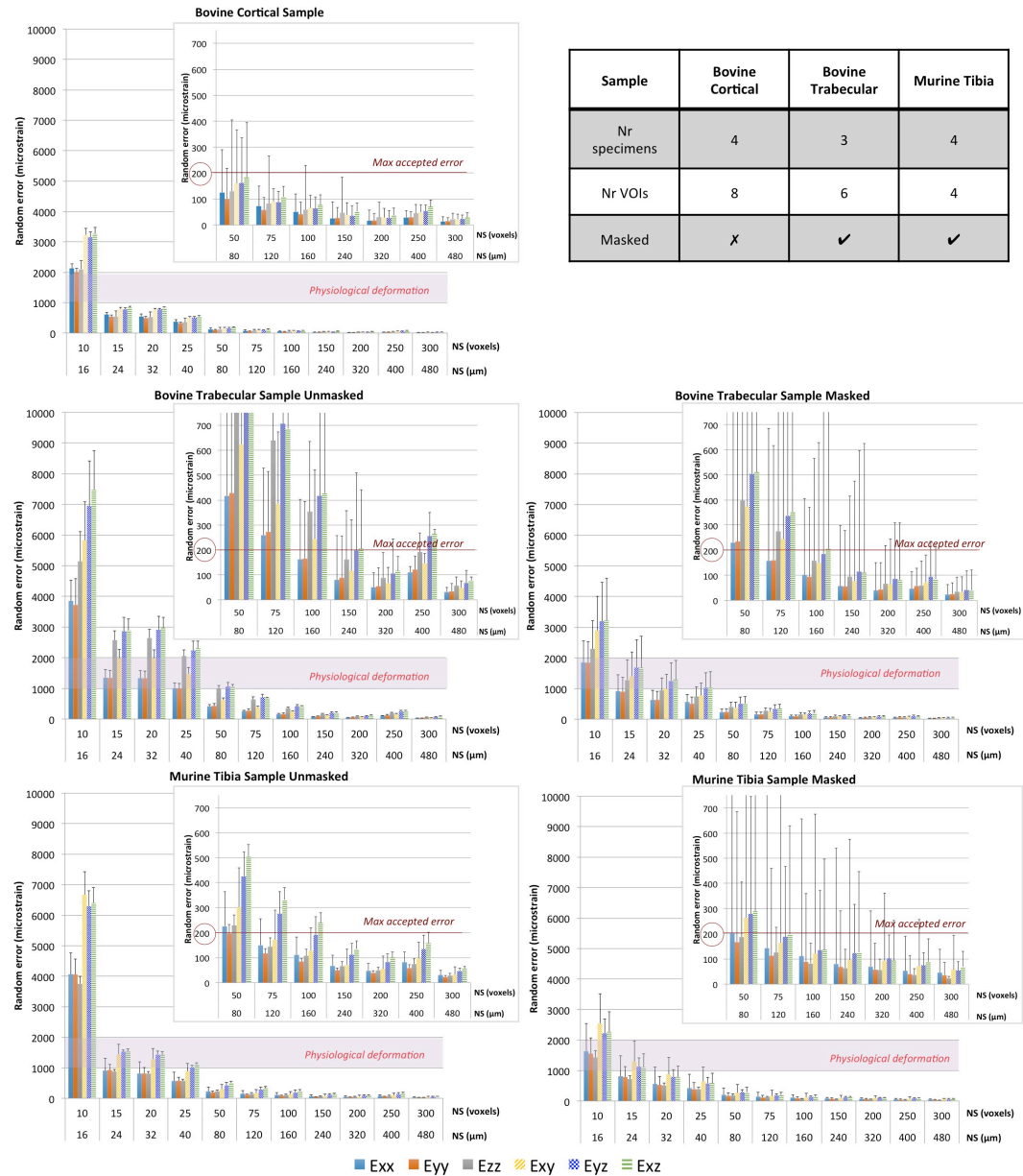


Fig. 5: Median of the random error for each bone type (cortical bone on the top, trabecular bone in the middle and murine tibiae on the bottom), for each registration methods (from unmasked images on the left, from masked images on the right), for each component of strain, as a function of NS. To improve the readability, error bars representing standard deviations were reported only on the top of each histogram. To help interpreting the results, a range for the typical physiological deformations (1000-2000 microstrain (Yang et al., 2011)) is indicated. For the scope of this study, also the target value for the measurement error is indicated (one order of magnitude lower: 200 microstrain).

As observed for the displacement, bovine cortical bone showed the lowest random errors, with medians ranging between 14-3,271 microstrain. Bovine

trabecular bone was associated to random errors of 32-7,480 and 23-3,228 microstrain using unmasked images, and masked images, respectively. The murine tibiae showed errors of 23-6,669 and 23-2,543 microstrain using unmasked and masked images, respectively. Random errors were largest for the shear strains in all cases (approximately 1.5 times higher than for the normal strain). The same trend was observed for the downsampled images. Here, the murine tibiae had the lowest random errors (57-12,051 microstrain). The bovine cortical bone had errors between 77-18,810 microstrain and the bovine trabecular bone between 249-25,185 microstrain.

9.3.5 Strain distribution of the errors

The distribution of the apparent normal strain along the z-direction varied between bone types, and even more pronouncedly with the NS (Fig.6). Having applied the DVC to repeated images of the same undeformed specimens (zero-strain condition), this strain represents the error distribution within each bone structure.

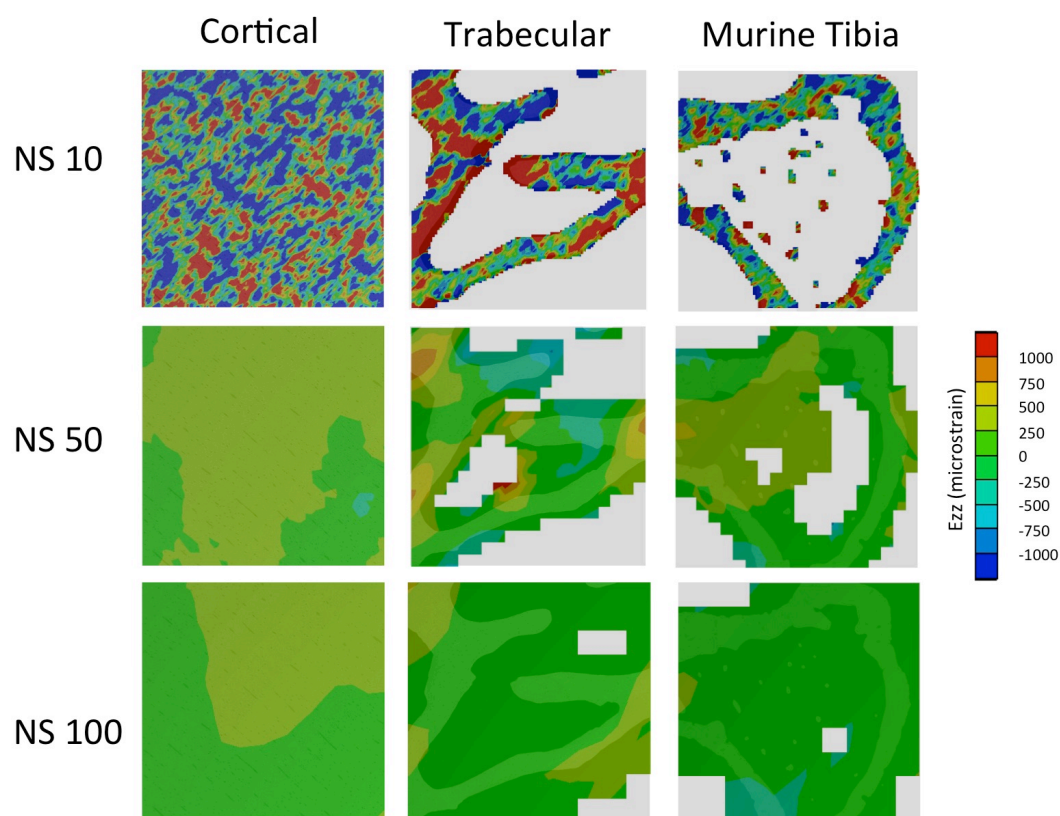


Fig. 6: Distribution of z-direction normal strain shown for a mid-height cross-section for a typical specimen of each bone type for three nodal spacing (10, 50, 100). For trabecular bone and murine tibiae the masked images were used for this analyses. As the DVC was applied to repeated images of the same undeformed specimens, the reported strain represents in fact the DVC measurement uncertainties. The cross-section image of the corresponding slice was overlapped to the strain error map. For every microstructure, the side length of the image is 1600 micrometers.

For bovine cortical bone, a reasonably uniform strain distribution was obtained with NS equal to 50 and 100 voxels (80 and 160 micrometers). Conversely, for

the bovine trabecular bone and murine tibiae, the bone surface and those regions with limited number of features within the volume (e.g. central portion of the murine tibia) showed larger strain errors. It must be noted that for trabecular bone with NS equal to 50 voxels (80 micrometers) the peak errors were in most cases in regions outside the bone or close to the border of the image.

9.4 Discussion

The potential of DVC for bone applications is still partially unexplored, as this approach has not been yet applied intensively to high-quality images. In this study measurement uncertainties of a SR-microCT based DVC approach were evaluated for the first time for three different types of bone by using Repeated-Scan-Tests (Palanca et al., 2015b).

In line with previous studies performed on LS-microCT images (Dall'Ara et al., 2014; Palanca et al., 2015b; Palanca et al., 2016b; Tozzi et al., 2017), also for DVC based on SR-microCT, the larger the NS the lower the measurement uncertainties. This trend is probably due to the fact that even for higher image quality, the displacement errors were only modestly affected by the NS (e.g. for NS 10 and 100 voxels, the random error was reduced by a factor 2 if the NS was increased by a factor 10, Table1), which lead to increased strain errors for smallest distance between the nodes of the grid.

For the bovine trabecular bone, registrations based on masked images showed lower errors compared to the ones obtained by registering unmasked images. This finding highlights how the exclusion of low-contrast marrow regions, for which noise and artifacts probably dominate the registration, is beneficial for DVC. Conversely for murine tibiae the SDERs computed with unmasked or masked images were similar for NSs larger than 10 voxels (16 micrometers). This different effect of the masking could be due to differences in size and shape of the bone features that form the two microstructures.

This study explored the relationships between spatial resolution of the DVC strain measurements and the associated error for the different bone types. Not surprisingly, the trend of the DVC uncertainties followed a power law for all bone types, confirming what was previously found for LS-microCT based bone specimens (Dall'Ara et al., 2014; Roberts et al., 2014) or for polypropylene-foam specimens (Roux et al., 2008). For NSs of 40 micrometers or larger, the SDER for the cortical bone images were lower than 200 microstrain, acceptable error when investigating deformations in the physiological range. For registrations using the masked images, median SDER lower than 200 microstrain were found for NS larger than 80 micrometers for the murine tibiae, or larger than 120 micrometers for the bovine trabecular bone. Larger NSs were required to reduce the error associated to each component of strain below 200 microstrain (80 micrometers for the cortical bone, 160 micrometers for masked trabecular bone, and 120 micrometers for masked murine tibiae). These values are acceptable for measurements performed on bone structural units, and suggest that the SR-microCT based DVC can be used to validate computational models that aim to

predict local strains at the tissue level (Chen et al., 2016; Eswaran et al., 2007; Van Rietbergen et al., 1995; Verhulp et al., 2006).

In the present study the errors were vastly lower than those obtained processing traditional LS-microCT (voxel size of ~ 10 micrometers) images (Dall'Ara et al., 2014) of similar specimens from the same femur processed in this study, using the same DVC approach on Repeated-Scan-Tests. In that study, SDER below 200 microstrain were achieved only for NS above 472 micrometers for trabecular bone, and 536 micrometers for cortical bone. The present study proved that the DVC uncertainties could be reduced, improving the measurement spatial resolution almost fourteen times for cortical bone and almost four times for trabecular bone. This difference could be due to the superimposition of two effects in the SR-microCT images: the smaller effective voxel size and the higher signal-to-noise ratio. When the downsampled images were analyzed, SDER of 200 microstrain were achieved with a measurement spatial resolution of 176 micrometers for the cortical bone (five times coarser than the 34 micrometers needed for the original images), and of 402 micrometers for the trabecular bone (four times coarser than the 97 of the original images). These analyses showed that a finer voxel size can explain only partially the lower SDER of the DVC with SR-microCT. Such measurement spatial resolutions were still better than those required to obtain the same SDER with LS-microCT (Dall'Ara et al., 2014). The larger improvement for cortical bone is likely due to the much higher number of features (i.e. the osteocyte lacunae around the vascular pores) resolvable with SR-microCT images for such microstructure compared to LS-microCT images. However, as comparisons were made between SR-microCT and LS-microCT images of similar (but not identical) specimens, further investigations could help to better clarify the sources of errors.

To the authors' knowledge, this is the first study where the displacement and strain errors of a global DVC approach based on SR-microCT images were evaluated with Repeated-Scan-Tests for different types of bone specimens. Another study used synchrotron images on a DVC approach and performed a preliminary evaluation of the error (Christen et al., 2012) on virtually moved and stretched images of murine femur. That DVC approach, based on demons deformable registration algorithm, was applied to SR-microCT images (voxel size of 740 nanometers) with a NS of approximately 30 micrometers and provided SDER of approximately 1,800 microstrain, more than four times larger than that found for masked murine tibiae in this study. This difference might be due to differences in microstructure, tomographic resolution and registration method. However, considering that in that study the SDER was computed on virtually moved images that do not include the effect of image noise, the method proposed in this study is by far the one with the highest precision (lowest SDER) reported in the literature to date for analyses on bone specimens. It remains to be investigated if other DVC approaches would achieve similar (or better) precision if based on the same images used in the present study.

Despite the high potential of SR-microCT based DVC, bone damage induced by X-ray synchrotron irradiation is apparently the major limitation for its application in time-lapsed *in situ* mechanical tests (Barth et al., 2010). Previous authors have attempted to mechanically test bone samples within a synchrotron facility (Christen et al., 2012; Thurner et al., 2006) but reported that the irradiation and/or associated heat affected the local material properties of the tissue (Barth

et al., 2010). In order to apply this DVC approach to SR-microCT *in situ* mechanically tested and imaged bone samples further scanning optimization (Pacureanu et al., 2012) and analysis to reduce this problem by, for example, reducing exposure times, suppressing lower X-ray frequencies or submerging samples in aqueous buffer, would form the basis of a useful methodological study.

The main limitation of this study is that the measurement uncertainties were investigated only in a homogeneous zero-strain case. It would be interesting to further study the evolution of errors within strained specimens, especially where the gradients of strains are highest. Moreover, the error associated to the strain and displacement measurements was evaluated for a global DVC approach and remaining to be investigated if similar trends would be found for local DVC algorithms (Palanca et al., 2015b). While similar trends can be expected also for local DVC approaches (Leclerc et al., 2012; Palanca et al., 2015b) researchers are welcome to contact the corresponding author who will share the data used in this study for comparing different methods.

9.5 Conclusion

The uncertainties associated with a global DVC approach applied to Synchrotron tomograms with small voxel size are sufficiently low to allow reliable strain measurements at the tissue-level in different bone structures. This method can be used to evaluate local bone deformations under loading, and to validate the strain predicted by computational models at the tissue-level.

Chapter X

Conclusions

In this PhD project a full-field analysis was applied on spine segments to explore their biomechanics. Displacement and strain measurements were reported on the surface and inside the spine segment using full-field and contactless measurement tools: the Digital Image Correlation and the Digital Volume Correlation.

The first part of the research, regarding the surface measurements, started with a deep review of the literature of the Digital Image Correlation applications in the biomechanical field. An analysis and discussion of a series of work at different dimensional scales and on a wide range of biological specimens allowed highlighting the pros (full-field measurement, for small and large deformation, not invasive, usable in vivo) and cons (problem related to precision, requirement of a careful optimization, not real time) of this novel measurement tool.

The know-how acquired in the literature was moved and applied for a preliminary study on biological specimen (vertebra). Through a careful validation and optimization of the Digital Image Correlation, the systematic and random errors on the surface of a human vertebra were reduced, compared with the initial situation, respectively up to 10 microstrain and 110 microstrain. These results were potentially useful for the exploration of the strain associated to physiological loads (around 1000 – 2000 microstrain).

The next step was to expand this preliminary study to spine segments, in order to define a new way to study the spine, in addition to the well-known measurement of the range of motion and stiffness. This goal was reached on porcine spines, tested in two different loading configurations (anterior bending and lateral bending), acquiring two different points of view.

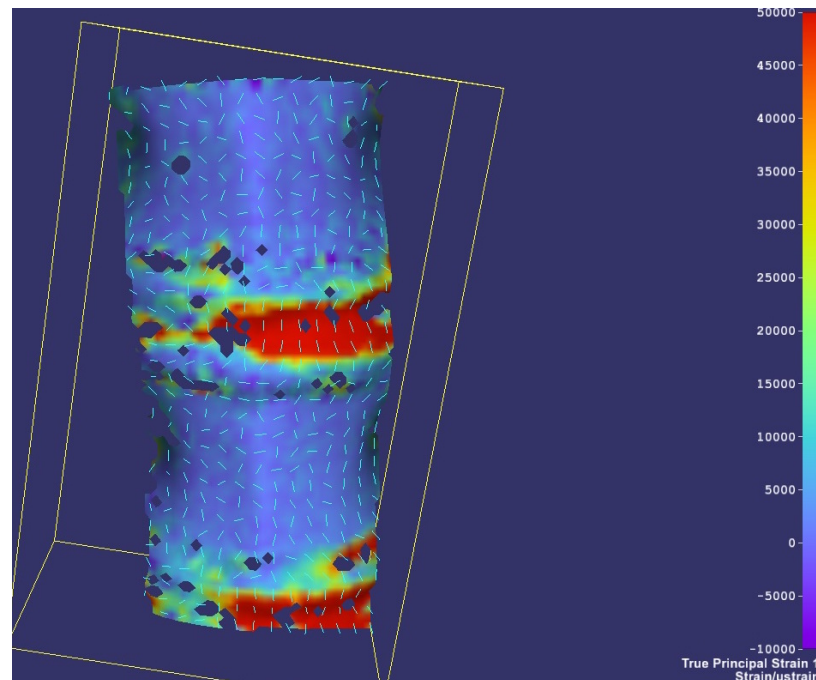


Fig. 1: Maximum principal strain ($\mu\epsilon$) evaluated on the surface of a spine segments loaded in lateral bending.

The preparation of a suitable speckle pattern, the validation and optimization of the Digital Image Correlation allowed evaluating the strain maps in all tested conditions without substantial loss of correlation and limiting the entities of the errors to acceptable level (systematic error of ten microstrain, random error around hundred microstrain). The strains on the intervertebral discs and on vertebrae were evaluated simultaneously in a full-field and contactless way. The high gradients, showed the need of exploring the spine in a full-field way (Fig. 1). This application of Digital Image Correlation to spine segments can open the way to a new approach both to basic, and translational research.

A similar approach was used in the second part of this research, focused on the measurements inside the specimen.

The Digital Volume Correlation is an emerging measurement tools in the field of biomechanics; before starting to work on it, a validation study was mandatory. But the validation can be performed only partially, because no other measurement techniques provided comparable measurements. In fact, the review of the works that focused assessing the measurement uncertainties of Digital Volume Correlation showed a wide range of results, and the lack of a benchmark, to standardize the performance of the algorithms.

Different, simplified and *a priori* known situations (zero-strain tests, virtually moved test, virtually stretched test) were reproduced to ensure the reliability of the tool; but a complete validation was still not developed.

The effects of the single inputs:

- Bone specimens (organ level: cortical and trabecular bones, tissue level: natural vertebrae, augmented vertebrae);
- Imaging source (laboratory source microCT, synchrotron radiation microCT);
- Algorithms (local and global approach);
- Computational parameters (subvolume size, overlap, multipass, etc);

were analyzed performing a quantitative validation and optimization of the DVC for biomechanical applications and using a wide factorial design.

For each combination of these parameters, the measurement uncertainties were computed. Moreover, in order to provide benchmark materials to test and compare DVC approaches, the inputs images were publically shared.

The imaging source, especially the combinations of signal-to-noise ratio and spatial resolution, and the computational parameters have the larger impact on the reduction of the measurement uncertainties. Conversely, the tissue types and the used algorithms minimally influence the final results (Fig. 2).

In conclusion of this analysis was showed that when sufficient care is dedicated to preliminary methodological work, the overall error could be reduced and potentially acceptable to explore strain failure and strain associated to physiological loads (< 200 microstrain).

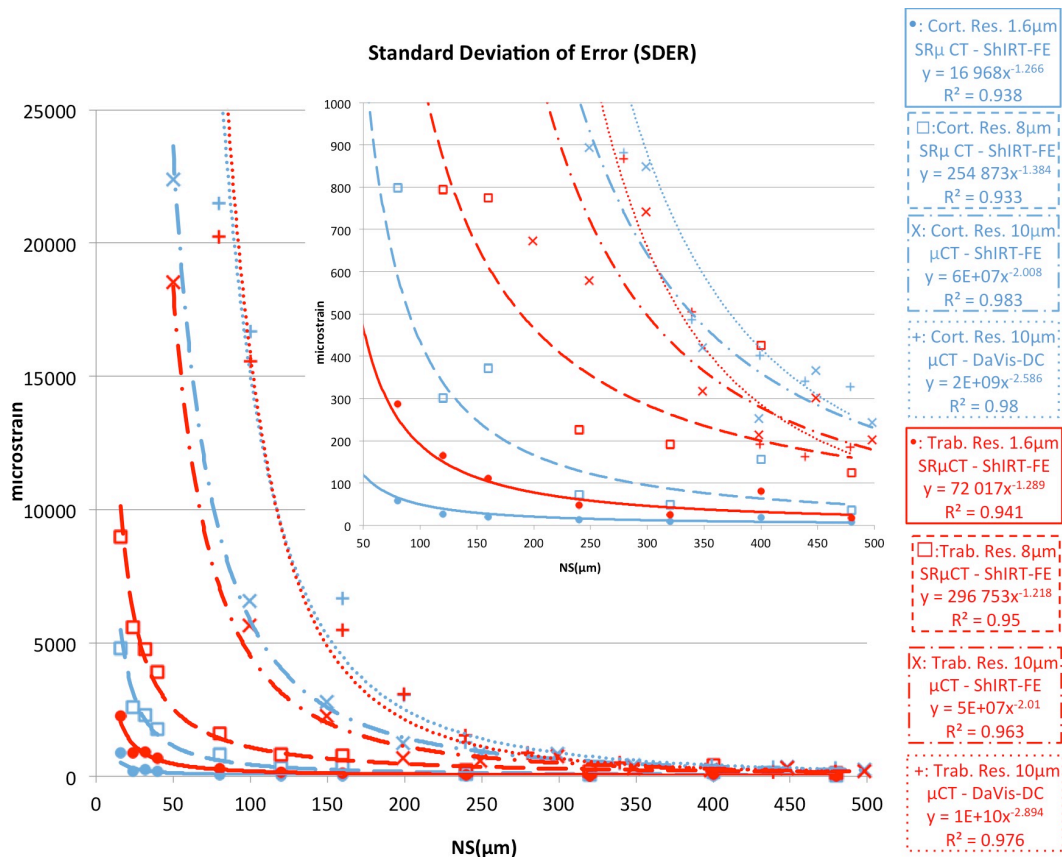


Fig. 2: Overview of the measurement uncertainties evaluated as standard deviation of the error (SDER) using 2 different bone types (blue: cortical bovine bone, red: trabecular bovine bone), 2 different imaging systems (synchrotron radiation microCT and laboratory source microCT), 2 different DVC approaches (global: ShIRT-FE, local: DaVis-DC), and different spatial resolution (voxel size: 1.6, 8, 10 micrometers).

Of course, a compromise between the measurement spatial resolution and the measurement uncertainties should be always taken in account. Finally, this large methodological background on the optimization of the Digital Volume Correlation was employed in preliminary tests on porcine vertebra, in elastic regime until failure. The DVC successfully evaluated since the elastic regime where the failure point inside a vertebra will be placed.

The work is completed in terms of exploring the feasibility of these new full-field procedures on spine segments. In the next years, the real application of the methods should be performed on human specimens: applying more complex loading scenarios and exploring the biomechanics in physiological, pathological and instrumented specimens.

Appendix

Application of Digital Volume Correlation on vertebrae

from the manuscript:

Elastic Full-Field Strain Analysis and Microdamage Progression in the Vertebral Body from Digital Volume Correlation

G. Tozzi¹, V. Danesi², M. Palanca², L. Cristofolini²

¹ School of Engineering, University of Portsmouth, Portsmouth (UK)

² School of Engineering and Architecture, Alma Mater Studiorum – Università
di Bologna, Bologna (IT)

Published in: *Strain*, 2016, 52 (5), 446-455

1 Introduction

Pathologies such as osteoporosis and bone metastases are the major causes of vertebral fractures, often in combination with trauma or para-physiological overloading. These vertebrae are weak because their micro- and/or macro-structure are pathologically compromised. If untreated, they might fracture, causing severe disabilities and in some cases even mortality (Ferrar et al., 2005; Tancioni et al., 2011). For this reason, knowledge of the failure mechanism in the vertebra is of fundamental importance to understand vertebral biomechanics (Cristofolini, 2015), improve diagnosis and prophylactic treatments (Goel et al., 2006; Pollintine et al., 2010).

In vitro testing of the vertebral body has been extensively carried out in the past (Brandolini et al., 2014; Lochmüller et al., 2002; Singer et al., 1995). The strain distribution in the vertebral body was investigated using different experimental techniques but mainly with strain gauges (Cristofolini et al., 2013), where the full-field strain distribution was not investigated. Furthermore, strain gauges are associated with a reinforcement effect that in the case of a thin shell of cortical bone cannot be neglected (Ajovalasit and Zuccarello, 2005; Freddi et al., 2015; Grassi and Isaksson, 2015).

More recently, digital image correlation (DIC) was adopted to investigate the full-field strain distribution on the cortical surface of vertebrae, in an attempt to avoid direct contact measurement (i.e. via strain gauges) that could potentially produce important artifacts in the local strain determination (Palanca et al., 2015a). To this extent, (Gustafson et al., 2016) presented a comparison of strain rosettes and DIC to measure the vertebral body strain. In that study porcine vertebrae were prepared with a strain rosette plus a speckled paint pattern for DIC and loaded in compression. However, it must be pointed out that also the specimen preparation for an appropriate DIC measurement (i.e. speckle pattern distribution) must be planned carefully if reliable results are to be achieved (Lionello and Cristofolini, 2014; Palanca et al., 2015a). When measuring strain in bone one must consider the magnitude of strain experienced during physiological tasks (1000-2000 microstrain, (Lanyon, 1980; Yang et al., 2011)), and the failure strain of bone tissue (7000-10000 microstrain, (Bayraktar et al., 2004)). The overall precision that can be obtained with strain gauges when applied to bone is of the order of 1-2% of the readout (Cristofolini and Viceconti, 1997; Freddi et al., 2015), which corresponds to 10-20 microstrain when loads, that cause strains comparable to those obtained during physiological tasks (Bergmann, 2011), are applied *in vitro*. The overall precision that can be obtained with DIC (which is mainly limited by noise) is of the order of 100-300 microstrain (Palanca et al., 2016a).

In any case, for all the above studies with strain gauges and DIC the main limitation is represented by the inability to capture and quantify internal microdamage evolution and full-field strain distribution under load. As the internal trabecular bone of the vertebral body plays a fundamental structural role (Bouxsein, 2003; Cristofolini, 2015; Fung, 1980), it would be extremely important to measure the internal strain distribution. In fact, a number of studies have shown that in several cases failure starts inside the vertebral body itself (Silva et al., 1997; Wang et al., 2007). In this perspective, digital volume

correlation (DVC) is ideal to investigate the internal strain distribution and the local damage inside the vertebra. In recent years, DVC has become a powerful tool to examine full-field internal deformations mainly in trabecular (Dall'Ara et al., 2014; Gillard et al., 2014; Liu and Morgan, 2007; Palanca et al., 2015b; Roberts et al., 2014) and cortical bone (Christen et al., 2012; Dall'Ara et al., 2014; Palanca et al., 2015b). The use of DVC to investigate the strain distribution in vertebrae has been firstly introduced by (Hardisty and Whyne, 2009). In that study a new image registration algorithm was developed to spatially resolve strain in whole bones (rat vertebrae) using micro-CT images. Since then, a number of studies investigated the full-field strain distribution in vertebral bodies without (Hussein et al., 2012) and with the adjacent intervertebral discs (Hussein et al., 2013), as well as entire vertebrae (Hardisty et al., 2012) under compressive loading. In (Hussein et al., 2012) the highest strain magnitudes (minimum principal strain) were distributed in the superior-inferior (axial) direction ranging between -20000 and -40000 microstrain, in human vertebral bodies. In a following study from the same Authors (Hussein et al., 2013), a comparison between vertebral body (rabbits) without and with the presence of adjacent intervertebral discs highlighted a different minimum principal strain distribution in the two configurations for yield and failure conditions, with maximum differences of -10000 microstrain for the average strain magnitude in the two configurations (with and without discs). However, in both studies (Hussein et al., 2012; Hussein et al., 2013) there is no information on the progression of strain levels from the elastic regime (more physiological), preceding the final failure event. Also, the influence of strain directionality and local levels of strain on microdamage evolution in the vertebra has not been investigated. Hardisty et al. (Hardisty et al., 2012) is the only study to date to report the microdamage in metastatic and healthy vertebrae (rat models) associated with full-field strain from DVC, but only for the axial strain. That work reported an average axial strain at failure of -27000 microstrain for the healthy group (5 specimens), but no information of the critical strain values in different locations of the vertebrae. Another important aspect to be considered is the level of uncertainty of the DVC-computed strain distribution, that can be associated to imaging conditions, bone type, image preparation, computation sub-volume size and nature of the DVC approach (i.e. local vs global). Very recently, an in-depth methodological investigation of all those aspects for natural and augmented vertebral bodies (porcine models) was carried out (Palanca et al., 2016b; Tozzi et al., 2017). Those studies reported that strain uncertainties can be reduced below 300 microstrain for both local and global approaches, for this kind of specimens and images. To obtain those results the images are adequately prepared (excluding the non-tissue background), and a wide investigation of the DVC parameters was performed before choosing the better compromise between uncertainties and spatial (i.e. 48 voxels for a 39 micrometers voxel size image).

In this study, full-field strain distributions inside porcine vertebral bodies were obtained through DVC under compressive load. Specifically, the main aims of this paper were:

- To measure the internal strain up to failure;
- To analyse the distribution of the different components of strain (axial, antero-posterior and lateral-lateral) for each specimen;

- To identify microdamage initiation/progression during loading, and to damage with the distribution of the three components of strain.

2 Methods

2.1 Material and experimental procedures

Three thoracic vertebrae (specimens T1, T2, T3) were harvested from animals that were bred and slaughtered for alimentation purposes. All the surrounding soft tissues were removed, including the ligaments and discs. The vertebrae were obtained from young animals, where the growth plates were still fully open. To avoid the presence of soft tissue and prevent viscoelastic phenomena (which might compromise image acquisition under load), the growth plates were removed together with the adjacent endplates (due to the young age of the animals at sacrifice, this could be performed with little manual effort). The endplate areas of the vertebrae were aligned and potted in poly-methyl-methacrylate (PMMA) for a depth of about 4 mm for each side following a procedure adapted from (Danesi et al., 2014). The spinous process was used to center the specimen in the transverse plane and align it about its vertical axis. The posterior arch was subsequently removed.

Step-wise compression testing of the vertebrae in combination with time-lapsed micro-CT imaging was performed. *In situ* testing was conducted by means of a loading device (CT5000, Deben Ltd, UK), equipped with a 5kN load cell and a custom-designed environmental chamber which was filled with physiological saline solution (Fig. 1).

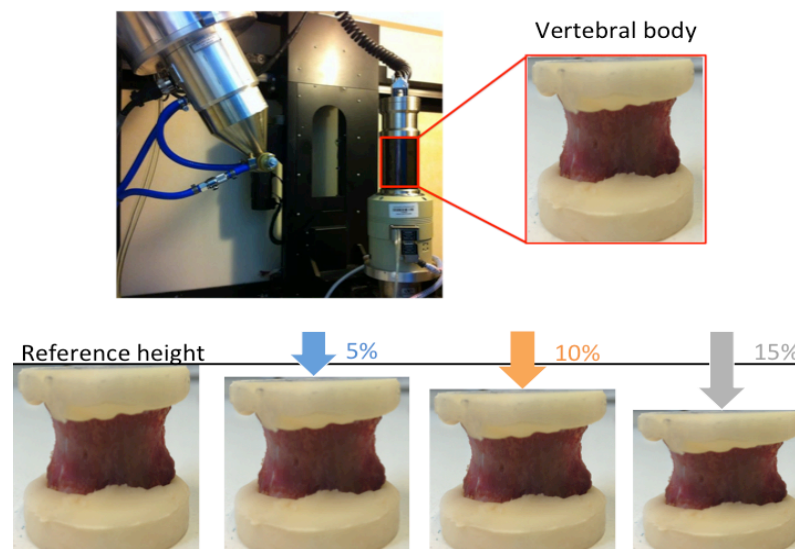


Fig. 1: The micromechanical loading device inside the micro-CT chamber (top-left). The specimen was potted in PMMA and aligned to the rotation axis of the micro-CT (top-right). On the bottom, the three compressive steps; namely 5%, 10%, 15% of apparent strain.

The specimens were constrained against rotation inside the loading device with sandpaper discs applied to the bottom compressive platen. A preload of 50 N was applied. Each specimen was compressed axially under displacement control in a step-wise fashion. The compression steps were adjusted for each specimen based on its height, so that at each step the free height was compressed by 5% (this corresponded to actuator steps of 0.54-0.66 mm, depending on the specimen's size). All tests were carried out at a constant actuator speed of 0.1 mm/sec. At each compression step the specimens were allowed to relaxate to reach a steady state for 15 minutes before imaging.

Micro-CT imaging (XTH225, Nikon Metrology, UK) was carried out at each step (0% with 50N preload, 5%, 10% and 15% compression). The micro-CT scanner was set to a voltage of 88-89 kV, a current of 115-116 microA and exposure time of 2 s. The image acquisition was performed at a rotational step of 0.23° over 360° for a scanning time of approximately 90 min at each compression step. The reconstructed micro-CT images had an isotropic voxel size of 38.8 micrometers.

2.2 Digital Volume Correlation (DVC)

DaVis DVC software (v8.3, LaVision, Germany) was used to compute the full-field strains in the vertebra along the axial, antero-posterior and lateral-lateral directions. The operating principle of the DaVis DVC has been detailed elsewhere (Palanca et al., 2015b; Tozzi et al., 2014). Briefly, DaVis sub-divides the 3D images into smaller sub-volumes that can be correlated independently (local approach) as a discrete function of grey-levels. The matching between the sub-volumes corresponding to the different stages of loading is achieved via a direct correlation function (DaVis-DC). Additionally, a piece-wise linear shape function and a third-order spline interpolation in the image reconstruction are employed to help correlation of the pattern information contained in the reference and deformed images. The displacement vector field is obtained at the center of each sub-volume. The strain field is subsequently computed using a centered finite differences (CFD) scheme. The original micro-CT images were masked in order to remove the background areas where no bone was present. In fact, it was shown that regions that do not contain useful feature for the correlation algorithm are associated with large strain artifacts (Palanca et al., 2016b; Tozzi et al., 2017). A user-defined polygon mask was created, which corresponded to the contour shape of each vertebral body. The mask was defined in the transverse plane of the vertebral body and sequentially adapted in the caudal-cranial direction to follow the shape of the vertebra. The geometric mask enabled the DVC software to include only the voxels inside the mask (vertebral body area).

The DVC computation relied on final sub-volumes of 48 voxels, reached after successive (predictor) passes using sub-volumes of 128 voxels, 112 voxels, 96 voxels, 80 voxels and 64 voxels, with a 0% overlap. This multipass sequence and the final sub-volume were found to produce the lowest strain error in DaVis-DC, after a wide investigation (Palanca et al., 2016b; Tozzi et al., 2017), for such type of specimens, with the same imaging and environmental settings. Briefly, repeated micro-CT scans in zero-strain conditions were processed using a wide range of sub-volume size. The systematic and random errors were evaluated and finally selected the unavoidable compromise between measurement uncertainties and measurement spatial resolution. Given the voxel size of the

acquired micro-CT images, the final computation sub-volume size corresponded to 1862 micrometers.

In order to evaluate the strain distribution in the vertebra and to associate local high-strains with visible microdamage, dedicated Matlab (v2014a, MathWorks, US) scripts were developed. These allowed 2D visualization of the evaluated 3D strain maps for the three components of normal strain, in order to easily show the strain distribution inside the specimens. Moreover, for each compression step, the average of the measurement points within each cross-section, for each normal component of strains (axial, antero-posterior and lateral-lateral strain), was computed.

3 Results

The force-displacement curves showed a monotonic trend for all specimens while load was increased (Fig. 2).

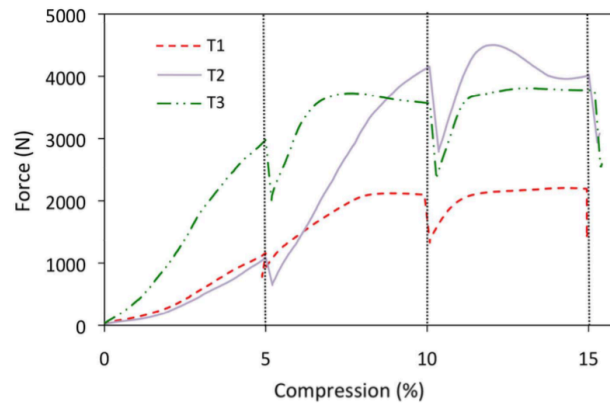


Fig. 2: Force-compression curves for the three specimens. The load shows a drop at the end of each step of compression: this corresponds to relaxation while the specimen was allowed to settle (15 minutes) before the micro-CT scan took place (90 minutes).

Specimen failure (clearly visible as a plateau and decrease in the force-displacement plots) occurred at 10% or 15% steps in all specimens. The loads applied onto the three specimens for each loading steps are reported in Table 1.

Table 1: Loads experienced by the three specimens (T1, T2, T3) in each loading step of 5%, 10% and 15% apparent strain, under displacement control.

Loading step	Loads T1 (N)	Loads T2 (N)	Loads T3 (N)
5% apparent strain	1115	1025	2917
10% apparent strain	2104	4118	3576
15% apparent strain	2198	3994	3777

Relaxation was also visible at the end of each step of compression, when the actuator was stopped to allow micro-CT scanning. The internal strain distributions (axial, antero-posterior and lateral-lateral components of strain) for the three compression steps (5%, 10% and 15%) on the sagittal section of

the three specimens are reported in Figures 3-5. The micro-CT images of specimen T1 showed a main microdamage localized in the trabecular bone (caudal region), which started to appear at the 10% compressive step, and degenerated into a trabecular collapse at 15% (Fig. 3). Such a collapse gradually led to a weakening of the vertebral body in the transverse plane, with damage extending to the cortical bone anteriorly. The distribution of the three components of strain well described the damage events, with the maximum strains located in regions adjacent to the crushed zone; away from the crushed region the strains were significantly lower (Fig. 3).

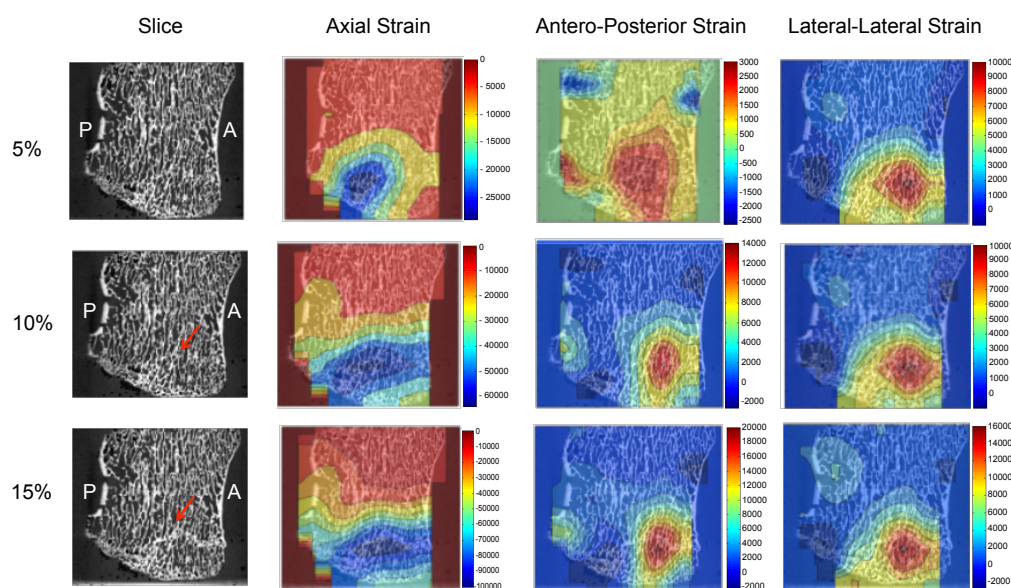


Fig 3: Internal strain distribution (Axial, Antero-Posterior and Lateral-Lateral strain) and corresponding microdamage progression under compression load for specimen T1. Sagittal micro-CT views taken at 5%, 10% and 15% compression steps are shown on the left (the antero (A) and posterior (P) direction are also indicated). The crushed zone of specimen is visible in the 10% and 15% compression steps. Strain maps in sagittal section are overlapped to the micro-CT images. The most strained region corresponded to the damaged area, which gradually progressed in a crack propagating throughout the vertebra, in an approximately transverse plane.

A similar agreement between the damage (visible in the micro-CT images) and the distribution of strain (computed by means of DVC) was found in the other two specimens, although the damage pattern was different (Fig. 4 and 5).

In specimen T2 the microdamage seemed to be localized in the trabecular structure as a gradual collapse that initiated (10%) and then propagated (15%) posteriorly, along the caudal-cranial direction (Fig. 4), similarly to specimen T1. In specimen T3 damage initiated in the cranial region (10% compression) and progressively extended as a collapse in a transverse plane (15% compression) (Fig. 5).

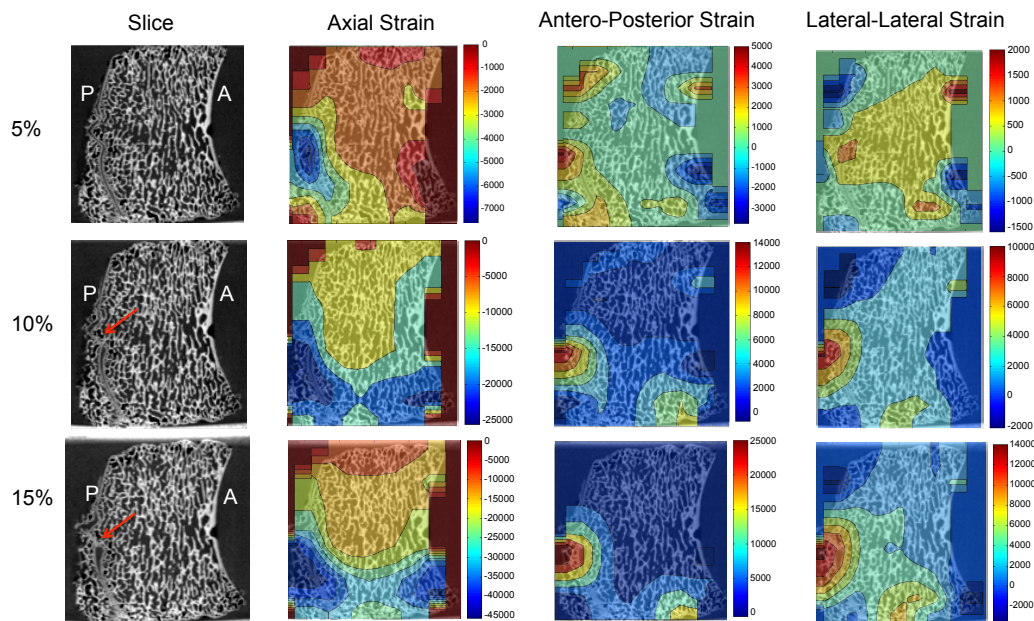


Fig 4: Internal strain distribution (Axial, Antero-Posterior and Lateral-Lateral strain) and corresponding microdamage progression under compression load for specimen T2. Sagittal micro-CT views taken at 5%, 10% and 15% compression steps are shown on the left (the antero (A) and posterior (P) direction are also indicated). The crushed zone of specimen is visible in the 10% and 15% compression steps. Strain maps in sagittal section are overlapped to the micro-CT images. The most strained region corresponded to the damaged area, which gradually progressed in a crack propagating throughout the vertebra, in an approximately caudal-cranial direction.

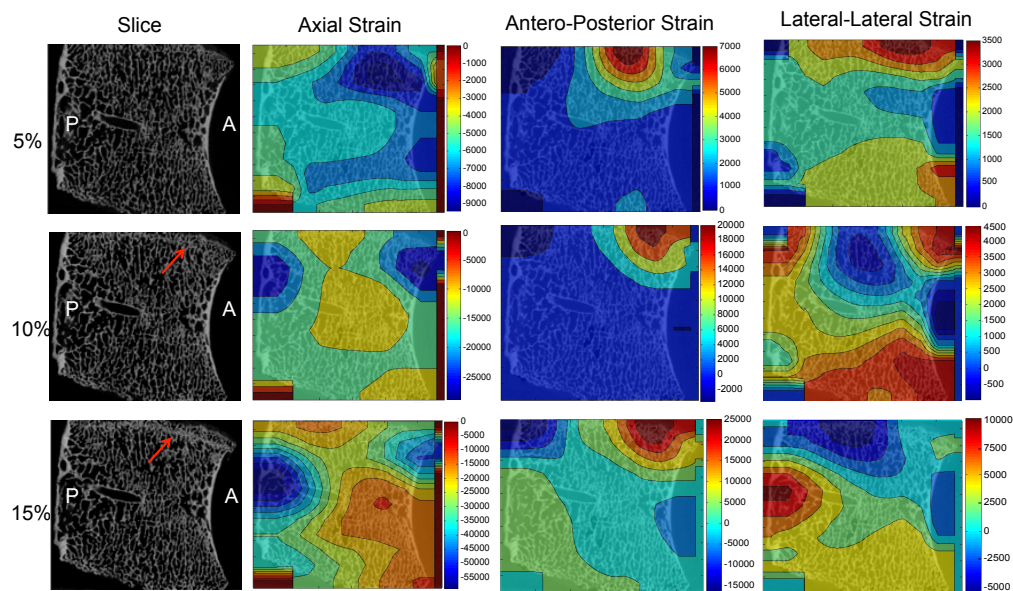


Fig 5: Internal strain distribution (Axial, Antero-Posterior and Lateral-Lateral strain) and corresponding microdamage progression under compression load for specimen T2. Sagittal micro-CT views taken at 5%, 10% and 15% compression steps are shown on the left (the antero (A) and posterior (P) direction are also indicated). The crushed zone of specimen is visible in the 10% and 15% compression steps. Strain maps in sagittal section are overlapped to the micro-CT images. The most strained region corresponded to the damaged area, which gradually progressed in a crack propagating throughout the vertebra, in an approximately transverse plane.

In general, for all specimens the increase of strain was larger from 10% to 15% compression, than from 5% to 10% compression, both for the axial component of strain (compressive), and the antero-posterior and lateral-lateral ones (tensile). For all specimens, the strain distribution in the elastic regime (first step of loading, 5%) showed a non-uniform strain distribution, which seemed to predict the location of damage initiation before it actually became identifiable (Fig. 3-5). The progression of strain (axial, antero-posterior and lateral-lateral components of strain) during compression for the three specimens is shown in Figure 6 in terms of average strain at each cross-section. Specimen T1 experienced the highest axial compressive strain (-75689 microstrain, average over the most strained cross-section), followed by specimen T3 (-42005 microstrain) and specimen T2 (-32859 microstrain). For the antero-posterior component of strain, the most strained regions experienced a strain between 6161 and 7940 microstrain (average over the most strained cross-section), in all specimens. For the lateral-lateral component of strain, the most strained regions experienced a strain between 3430 and 9013 microstrain (average over the most strained cross-section), in all specimens. The strain pattern along the caudal-cranial direction was similar for specimens T1 and T2, with the largest deformation localized in correspondence of the first quarter caudal. In specimen T3 the highest axial strain magnitudes were found where the cortical shell was mostly curved (first quarter cranial); the largest antero-posterior and lateral-lateral strains were observed in correspondence of the cranial and caudal endplates. The cranial-posterior portion of this specimen was in a compressive state, with the largest strain (-5327 microstrain) at 15% loading step.

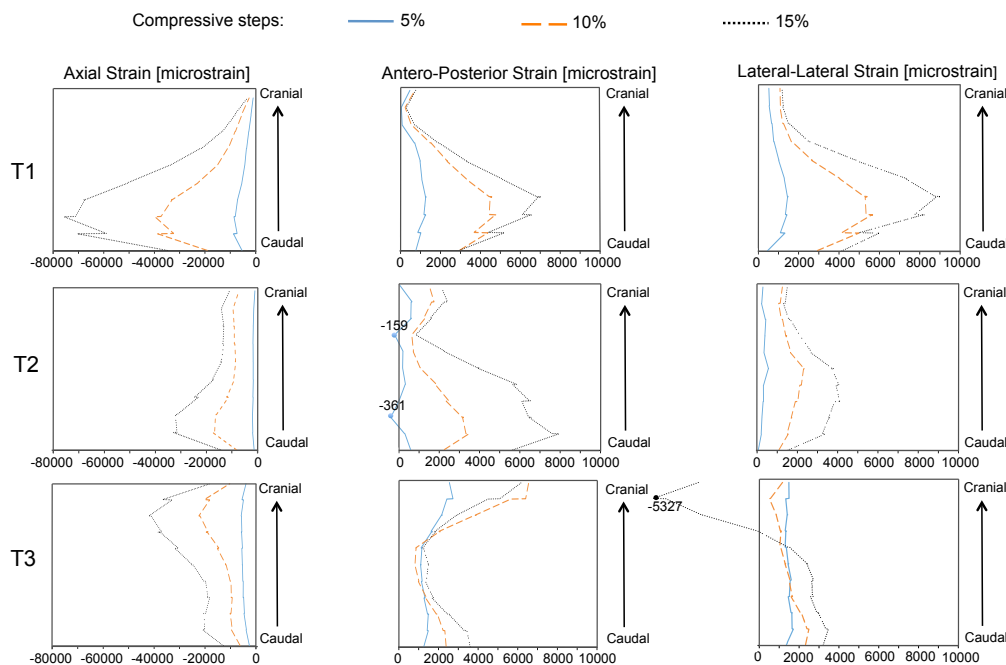


Fig 6: Comparison of the average strains obtained from DVC analysis along the caudal-cranial direction. The average strains were computed for each transverse slice of the 3D strain map in the Axial, Antero-Posterior and Lateral-Lateral directions. The average strains are plotted for 5%, 10% and 15% steps in each specimen. In general, an incremental strain pattern among the consecutive compression steps is observed.

4 Discussion

The first aim of this paper was to evaluate the internal strain distribution (axial, antero-posterior and lateral-lateral components of strain) from DVC in porcine vertebral body, under applied compressive load. A deeper understanding of the internal elastic full-field strain distribution was achieved. In fact, despite a number of studies used DVC to investigate the vertebral global fracture under compression (Hardisty et al., 2012; Hussein et al., 2012; Hussein et al., 2013), the elastic strain distribution is still unexplored. The results clearly showed how local strain built up from the elastic regime, and highlighted those internal weaker regions that could result in microdamage initiation and progression up to vertebral failure (Fig. 3-5). When a compression of 5% was applied, all specimens experienced levels of internal tensile and compressive strains above or close to the typical values of bone tissue failure (i.e. 7000 microstrain for tensile and -10000 microstrain for compression as reported in (Cristofolini, 2015)). For two specimens (T1 and T2) rather regular strain maps were identified for each component of strain, and for the steps of applied compression. Conversely, the third specimen (T3) exhibited a more irregular strain distribution, possibly associated with the superimposition of compression and some degree of bending.

The benefit of using DVC compared to surface strain measurement techniques (i.e. strain gauges or DIC) is particularly evident in specimen T1. In fact, surface strain measurement in the 5% compression step (load of 1115 N) would have only provided information on the strain distribution on the cortical shell that was mostly below the yield values for bone in both compression and tension (Fig. 3 and 6). Particularly, strains of the order of 500 to 1500 microstrain were found in the cortical shell of vertebral bodies using strain gauges for a 1470 N compressive load (Shah et al., 1978) and average compressive and tensile strains (minimum and maximum principal strains) from DIC were found to be -2587 microstrain and 678 microstrain for a compressive load equal to 2050 N (Gustafson et al., 2016). These values would have therefore obscured the real nature of internal strain distribution and made impossible to predict where the damage in the vertebral body would initiate. In this context the ability of DVC in identifying internal strain represents an invaluable resource despite its higher strain precision errors at organ level (few hundreds microstrain) (Palanca et al., 2016b; Tozzi et al., 2017), when compared to DIC (few tens and up to hundred microstrain) (Grassi and Isaksson, 2015; Palanca et al., 2015a) or strain gauges (few microstrain) (Gustafson et al., 2016).

Another important advantage of DVC relies in its ability to quantify internal microdamage in the bone microstructures. The use of micro-CT image-guided failure assessment (Nazarian and Müller, 2004; Tozzi et al., 2012) has allowed three-dimensional analysis of microdamage in bone tissue, allowing the assessment of damage onset and progression under load. In trabecular bone the microdamage is mainly characterised by bending and buckling of the trabeculae at different locations (Tozzi et al., 2013; Tozzi et al., 2012). The use of a specific script allowed a successful coupling of a qualitative microdamage inspection (from micro-CT images) to quantitative information about the strain fields (from DVC), throughout the entire volume of the specimens (Tozzi et al., 2014).

Interestingly, the use of DVC in vertebral mechanics rarely focused on the coupling of microdamage with strain distribution in the failure region. When this was done, it mainly involved the axial strain (Hardisty et al., 2012), which is surely important in a compression loading but provides only incomplete physiological information. Conversely, when the main physiological directions (axial, antero-posterior and lateral-lateral components of strain) were considered, the microdamage development associated to that specific strain condition was not analyzed (Hussein et al., 2012; Hussein et al., 2013). Moreover, only scattered information on the average strains at the different levels along the vertebral body are reported (Hussein et al., 2013). Hussein et al. [25] presented an average compressive strain (minimum principal strain) in six vertebral bodies at three locations; namely superior (-44000 ± 53000 microstrain), central (-49000 ± 76000 microstrain) and inferior (-50000 ± 65000 microstrain) regions. However, no details on the single vertebral bodies were reported and, as indicated by the large scatter in the results, a number of different damage patterns are to be expected. Our findings are in agreement with the results from Hussein et al. (Hussein et al., 2013) where the most important compressive strains were found in caudal direction (or inferior) for both specimen T1 (-75689 microstrain) and specimen T2 (-32859 microstrain). Dissimilarly, the third specimen (T3) experienced highest compressive strains (-42005 microstrain) in the cranial region, confirming the high standard deviations reported by (Hussein et al., 2013).

The current study has two main limitations. Firstly, the use of three specimens could not provide enough statistical power to identify consistent trends. However, this sample was sufficient to demonstrate the feasibility of measuring internal strain in the elastic regime, to correlate such elastic strain with the final failure mechanism and to understand the basic strain distribution associated with microdamage in vertebral bodies. A second limitation relates to the use of animal vertebrae (which are certainly different from the human ones (Cristofolini et al., 2013)). This choice was driven by easier tissue availability compared to human, and by the possibility of fitting the entire vertebral body in the micro-CT scanner and its loading device. Additionally, animal tissue was also used in similar studies (Hardisty et al., 2012; Hardisty and Whyne, 2009; Hussein et al., 2013) and fully justified for explorative *in vitro* testing of vertebrae (Brandolini et al., 2014).

5 Conclusions

In this paper building up of internal full-field strain from DVC in the elastic regime and progression up to failure was measured in vertebral bodies loaded under step-wise compression loading. Regions of internal microdamage were successfully matched with the distribution of strains, where axial, antero-posterior and lateral-lateral strains were monitored for all specimens at all levels of compression. The results obtained in this study clearly showed how different vertebral bodies might be subjected to different damage/strain distribution. Thus, consequent microdamage can develop and progress in different ways

towards the final failure of the vertebra. Interestingly, DVC-computed strains in the elastic regime had the ability to predict high-strain concentration and therefore damage before failure actually occurred. This has the potential to be implemented in clinical CT assessment of vertebrae, given controlled loading conditions during imaging.

Acknowledgments

The authors would like to thank Mr. Remo Antelli for donating the porcine spines, Mr. Colin Lupton (University of Portsmouth) for technical support in micro-CT maintenance, Dr. Dave Hollis (LaVision Ltd) for assistance with DVC software and Mr. Marco Curto for technical support. Funding was provided by the Royal Society (RG130831), University of Portsmouth and European Society of Biomechanics (ESB mobility award 2014).

Bibliography

Aamodt, A., Lund-Larsen, J., Eine, J., Andersen, E., Benum, P., Husby, O.S., 1997. In vivo measurements show tensile axial strain in the proximal lateral aspect of the human femur. *J Orthop Res.* 15, 927-931.

Aebi, M., 2005. The adult scoliosis. *Eur Spine J* 14, 925-948.

Affagard, J.S., Bensamoun, S.F., Feissel, P., 2014. Development of an inverse approach for the characterization of in vivo mechanical properties of the lower limb muscles. *Journal of biomechanical engineering* 136.

Affairs, D.o.E.a.S., 2007. Development in an Ageing World, in: Nations, U. (Ed.), New York.

Agency for Healthcare Research and Quality, A., Healthcare cost and utilization project, Available at: <http://www.ahrq.gov/data/hcup/>.

Ahn, B., Kim, J., 2010. Measurement and characterization of soft tissue behavior with surface deformation and force response under large deformations. *Med Image Anal* 14, 138-148.

Ahn, H.S., DiAngelo, D.J., 2007. Biomechanical testing simulation of a cadaver spine specimen: development and evaluation study. *Spine (Phila Pa 1976)* 32, E330-336.

Ajovalasit, A., D'Acquisto, L., Fracapane, S., Zuccarello, B., 2007. Stiffness and Reinforcement Effect of Electrical Resistance Strain Gauges. *Strain* 43, 229-305.

Ajovalasit, A., Zuccarello, B., 2005. Local Reinforcement Effect of a Strain Gauge Installation on Low Modulus Materials. *The Journal of Strain Analysis for Engineering Design* 40, 643-653.

Alkalay, R.N., Sharpe, D., Blader, D.L., 1999. The effects of design and configuration on the biomechanical response of an internal spinal fixator. *Proc. Instn. Mech. Engrs. Part H: J. Engineering in Medicine* 213, 137-146.

Amin Yavari, S., van der Stok, J., Weinans, H., Zadpoor, A.A., 2013. Full-field strain measurement and fracture analysis of rat femora in compression test. *Journal of biomechanics* 46, 1282-1292.

Amiot, F., Bornert, M., Doumalin, P., Dupré, J.C., Fazzini, M., Orteu, J.J., Poilâne, C., Robert, L., Rotinat, R., Toussaint, E., Wattrisse, B., Wienin, J.S., 2013. Assessment of Digital Image Correlation Measurement Accuracy in the Ultimate Error Regime: Main Results of a Collaborative Benchmark. *Strain* 49, 483-496.

Anderson, A.L., McIff, T.E., Asher, M.A., Burton, D.C., Glattes, R.C., 2009. The Effect of Posterior Thoracic Spine Anatomical Structures on Motion Segment Flexion Stiffness. *Spine* 34, 441 - 446.

- Anderst, W.J., Donaldson, W.F., 3rd, Lee, J.Y., Kang, J.D., 2014. Continuous cervical spine kinematics during in vivo dynamic flexion-extension. *The spine journal : official journal of the North American Spine Society* 14, 1221-1227.
- Ashton, A.W., Aishima, J., Basham, M., Chang, P., El Kassaby, B., Filik, J., Gerring, M., Levik, K., Sikharulidze, I., Webber, M., Wharmby, M.T., 2015. Dawn Science v1.7 (DLS Edition).
- Aspden, R.M., 1992. Review of the functional anatomy of the spinal ligaments and the lumbar erector spinae muscles. *Clinical Anatomy* 5, 372-387.
- Babuska, I., Oden, J.T., 2004. Verification and validation in computational engineering and science: basic concepts. *Computer Methods in Applied Mechanics and Engineering* 193, 4057-4066.
- Baldoni, J., Lionello, G., Zama, F., Cristofolini, L., 2016. Comparison of different strategies to reduce noise in strain measurements with Digital Image Correlation. *J Strain Analysis for Engineering Design* 51, 416-430.
- Barber, D.C., Hose, D.R., 2005. Automatic segmentation of medical images using image registration: diagnostic and simulation applications. *J Med Eng&Tech* 29, 53-63.
- Barber, D.C., Oubel, E., Frangi, A.F., Hose, D.R., 2007. Efficient computational fluid dynamics mesh generation by image registration. *Med Image Anal* 11, 648-662.
- Barranger, Y., Doumalin, P., Dupré, J.C., Germaneau, A., 2010. Digital Image Correlation accuracy: influence of kind of speckle and recording setup. *EPJ Web of Conferences* 6, 31002.
- Barrett, E., McCreesh, K., Lewis, J., 2014. Reliability and validity of non-radiographic methods of thoracic kyphosis measurement: a systematic review. *Man Ther* 19, 10-17.
- Barth, H.D., Launey, M.E., Macdowell, A.A., Ager, J.W., 3rd, Ritchie, R.O., 2010. On the effect of X-ray irradiation on the deformation and fracture behavior of human cortical bone. *Bone* 46, 1475-1485.
- Basham, M., Filik, J., Wharmby, M.T., Chang, P.C., El Kassaby, B., Gerring, M., Aishima, J., Levik, K., Pulford, B.C., Sikharulidze, I., Sneddon, D., Webber, M., Dhese, S.S., Maccherozzi, F., Svensson, O., Brockhauser, S., Naray, G., Ashton, A.W., 2015. Data Analysis WorkbeNch (DAWN). *J Synchrotron Radiat* 22, 853-858.
- Basler, S.E., Mueller, T.L., Christen, D., Wirth, A.J., Muller, R., van Lenthe, G.H., 2011. Towards validation of computational analyses of peri-implant displacements by means of experimentally obtained displacement maps. *Computer Methods in Biomechanics and Biomedical Engineering* 14, 165-174.
- Bay, B.K., 1995. Texture Correlation: a method for the measurement of detailed strain distributions within trabecular bone. *J Orthop Res* 13, 258-267.
- Bay, B.K., Smith, T.S., Fyhrie, D.P., Saad, M., 1999a. Digital Volume Correlation: Three-dimensional Strain Mapping Using X-ray Tomography. *Experimental Mechanics* 39, 217 - 226.

- Bay, B.K., Yerby, S.A., McLain, R.F., Toh, E., 1999b. Measurement of strain distributions within vertebral body sections by texture correlation. *Spine (Phila Pa 1976)* 24, 10-17.
- Bayraktar, H.H., Morgan, E.F., Niebur, G.L., Morris, G.E., Wong, E.K., Keaveny, T.M., 2004. Comparison of the elastic and yield properties of human femoral trabecular and cortical bone tissue. *Journal of biomechanics* 37, 27-35.
- Becker, W.R., De Vita, R., 2015. Biaxial mechanical properties of swine uterosacral and cardinal ligaments. *Biomech Model Mechanobiol* 14, 549-560.
- Been, E., Kalichman, L., 2014. Lumbar lordosis. *The spine journal : official journal of the North American Spine Society* 14, 87-97.
- Benecke, G., Kerschnitzki, M., Fratzl, P., Gupta, H.S., 2011. Digital image correlation shows localized deformation bands in inelastic loading of fibrolamellar bone. *Journal of Materials Research* 24, 421-429.
- Benoit, A., Guerard, S., Gillet, B., Guillot, G., Hild, F., Mitton, D., Perie, J.N., Roux, S., 2009. 3D analysis from micro-MRI during in situ compression on cancellous bone. *Journal of biomechanics* 42, 2381-2386.
- Bergmann, G., 2011. (ed.), Charite – Universitaetsmedizin Berlin "OrthoLoad". Retrieved July 1, 2011. <<http://www.OrthoLoad.com>>.
- Boos, N., 2009. The impact of economic evaluation on quality management in spine surgery. *Eur Spine J* 18 Suppl 3, 338-347.
- Borchers, N., Reinsch, N., Kalm, E., 2004. The number of ribs and vertebrae in Piétrain cross: variation, heritability and effects on performance traits. *J. Anim. Breed. Genet.* 121, 392-403.
- Botelho, R.V., de Oliveira, M.F., Rotta, J.M., 2013. Quantification of vertebral involvement in metastatic spinal disease. *The Open Orthopaedics Journal* 7, 286 - 291.
- Bouxsein, M.L., 2003. Bone quality: where do we go from here? *Osteoporos Int* 14 Suppl 5, S118-127.
- Boyce, B.L., Grazier, J.M., Jones, R.E., Nguyen, T.D., 2008. Full-field deformation of bovine cornea under constrained inflation conditions. *Biomaterials* 29, 3896-3904.
- Boyce, B.L., Jones, R.E., Nguyen, T.D., Grazier, J.M., 2007. Stress-controlled viscoelastic tensile response of bovine cornea. *Journal of biomechanics* 40, 2367-2376.
- Brandolini, N., Cristofolini, L., Viceconti, M., 2014. Experimental Method for the Biomechanical Investigation of Human Spine: a Review *Journal Of Mechanics in Medicine and Biology* 14, 1430002.
- Bruck, H.A., McNeill, S.R., Sutton, M.A., Peters, W.H., 1989. Digital Image Correlation Using Newton-Raphson Method of Partial Differential Correction. *Experimental Mechanics* September 1989, 261 - 267.
- Brunon, A., Bruyere-Garnier, K., Coret, M., 2011. Characterization of the nonlinear behaviour and the failure of human liver capsule through inflation tests. *J Mech Behav Biomed Mater* 4, 1572-1581.

- Busscher, I., Ploegmakers, J., Verkerke, G., Veldhuizen, A., 2010a. Comparative anatomical dimensions of the complete human and porcine spine. *European spine journal* 19, 1104-1114.
- Busscher, I., van der Veen, A.J., van Dieen, J.H., Kingma, I., Verkerke, G.J., Veldhuizen, A.G., 2010b. In vitro biomechanical characteristics of the spine: a comparison between human and porcine spinal segments. *Spine (Phila Pa 1976)* 35, E35-42.
- Busscher, I., van Dieen, J.H., Kingma, I., van der Veen, A.J., Verkerke, G.J., Veldhuizen, A.G., 2009. Biomechanical Characteristics of Different Regions of the Human Spine. *Spine* 34, 2858-2864.
- Cardoso, M.J., Dmitriev, A.E., Helgeson, M., Lehman, R.A., Kuklo, T.R., Rosner, M.K., 2008. Does Superior-Segment Facet Violation of Laminectomy Destabilize the Adjacent Level in Lumbar Transpedicular Fixation? An in Vitro Human Cadaveric Assessment. *Spine* 33, 2868-2873.
- Carriero, A., Abela, L., Pitsillides, A.A., Shefelbine, S.J., 2014. Ex vivo determination of bone tissue strains for an in vivo mouse tibial loading model. *Journal of biomechanics* 47, 2490-2497.
- Cassidy, J.J., Hiltner, A., Baer, E., 1989. Hierarchical Structure of the Intervertebral Disc. *Connective Tissue Research* 23, 75 - 88.
- Cassidy, J.J., Hiltner, A., Baer, E., 1990. The response of the hierarchical structure of the intervertebral disc to uniaxial compression. *Journal of Materials Science: Materials in Medicine* 1, 69-80.
- Causa, F., Manto, L., Borzacchiello, A., De Santis, R., Netti, P.A., Ambrosio, L., Nicolais, L., 2002. Spatial and structural dependence of mechanical properties of porcine intervertebral disc. *J. Mater. Science: Material in Medicine* 13, 1277 - 1280.
- Cheminet, A., Leclaire, B., Champagnat, F., Plyer, A., Yegavian, R., Le Besnerais, G., 2014. Accuracy assessment of a Lucas-Kanade based correlation method for 3D PIV. 17th International Symposium on Applications of Laser Techniques to Fluid Mechanics, Lisbon, Portugal, 07-10 July.
- Chen, Y., Dall'Ara, E., Sales, E., Manda, K., Wallace, R., Pankaj, P., Viceconti, M., 2016. Micro-CT based finite element models of cancellous bone predict accurately displacement once the boundary condition is well replicated: A validation study. *Journal of Mechanical Behavior of Biomedical Materials* 65, 644-651.
- Choi, D., Crockard, A., Bungler, C., Harms, J., Kawahara, N., Mazel, C., Melcher, R., Tomita, K., Global Spine Tumor Study, G., 2010. Review of metastatic spine tumour classification and indications for surgery: the consensus statement of the Global Spine Tumour Study Group. *Eur Spine J* 19, 215-222.
- Cholewicki, J., McGill, S.M., 1996. Mechanical stability of the in vivo lumbar spine: implications for injury and chronic low back pain. *Clin Biomech* 11, 1-15.
- Christen, D., Levchuk, A., Schori, S., Schneider, P., Boyd, S.K., Muller, R., 2012. Deformable image registration and 3D strain mapping for the quantitative

assessment of cortical bone microdamage. *Journal of Mechanical Behavior of Biomedical Materials* 8, 184-193.

Christodoulou, C., Cooper, C., 2003. What is osteoporosis? *Postgraduate Medical Journal* 79, 133-138.

Chu, T.C., Ranson, W.F., Sutton, M.A., Peters, W.H., 1985. Applications of Digital Image Correlation Techniques to Experimental Mechanics. *Experimental Mechanics* 25, 232 - 244.

Chuang, S.F., Chang, C.H., Chen, T.Y., 2011. Contraction behaviors of dental composite restorations--finite element investigation with DIC validation. *J Mech Behav Biomed Mater* 4, 2138-2149.

Cook, D.J., Yeager, M.S., Cheng, B.C., 2015. Range of motion of the intact lumbar segment: a multivariate study of 42 lumbar spines. *Int J Spine Surg* 9, 5.

Cooper, C., Westlake, S., Harvey, N., Javaid, K., Dennison, E., Hanson, M., 2006. Review: developmental origins of osteoporotic fracture. *Osteoporosis International* 17, 337-347.

Corse, M.R., Renberg, W.C., Friis, E.A., 2003. In vitro evaluation of biomechanical effects of multiple hemilaminectomies on the canine lumbar vertebral column. *American Journal of Veterinary Research* 64, 1139-1145.

Coudrillier, B., Boote, C., Quigley, H.A., Nguyen, T.D., 2013. Scleral anisotropy and its effects on the mechanical response of the optic nerve head. *Biomech Model Mechanobiol* 12, 941-963.

Coudrillier, B., Tian, J., Alexander, S., Myers, K.M., Quigley, H.A., Nguyen, T.D., 2012. Biomechanics of the human posterior sclera: age- and glaucoma-related changes measured using inflation testing. *Invest Ophthalmol Vis Sci* 53, 1714-1728.

Cox, M.A., Driessen, N.J., Boerboom, R.A., Bouten, C.V., Baaijens, F.P., 2008. Mechanical characterization of anisotropic planar biological soft tissues using finite indentation: experimental feasibility. *Journal of biomechanics* 41, 422-429.

Crammond, G., Boyd, S.W., Dulieu-Barton, J.M., 2013. Speckle pattern quality assessment for digital image correlation. *Optics and Lasers in Engineering* 51, 1368-1378.

Cristofolini, L., 2015. In vitro evidence of the structural optimization of the human skeletal bones. *Journal of biomechanics* 48, 787-796.

Cristofolini, L., Brandolini, N., Danesi, V., Juszczuk, M.M., Erani, P., Viceconti, M., 2013. Strain distribution in the lumbar vertebrae under different loading configurations. *The spine journal : official journal of the North American Spine Society* 13, 1281-1292.

Cristofolini, L., Cappello, A., Toni, A., 1994. Experimental errors in the application of photoelastic coating on human femurs with uncemented hip stems. *Strain* 30, 95 - 103.

Cristofolini, L., Conti, G., Juszczuk, M., Cremonini, S., Van Sint Jan, S., Viceconti, M., 2010a. Structural behaviour and strain distribution of the long bones of the human lower limbs. *Journal of biomechanics* 43, 826-835.

- Cristofolini, L., Juszczuk, M., Martelli, S., Taddei, F., Viceconti, M., 2007. In vitro replication of spontaneous fractures of the proximal human femur. *Journal of biomechanics* 40, 2837-2845.
- Cristofolini, L., Juszczuk, M., Taddei, F., Viceconti, M., 2009. Strain distribution in the proximal human femoral metaphysis. *Proc Inst Mech Eng H* 223, 273-288.
- Cristofolini, L., McNamara, B., Freddi, A., Viceconti, M., 1997. In vitro measured strains in the loaded femur: quantification of experimental error. *The Journal of Strain Analysis for Engineering Design* 32, 193-200.
- Cristofolini, L., Metti, C., Viceconti, M., 2003. Strain patterns induced by press-fitting and by an external load. *J. Strain Analysis* 38, 290-301.
- Cristofolini, L., Schileo, E., Juszczuk, M., Taddei, F., Martelli, S., Viceconti, M., 2010b. Mechanical testing of bones: the positive synergy of FE models and in vitro experiments. *Philos Transact A Math Phys Eng Sci* 368, 2725-2763.
- Cristofolini, L., Viceconti, M., 1997. Comparison of Uniaxial and Triaxial Rosette Gages for Strain Measurement in the Femur. *Experimental Mechanics* 37, 350 - 354.
- Currey, J.D., 1982. Bone as a mechanical structure, in: Huiskes, R., van Campen, D.H., de Wijn, J.R. (Eds.), *Biomechanics - Principles and applications*. Martinus Nijhoff Publishers, pp. 75-85.
- Cyganik, L., Binkowski, M., Kokot, G., Rusin, T., Popik, P., Bolechala, F., Nowak, R., Wrobel, Z., John, A., 2014. Prediction of Young's modulus of trabeculae in microscale using macro-scales relationships between bone density and mechanical properties. *J Mech Behav Biomed Mater* 36, 120-134.
- Dall'ara, E., 2012. QCT based Finite Element Models of the Human Vertebra and Femur: Validation with Experiments and comparison with Bone Densitometry. PhD Thesis, Technische Universität Wien, Fakultät für Maschinenwesen und Betriebswissenschaften.
- Dall'Ara, E., Barber, D., Viceconti, M., 2014. About the inevitable compromise between spatial resolution and accuracy of strain measurement for bone tissue: A 3D zero-strain study. *Journal of biomechanics* 47, 2956 - 2963.
- Dall'Ara, E., Luisier, B., Schmidt, R., Kainberger, F., Zysset, P., Pahr, D., 2013. A nonlinear QCT-based finite element model validation study for the human femur tested in two configurations in vitro. *Bone* 52, 27-38.
- Dall'Ara, E., Pahr, D., Varga, P., Kainberger, F., Zysset, P., 2012. QCT-based finite element models predict human vertebral strength in vitro significantly better than simulated DEXA. *Osteoporos Int* 23, 563-572.
- Dall'Ara, E., Schmidt, R., Pahr, D., Varga, P., Chevalier, Y., Patsch, J., Kainberger, F., Zysset, P., 2010. A nonlinear finite element model validation study based on a novel experimental technique for inducing anterior wedge-shape fractures in human vertebral bodies in vitro. *Journal of biomechanics* 43, 2374-2380.
- Danesi, V., Erani, P., Brandolini, N., Juszczuk, M., Cristofolini, L., 2016a. Effect of the In Vitro Boundary Conditions on the Surface Strain Experienced by the Vertebral Body in the Elastic Regime. *Journal of biomechanical engineering* 138, 104503-104501/104509.

- Danesi, V., Tozzi, G., Cristofolini, L., 2016b. Application of digital volume correlation to study the efficacy of prophylactic vertebral augmentation. *Clinical biomechanics* 39, 14-24.
- Danesi, V., Zani, L., Scheele, A., Berra, F., Cristofolini, L., 2014. Reproducible reference frame for in vitro testing of the human vertebrae. *Journal of biomechanics* 47, 313-318.
- de Bakker, P.M., Manske, S.L., Ebacher, V., Oxland, T.R., Cripton, P.A., Guy, P., 2009. During sideways falls proximal femur fractures initiate in the superolateral cortex: evidence from high-speed video of simulated fractures. *Journal of biomechanics* 42, 1917-1925.
- de Magalhaes, F., Vannozzi, G., Gatta, G., Fantozzi, S., 2015. Wearable inertial sensors in swimming motion analysis: a systematic review. *J Sports Sci* 2015, 7.
- Dickinson, A.S., Taylor, A.C., Browne, M., 2012. The influence of acetabular cup material on pelvis cortex surface strains, measured using digital image correlation. *Journal of biomechanics* 45, 719-723.
- Dickinson, A.S., Taylor, A.C., Ozturk, H., Browne, M., 2011. Experimental validation of a finite element model of the proximal femur using digital image correlation and a composite bone model. *Journal of biomechanical engineering* 133, 014504.
- Donzelli, S., Poma, S., Balzarini, L., Borboni, A., Respizzi, S., Villafane, J.H., Zaina, F., Negrini, S., 2015. State of the art of current 3-D scoliosis classifications: a systematic review from a clinical perspective. *J Neuroeng Rehabil* 12, 91.
- Doube, M., Klosowski, M.M., Arganda-Carreras, I., Cordeliers, F., Dougherty, R.P., Jackson, J., Schmid, B., Hutchinson, J., Shefelbine, S., 2010. BoneJ: free and extensible bone image analysis in ImageJ. *Bone* 47, 1076-1079.
- Dreischarf, M., Albiol, L., Zander, T., Arshad, R., Graichen, F., Bergmann, G., Schmidt, H., Rohlmann, A., 2015. In vivo implant forces acting on a vertebral body replacement during upper body flexion. *Journal of biomechanics* 48, 560-565.
- Esses, S.I., Sachs, B.L., Dreyzin, V., 1993. Complications associated with the technique of pedicle screw fixation. A selected survey of ABS member. *Spine* 18, 2231-2238.
- Estrada, J.B., Franck, C., 2015. Intuitive Interface for the Quantitative Evaluation of Speckle Patterns for Use in Digital Image and Volume Correlation Techniques. *Journal of Applied Mechanics* 82, 095001.
- Eswaran, S.K., Gupta, A., Keaveny, T.M., 2007. Locations of bone tissue at high risk of initial failure during compressive loading of the human vertebral body. *Bone* 41, 733-739.
- Evans, S.L., Holt, C.A., 2009. Measuring the mechanical properties of human skin in vivo using digital image correlation and finite element modelling. *The Journal of Strain Analysis for Engineering Design* 44, 337-345.
- Fairbank, J., Frost, H., Wilson-MacDonald, J., Yu, L.M., Barker, K., Collins, R., 2005. Randomised controlled trial to compare surgical stabilisation of the lumbar spine

with an intensive rehabilitation programme for patients with chronic low back pain: the MRC spine stabilisation trial. *Br Med J* 330.

Ferrar, L., Jiang, G., Adams, J., Eastell, R., 2005. Identification of vertebral fractures: An update. *Osteoporosis International* 16, 717-728.

Field, R.E., Rushton, N., 1989. Proximal femoral surface strain gauge analysis of a new epiphyseal prosthesis. *J. Biomed. Eng.* 11, 123-129.

Freddi, A., Olmi, G., Cristofolini, L., 2015. *Experimental Stress Analysis for Materials and Structures: Stress Analysis Models for Developing Design Methodologies*. Springer.

Fujimori, T., Iwasaki, M., Nagamoto, Y., Matsuo, Y., Ishii, T., Sugiura, T., Kashii, M., Murase, T., Sugamoto, K., Yoshikawa, H., 2014. Kinematics of the thoracic spine in trunk lateral bending: in vivo three-dimensional analysis. *The spine journal : official journal of the North American Spine Society* 14, 1991-1999.

Fung, Y.C., 1980. *Bone and cartilage, Biomechanics - Mechanical properties of living tissues*. Springer Verlag, New York, pp. 383-415.

Galbusera, F., Schmidt, H., Noailly, J., Malandrino, A., Lacroix, D., Wilke, H.J., Shirazi-Adl, A., 2011. Comparison of four methods to simulate swelling in poroelastic finite element models of intervertebral discs. *J Mech Behav Biomed Mater* 4, 1234-1241.

Gao, J., Xu, W., Geng, J., 2006. 3D shape reconstruction of teeth by shadow speckle correlation method. *Optics and Lasers in Engineering* 44, 455-465.

Gao, Z., Desai, J.P., 2010. Estimating zero-strain states of very soft tissue under gravity loading using digital image correlation. *Med Image Anal* 14, 126-137.

Gates, M., Lambros, J., Heath, M.T., 2010. Towards High Performance Digital Volume Correlation. *Experimental Mechanics* 51, 491-507.

Genovese, K., Casaletto, L., Humphrey, J.D., Lu, J., 2014. Digital image correlation-based point-wise inverse characterization of heterogeneous material properties of gallbladder in vitro. *Proceedings of the Royal Society A: Mathematical, Physical and Engineering Sciences* 470, 20140152-20140152.

Genovese, K., Casaletto, L., Rayas, J.A., Flores, V., A., M., 2013a. Stereo-Digital Image Correlation (DIC) measurements with a single camera using biprism. *Optics and Lasers in Engineering* 51, 278 - 285.

Genovese, K., Collins, M.J., Lee, Y.U., Humphrey, J.D., 2012. Regional Finite Strains in an Angiotensin-II Induced Mouse Model of Dissecting Abdominal Aortic Aneurysms. *Cardiovascular Engineering and Technology* 3, 194-202.

Genovese, K., Humphrey, J.D., 2015. Multimodal optical measurement in vitro of surface deformations and wall thickness of the pressurized aortic arch. *J Biomed Opt* 20, 046005.

Genovese, K., Lee, Y.-U., Lee, A.Y., Humphrey, J.D., 2013b. An improved panoramic digital image correlation method for vascular strain analysis and material characterization. *Journal of Mechanical Behavior of Biomedical Materials* 27, 132-142.

- Genovese, K., Lee, Y.U., Humphrey, J.D., 2011. Novel optical system for in vitro quantification of full surface strain fields in small arteries: II. Correction for refraction and illustrative results. *Computer Methods in Biomechanics and Biomedical Engineering* 14, 227-237.
- Genovese, K., Montes, A., Martinez, A., Evans, S.L., 2015. Full-surface deformation measurement of anisotropic tissues under indentation. *Med Eng Phys* 37, 484-493.
- Ghosh, R., Gupta, S., Dickinson, A., Browne, M., 2012. Verification of the Digital Image Correlation Technique for Bone Surface Strain Measurements. *Journal of biomechanics* 45, S277.
- Gilchrist, S., Guy, P., Crompton, P.A., 2013. Development of an inertia-driven model of sideways fall for detailed study of femur fracture mechanics. *Journal of biomechanical engineering* 135, 121001.
- Gillard, F., Boardman, R., Mavrogordato, M., Hollis, D., Sinclair, I., Pierron, F., Browne, M., 2014. The application of digital volume correlation (DVC) to study the microstructural behaviour of trabecular bone during compression. *J Mech Behav Biomed Mater* 29, 480-499.
- Gillespie, K.A., Dickey, J.P., 2004. Biomechanical Role of Lumbar Spine Ligaments in flexion and extension: determination using a parallel linkage robot and a porcine model. *Spine* 29, 1208-1216.
- Goel, V.K., Panjabi, M.M., Patwardhan, A.G., Dooris, A.P., Serhan, H., 2006. Test Protocols for Evaluation of Spinal Implants. *Journal of Bone and Joint Surgery* 88, 103-109.
- Grassi, L., Isaksson, H., 2015. Extracting accurate strain measurements in bone mechanics: A critical review of current methods. *J Mech Behav Biomed Mater* 50, 43-54.
- Grassi, L., Vaananen, S.P., Amin Yavari, S., Weinans, H., Jurvelin, J.S., Zadpoor, A.A., Isaksson, H., 2013. Experimental validation of finite element model for proximal composite femur using optical measurements. *J Mech Behav Biomed Mater* 21, 86-94.
- Grassi, L., Vaananen, S.P., Yavari, S.A., Jurvelin, J.S., Weinans, H., Ristinmaa, M., Zadpoor, A.A., Isaksson, H., 2014. Full-field strain measurement during mechanical testing of the human femur at physiologically relevant strain rates. *Journal of biomechanical engineering* 136.
- Gray, H., 1858. *Gray's anatomy*.
- Gustafson, H., Siegmund, G., Crompton, P., 2016. Comparison of Strain Rosettes and Digital Image Correlation for Measuring Vertebral Body Strain. *Journal of biomechanical engineering* 138, 054501-054501/054501-054506.
- Haddadi, H., Belhabib, S., 2008. Use of rigid-body motion for the investigation and estimation of the measurement errors related to digital image correlation technique. *Optics and Lasers in Engineering* 46, 185-196.
- Han, Y., Kim, D.W., Kwon, H.J., 2012. Application of digital image cross-correlation and smoothing function to the diagnosis of breast cancer. *J Mech Behav Biomed Mater* 14, 7-18.

- Hansson, T.H., Keller, T.S., Spengler, D.M., 1987. Mechanical behavior of the human lumbar spine. II. Fatigue strength during dynamic compressive loading. *J Orthop Res* 5, 479-487.
- Hardisty, M., Akens, M., Hojjat, S., Yee, A., Whyne, C., 2012. Quantification of the Effect of Osteolytic Metastases on Bone Strain within Whole Vertebrae Using Image Registration. *J Orthop Res* 30, 1032-1039.
- Hardisty, M., Akens, M., Yee, A., Whyne, C., 2010. Image Registration Demonstrates the Growth Plate has a Variable Affect on Vertebral Strain. *Annals of Biomedical Engineering* 38, 2948-2955.
- Hardisty, M.R., Whyne, C.M., 2009. Whole bone strain quantification by image registration: a validation study. *Journal of biomechanical engineering* 131, 064502.
- Helgason, B., Gilchrist, S., Ariza, O., Chak, J.D., Zheng, G., Widmer, R.P., Ferguson, S.J., Guy, P., Crompton, P.A., 2014. Development of a balanced experimental-computational approach to understanding the mechanics of proximal femur fractures. *Med Eng Phys* 36, 793-799.
- Helm, J.D., McNeill, S.R., Sutton, M.A., 1996. Improved three-dimensional image correlation for surface displacement measurement. *Optical Engineering* 35, 1911 - 1920.
- Hild, F., Roux, S., 2006. Digital Image Correlation: from Displacement Measurement to Identification of Elastic Properties - a Review. *Strain* 42, 69 - 80.
- Hild, F., Roux, S., 2012. Comparison of local and global approaches to digital image correlation. *Experimental Mechanics* 52, 1503-1519.
- Hindle, R.J., Pearcy, M., Cross, A., 1990. Mechanical function of the human lumbar interspinous and supraspinous ligament. *J Biomed Eng* 12, 340-344.
- Hoc, T., Henry, L., Verdier, M., Aubry, D., Sedel, L., Meunier, A., 2006. Effect of microstructure on the mechanical properties of Haversian cortical bone. *Bone* 38, 466-474.
- Hokka, M., Mirow, N., Nagel, H., Iqrsusi, M., Vogt, S., Kuokkala, V.T., 2015. In-vivo deformation measurements of the human heart by 3D Digital Image Correlation. *Journal of biomechanics* 48, 2217-2220.
- Holroyd, C., Cooper, C., Dennison, E., 2008. Epidemiology of osteoporosis. *Best Practice & Research Clinical Endocrinology & Metabolism* 22, 671-685.
- Holsgrove, T.P., Cazzola, D., Preatoni, E., Trewartha, G., Miles, A.W., Gill, H.S., Gheduzzi, S., 2015. An investigation into axial impacts of the cervical spine using digital image correlation. *The spine journal : official journal of the North American Spine Society* 15, 1856-1863.
- Holzapfel, G.A., 2006. Determination of material models for arterial walls from uniaxial extension tests and histological structure. *Journal of theoretical biology* 238, 290-302.
- Hussein, A.I., Barbone, P.E., Morgan, E.F., 2012. Digital Volume Correlation for Study of the Mechanics of Whole Bones. *Procedia IUTAM* 4, 116-125.

- Hussein, A.I., Mason, Z.D., Morgan, E.F., 2013. Presence of intervertebral discs alters observed stiffness and failure mechanisms in the vertebra. *Journal of biomechanics* 46, 1683-1688.
- Johnell, O., Kanis, J.A., 2006. An estimate of the worldwide prevalence and disability associated with osteoporotic fractures. *Osteoporos Int* 17, 1726-1733.
- Jones, A.C., Wilcox, R.K., 2008. Finite element analysis of the spine: towards a framework of verification, validation and sensitivity analysis. *Med Eng Phys* 30, 1287-1304.
- Jordan, J., Konstantinou, K., O'Dowd, J., 2011. Herniated lumbar disc. *Clinical Evidence* Jun 28, 2011.
- Jungmann, R., Szabo, M.E., Schitter, G., Tang, R.Y., Vashishth, D., Hansma, P.K., Thurner, P.J., 2011. Local strain and damage mapping in single trabeculae during three-point bending tests. *J Mech Behav Biomed Mater* 4, 523-534.
- Juszczak, M.M., Cristofolini, L., Viceconti, M., 2011. The human proximal femur behaves linearly elastic up to failure under physiological loading conditions. *Journal of biomechanics* 44, 2259-2266.
- Jutte, P.C., Castelein, R.M., 2002. Complications of pedicle screws in lumbar and lumbosacral fusions in 105 consecutive primary operations. *Eur Spine J* 11, 594-598.
- Karaguzel, G., Holick, M.F., 2010. Diagnosis and treatment of osteopenia. *Rev Endocr Metab Disord* 11, 237-251.
- Karakolis, T., Callaghan, J.P., 2015. Localized strain measurements of the intervertebral disc annulus during biaxial tensile testing. *Comput Methods Biomech Biomed Engin* 18, 1737-1743.
- Karimi, A., Navidbakhsh, M., Haghghatnama, M., Haghi, A.M., 2015. Determination of the axial and circumferential mechanical properties of the skin tissue using experimental testing and constitutive modeling. *Comput Methods Biomech Biomed Engin* 18, 1768-1774.
- Keaveny, Tania, P.P., Crawford, R.P., David, L.K., Albert, L., 1997. Systematic and random errors in compression testing of trabecular bone. *Journal of Orthopaedic Research* 15, 101-110.
- Keaveny, T.M., McClung, M.R., Genant, H.K., Zanchetta, J.R., Kendler, D., Brown, J.P., Goemaere, S., Recknor, C., Brandi, M.L., Eastell, R., Kopperdahl, D.L., Engelke, K., Fuerst, T., Radcliffe, H.S., Libanati, C., 2014. Femoral and vertebral strength improvements in postmenopausal women with osteoporosis treated with denosumab. *J Bone Miner Res* 29, 158-165.
- Kelleher, J.E., Zhang, K., Siegmund, T., Chan, R.W., 2010. Spatially varying properties of the vocal ligament contribute to its eigenfrequency response. *J Mech Behav Biomed Mater* 3, 600-609.
- Kelley, C.T., 1999. Iterative methods for Optimization.
- Kelly, T.A., Ng, K.W., Wang, C.C., Ateshian, G.A., Hung, C.T., 2006. Spatial and temporal development of chondrocyte-seeded agarose constructs in free-

swelling and dynamically loaded cultures. *Journal of biomechanics* 39, 1489-1497.

Khodabakhshi, G., Walker, D., Scutt, A., Way, L., Cowie, R.M., Hose, D.R., 2013. Measuring three-dimensional strain distribution in tendon. *J Microsc* 249, 195-205.

Kim, J.H., Badel, P., Duprey, A., Favre, J.P., Avril, S., 2011. Characterisation of failure in human aortic tissue using digital image correlation. *Computer Methods in Biomechanics and Biomedical Engineering* 14, 73-74.

Lanyon, I.E., 1980. Bone remodelling, mechanical stress, and osteoporosis, in: De Luca, H.F. (Ed.), *Osteoporosis*. University Park Press, Baltimore, pp. 129-138.

Lanyon, L.E., Hampson, W.G.J., Goodship, A.E., Shah, J.S., 1975. Bone deformation recorded in vivo from strain gauges attached to the human tibial shaft. *Acta Orthop. Scand.* 46, 256-268.

Larrabee, W.J., 1986. A finite element model of skin deformation. I. Biomechanics of skin and soft tissue: a review. *Laryngoscope* 96, 399-405.

Lava, P., Cooreman, S., Coppieters, S., De Strycker, M., Debruyne, D., 2009. Assessment of measuring errors in DIC using deformation fields generated by plastic FEA. *Optics and Lasers in Engineering* 47, 747-753.

Lava, P., Cooreman, S., Debruyne, D., 2010. Study of systematic errors in strain fields obtained via DIC using heterogeneous deformation generated by plastic FEA. *Optics and Lasers in Engineering* 48, 457-468.

Lava, P., Coppieters, S., Wang, Y., Van Houtte, P., Debruyne, D., 2011. Error estimation in measuring strain fields with DIC on planar sheet metal specimens with a non-perpendicular camera alignment. *Optics and Lasers in Engineering* 49, 57-65.

Leclerc, H., Perle, J.N., Hild, F., Roux, S., 2012. Digital volume correlation: what are the limits to the spatial resolution? *Mechanics & Industry* 13, 361-371.

Lecompte, D., Bossuyt, S., Cooreman, S., Sol, H., Vantomme, J., 2007. Study and generation of optimal speckle patterns for DIC, SEM Annual Conference & Exposition on Experimental and Applied Mechanics.

Lecompte, D., Smits, A., Bossuyt, S., Sol, H., Vantomme, J., Van Hemelrijck, D., Habraken, A.M., 2006. Quality assessment of speckle patterns for digital image correlation. *Optics and Lasers in Engineering* 44, 1132-1145.

Lee, J., Park, Y.-S., 2016. Proximal Junctional Kyphosis: Diagnosis, Pathogenesis, and Treatment. *Asian Spine Journal* 10, 593-600.

Lee, M.J., Bransford, R.J., Bellabarda, C., Chapman, J.R., Cohen, A.M., Harrington, R.M., Ching, R.P., 2010. The Effect of Bilateral Laminotomy Versus Laminectomy on the Motion and Stiffness of the Human Lumbar Spine: A Biomechanical Comparison. *Spine* 35, 1789-1793.

Lee, S., Harris, K.G., Nassif, J., Goel, V., Clark, C., 1993. In vivo kinematics of the cervical spine. Part I: Development of a roentgen stereophotogrammetric technique using metallic markers and assessment of its accuracy. *J Spinal Disord* 6, 522-534.

- Lerebours, C., Buenzli, P.R., Scheiner, S., Pivonka, P., 2015. A multiscale mechanobiological model of bone remodelling predicts site-specific bone loss in the femur during osteoporosis and mechanical disuse. *Biomech Model Mechanobiol* 15, 1.
- Levchuk, A., Zwahlen, A., Weigt, C., Lambers, F.M., Badilatti, S.D., Schulte, F.A., Kuhn, G., Muller, R., 2014. The Clinical Biomechanics Award 2012 - presented by the European Society of Biomechanics: large scale simulations of trabecular bone adaptation to loading and treatment. *Clinical biomechanics* 29, 355-362.
- Li, J., Fok, A.S., Satterthwaite, J., Watts, D.C., 2009. Measurement of the full-field polymerization shrinkage and depth of cure of dental composites using digital image correlation. *Dent Mater* 25, 582-588.
- Libertiaux, V., Pascon, F., Cescotto, S., 2011. Experimental verification of brain tissue incompressibility using digital image correlation. *J Mech Behav Biomed Mater* 4, 1177-1185.
- Lionello, G., Cristofolini, L., 2014. A practical approach to optimizing the preparation of speckle patterns for digital-image correlation. *Measurement Science and Technology* 25, 107001.
- Lionello, G., Sirieix, C., Baleani, M., 2014. An effective procedure to create a speckle pattern on biological soft tissue for digital image correlation measurements. *J Mech Behav Biomed Mater* 39, 1-8.
- Little, E.G., Tocher, D., O'Donnel, P., 1990. Strain gauge reinforcement of plastics. *Strain* 26, 91-98.
- Liu, L., Morgan, E.F., 2007. Accuracy and precision of digital volume correlation in quantifying displacements and strains in trabecular bone. *Journal of biomechanics* 40, 3516-3520.
- Lochmüller, E.M., Burklein, D., Kuhn, V., Glaser, C., Muller, R., Gluer, C.C., Eckstein, F., 2002. Mechanical strength of the thoracolumbar spine in the elderly: prediction from in situ dual-energy X-ray absorptiometry, quantitative computed tomography (QCT), upper and lower limb peripheral QCT, and quantitative ultrasound. *Bone* 31, 77-84.
- Lu, Y., Boudiffa, M., Dall'Ara, E., Bellantuono, I., Viceconti, M., 2015. Evaluation of in-vivo measurement errors associated with micro-computed tomography scans by means of the bone surface distance approach. *Med Eng Phys* 37, 1091-1097.
- Luca, A., Ottardi, C., Sasso, M., Prosdocimo, L., La Barbera, L., Brayda-Bruno, M., Galbusera, F., Villa, T., 2016. Instrumentation failure following pedicle subtraction osteotomy: the role of rod material, diameter, and multi-rod constructs. *Eur Spine J*.
- Luo, P.F., Chao, Y.J., Sutton, M.A., 1994. Application of stereo vision to three-dimensional deformation analyses in fracture experiments. *Optical Engineering* 33, 981 - 990.
- Luo, P.F., Chao, Y.J., Sutton, M.A., Peters, W.H., 1992. Accurate Measurement of Three-dimensional Deformations in Deformable and Rigid Bodies Using Computer Vision. *Experimental Mechanics* June 1993, 123 - 132.

- Luyckx, T., Verstraete, M., De Roo, K., De Waele, W., Bellemans, J., Victor, J., 2014. Digital image correlation as tool for 3D strain analysis in human tendon tissue. *The journal of experimental orthopedics* 1.
- Madi, K., Tozzi, G., Zhang, Q.H., Tong, J., Cossey, A., Au, A., Hollis, D., Hild, F., 2013. Computation of full-field displacements in a scaffold implant using digital volume correlation and finite element analysis. *Med Eng Phys* 35, 1298-1312.
- Malandrino, A., Noailly, J., Lacroix, D., 2014. Numerical exploration of the combined effect of nutrient supply, tissue condition and deformation in the intervertebral disc. *Journal of biomechanics* 47, 1520-1525.
- Malandrino, A., Planell, J.A., Lacroix, D., 2009. Statistical factorial analysis on the poroelastic material properties sensitivity of the lumbar intervertebral disc under compression, flexion and axial rotation. *Journal of biomechanics* 42, 2780-2788.
- Mann, K.A., Miller, M.A., Cleary, R.J., Janssen, D., Verdonshot, N., 2008. Experimental micromechanics of the cement-bone interface. *J Orthop Res* 26, 872-879.
- Marino Cugno Garrano, A., La Rosa, G., Zhang, D., Niu, L.N., Tay, F.R., Majd, H., Arola, D., 2012. On the mechanical behavior of scales from *Cyprinus carpio*. *J Mech Behav Biomed Mater* 7, 17-29.
- Matz, P.G., Meagher, R.J., Lamer, T., Tontz, W.L., Jr., Annaswamy, T.M., Cassidy, R.C., Cho, C.H., Dougherty, P., Easa, J.E., Enix, D.E., Gunnoe, B.A., Jallo, J., Julien, T.D., Maserati, M.B., Nucci, R.C., O'Toole, J.E., Rosolowski, K., Sembrano, J.N., Villavicencio, A.T., Witt, J.P., 2016. Guideline summary review: An evidence-based clinical guideline for the diagnosis and treatment of degenerative lumbar spondylolisthesis. *The spine journal : official journal of the North American Spine Society* 16, 439-448.
- McKinley, T.O., Bay, B.K., 2003. Trabecular bone strain changes associated with subchondral stiffening of the proximal tibia. *Journal of biomechanics* 36, 155-163.
- Metzger, M.F., Robinson, S.T., Svet, M.T., Liu, J.C., Acosta, F.L., 2016. Biomechanical Analysis of the Proximal Adjacent Segment after Multilevel Instrumentation of the Thoracic Spine: Do Hooks Ease the Transition? *Global Spine J* 6, 335-343.
- Mobilio, S., Boscherini, F., Meneghini, C., 2015. *Synchrotron Radiation: Basics, Methods and Applications*.
- Moerman, K.M., Holt, C.A., Evans, S.L., Simms, C.K., 2009. Digital image correlation and finite element modelling as a method to determine mechanical properties of human soft tissue in vivo. *Journal of biomechanics* 42, 1150-1153.
- Morita, M., Ebihara, A., Itoman, M., Sasada, T., 1994. Progression of osteoporosis in cancellous bone depending on trabecular structure. *Annals Biomed. Eng.* 22, 532-539.
- Myers, E.R., Wilson, S.E., 1997. Biomechanics of osteoporosis and vertebral fracture. *Spine* 22, 25S-31S.
- Myers, K.M., Coudrillier, B., Boyce, B.L., Nguyen, T.D., 2010. The inflation response of the posterior bovine sclera. *Acta biomaterialia* 6, 4327-4335.

- Myers, K.M., Paskaleva, A.P., House, M., Socrate, S., 2008. Mechanical and biochemical properties of human cervical tissue. *Acta biomaterialia* 4, 104-116.
- Nagarkatti, D.G., McKeon, B.P., Donahue, B.S., Fulkerson, J.P., 2001. Mechanical Evaluation of a Soft Tissue Interference Screw in Free Tendon Anterior Cruciate Ligament Graft Fixation. *The American Journal of Sports Medicine* 29, 67 - 71.
- Narmoneva, D.A., 2002. Direct Measurement of the Poisson's Ratio of Human Patella Cartilage in Tension. *Journal of biomechanical engineering* 124, 223.
- Nazarian, A., Müller, R., 2004. Time-lapsed microstructural imaging of bone failure behavior. *Journal of biomechanics* 37, 55-65.
- Nicolella, D.P., Bonewald, L.F., Moravits, D.E., Lankford, J., 2005. Measurement of microstructural strain in cortical bone. *Eur J Morphol* 42, 23-29.
- Nicolella, D.P., Moravits, D.E., Gale, A.M., Bonewald, L.F., Lankford, J., 2006. Osteocyte lacunae tissue strain in cortical bone. *Journal of biomechanics* 39, 1735-1743.
- Nicolella, D.P., Nicholls, A.E., Lankford, J., Davy, D.T., 2001. Machine vision photogrammetry: a technique for measurement of microstructural strain in cortical bone. *Journal of biomechanics* 34, 135 - 139.
- Ning, J., Xu, S., Wang, Y., Lessner, S.M., Sutton, M.A., Anderson, K., Bischoff, J.E., 2010. Deformation measurements and material property estimation of mouse carotid artery using a microstructure-based constitutive model. *Journal of biomechanical engineering* 132, 121010.
- Noailly, J., Wilke, H.J., Planell, J.A., Lacroix, D., 2007. How does the geometry affect the internal biomechanics of a lumbar spine bi-segment finite element model? Consequences on the validation process. *Journal of biomechanics* 40, 2414-2425.
- O'Connell, G.D., Vresilovic, E.J., Elliott, D.M., 2011. Human intervertebral disc internal strain in compression: the effect of disc region, loading position, and degeneration. *J Orthop Res* 29, 547-555.
- Oda, I.M.D., Abumi, K.M.D., Cunningham, B.W.M., Kaneda, K.M.D.a., McAfee, P.C.M.D., 2002. An In Vitro Human Cadaveric Study Investigating the Biomechanical Properties of the Thoracic Spine. *Spine* 27, E64-E70.
- Öhman, C., Dall'Ara, E., Baleani, M., Van Sint Jan, S., Viceconti, M., 2008. The effects of embalming using a 4% formalin solution on the compressive mechanical properties of human cortical bone. *Clinical biomechanics* 23, 1294-1298.
- Okotie, G., Duenwald-Kuehl, S., Kobayashi, H., Wu, M.J., Vanderby, R., 2012. Tendon strain measurements with dynamic ultrasound images: evaluation of digital image correlation. *Journal of biomechanical engineering* 134, 024504.
- Op Den Buijs, J., Dragomir-Daescu, D., 2011. Validated finite element models of the proximal femur using two-dimensional projected geometry and bone density. *Computer methods and programs in biomedicine* 104, 168-174.
- Ottenio, M., Tran, D., Ni Annaidh, A., Gilchrist, M.D., Bruyere, K., 2015. Strain rate and anisotropy effects on the tensile failure characteristics of human skin. *J Mech Behav Biomed Mater* 41, 241-250.

- Oxland, T.R., Lund, T., 2000. Biomechanics of stand-alone cages and cages in combination with posterior fixation: a literature review. *European spine journal* 9, S095-S101.
- Pacureanu, A., Langer, M., Boller, E., Tafforeau, P., Peyrin, F., 2012. Nanoscale imaging of the bone cell network with synchrotron X-ray tomography: optimization of acquisition setup. *Med Phys* 39, 2229-2238.
- Palanca, M., Brugo, T.M., Cristofolini, L., 2015a. Use of Digital Image Correlation to Understand the Biomechanics of the Vertebra. *Journal Of Mechanics in Medicine and Biology* 15, 1540004-1540001/1540004-1540010.
- Palanca, M., Tozzi, G., Cristofolini, L., 2016a. The Use Of Digital Image Correlation In The Blomechanical Field: A Review. *Inter Biomech* 3, 1-21.
- Palanca, M., Tozzi, G., Cristofolini, L., Viceconti, M., Dall'Ara, E., 2015b. 3D Local Measurements of Bone Strain and Displacement: Comparison of Three Digital Volume Correlation Approaches. *J. Biomech Eng. (ASME)* 137, 071006-071001/071006-071014.
- Palanca, M., Tozzi, G., Dall'Ara, E., Curto, M., Innocente, F., Danesi, V., Cristofolini, L., 2016b. Digital Volume Correlation can be used to estimate local strains in natural and augmented vertebrae: An organ-level study. *Journal of biomechanics* 49, 3882-3890.
- Pallottino, G.V., 2011. *Il rumore elettrico: dalla fisica alla progettazione*. Ed. Springer.
- Pan, B., Qian, K., Xie, H., Asundi, A., 2009. Two-dimensional digital image correlation for in-plane displacement and strain measurement: a review. *Measurement Science and Technology* 20, 062001.
- Pan, B., Wang, B., Wu, D., Lubineau, G., 2014. An efficient and accurate 3D displacements tracking strategy for digital volume correlation. *Optics and Lasers in Engineering* 58, 126-135.
- Pan, B., Xie, H.M., Wang, Z., Qian, K.M., 2008. Study on subset size selection in digital image correlation for speckle patterns. *Opt. Express* 16, 7037 - 7048.
- Pan, B., Yu, L., Wu, D., 2013. High-Accuracy 2D Digital Image Correlation Measurements with Bilateral Telecentric Lenses: Error Analysis and Experimental Verification. *Experimental Mechanics* 53, 1719-1733.
- Panjabi, M.M., 2007. Hybrid multidirectional test method to evaluate spinal adjacent-level effects. *Clinical biomechanics* 22, 257-265.
- Panjabi, M.M., Brand, R.I., White, A.A., 1976. Mechanical properties of the human thoracic spine. *J. Bone Jt. Surg. Am.* 58, 542-552.
- Panjabi, M.M., Hausfeld, J.N., White, A.A., 2009. A Biomechanical Study of the Ligamentous Stability of the Thoracic Spine in Man. *Acta Orthopaedica Scandinavica* 52, 315-326.
- Panjabi, M.M., Krag, M.H., Goel, V.K., 1981. A technique for measurement and description of three-dimensional six degree-of-freedom motion of a body joint with an application to the human spine. *Journal of biomechanics* 14, 447-449, 451-460.

- Panjabi, M.M., Oxland, T.R., Yamamoto, I., Crisco, J.J., 1994. Mechanical behavior of the human lumbar and lumbosacral spine as shown by three-dimensional load-displacement curves. *J Bone Joint Surg Am* 76, 413-424.
- Patterson, E.A., Hack, E., Brailly, P., Burguete, R.L., Saleem, Q., Siebert, T., Tomlinson, R.A., Whelan, M.P., 2007. Calibration and evaluation of optical systems for full-field strain measurement. *Optics and Lasers in Engineering* 45, 550-564.
- Peters, W.H., Ranson, W.F., 1982. Digital imaging techniques in experimental stress analysis. *Optical Engineering* 21, 427 - 431.
- Pihlajamaki, H., Myllynen, P., Bostman, O., 1997. Complications of transpedicular lumbosacral fixation for non-traumatic disorders. *The Journal of Bone and Joint Surgery* 79-B, 183-189.
- Pintar, F.A., Yoganandan, N., Pesigan, M., Reinartz, J., Sances, J.A., Cusick, J.F., 1995. Cervical Vertebral Strain Measurements Under Axial and Eccentric Loading. *Journal of biomechanical engineering* 117, 474-478.
- Pollintine, P., van Tunen, M.S., Luo, J., Brown, M.D., Dolan, P., Adams, M.A., 2010. Time-dependent compressive deformation of the ageing spine: relevance to spinal stenosis. *Spine (Phila Pa 1976)* 35, 386-394.
- Polly, D.W., Glassman, S.D., Schwender, J.D., Shaffrey, C.I., Branch, C., Burkus, J.K., Gornet, M.F., 2007. SF-36 PCS benefit-cost ration of lumbar fusion comparison to other surgical interventions: a thought experiment. *Spine* 32, S20-S26.
- Post, D., Han, B., 2008. Moiré interferometry, in: Springer (Ed.), *Handbook on experimental mechanics*, NY.
- Preece, S.J., Mason, D., Bramah, C., 2016. The coordinated movement of the spine and pelvis during running. *Hum Mov Sci* 45, 110-118.
- Pyne, J.D., Genovese, K., Casaletto, L., Vande Geest, J.P., 2014. Sequential-digital image correlation for mapping human posterior sclera and optic nerve head deformation. *Journal of biomechanical engineering* 136, 021002.
- Reitmaier, S., Shirazi-Adl, A., Bashkuev, M., Wilke, H.J., Gloria, A., Schmidt, H., 2012. In vitro and in silico investigations of disc nucleus replacement. *J R Soc Interface* 9, 1869-1879.
- Ritzel, H., Amling, M., Posl, M., Hahn, M., Delling, G., 1997. The thickness of human vertebral cortical bone and its changes in aging and osteoporosis: a histomorphometric analysis of the complete spinal column from thirty-seven autopsy specimens. *J Bone Miner Res* 12, 89-95.
- Roberts, B.C., Perilli, E., Reynolds, K.J., 2014. Application of the digital volume correlation technique for the measurement of displacement and strain fields in bone: A literature review. *Journal of biomechanics* 47, 923-934.
- Rohlmann, A., Bergmann, G., Graichen, F., 1994. A spinal fixation device for in vivo load measurement. *J Biomech.* 22, 961-967.
- Rohlmann, A., Bergmann, G., Graichen, F., 1997. Loads on an internal spinal fixation device during walking. *Journal of biomechanics* 30, 41-47.

- Rohlmann, A., Bergmann, G., Graichen, F., 1999. Loads on internal spinal fixators measured in different body positions. *European spine journal* 8, 354-359.
- Rohlmann, A., Gabel, U., Graichen, F., Bender, A., Bergmann, G., 2007. An instrumented implant for vertebral body replacement that measures loads in the anterior spinal column. *Medical Engineering & Physics* 29, 580-585.
- Rohlmann, A., Neller, S., Claes, L., Bergmann, G., Wilke, H.J., 2001. Influence of a follower load on intradiscal pressure and intersegmental rotation of the lumbar spine. *Spine (Phila Pa 1976)* 26, E557-561.
- Ross, S.M., 2003. Peirce's criterion for the elimination of suspect experimental data. *J. Engineering Technology* 2003, 1-12.
- Roux, S., Hild, F., Viot, P., Bernard, D., 2008. Three-dimensional image correlation from X-ray computed tomography of solid foam. *Composites Part A: Applied Science and Manufacturing* 39, 1253-1265.
- Sachs, C., Fabritius, H., Raabe, D., 2006. Experimental investigation of the elastic-plastic deformation of mineralized lobster cuticle by digital image correlation. *J Struct Biol* 155, 409-425.
- Scarano, F., 2013. Tomographic PIV: principles and practice. *Measurement Science and Technology* 24, 012001.
- Schileo, E., Dall'ara, E., Taddei, F., Malandrino, A., Schotkamp, T., Baleani, M., Viceconti, M., 2008a. An accurate estimation of bone density improves the accuracy of subject-specific finite element models. *Journal of biomechanics* 41, 2483-2491.
- Schileo, E., Taddei, F., Cristofolini, L., Viceconti, M., 2008b. Subject-specific finite element models implementing a maximum principal strain criterion are able to estimate failure risk and fracture location on human femurs tested in vitro. *Journal of biomechanics* 41, 356-367.
- Schmidt, T., Tyson, J., Galanulis, K., 2003. Full-field dynamic displacement and strain measurement using advanced 3D image correlation photogrammetry: part I. *Experimental techniques* 27, 47 - 50.
- Schultheiss, M., Hartwig, E., Sarkar, M., Kinzl, L., Claes, L., Wilke, H.J., 2006. Biomechanical in vitro comparison of different mono- and bisegmental anterior procedures with regard to the strategy for fracture stabilisation using minimally invasive techniques. *Eur Spine J* 15, 82-89.
- Sebastian, C., Patterson, E.A., 2012. Calibration of a Digital Image Correlation System. *Experimental Techniques*, no-no.
- Shah, J., Hampson, W., Jayson, M., 1978. The distribution of surface strain in the cadaveric lumbar spine. *J Bone Joint Surg Br* 60-B, 246-251.
- Shah, J.S., Coggins, J., Rogers, R., Jayson, M.I., Hampson, W.G., 1976. Surface strain distribution in isolated single lumbar vertebrae. *Ann Rheum Dis* 35, 51-55.
- Shim, V.P.W., Liu, J.F., Lee, V.S., 2006. A Technique for Dynamic Tensile Testing of Human Cervical Spine Ligaments. *Experimental Mechanics* 46, 77-89.
- Shin, T.J., Vito, R.P., Johnson, L.W., McCarey, B.E., 1997. The distribution of strain in the human cornea. *Journal of biomechanics* 30, 497-503.

- Silva, M.J., 2007. Biomechanics of osteoporotic fractures. *Injury* 38 Suppl 3, S69-76.
- Silva, M.J., Keaveny, T.M., Hayes, W.C., 1997. Load sharing between the shell and centrum in the lumbar vertebral body. *Spine (Phila Pa 1976)* 22, 140-150.
- Singer, K., Edmondston, S., Day, R., Breidahl, P., Price, R., 1995. Prediction of thoracic and lumbar vertebral body compressive strength: correlations with bone mineral density and vertebral region. *Bone* 17, 167-174.
- Smith, J.S., Sansur, C.A., Donaldson, W.F., 3rd, Perra, J.H., Mudiya, R., Choma, T.J., Zeller, R.D., Knapp, D.R., Jr., Noordeen, H.H., Berven, S.H., Goytan, M.J., Boachie-Adjei, O., Shaffrey, C.I., 2011. Short-term morbidity and mortality associated with correction of thoracolumbar fixed sagittal plane deformity: a report from the Scoliosis Research Society Morbidity and Mortality Committee. *Spine (Phila Pa 1976)* 36, 958-964.
- Smith, T.S., Bay, B.K., Rashid, F., 2002. Digital Volume Correlation Including Rotational Degrees of Freedom during Minimization. *Experimental Mechanics* 42, 272 - 278.
- Sobczak, S., Salvia, P., Dugailly, P.M., Lefevre, P., Feipel, V., Van Sint Jan, S., Rooze, M., 2011. Use of embedded strain gages for the in-vitro study of proximal tibial cancellous bone deformation during knee flexion-extension movement: development, reproducibility and preliminary results of feasibility after frontal low femoral osteotomy. *Journal of Orthopaedic Surgery and Research* 6, 1 - 10.
- Soons, J., Lava, P., Debruyne, D., Dirckx, J., 2012. Full-field optical deformation measurement in biomechanics: digital speckle pattern interferometry and 3D digital image correlation applied to bird beaks. *J Mech Behav Biomed Mater* 14, 186-191.
- Spencer, M., Siegmund, T., Mongeau, L., 2008. Determination of superior surface strains and stresses, and vocal fold contact pressure in a synthetic larynx model using digital image correlation. *J Acoust Soc Am* 123, 1089-1103.
- Spera, D., Genovese, K., Voloshin, A., 2011. Application of Stereo-Digital Image Correlation to Full-Field 3-D Deformation Measurement of Intervertebral Disc. *Strain* 47, e572-e587.
- Stagni, R., Fantozzi, S., Cappello, A., 2009. Double calibration vs. global optimisation: performance and effectiveness for clinical application. *Gait Posture* 29, 119-122.
- Stock, S.R., 2009. *MicroComputed Tomography: Methodology and Applications*. Taylor and Francis Group.
- Stokes, I., 1987. Surface Strain on Human Intervertebral Discs. *Journal of Orthopaedic Research* 5, 348-355.
- Stoller, D.W., 2006. *Magnetic Resonance Imaging in Orthopaedics And Sports Medicine*, 3rd ed.
- Sutton, M.A., Ke, X., Lessner, S.M., Goldbach, M., Yost, M., Zhao, F., Schreier, H.W., 2008a. Strain field measurements on mouse carotid arteries using microscopic three-dimensional digital image correlation. *Journal of biomedical materials research. Part A* 84, 178-190.

- Sutton, M.A., Orteu, J.J., Schreier, H.W., 2009. *Image Correlation for Shape, Motion and Deformation Measurements*. Springer Science.
- Sutton, M.A., Wolters, W.J., Peters, W.H., Ranson, W.F., McNeill, S.R., 1983. Determination of displacement using an improved digital image correlation method. *Image and Vision Computing* 1, 133 - 139.
- Sutton, M.A., Yan, J.H., Tiwari, V., Schreier, H.W., Orteu, J.J., 2008b. The effect of out-of-plane motion on 2D and 3D digital image correlation measurements. *Optics and Lasers in Engineering* 46, 746-757.
- Sztefek, P., Vanleene, M., Olsson, R., Collinson, R., Pitsillides, A.A., Shefelbine, S., 2010. Using digital image correlation to determine bone surface strains during loading and after adaptation of the mouse tibia. *Journal of biomechanics* 43, 599-605.
- Tafazzol, A., Arjmand, N., Shirazi-Adl, A., Parnianpour, M., 2014. Lumbopelvic rhythm during forward and backward sagittal trunk rotations: combined in vivo measurement with inertial tracking device and biomechanical modeling. *Clinical biomechanics* 29, 7-13.
- Tan, T., Davis, F.M., Gruber, D.D., Massengill, J.C., Robertson, J.L., De Vita, R., 2015. Histo-mechanical properties of the swine cardinal and uterosacral ligaments. *J Mech Behav Biomed Mater* 42, 129-137.
- Tanasic, I., Milic-Lemic, A., Tihacek-Sojic, L., Stancic, I., Mitrovic, N., 2012. Analysis of the compressive strain below the removable and fixed prosthesis in the posterior mandible using a digital image correlation method. *Biomech Model Mechanobiol* 11, 751-758.
- Tancioni, F., Lorenzetti, M.A., Navarra, P., Pessina, F., Draghi, R., Pedrazzoli, P., Scorsetti, M., Alloisio, M., Santoro, A., Rodriguez y Baena, R., 2011. Percutaneous vertebral augmentation in metastatic disease: state of the art. *J Support Oncol* 9, 4-10.
- Tang, T., Ebacher, V., Cripton, P., Guy, P., McKay, H., Wang, R., 2015. Shear deformation and fracture of human cortical bone. *Bone* 71, 25-35.
- Taylor, J.R., 1975. Growth of human intervertebral discs and vertebral bodies. *J. Anat.* 120, 49-68.
- Tayton, E., Evans, S., O'Doherty, D., 2010. Mapping the strain distribution on the proximal femur with titanium and flexible-stemmed implants using digital image correlation. *Journal of Bone & Joint Surgery, British Volume* 92-B, 1176-1181.
- Thompson, M.L., Backman, D., Branemark, R., Mechefske, C.K., 2011. Evaluating the bending response of two osseointegrated transfemoral implant systems using 3D digital image correlation. *Journal of biomechanical engineering* 133, 051006.
- Thompson, M.S., Schell, H., Lienau, J., Duda, G.N., 2007. Digital image correlation: a technique for determining local mechanical conditions within early bone callus. *Med Eng Phys* 29, 820-823.
- Turner, P.J., Wyss, P., Voide, R., Stauber, M., Stampanoni, M., Sennhauser, U., Müller, R., 2006. Time-lapsed investigation of three-dimensional failure and

damage accumulation in trabecular bone using synchrotron light. *Bone* 39, 289 - 299.

Tiossi, R., Lin, L., Conrad, H.J., Rodrigues, R.C., Heo, Y.C., de Mattos Mda, G., Fok, A.S., Ribeiro, R.F., 2012. Digital image correlation analysis on the influence of crown material in implant-supported prostheses on bone strain distribution. *J Prosthodont Res* 56, 25-31.

Tiossi, R., Lin, L., Rodrigues, R.C., Heo, Y.C., Conrad, H.J., de Mattos Mda, G., Ribeiro, R.F., Fok, A.S., 2011. Digital image correlation analysis of the load transfer by implant-supported restorations. *Journal of biomechanics* 44, 1008-1013.

Titarenko, S., Withers, P.J., Yagola, A., 2010. An analytical formula for ring artefact suppression in X-ray tomography. *Applied Mathematics Letters* 23, 1489-1495.

Tozzi, G., Dall'Ara, E., Palanca, M., Curto, M., Innocente, F., Cristofolini, L., 2017. Strain uncertainties from two DVC approaches in prophylactically augmented vertebrae: local analysis on bone and bone-cement microstructures. *Journal of the Mechanical Behavior of Biomedical Materials* 67, 117-126.

Tozzi, G., Danesi, V., Palanca, M., Cristofolini, L., 2016. Elastic Full-Field Strain Analysis and Microdamage Progression in the Vertebral Body from Digital Volume Correlation. *Strain* 52, 446-455.

Tozzi, G., Zhang, Q.H., Lupton, C., Tong, J., Guillen, T., Ohrndorf, A., Christ, H.J., 2013. Characterisation of a metallic foam-cement composite under selected loading conditions. *J Mater Sci Mater Med* 24, 2509-2518.

Tozzi, G., Zhang, Q.H., Tong, J., 2012. 3D real-time micromechanical compressive behaviour of bone-cement interface: experimental and finite element studies. *Journal of biomechanics* 45, 356-363.

Tozzi, G., Zhang, Q.H., Tong, J., 2014. Microdamage assessment of bone-cement interfaces under monotonic and cyclic compression. *Journal of biomechanics* 47, 3466 - 3474.

Tyson, J., Schmidt, T., Galanulis, K., 2002. Biomechanics deformation and strain measurements with 3D image correlation photogrammetry. *Experimental techniques* 26, 39 - 42.

Vaananen, S.P., Amin Yavari, S., Weinans, H., Zadpoor, A.A., Jurvelin, J.S., Isaksson, H., 2013. Repeatability of digital image correlation for measurement of surface strains in composite long bones. *Journal of biomechanics* 46, 1928-1932.

Van Rietbergen, B., Weinans, H., Huiskes, R., Odgaard, A., 1995. A New Method to Determine Trabecular Bone Elastic Properties and Loading Using Micromechanical Finite-Element Models. *Journal of biomechanics* 28, 69-81.

Verhulp, E., van Rietbergen, B., Huiskes, R., 2004. A three-dimensional digital image correlation technique for strain measurements in microstructures. *Journal of biomechanics* 37, 1313-1320.

Verhulp, E., van Rietbergen, B., Huiskes, R., 2006. Comparison of micro-level and continuum-level voxel models of the proximal femur. *Journal of biomechanics* 39, 2951-2957.

- Viceconti, M., Henney, A., Morley-Fletcher, E., 2016. *in silico* Clinical Trials: How Computer Simulation will Transform the Biomedical Industry. Research and Technological Development Roadmap, in: Consortium, A. (Ed.), Brussels.
- Wahba, G., 1975. Smoothing Noisy Data with Spline Function. *Numerische Mathematik* 24, 383-393.
- Wang, C.C.B., Chahine, N.O., Hung, C.T., Ateshian, G.A., 2003. Optical determination of anisotropic material properties of bovine articular cartilage in compression. *Journal of biomechanics* 36, 339-353.
- Wang, C.C.B., Deng, J.-M., Ateshian, G.A., Hung, C.T., 2002. An Automated Approach for Direct Measurement of Two-Dimensional Strain Distributions Within Articular Cartilage Under Unconfined Compression. *Journal of biomechanical engineering* 124, 557.
- Wang, S., Park, W.M., Kim, Y.H., Cha, T., Wood, K., Li, G., 2014. In vivo loads in the lumbar L3-4 disc during a weight lifting extension. *Clinical biomechanics* 29, 155-160.
- Wang, X.-Y., Dai, L.-Y., Xu, H.-Z., Chi, Y.-L., 2007. The Load-Sharing Classification of Thoracolumbar Fractures: An In Vitro Biomechanical Validation. *Spine* 32, 1214-1219 [10.1097/BRS.1210b1013e318053ec318069](https://doi.org/10.1097/BRS.1210b1013e318053ec318069).
- Wang, Y., Lava, P., Coppieters, S., De Strycker, M., Van Houtte, P., Debruyne, D., 2012. Investigation of the Uncertainty of DIC Under Heterogeneous Strain States with Numerical Tests. *Strain* 48, 453-462.
- Wang, Y., Sutton, M.A., Bruck, H.A., Schreier, H.W., 2009. Quantitative Error Assessment in Pattern Matching: Effects of Intensity Pattern Noise, Interpolation, Strain and Image Contrast on Motion Measurements. *Strain* 45, 160 - 178.
- Weinans, H., Blankevoort, L., 1995. Reconstruction of bone loading conditions from in vivo strain measurements. *Journal of biomechanics* 28, 739 - 744.
- Weisbecker, H., Pierce, D.M., Regitnig, P., Holzapfel, G.A., 2012. Layer-specific damage experiments and modeling of human thoracic and abdominal aortas with non-atherosclerotic intimal thickening. *J Mech Behav Biomed Mater* 12, 93-106.
- Wentzell, S., Nesbitt, R.S., Macione, J., Kotha, S., 2015. Measurement of lacunar bone strains and crack formation during tensile loading by digital volume correlation of second harmonic generation images. *J Mech Behav Biomed Mater* 60, 148-156.
- White III, A.A., Panjabi, M.M., 1990. *Clinical Biomechanics of the Spine*, Second Edition ed. Lippincott Williams & Wilkins.
- WHO, 1994. Assessment of fracture risk and its application to screening for postmenopausal osteoporosis. Report of a WHO study group. WHO Technical Report Series, World Health Organization, Geneva, Switzerland, 843: 1-130.
- WHO, 2004. scientific group on the assessment of osteoporosis at primary health care level, Brussels, Belgium.
- WHO, 2007. Scientific group on the assessment of osteoporosis at primary health care level, p. 17.

- Wilcox, R.K., 2004. The biomechanics of vertebroplasty: a review. *Proc Inst Mech Eng H* 218, 1-10.
- Wilke, H., Kettler, A.A., Claes, E.L., 1997. Are Sheep Spines a Valid Biomechanical Model for Human Spines? *Spine* 22, 2365-2374.
- Wilke, H.J., Geppert, J., Kienle, A., 2011. Biomechanical in vitro evaluation of the complete porcine spine in comparison with data of the human spine. *Eur Spine J* 20, 1859-1868.
- Wilke, H.J., Schmidt, H., Werner, K., Schmolz, W., Drumm, J., 2006. Biomechanical evaluation of a new total posterior-element replacement system. *Spine (Phila Pa 1976)* 31, 2790-2796; discussion 2797.
- Woltring, H.J., 1985. An Optimal Smoothing and Derivative Estimation from Noisy Displacement Data in Biomechanics. *Human Movement Science* 4, 229-245.
- Yamaguchi, H., Kikugawa, H., Asaka, T., Kasuya, H., Kuninori, M., 2011. Measurement of Cortical Bone Strain Distribution by Image Correlation Techniques and from Fracture Toughness. *Materials Transactions* 52, 1026-1032.
- Yang, P.F., Bruggemann, G.P., Ritteweger, J., 2011. What do we currently know from in vivo bone strain measurements in humans? *J. Musculoskelet Neuronal Interact* 11, 8 - 20.
- Yang, S.C., Chen, W.J., Yu, S.W., Tu, Y.K., Kao, Y.H., Chung, K.C., 2008. Revision strategies for complications and failure of vertebroplasties. *Eur Spine J* 17, 982-988.
- Yaofeng, S., Pang, J.H.L., 2007. Study of optimal subset size in digital image correlation of speckle pattern images. *Optics and Lasers in Engineering* 45, 967-974.
- Ye, J., Coleman, J., Hunter, M.G., Craigon, J., Campbell, K.H.S., Luck, M.R., 2007. Physiological temperature variants and culture media modify meiotic progression and developmental potential of pig oocytes *in vitro*. *Reproduction* 133, 877 - 886.
- Yoneyama, S., 2006. Lens distortion correction for digital image correlation by measuring rigid body displacement. *Optical Engineering* 45, 023602.
- Zander, T., Dreischarf, M., Schmidt, H., Bergmann, G., Rohlmann, A., 2015. Spinal loads as influenced by external loads: A combined in vivo and in silico investigation. *Journal of biomechanics* 48, 578-584.
- Zani, L., Erani, P., Grassi, L., Taddei, F., Cristofolini, L., 2015. Strain distribution in the proximal Human femur during in vitro simulated sideways fall. *Journal of biomechanics* 48, 2130-2143.
- Zael, R., Yeni, Y.N., Bay, B.K., Dong, X.N., Fyhrie, D.P., 2006. Comparison of the linear finite element prediction of deformation and strain of human cancellous bone to 3D digital volume correlation measurements. *Journal of biomechanical engineering* 128, 1-6.

- Zhang, D., Arola, D.D., 2004. Applications of digital image correlation to biological tissues. *J Biomed Opt* 9, 691-699.
- Zhang, D., Arola, D.D., Eggleton, C., 2002a. Measurement of Poisson's Ratio of Bovine Aorta Using Digital Image Correlation. *Proceedings of the Institution of Second Joint EMBS*, 1276 - 1277.
- Zhang, D., C.D., E., Arola, D.D., 2002b. Evaluating the Mechanical Behavior of Arterial Tissue using Digital Image Correlation. *Experimental Mechanics* 42, 409 - 416.
- Zhang, D., Nazari, A., Soappman, M., Bajaj, D., Arola, D., 2007. Methods for Examining the Fatigue and Fracture Behavior of Hard Tissues. *Experimental Mechanics* 47, 325-336.
- Zhang, J., Jin, G.C., Meng, L.B., Jian, L.H., Wang, A.Y., Lu, S.B., 2005. Strain and mechanical behavior measurements of soft tissues with digital speckle method. *J Biomed Opt* 10, 034021.
- Zhu, M.L., Zhang, Q.H., Lupton, C., Tong, J., 2015. Spatial resolution and measurement uncertainty of strains in bone and bone-cement interface using digital volume correlation. *J Mech Behav Biomed Mater* 57, 269-279.
- Zysset, P., Pahr, D., Engelke, K., Genant, H.K., McClung, M.R., Kendler, D.L., Recknor, C., Kinzl, M., Schwiedrzik, J., Museyko, O., Wang, A., Libanati, C., 2015. Comparison of proximal femur and vertebral body strength improvements in the FREEDOM trial using an alternative finite element methodology. *Bone* 81, 122-130.

Acknowledgments

At the end of this route, I would like to thank all the people who in a way or another contributed to the realization of this work. You're mentioned in random order because just few hours are left before the submission.

First of all, thanks to my family who supported me during these years, and sponsored me when the salary was too short and the month was too long. I hope you are happy of my choices.

Thanks to my friends, if I was enrolled in the PhD in Bioengineering, it is for your merit... or guilt. Thank you for the moments spent together.

Thanks to Prof. Harry van Lenthe and Prof. Angelo Cappello for reading my thesis and suggesting improvements.

Thanks to Dott. Gianluca Tozzi who welcomed me in Portsmouth, thanks for all the discussions and suggestions, you already know... I cannot forget that amazing August in England.

Thanks to Dott. Enrico Dall'Ara and sorry for having exasperated you with all my questions! You taught me actually a lot of matters from the biomechanics to the genius' humility, since the first Skype call. Thanks Enrico!

Of course, thanks to the guys of Portsmouth and Sheffield, for the days of work and nights of parties.

A special thanks to my supervisor Prof. Luca Cristofolini. Luca thanks for giving me an opportunity, sorry more than an opportunity, your knowledge, your suggestions and for introducing me to the science world. Today I can confirm, *non mi hai lasciato a piedi*. I'm very happy having known the man over the Professor. Again, thanks for these years. And, congratulation Luca for having created a fantastic working environment!

Kavin, Valentina, Alberto, Toti and Federico thank you! It was really a pleasure working with you and sharing our ideas! "Work hard play hard" is our maxim. This work would not have been possible without you.

Miguel, Kamila and Busra thank you for helping me during my projects. The time with you in the lab was really inspiring.

Thanks to the students: sometimes working with you was hard, but seeing you reaching your goals is really rewarding.

Last but not least, *una pioggia di ringraziamenti cada su Federica!* As you can see I kept in mind my promise. I hope you are proud of me. This thesis, which could inspire you in the future, is dedicated to you.

Probably now I'm forgetting someone. Anyway, sorry and thank you too!

Marco

Scientific Publications of the candidate

Papers in International Journals

Palanca M., Brugo T.M., Cristofolini L., 2015, Use of Digital Image Correlation to Understand the Biomechanics of the Vertebra, *Journal of Mechanics in Medicine and Biology*, 15(2): 1540004-1/1540004-10

Palanca M., Tozzi G., Cristofolini L., Viceconti M., Dall'Ara E., 2015, 3D Local Measurements of Bone Strain and Displacement: Comparison of Three Digital Volume Correlation Approaches, *Journal of Biomechanical Engineering*, 137(7): 071006-1/071006-14

Palanca M., Tozzi G., Cristofolini L., 2016, The Use Of Digital Image Correlation In The Biomechanical Field: A Review, *International Biomechanics*, 3(1): 1 – 21

Tozzi G., Danesi V., Palanca M., Cristofolini L., 2016, Elastic Full-Field Strain Analysis and Microdamage Progression in the Vertebral Body from Digital Volume Correlation, *Strain*, 52(5): 446-455

Palanca M., Cristofolini L., Dall'Ara E., Curto M., Innocente F., Danesi V., Cristofolini L., 2016, Digital Volume Correlation Can Be Used to Estimate Local Strains in Natural and Augmented Vertebrae: an Organ-level Study, *Journal of Biomechanics*, 49(16): 3882-3890

Tozzi G., Dall'Ara E., Palanca M., Curto M., Innocente F., Cristofolini L., 2017, Strain uncertainties from two DVC approaches in prophylactically augmented vertebrae: local analysis on bone and bone-cement microstructures, *Journal of Mechanical Behavior of Biomedical Materials*, 67: 117-126

Palanca M., Bodey A., Giorgi M., Viceconti M., Lacroix D., Cristofolini L., Dall'Ara E., 2016, Local Displacement and Strain Uncertainties in Different Bone Types by Digital Volume Correlation of Synchrotron micro-tomograms, *Journal of Biomechanics*, under revision

Palanca M., Marco M., Ruspi M.L., Faldini C., Cristofolini L., 2017, Exploring the strain distribution of thoracolumbar spine segments: An application of Digital Image Correlation, paper in preparation

Proceedings of International Conferences

Palanca M., Danesi V., Cristofolini L., Use of Digital Image Correlation to Investigate the Biomechanics of the Vertebra, International Conference on Mechanics in Medicine and Biology, Bologna (IT), September 2014

Danesi V., Tozzi G., Palanca M., Cristofolini L., Application of Digital Volume Correlation to Investigate the Strain Distribution in Augmented Vertebral Body, International Conference on Mechanics in Medicine and Biology, Bologna (IT), September 2014

Palanca M., Tozzi G., Dall'Ara E., Viceconti M., Cristofolini L., Comparison of Three Different Digital Volume Correlation Approaches on Bone, European Society of Biomechanics, Praha (CZ), July 2015

Tozzi G., Palanca M., Dall'Ara E., Viceconti M., Cristofolini L., Accuracy and Precision of Digital Volume Correlation on Different Bone-Biomaterials Constructs, International Conference on Computational Bioengineering, Barcelona (ES), September 2015

Palanca M., Tozzi G., Cristofolini L., Accuracy and Precision of three Digital Volume Correlation Approaches, International Conference in Experimental Mechanics, Edinburgh (UK), September 2015

Palanca M., Tozzi G., Dall'Ara E., Cristofolini L., Strain Uncertainties of Global and Local Digital Volume Correlation Approaches in Bone at Organ Level, Postgraduate Experimental Mechanics Conference, Southampton (UK), November 2015

Palanca M., Bodey A., Viceconti M., Lacroix D., Cristofolini L., Dall'Ara E., Strain Measurement Uncertainties of Global Digital Volume Correlation Approach Based on Synchrotron Microtomograms of Bone, European Society of Biomechanics, Lyon (FR), July 2016

Tozzi G., Palanca M., Cristofolini L., Kinene E., Blunn G., Strain Uncertainties from Digital Volume Correlation in pedCAT Clinical CT: a Feasibility Study, European Society of Biomechanics, Lyon (FR), July 2016

Marco M., Ozog K., Palanca M., Cristofolini L., Displacements and Strains in Multi-Vertebra Spine Segments Measured by means of Digital Image Correlation, European Society of Biomechanics, Lyon (FR), July 2016

Palanca M., Bodey A., Viceconti M., Lacroix D., Cristofolini L., Dall'Ara E., Synchrotron radiation for microtomography improves the precision of digital volume correlation for bone samples, Europeans Orthopaedic Research Society, Bologna (IT), September 2016

Palanca M., Marco M., Ozog K., Cristofolini L., In vitro evaluation of strain on a spine segment using a non-contact measurement technique, European Orthopaedic Research Society, Bologna (IT), September 2016

Palanca M., Cristofolini L., Pani M., Kinene E., Blunn G., Madi K., Tozzi G.,
Feasibility Study for a Clinical Application of Digital Volume Correlation,
European Orthopaedic Research Society, Bologna (IT), September 2016

Proceedings of National Conferences

Palanca M., Studio della biomeccanica delle vertebre attraverso correlazione digitale di immagini, Associazione Italiana per Analisi delle Sollecitazioni, Rimini, September 2014

Palanca M., Tozzi G., Dall'Ara E., Viceconti M., Cristofolini L., Evaluation of the Accuracy and Precision of a Local Digital Volume Correlation Approach, European Society of Biomechanics – Capitolo Italiano, Milano, June 2015

Palanca M., Marco M., Ozog K., Cristofolini L., The evaluation of strain on spine segments in a contactless way and full-field view, European Society of Biomechanics – Capitolo Italiano, Napoli, June 2016